University of Trento

Department of physics

Experiments with Coherently-Coupled Bose-Einstein condensates: from magnetism to cosmology

Doctoral Thesis
submitted to the
Doctoral School of Physics - XXXVI Cycle
by

Riccardo Cominotti

for the degree of
Doctor of Philosophy - Dottore di Ricerca

Supervisor: Gabriele Ferrari
Referees: Karina Jiménez-García
Chiara Fort

November 2023

Riccardo Cominotti

Experiments with Coherently-Coupled Bose-Einstein condensates: from magnetism to cosmology

Ph.D. Thesis in Physics

Università di Trento

November 2023

To my family,
to my Lab,
to all my friends around the world,
to Casa Veneto,
to Meri.

Contents

List of Figures

List of Tables

Introduction

The physics of ultracold atomic gases has been the subject of a long standing theoretical and experimental research over the last half century. The development of evaporative cooling techniques and the realization of the first Bose-Einstein Condensate (BEC) in 1995 gave a great advantage to the field, leading to the development of many laboratories all over the world, investigating different atomic species and physical phenomena. A great experimental knowledge of the fundamental properties of BECs, such as long-range coherence, superfluidity and topological excitations, has now been acquired. On top of these advances, current research on ultracold atoms is also focusing on quantum simulations, which aim at building analogue models of otherwise difficult to compute physical systems in the lab. In this context, BECs, with their enhanced coherence, many-body dynamics and superfluid character offer a powerful platform for advances in the field.

Shortly after the first realization of a BEC, research started also investigating the physics of quantum mixtures of a BECs, either composed of different atomic species or isotopes, or of atoms occupying different hyperfine states. The latter are known as spin mixtures, or spinor condensates. The presence of multiple components interacting through mutual contact interactions enriches the physics of the condensate, introducing ground states with magnetic ordering as well as spin dynamics, which can be order of magnitudes less energetic than the density one. On top of this, hyperfine states can be coherently coupled with an external resonant radiation, either homogeneous or localized in space. Interesting physics arises when the strength of the coupling is comparable with the energy of spin excitations, an example of which is given by the emergence of the internal Josephson effect. This regime has been the subject of intense theoretical studies in the past twenty years, however its experimental realization on ultracold atomic platforms have been proven to be challenging, with experiments strongly limited by coherence times of few tens of milliseconds. In fact, the small energy scale of spin excitations reflects in a high sensitivity coupling to environmental magnetic noise, which affects the resonant condition. The experimental apparatus on which I worked during my Ph.D. solve this problem employing a magnetic shield that surrounds the science chamber, attenuating external magnetic fields by 6 orders of magnitudes.

During the course of my Ph.D., I investigated the properties of a coherently coupled mixture of BEC of ^{23}Na, performing different experiments in two atomic configurations. The first configuration consist of a mixture of hyperfine states, namely the $|\mathrm{F}=1,\mathrm{m_F}=-1\rangle$ and $|\mathrm{F}=1,\mathrm{m_F}=+1\rangle$, which is characterized by miscibility in the ground state. This mixture, coupled by a two-photon transition, has the peculiar properties of being equivalent under the exchange of the two species, and of having an energy scale for the spin excitations order of magnitudes lower than the density one, effectively decoupling the dynamics of spin and density degrees of freedom. Another configuration was instead realized working with a strongly immiscible mixture of $|\mathrm{F}=1,\mathrm{m_F}=-1\rangle$ and $|\mathrm{F}=2,\mathrm{m_F}=-2\rangle$. With respect to the miscible states, this mixture is not equivalent upon the exchange of particles, but it can be easily coupled with a one photon transition, and, most importantly, it is robust against spin changing collisions, that might induce atom loss.

My first experiment was devoted to the characterization of different methods of manipulation of the coupled miscible mixture in an elongated quasi-1D geometry. The dynamics of the system, in Local Density Approximation (LDA), can be fully described as an internal Josephson junction. The Josephson effect may arise in quantum systems when a macroscopic wavefunction is distributed in two weakly coupled quantum states, with the mean field energy of each state depending on the average number of particles in the respective state. In this case, the dynamics depends on the atom number difference, the relative phase, and coupling to mean field energy ratio. Josephson physics has been first studied in superconductors, and recently it was extended to cold atomic systems in point-like geometries. In our work, we characterized the dynamics of an extended Josephson junctions with an inhomogeneous spatial profile, developing three different protocols for state manipulations. Remarkably, one of the three protocols, relying on an Adiabatic Rapid Passage technique, gives rise to a state of homogeneous zero magnetization despite the non-homogeneity in the density profile.

In a second experiment, I developed a protocol to generate Faraday waves in an unpolarized miscible mixture. Faraday waves are classical non-linear waves characterized by a regular pattern, that originate in classical and quantum fluids via a parametric excitation in the fluid. In quantum fluids, it can be demonstrated that they originate through the interference of pairs of phonons with opposite momentum, generated parametrically in the bulk. The energy, fixed by the frequency of the modulation, and the wavevector of the emitted phonons are linked by the dispersion relation of elementary excitations, which in the case of a BEC are Bogoliubov quasi-particles. Interestingly enough, this process resembles the phase of reheating of the early universe, where the oscillation of the inflaton field is thought to have excited particles out of the vacuum. In analogy with this phenomenon, the oscillation of the inflaton field can be simulated with the periodic modulation of the trapping potential.
In a spin mixture, the parametric modulation can excite either in-phase (density) modes or out-of-phase (spin) modes, as two possible elementary excitations are present in the system. By extracting the spatial periodicity of the generated pattern at different modulation frequencies, I was then able to measure the dispersion relations for both density

and spin modes of the system. In the presence of the coherent coupling, when spin excitations becomes gapped, we further demonstrate the scaling of the gap with the strength of the coupling radiation.

The third experiment I realized concerned the characterization of the magnetic ground state of a spatially extended immiscible mixture in the presence of the coherent coupling. The Hamiltonian of such a system is formally equivalent, in one dimension, to a continuous version of the transverse field Ising model, which describes magnetic materials at zero temperature. In this mapping, a nonlinear interaction term arises from the ratio between the self-interaction energy and the strength of the coupling, which acts as the *transverse field*. As the ratio between the two quantities is varied above and below one, the ground state of the system spontaneously changes from a paramagnetic phase to an ordered ferromagnetic phase, featuring two equivalent and opposite magnetizations, a signature of the occurrence of a second order quantum phase transition (QPT). Furthermore, in the magnetic model, the degeneracy between the two ferromagnetic ground states can be broken by introducing an additional *longitudinal field*, using the ordinary notation of magnetism in condensed matter physics. In the atomic case, the role of this additional field is taken by the detuning between the coupling radiation and the resonant transition frequency of non-interacting atoms.
While the transition between the two paramagnetic and ferromagnetic phases have been already studied both theoretical and experimentally with quench protocols, a full experimental characterization of the ground state was still missing, due to the lack of both long coherence times and a spatial degrees of freedom in extended geometries. Such a control of the ground state in the different magnetic phases would be of paramount importance for the study of magnetic phenomena in a defect free environment.
I characterized the QPT developing protocols to manipulate the spin mixture in its spatially extended ground state, varying the longitudinal field. Leveraging on the inhomogeneity of a BEC trapped in the harmonic potential, a smooth variation of the spin self-interaction energy occurs spontaneously in space, introducing different magnetic regimes at fixed coupling strength. These protocols gave access to a characterization of static properties typical of magnetic materials, such as the presence of an hysteresis cycle, that occurs when varying the detuning of the coupling (longitudinal field). The occurrence of the phase transition was instead validated by a measurement of the magnetic susceptibility and corresponding fluctuations, which both show a divergence when crossing the QPT critical point. At last, I developed a protocol to smoothly manipulate the position of magnetic domain walls, the least energetic excitations in a ferromagnet. The smooth control of the excitations stems from the superfluid character of the BEC. All the results were validated by GPE simulations and theoretical calculations.

While the previous study focused on static properties, the last experimental investigation presented in my thesis was devoted to the study of the dynamics of the metastable ferromagnetic region of the BEC. As a result of the presence of an hysteresis cycle, by tuning the detuning it is possible to engineer states of the ferromagnetic energy landscape that are homogeneously prepared either in the global minimum, with trivial dynamics, or in the metastable, higher energy, local minima. In the latter case, a classical system

should eventually decay towards the global minimum, driven by temperature fluctuations which overtop the energy barrier separating the two minima. For a quantum system described by a field theory, such as a ferromagnetic BEC, this process is of different nature, as it occurs by tunneling through the barrier, triggered by quantum fluctuations. The event of tunneling is known as False Vacuum Decay (FVD), and is of outstanding relevance also for high energy physics and cosmology, were the first theoretical models were developed. In the FVD model, the decay towards the global minimum, the *true vacuum*, is a stochastic process that occurs only if a resonant bubble of true vacuum is formed. Once formed, the bubble will eventually expand throughout the whole system, as the true vacuum is energetically favourable. The probability for such a bubble to form can be approximately calculated analytically in 1D, and should depend exponentially on the height of the barrier the field has to tunnel through. Due to the exponentially long time scale of the process, experimental observations of FVD were still lacking.
Thanks to the enhanced coherence time of the superfluid ferromagnetic mixture, and to the precise control of the barrier height through the detuning from atomic resonance, we were able to observe the event of bubble nucleation in a ferromagnetic BEC. To corroborate the observation, I measured the characteristic timescale of the decay for different values of the control parameters. Results were successfully compared first with numerical simulation, and then validated by instanton theory.

Thesis Structure

- The first chapter contains a brief review of theoretical concept and literature on the main topics of this thesis. I introduce the mathematical description, starting from a GPE formulation of a coherently coupled spin mixture, and review the key theoretical and experimental results, defining the current state of the art in the field.
- In the second chapter I describe the experimental apparatus on which I worked, focusing on the experimental methods used to manipulate the mixture, and the constraints imposed by the regime of low coherent coupling strength.
- The third chapter describes and compare different methods for the experimental manipulation of a miscible mixture in the presence of coherent coupling.
- In the fourth chapter, I report on the observation of Faraday waves in miscible spin mixture in the absence and presence of coherent coupling. I first describe the protocol, then the image analysis method used to extract the periodic pattern of Faraday waves. This technique allows for the accurate measurement of the dispersion relations of elementary excitations in the mixture.
- The fifth chapter is devoted to the characterization of the ferromagnetic ground state of the coherently coupled immiscibile mixture. I first describe the map-

ping between the atomic Hamiltonian and a semiclassical energy functional of a continuous magnetic material. I then describe the experimental protocol used to characterize the system, focusing on the role of systematic errors introduced by the experimental procedure and the dimensionality of the sample. Experimental evidence of ferromagnetic behaviour, as well as the occurrence of a paramagnetic-ferromagnetic QPT, are then reported.

- In the sixth chapter I discuss the observation of False Vacuum Decay in a superfluid metastable ferromagnetic mixture. After discussing the theory of FVD and how it applies to coherently coupled BECs, I describe the protocol used to generate bubbles of true vacuum from the metastable ferromagnetic state. The observation of bubbles is then reported, along with a measurement of the scaling of the characteristic decay rate with respect to control parameters.

Chapter 1

Theoretical Background on Bose-Bose Mixtures

Contents

Bose-Einstein condensation is a many-body phase transition, arising from quantum statistics in a system of indistinguishable bosons. Its experimental realization almost 30 years ago in a gas of ultracold atoms [1] opened the way towards a plethora of studies on ultracold atomic gases, later extended to other platforms of bosonic systems, such as polariton condensates [2] and photon BECs in cavity [3]. The research in the field of atomic BEC now addresses both fundamental questions about the nature and the dynamics of quantum many-body systems, as well as its implementation as an analogue system.

A subfield of research focuses on characterization of multi-species BECs, where two atomic species are Bose-condensed together. The species can be either heteronuclear, or homonuclear with different internal states. In the latter case, the scenario can be further enriched by adding a coherent coupling term between the two atomic species.

In this Chapter I will provide the theoretical tools that will be used throughout the rest of this Thesis. I will first start introducing the Gross-Pitaevskii formalism for both single and two-component systems. I will then show how, in the presence of coherent radiation that couples the two states, the equations can be recasted in a more general equation of

motion for the field, which carries analogy with other sectors of physics, e.g., magnetic systems.

1.1 Bose-Einstein condensation and Gross-Pitaevskii equation

Bose-Einstein condensation is a phase transition occurring when a gas of identical bosons, once cooled below critical temperature T_c, that depends on its density, macroscopically occupies the ground state of the system.
As a result of the spontaneous symmetry breaking of a U(1) symmetry, the system is characterized by the emergence of a complex order parameter, the *condensate wavefunction*, which describes the macroscopic state of the system and it features long-range order.

Gross-Pitaevskii equation. Bose-Einstein condensation emerges from quantum statistical mechanics, and theoretically can occur in ideal systems of non-interacting particles. However, a more realistic description must take into account interactions between particles.
A useful approximation, for ordinary experimental conditions, in the regime of *weak coupling*, considers interactions among particles via elastic 2-body collisions, with s-wave scattering length a. Typically, this regime is characterized by the diluteness condition $na^3 \ll 1$ [4], with n the atomic density of the cloud, usually in the order of 10^{20} m^{-3}, while a is in the order of few tens of the Bohr radius [5].
The Hamiltonian of the N-body system can then be expressed in terms of the field operator $\hat{\psi}(\boldsymbol{r})$:

$$\begin{aligned}\hat{H} = &\int d\boldsymbol{r}\hat{\psi}^\dagger(\boldsymbol{r})\Big(-\frac{\hbar^2}{2m}\boldsymbol{\nabla}^2 + V_{\text{ext}}(\boldsymbol{r})\Big)\hat{\psi}(\boldsymbol{r}) \\ &+ \frac{1}{2}\int d\boldsymbol{r}d\boldsymbol{r'}\hat{\psi}^\dagger(\boldsymbol{r'})\hat{\psi}^\dagger(\boldsymbol{r})V(\boldsymbol{r'}-\boldsymbol{r})\hat{\psi}(\boldsymbol{r'})\hat{\psi}(\boldsymbol{r})\end{aligned} \tag{1.1}$$

where $V_{\text{ext}}(\boldsymbol{r})$ is the external trapping potential and $V(\boldsymbol{r'}-\boldsymbol{r})$ is the two-body potential. This Hamiltonian, being expressed in terms of a quantum field, fully describes the dynamics of the system, which obeys the equation of motion $i\hbar\frac{\partial\hat{\psi}}{\partial t} = [\hat{\psi}, \hat{H}]$. To first approximation, one can neglect quantum fluctuations and obtain a classical equation of motion for the quantum field $\hat{\psi}$, substituting it with a complex classical field $\psi(\boldsymbol{r}) = \sqrt{n(\boldsymbol{r})}e^{i\phi}$, where ϕ is the phase of the condensate. This substitution is correct only if the field function is normalized to the total number of particles N, i.e. all the particles occupy the ground state. In this case, one can also correctly substitute the two-body potential V with an effective potential V_{eff}, that relies on the Born-Oppenheimer approximation. This approximated potential smears out any short-range details of the scattering problem, considering only low momenta interactions. Keeping into account

the low energy behaviour of the atomic cloud, it can be further expressed via a constant potential term parametrized by the *coupling constant*

$$g = \frac{4\pi\hbar^2 a}{m}, \tag{1.2}$$

which depends only on the scattering length a. Solving the Heisenberg equation with the simplified potential, and substituting the quantum field with its classical counterpart, we obtain the notorious Gross-Pitaevskii equation (GPE):

$$i\hbar\frac{\partial\psi(\boldsymbol{r},t)}{\partial t} = \Big(-\frac{\hbar^2}{2m}\boldsymbol{\nabla}^2 + V_{\text{ext}}(\boldsymbol{r}) + g|\psi(\boldsymbol{r},t)|^2\Big)\psi(\boldsymbol{r},t) \tag{1.3}$$

The GPE fully describes the dynamics of the condensate wavefunction in the limit $N \to \infty$, as it contains a mean-field interaction term, which is a valid approximation in the thermodynamic limit. Although the external potential V_{ext} can take arbitrary shapes, in the experiments presented in this thesis we will use an axially symmetric 3D harmonic confinement with shape:

$$V_{\text{ext}}(x, r_\perp) = \frac{1}{2}m(\omega_x^2 x^2 + \omega_\perp^2 r_\perp^2) \tag{1.4}$$

with ω_x, $\omega_\perp$ the angular trapping frequency along the axial and perpendicular directions, and $r_\perp^2 = z^2 + y^2$ the radial direction in cylindrical coordinates.
Notice that the GPE can be also derived by converting Eq. 1.1 in an energy functional, upon the substitution of $\hat{\psi} \to \psi$. Applying a variational principle we obtain [6]:

$$i\hbar\frac{\partial\psi(\boldsymbol{r},t)}{\partial t} = \frac{\partial E}{\partial\psi^*(\boldsymbol{r},t)} \tag{1.5}$$

Thomas-Fermi limit. Ground state properties of the condensed state can be obtained looking for stationary solutions of the GPE. The time dependence is factorized in the phase factor, which evolves as $\phi = \mu t/\hbar$. Here, μ is the chemical potential, defined as $\mu = \partial E/\partial N$. A good approximation, for spatially homogeneous or slowly varying settings, is to neglect the *quantum pressure* term $\hbar^2\boldsymbol{\nabla}^2/2m$ in the GPE. In this limit, known as *Thomas-Fermi limit*, we obtain a simple solution for the density of the BEC, $n(\boldsymbol{r}) = |\psi|^2$:

$$n(\boldsymbol{r}) = \begin{cases} \frac{\mu - V_{\text{ext}}(\boldsymbol{r})}{g} & \mu > V_{\text{ext}}(\boldsymbol{r}), \\ 0 & \mu < V_{\text{ext}}(\boldsymbol{r}). \end{cases} \tag{1.6}$$

This equation shows that the *density* distribution of the condensate is fixed by the external potential, which for a harmonic trap is given by an inverted parabola with peak density $gn_0 = \mu$ in the center of the trap. This is also the expression that relates the chemical potential to the density in the case of vanishing spatial curvature of the trapping potential. The chemical potential can be derived from the normalization condition $\int d\boldsymbol{r}|\psi(\boldsymbol{r})|^2| = N$, and for harmonic confinement reads [4, 6]

$$\mu = \frac{\hbar\omega_{ho}}{2}\left(15\frac{Na}{a_{ho}}\right)^{2/5} \tag{1.7}$$

Here, $a_{ho} = \sqrt{\hbar/(m\omega_{ho})}$ is the oscillator length associated to the geometrical average $\omega_{ho} = \sqrt[3]{\omega_x \omega_\perp^2}$ of the two oscillator angular frequencies. The dimensions of the condensate, the so called *Thomas-Fermi radii*, R_x and $R_\perp$, are also fixed by the chemical potential and the trapping frequencies, and can be calculated from Eq. 1.6 as:

$$R_i = \sqrt{\frac{2\mu}{m\omega_i^2}} \tag{1.8}$$

with $i = x, \perp$.
The quantum pressure term becomes instead relevant if the density varies abruptly on a length scale such that the kinetic energy balances the interaction energy. The length scale ξ at which this occurs reads [6, 4]:

$$\xi = \frac{\hbar}{\sqrt{2mgn}} \tag{1.9}$$

and is called *healing length*, as it gives the minimum size of an excitation in the condensate. Typically, the healing length is much larger than the atomic separation distance.

Fundamental excitations and dispersion relations. So far we discussed the static properties of the condensate, extracted from the stationary solution of the GPE. Perturbations, however, might occur either in the density or in the phase of a condensate. We can extract an expression for their dynamics by linearizing the GPE around equilibrium, i.e., by solving the GPE for $\psi(\boldsymbol{r},t)e^{-i\mu t/\hbar} \to (\psi(\boldsymbol{r}) + \delta\psi(\boldsymbol{r},t))e^{-i\mu t/\hbar}$, with $\delta\psi$ a complex field [6, 7]. Neglecting all terms $\delta\psi^2$, we get two coupled equations:

$$\begin{aligned} i\hbar\frac{\partial\delta\psi}{\partial t} &= (H_0 - \mu + 2gn)\delta\psi + g\psi^2\delta\psi^* \\ -i\hbar\frac{\partial\delta\psi^*}{\partial t} &= (H_0 - \mu + 2gn)\delta\psi^* + g(\psi^*)^2\delta\psi \end{aligned} \tag{1.10}$$

with $H_0 = -\frac{\hbar^2\boldsymbol{\nabla}^2}{2m} + V_{\text{ext}}$. We can now expand the perturbation, looking for solutions which are periodic in time as $\delta\psi(\boldsymbol{r},t) = \sum_k u_k(\boldsymbol{r})e^{-i\omega t} + v_k^*(\boldsymbol{r})e^{i\omega t}$. By collecting all terms which evolve as $e^{i\omega_k t}$ and $e^{-i\omega_k t}$, we obtain two coupled equations known as *Bogoliubov equations*:

$$\begin{aligned} \hbar\omega_k u_k(\boldsymbol{r}) &= (H_0 - \mu + 2gn(\boldsymbol{r}))u_k(\boldsymbol{r}) + gn(\boldsymbol{r})v_k(\boldsymbol{r}) \\ -\hbar\omega_k v_k(\boldsymbol{r}) &= (H_0 - \mu + 2gn(\boldsymbol{r}))v_k(\boldsymbol{r}) + gn(\boldsymbol{r})u_k(\boldsymbol{r}) \end{aligned} \tag{1.11}$$

In the particular case of a uniform gas, $V_{\text{ext}} = 0$, $\mu = gn$, and the two amplitudes u_k and v_k are plane waves, with momentum k. One can then recast the two coupled equations in a system:

$$\begin{pmatrix} \frac{\hbar^2k^2}{2m} + gn - \hbar\omega_k & gn \\ gn & \frac{\hbar^2k^2}{2m} + gn + \hbar\omega_k \end{pmatrix} \begin{pmatrix} u_k \\ v_k \end{pmatrix} = \begin{pmatrix} 0 \\ 0 \end{pmatrix} \tag{1.12}$$

which admits a simple analytical solution, called the *dispersion relation*, as it relates the angular frequency ω of the excitation to its momentum k:

$$\hbar\omega(k) = \sqrt{\frac{\hbar^2 k^2}{2m}\left(\frac{\hbar^2 k^2}{2m} + 2gn\right)}. \tag{1.13}$$

The dispersion relation admits two different regimes. The first can be found at $k \to 0$, and is called the *phononic* regime, as $\omega(k) \approx ck$, with $c = \sqrt{gn/m}$ the sound velocity. These modes corresponds to collective excitations, or phonons, propagating in the condensate. They can be also identified with Goldstone modes, associated with the *spontaneous* breaking of the gauge symmetry occurring at the transition towards the condensed state. In the opposite regime we instead find that $\hbar\omega(k) = \frac{\hbar^2 k^2}{2m} + gn$, which can be identified with the dispersion relation of a free particle.
It is also interesting to point out that a similar result can be derived [8] starting from the full Hamiltonian, promoting the classical field ψ to a quantum field $\hat{\psi}$. The perturbation $\delta\psi$ can then be written as a quantum term, substituting $(u_p, v_p) \to (u_p\hat{a}_p, v_p\hat{a}_p^\dagger)$. Here, we introduced the creation and annihilation operators of the excitation of momentum p, that follow Bose commutation rules. The Hamiltonian can then be diagonalized, using the Bogoliubov relations, in the basis of the excitation $\hat{a}_k$, and reads $\hat{H} = \sum_k \hbar\omega_k \hat{a}_k^\dagger \hat{a}_k$. With this procedure, in the case of $V_{\text{ext}} = 0$, one recovers the result of Eq. 1.13.
However, this result is also valid in the case of harmonic trapping potential, as discussed in [4], provided that the wavevector of the excitation satisfy $k \gg L^{-1}$, where L is the dimension of the condensate. The dispersion relation of a BEC of ^{87}Rb atoms have been first measured in [9].

1.2 Quantum mixtures

The mean-field picture we have developed so far describes condensates with a single macroscopically occupied quantum state. It is however possible to trap simultaneously different atomic species, creating a *quantum mixture*. The dynamics becomes much richer, as it is also ruled by interactions between the two components, mediated by their mean-field energies.
One possibility to create a mixture is to reach quantum degeneracy with atoms of different atomic species, also called heteronuclear mixtures, with variable mass ratios. Mixtures of different statistics can be reached, realizing Bose-Bose, Fermi-Fermi or Bose-Fermi mixture. For instance, Bose-Bose mixtures have been realized with ^{41}K-^{87}Rb [10, 11], ^{7}Li-^{133}Cs [12], ^{87}Rb-^{133}Cs [13], Fermi-Fermi with ^{6}Li-^{40}K [14, 15], and recently with ^{161}Dy-^{40}K [16]. Bose-Fermi mixtures have been instead realized in ^{7}Li-^{6}Li [17, 18], ^{23}Na-^{6}Li [19], and ^{87}Rb-^{40}K [20]. In all these realizations, the populations of the two species are fixed, leaving the equilibrium and the dynamic properties governed uniquely by intra- and inter-component mean-field energies.
Another interesting route for the realization of quantum mixtures is to employ a single atomic species with an additional internal spin degree of freedom. The order parameter becomes multi-component and the system is referred to as a *spinor condensate*, because

it finds a suitable description in terms of a spinor field. The spinor condensate possess appealing properties, as it inherits the superfluid character of a single component BEC, and magnetic properties from its internal spin structure. An excellent review on the topic can be found at [21]. Spinor gases have been realized in alkali and alkali-earth atoms in mixture with spin 1/2 [22, 23, 24], spin 1 [25, 26, 27], and spin 2 [28] systems. Additionally, spinor condensates admit the possibility to change the relative population via spin-changing collision or with external radiation. In particular, the external radiation, either in the optical, microwave or radiofrequency regime, allows to select the spin composition of the mixture and to coherently manipulate its quantum state.
In the following, I will focus on the discussion of a two-component bosonic spin mixture, with the population of the two components independently conserved.

1.2.1 Extension of GPE to two-components BECs

In the previous section we have shown how static and dynamic properties of a single component BEC can be studied at the mean-field level, starting from the Gross Pitaevskii equation 1.3. It is not difficult to extend the same formulation to the case of a mixture of BECs. The two BECs can be described in terms of two classical complex fields $\psi_i(\boldsymbol{r}) = \sqrt{n_i(\boldsymbol{r})}e^{i\phi_i}$, with $i = 1, 2$ labelling the two atomic species. The energy functional of the system reads:

$$E_{mix} = \int d\boldsymbol{r} \left\{ \left[\sum_{i=1,2} \frac{\hbar^2}{2m_i} |\boldsymbol{\nabla}\psi_i(\boldsymbol{r})|^2 + V_i(\boldsymbol{r}) + \frac{1}{2} g_{ii} |\psi_i(\boldsymbol{r})|^4 \right] + g_{12} |\psi_1(\boldsymbol{r})|^2 |\psi_2(\boldsymbol{r})|^2 \right\} \tag{1.14}$$

with m_i the masses of the two atomic species, and V_i the external potential, which, in principle, is different for the two species. The *intraspecies* coupling constants $g_{ii} = 4\pi\hbar^2 a_{ii}/m_i$ take into account interactions among two atoms occupying the same state, while the *interspecies* one $g_{12} = 2\pi\hbar^2 a_{12}/m_r$ describes interactions between atoms 1 and 2, with m_r their reduced mass.
In the particular case of mixtures of hyperfine states of ^{23}Na, studied in this thesis, we can further simplify the previous expression, since $m_1 = m_2 = m = 2m_r$. Carefully engineering the trapping potential, we can also assume the potential to be the same regardless of the hyperfine state, i.e., $V_1 = V_2 = V_{\text{ext}}$. By applying the variational principle, for the two fields independently, it is possible to derive the coupled GPEs [6]:

$$\begin{aligned} i\hbar \frac{\partial \psi_1(\boldsymbol{r},t)}{\partial t} &= \left(-\frac{\hbar^2}{2m}\boldsymbol{\nabla}^2 + V_{\text{ext}}(\boldsymbol{r}) + g_{11}|\psi_1(\boldsymbol{r},t)|^2 + g_{12}|\psi_2(\boldsymbol{r},t)|^2 \right) \psi_1(\boldsymbol{r},t) \\ i\hbar \frac{\partial \psi_2(\boldsymbol{r},t)}{\partial t} &= \left(-\frac{\hbar^2}{2m}\boldsymbol{\nabla}^2 + V_{\text{ext}}(\boldsymbol{r}) + g_{22}|\psi_2(\boldsymbol{r},t)|^2 + g_{12}|\psi_1(\boldsymbol{r},t)|^2 \right) \psi_2(\boldsymbol{r},t) \end{aligned} \tag{1.15}$$

Similarly to what we did in the previous section, we can start from the pair of GPEs to study properties of the mixture. Stationary solutions of the system provide two chemical

potentials, $\mu_i = \frac{\partial E}{\partial N_i}$, which satisfy

$$\begin{aligned}\mu_1\psi_1(\boldsymbol{r}) &= \left(-\frac{\hbar^2}{2m}\boldsymbol{\nabla}^2 + V_{\text{ext}}(\boldsymbol{r}) + g_{11}|\psi_1(\boldsymbol{r})|^2 + g_{12}|\psi_2(\boldsymbol{r})|^2\right)\psi_1(\boldsymbol{r}),\\ \mu_2\psi_2(\boldsymbol{r}) &= \left(-\frac{\hbar^2}{2m}\boldsymbol{\nabla}^2 + V_{\text{ext}}(\boldsymbol{r}) + g_{22}|\psi_2(\boldsymbol{r})|^2 + g_{12}|\psi_1(\boldsymbol{r})|^2\right)\psi_2(\boldsymbol{r}).\end{aligned} \tag{1.16}$$

Miscibility and Immiscibility condition. The dependence of the energy functional 1.14 on the three interaction parameters implies a rich variety of ground state configurations, depending on the value of the coupling constants.
We can start the discussion investigating the stability against perturbations, in the case of homogeneous densities n_1 and n_2. To ensure stability, the energy functional must remain finite when adding particles. In other words, the system must be stable again perturbations in the density of either the two species. This condition is ensured if the Hessian $H(E)$ of the energy functional, $\frac{\partial^2 E}{\partial N_i \partial N_j}$, is positive definite [29]. In the homogeneous case, the energy density of the system reads:

$$\varepsilon = \frac{1}{2}g_{11}n_1^2 + \frac{1}{2}g_{22}n_2^2 + g_{12}n_1n_2 \implies H(\varepsilon) = \begin{pmatrix} g_{11} & g_{12} \\ g_{12} & g_{22}\end{pmatrix} \tag{1.17}$$

The intraspecies coupling constants g_{11}, g_{22} must be both independently positive, to separately ensure stability against collapse, which might occur if interactions are attractive. From Eq. 1.17, the stability condition implies

$$\sqrt{g_{11}g_{22}} > g_{12} \tag{1.18}$$

For repulsive interspecies interactions, $g_{12} > 0$, systems which satisfy the previous condition are called *miscible*, otherwise they are said to be *immiscible*, since they tend to phase separate. Indeed, an estimation of the energy in the two configurations, shows that if condition 1.18 is satisfied, the energy is minimized if the two species occupy the same volume [6]. Furthermore, if $g_{12} < 0$ and beyond mean-field effects are included [30], the system can form self-bounded states called *quantum droplets* [31, 32, 33], provided that the condition $g_{12} < -\sqrt{g_{11}g_{22}}$ is satisfied and a critical atom number is reached.
The previous result on the miscibility criterion generalizes also to the case of non-uniform mixtures, subject to an external harmonic potential. However, in this case, richer physics occurs, resulting from a possible imbalance in the intraspecies components $g_{11} \neq g_{22}$ [34]. Indeed, the two density distributions can be position dependent, and their shape will be determined by the interplay between the different mean-field energies, both in the miscible and immiscible regimes. Let us consider, for instance, the case of $g_{22} > g_{11}$. In this case, in order to balance the intraspecies mean-field energy, component 2 will move towards the edge of the trap, occupying a larger volume and lowering the density, while component 1 will remain in the center. This effect is know as *buoyancy*. Ground state configurations for different combinations of g_{11}, g_{22}, g_{12} are plotted in Fig. 1.1, where the two density profiles are obtained numerically through imaginary time evolution of

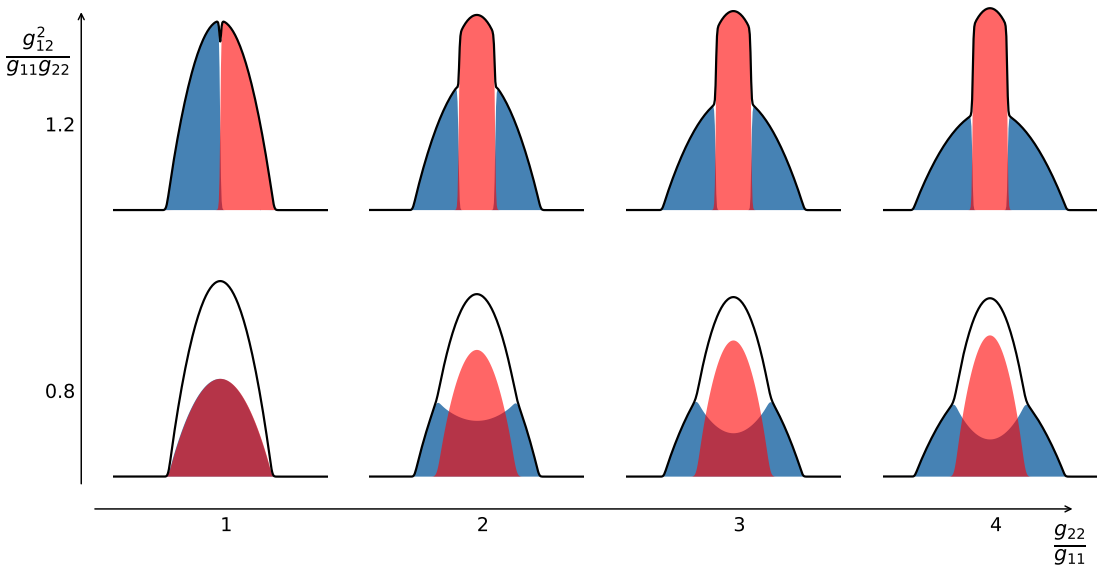

Figure 1.1: One dimensional space dependent density profile $|\psi_i(r)|^2$ of component 1 (red) and 2 (blue), as a function of the ratio g_{22}/g_{11} (horizontal axis), and of the stability condition $g_{12}^2/g_{11}g_{22}$ (vertical axis).

the coupled GPEs in 1.15, using a split-step algorithm [35].
Note that, even in the case of $g_{12} < \sqrt{g_{11}g_{22}}$, the two components overlap exactly only in the case $g_{11} = g_{22}$. The buoyancy effect is only a result of the imbalance between the intraspecies coupling constants, and it occurs independently of the stability condition. In the case of an immiscibile mixture, however, the two components are also separated by sharp interfaces. The width of each interface is called *spin healing length* and reads:

$$\xi_s = \frac{\hbar}{\sqrt{m(g_{11} + g_{22} - 2g_{12})n}} \tag{1.19}$$

In analogy with the single component case, the spin healing length can be calculated by the balance between the quantum pressure terms and the mean-field energy, and it takes an imaginary value in the immiscible case.

1.2.2 Dispersion relations for density and spin channels

Elementary excitations, as a result of quantum or thermal fluctuations, occurs also in spin mixtures. The presence of an additional degree of freedom, given by the presence of the second component, is naturally associated with the emergence of a second dispersion relation. To study it, it is easier to introduce new variables which correspond to the normal modes of the system.
In analogy with two coupled oscillators, it is easier to think of the normal modes of the system as “in-phase” and “out-of-phase” oscillations. In a two-component mixture, the

former are associated to perturbations in the total density $n = n_1 + n_2$, and the second to excitations of the difference in the two components, $s = n_2 - n_1$, also referred to as *spin* modes.
A derivation similar to the one discussed for a single component BEC [7] leads to the following dispersion relations for the density and the spin in the homogeneous case:

$$\hbar\omega_{d,s} = \sqrt{\frac{\hbar^2 k^2}{2m}\left(\frac{\hbar^2 k^2}{2m} + 2mc_{d,s}^2\right)} \tag{1.20}$$

Here, c_d and c_s are the density and spin speed of sounds, that read [6]:

$$c_{d,s}^2 = \frac{g_{11}n_1 + g_{22}n_2 \pm \sqrt{(g_{11}n_1 - g_{22}n_2)^2 + 4n_1 n_2 g_{12}^2}}{2m} \tag{1.21}$$

Considering a balanced mixture $n_1 = n_2 = n/2$ with equal intraspecies coupling constants $g_{11} = g_{22} = g$, the speeds of sound reduce to

$$c_d^2 = \frac{(g + g_{12})n}{2m}, \qquad c_s^2 = \frac{(g - g_{12})n}{2m} = \frac{\delta g n}{2m} \tag{1.22}$$

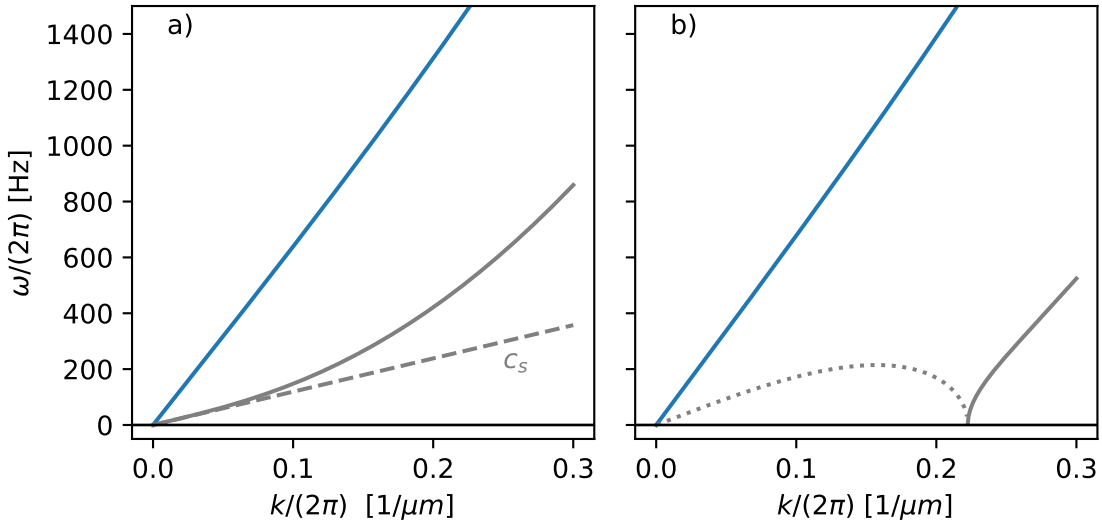

Figure 1.2: Dispersion relations for a spin mixture. In both panels the blue line refers to the density channel and the grey ones to the spin channel. (a) Miscible case. The dashed line represents the spin sound velocity, which well approximates the dispersion relation up to $k = 0.05\,\mu\text{m}^{-1}$. (b) Immiscible case. The density channel is unaffected, but the spin one contains an imaginary frequency (dot line). In the scale of the figure, the density channel always appears in the linear regime due to the higher value of the density sound velocity.

where we have introduced the relevant parameter $\delta g = g - g_{12}$. As in the case of a single component mixture, low-energy oscillations with long-wavelength can be identified with phononic excitations $\omega_{d,s} = c_{d,s}k$, that can occur either in the density or in the spin mode. Dispersion relations are plotted in Fig. 1.2, in both the miscible (left panel) and immiscible cases (right panel). Notice that in the immiscible regime an imaginary frequency emerges, for a wide range of k. It corresponds to a modulation instability of the system [36], that develops spontaneously, as soon as the two species mixes. The existence of two distinct sound velocities was first proven experimentally in miscible gas of ^{23}Na atoms in Ref.[37].
In the more general case of $g_{11} \neq g_{22} \neq g_{12}$, we can introduce the average intraspecies coupling constant g, and their difference

$$g = \frac{(g_{11} + g_{22})}{2}, \qquad \Delta = \frac{(g_{11} - g_{22})}{2} \tag{1.23}$$

in order to introduce the definition of δg as:

$$\delta g = \frac{g_{11} + g_{22}}{2} - g_{12} = g - g_{12} \tag{1.24}$$

It is also useful now to generalize the concept of the chemical potential to the density and spin channels, defined as [29]

$$\mu_d = \frac{g + g_{12}}{2} n; \quad \mu_s = \frac{g - g_{12}}{2} n \tag{1.25}$$

so that the speed of sound for the two modes reduces to $c_{d(s)} = \sqrt{\mu_{d(s)}/m}$.
In general, c_d and c_s can be greatly different, due to the difference between the coupling constants. For a miscible mixture of ^{23}Na hyperfine states $|1, -1\rangle$ and $|1, +1\rangle$, the spin sound velocity is ≈ 0.08 of the density one.

1.3 Coherently-Coupled BECs

In the previous section we described two-component mixtures, and discussed how ground state and excitation properties are governed by the interplay between the mean-field energies. So far, we have worked under the assumption that the densities of the components are separately conserved. Spin mixtures, however, may develop a much richer dynamics, as they admit interconversion processes between the populations of the components. Indeed, it is possible to introduce an external oscillating electromagnetic field to couple hyperfine states. Different fields can be employed. A radiofrequency (microwave) field can directly couple hyperfine states within the same electronic level, and produce a coupling homogeneous all over the sample. A more elaborate scheme involves the use of Raman transitions in the optical regime, which can be used to introduce a local coupling. The latter scheme also admits the possibility of transferring momentum to the atoms, in which case it is referred to as spin-orbit coupling, giving rise to interesting physics since it introduces a gauge field in the Hamiltonian [38, 39]. A good review on the topic can

be found in [40].
For the arguments explored in this thesis, I will focus on the case of a homogeneous microwave field, which coherently couples the internal states of the mixture. The system can be described, in analogy with a two-level model, introducing a time dependent field $\Omega_R(t)e^{-i\omega_{cpl}t+\phi}$. Here, $\Omega_R(t)$ is the time dependent amplitude of the complex field (with phase ϕ), whose frequency ω_{cpl} couples two generic atomic states $|1\rangle$ and $|2\rangle$ composing the mixture. In the rotating wave approximation, setting $\delta = \omega_{cpl} - \omega_{12}$ as the detuning from the transition frequency of the bare atomic states, we can add an energy term to the functional 1.14 as:

$$\begin{aligned} E_{cpl} &= -\frac{\hbar\Omega_R(t)}{2}\int d\boldsymbol{r}(\psi_1\psi_2^* + \psi_1^*\psi_2) + \frac{\hbar\delta(t)}{2}\int d\boldsymbol{r}(n_2^2 - n_1^2) \\ &= -\frac{\hbar\Omega_R(t)}{2}\int d\boldsymbol{r}\sqrt{n_1 n_2}\cos(\phi_2 - \phi_1) + \frac{\hbar\delta(t)}{2}\int d\boldsymbol{r}(n_2^2 - n_1^2) \end{aligned} \tag{1.26}$$

If we consider Ω_R to be real and positive, the explicit dependence of the energy functional on the relative phase of the components has important consequences. Indeed, the relative phase is explicitly locked by the presence of the coupling, resulting in a breaking of the conservation law for the relative number of particles. Later on, we will see how the symmetry breaking is associated with the disappearance of one the two Goldstone modes (gapless excitations) of the system.

Ground State (GS). Before diving into the dynamics of the system, it is interesting to examine the structure of the ground state. To illustrate the general concept, we will first consider the homogeneous case, with $n_i(\boldsymbol{r}) = n_i$, and zero detuning $\delta = 0$. Following the considerations presented in [41], the energy density reads

$$\varepsilon = \frac{1}{2}g_{11}n_1^2 + \frac{1}{2}g_{22}n_2^2 + g_{12}n_1n_2 - \hbar\Omega_R\sqrt{n_1n_2}\cos\phi \tag{1.27}$$

where $\phi = \phi_2 - \phi_1$ is the relative phase of the two components with respect to the phase of the coupling. In the case of equal intraspecies coupling constant $g_{11} = g_{22} = g$, the energy is minimized at $\phi = 0$. The equilibrium condition is the solution of

$$\Big(g - g_{12} + \frac{\hbar\Omega_R}{2\sqrt{n_1n_2}}\Big)(n_1 - n_2) = 0. \tag{1.28}$$

The previous equation admits two possible solutions, depending on the ratio between $\delta g = g - g_{12}$ and $\hbar\Omega_R$. The two solutions are:

$$\begin{aligned} &1) \quad n_1 - n_2 = 0 \\ &2) \quad n_1 - n_2 = \pm n\sqrt{1 - \left(\frac{\hbar\Omega_R}{\delta g n}\right)^2} \end{aligned} \tag{1.29}$$

corresponding to either an unpolarized ($s = 0$) or a polarized ($s \neq 0$) state. It is also

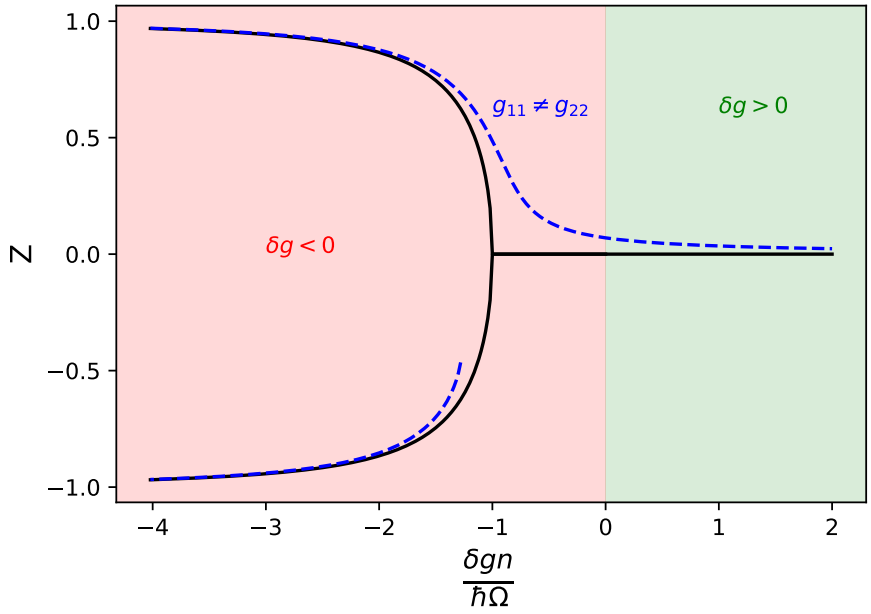

Figure 1.3: Ground state as a function of $\delta g n/(\hbar\Omega_R)$, for $\phi = 0$. The bifurcation occurs in the ground state, plotted in terms of $nZ = n_2 - n_1$, of the system in the case of negative δg (red region). For $\delta g > 0$ (green region) the ground state is always the unpolarized state. For an unbalanced mixture [blue dashed curve, calculated at $n(g_{11} - g_{22}) = 0.07\hbar\Omega_R$] the bifurcation disappears.

interesting to distinguish between the case, in the absence of coupling, of a miscible or immiscible mixture.
In the former case, $\delta g > 0$, and Eq. 1.28 admits only an unpolarized state as the ground state (solution 1). The opposite occurs if $\delta_g < 0$. In this case, the competition between the negative mean-field energy associated to the spin channel and the coupling energy, stabilizing the mixture, might result in a polarized ground state with opposite magnetization given by solution 2). This solution corresponds to the ground state provided that $|\delta g|n > \hbar\Omega_R$. If this condition is not satisfied, the ground state will be again an unpolarized state. The presence of two possible ground states as a function of $\delta g n/\hbar\Omega_R$ corresponds to a classical bifurcation occurring in the spin channel, and it was experimentally measured for the first time in Ref.[42]. The ground state structure is illustrated in Fig. 1.3.
Finally, the case of $\phi = \pi$, still gives rise to an extremum of the energy, but it will not be an energy minimum, as the energy increases by $\approx 2\Omega_R$. The excited state configuration will be exactly symmetric with respect to the sign of the interactions compared to the ground state. In other words, the bifurcation at $\delta g n = \hbar\Omega_R$ will occur in the excited state of a mixture with $\delta g > 0$, whereas a mixture with $\delta g < 0$ will always have an unpolarized excited state.

In the case of an imbalance between the intraspecies coupling constant $g_{11} \neq g_{22}$, for $\delta g > 0$ and $|\delta g| n < \hbar\Omega_R$, the GS will have a small but finite polarization. In the polarized regime, instead, the degeneracy between the two ground states disappears, and one of the two will become the true ground state of the system [43]. The unbalanced case is formally equivalent to the introduction of a detuning term in the energy functional, so the bifurcation can always be restored.

Excitations Elementary excitations of the system are, once again, described at the mean-field level by a set of coupled GPEs, which can be derived by a variational principle adding Eq.1.26 to the energy functional of the mixture state. These equations read

$$\begin{aligned} i\hbar\frac{\partial\psi_1(\boldsymbol{r},t)}{\partial t} &= \left(-\frac{\hbar^2}{2m}\boldsymbol{\nabla}^2 + V_{\text{ext}}(\boldsymbol{r}) + g_{11}|\psi_1(\boldsymbol{r},t)|^2 - \frac{\delta}{2} + g_{12}|\psi_2(\boldsymbol{r})|^2\right)\psi_1(\boldsymbol{r},t) - \frac{\hbar\Omega_R}{2}\psi_2 \\ i\hbar\frac{\partial\psi_2(\boldsymbol{r},t)}{\partial t} &= \left(-\frac{\hbar^2}{2m}\boldsymbol{\nabla}^2 + V_{\text{ext}}(\boldsymbol{r}) + g_{22}|\psi_2(\boldsymbol{r},t)|^2 + \frac{\delta}{2} + g_{12}|\psi_1(\boldsymbol{r})|^2\right)\psi_2(\boldsymbol{r},t) - \frac{\hbar\Omega_R}{2}\psi_1 \end{aligned} \tag{1.30}$$

which are analogous to equations 1.15, with additional terms explicitly coming from the coherent coupling.
The derivation of the dispersion relations follows the lines described previously [44], linearizing Eq.1.30 around the equilibrium solution. Important care must be taken, since now the equilibrium solution differs as a function of $|\delta g n|/\Omega_R$, as discussed previously [41].
In the case of a miscible mixture, the GS corresponds to $s = 0$, and, in the approximation $g_{11} = g_{22}$, the dispersion relations take the form

$$\begin{aligned} \hbar\omega_d &= \sqrt{\frac{\hbar^2k^2}{2m}\left(\frac{\hbar^2k^2}{2m} + (g + g_{12})n\right)} \\ \hbar\omega_s &= \sqrt{\left(\frac{\hbar^2k^2}{2m} + \hbar\Omega_R\right)\left(\frac{\hbar^2k^2}{2m} + (g - g_{12})n + \hbar\Omega_R\right)} \end{aligned} \tag{1.31}$$

These are plotted in Fig. 1.4(a), for two different values of the Rabi coupling Ω_R, below and above the interaction energy. Excitations in the density channel are not affected by the presence of the coupling, as one would expect. The spin mode, however, changes dramatically. For low momenta it goes as k^2, and it appears to be gapped at $k = 0$, with a frequency

$$\hbar\omega_s(k = 0) = \sqrt{\hbar\Omega_R(\hbar\Omega_R + \delta g n)} \tag{1.32}$$

also called the *plasma frequency*. The dependence of the gap on the Rabi coupling is clearly visible in Fig. 1.4(a). The gap is a consequence of the energy cost that has to be paid to change the relative phase $\delta\phi$ of the system. It results from the presence of the Rabi coupling that *explicitly* breaks the continuous U(1) symmetry in the relative phase, related to the conservation of the relative number of particles.

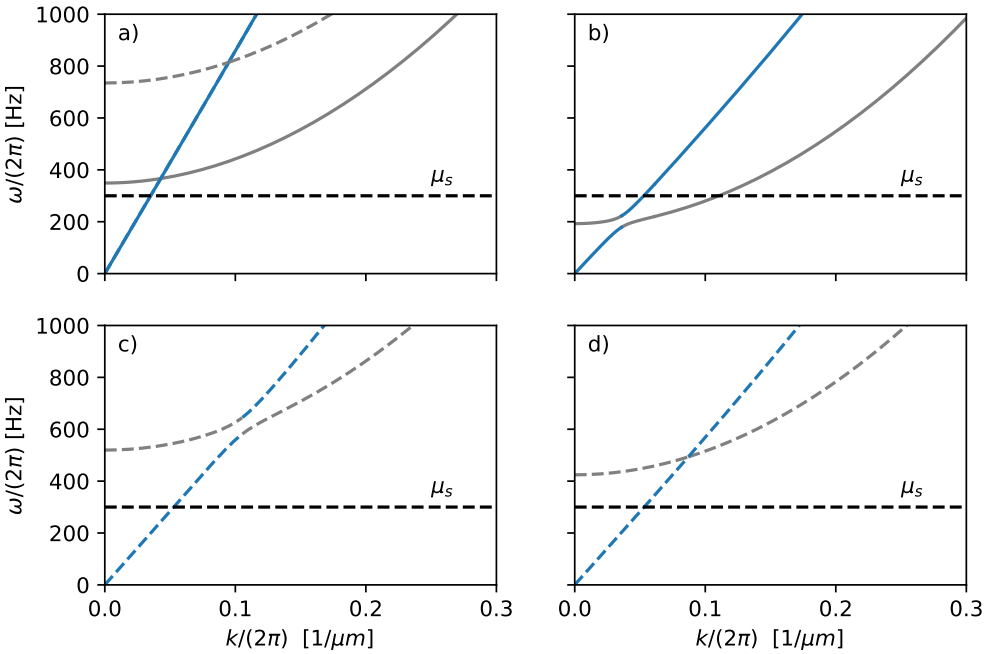

Figure 1.4: Dispersion relations with Rabi coupling for a miscible (panel a) and immiscibile mixture (panels b, c and d). The value of the spin chemical potential $\mu_s/h = 300\,\mathrm{Hz}$ is shown as a black dashed line, for the typical settings of the experiment in Trento. In all panels, solid lines are calculated at $\Omega_R/2\pi = 230\,\mathrm{Hz}$, dashed lines at $\Omega_R/2\pi = 600\,\mathrm{Hz}$. All dispersion relations are calculated around the ground state, which is $Z = 0$ for panel (a), (c) and (d), and $Z = 0.64$ for panel (b). We use as value of the coupling constants the ones for the mixtures discussed in Section 2.3. In panel (d) we used a detuning $\hbar\delta = -n(g_{11} - g_{22})$ that removes the avoided crossing shown in panel (c). In all panels the blue line refers to the density channel, while the grey ones to the spin one.

The situation is different in the case of an immiscible mixture. As already stated, the equilibrium condition, around which we can linearize the GPE, depends on the ratio between spin-interaction energy and coupling. In the unpolarized state ($\delta g n < \hbar\Omega_R$) the ground state is the same of the miscible mixture, hence we find a gapped dispersion relation, with a different value of the gap, as $\delta g < 0$ will lower the effective Rabi frequency [Fig. 1.4(c) and (d)]. An avoided crossing appears if the two intraspecies coupling constants differs [panel (c)], that vanishes if the coupling is detuned exactly by $\hbar\delta = -n(g_{11} - g_{22})$ [panel (d)]. On the other end, around the polarized state, while the functional shape remains the same, the finite polarization always introduces a coupling between density and spin modes, resulting in an avoided crossing, which can't be removed. The avoided crossing strongly depends on the ratio between $\delta g n$ and $\hbar\Omega_R$, i.e. on the GS polarization. For small $|n_1 - n_2|$, it is for $\delta g \gtrsim \hbar\Omega_R$, the avoided crossing occurs at low k, and the energy difference between the two modes will be small. The opposite is true for an almost fully polarized state $\delta g \gg \hbar\Omega_R$.

1.3.1 Bloch Sphere representation

An equivalent formulation of the spin dynamics can be derived starting from the Gross Pitaevskii equations 1.30 and writing the order parameter as a spinor complex field. This notation provides a more convenient description for the dynamics, and helps identifying this system in the more general framework of spin systems. We can start writing the two order parameters as:

$$\psi = \begin{pmatrix} \psi_1 \\ \psi_2 \end{pmatrix} = \begin{pmatrix} \sqrt{n_1} e^{i\phi_1} \\ \sqrt{n_2} e^{i\phi_2} \end{pmatrix}; \quad \Longrightarrow \quad \rho = \psi \otimes \psi^\dagger = \begin{pmatrix} n_1 & \psi_1\psi_2^* \\ \psi_1^*\psi_2 & n_2 \end{pmatrix} \tag{1.33}$$

where we have constructed the density matrix ρ. Taking advantage of the SU(2) algebra, it is convenient now to use as basis the set of Pauli matrices σ_i, with $i = 1, 2, 3$. This allows to extract a spin vector from the density matrix of the coupled BECs as

$$\vec{S} = \mathrm{Tr}\,(\vec{\sigma}\rho) = n\left(\sqrt{1 - Z^2}\cos\phi, \sqrt{1 - Z^2}\sin\phi, Z\right) \tag{1.34}$$

where we have introduced the *relative* magnetization Z, defined as $nZ = n_2 - n_1$, while ϕ is the relative phase between the two components. In this way we can directly represent the system on a Bloch sphere of unitary radius. The spin state can also be identified by a pair of variables (θ, ϕ), upon defining $Z = \cos\theta$. Note that a 3-dimensional spin vector exists only in the context of the Bloch sphere, and has nothing to do with the dimensionality of the physical sample.
Recalling definitions 1.23 for the coupling constants, we can introduce a 2x2 matrix for the current density in one spatial dimension [45], whose elements read

$$j_{ab} = \frac{i}{\hbar}\left[\psi_a \partial_x \psi_b^* - \psi_b \partial_x \psi_a^*\right] = j_{ab}^* \tag{1.35}$$

where a, b labels components 1 and 2.
From this matrix, we can derive separate hydrodynamic equations for the density and

spin channels. The former is characterized by a continuity equation for the density current $j_d = \mathrm{Tr}(j)$:

$$\partial_t n + \partial_x j_d = 0 \tag{1.36}$$

which is the conservation law related to the U(1) symmetry preserved in the density channel.
The spin channel behaves differently. It is useful to introduce the spin current, which is a vector in the space of spin

$$\vec{j}_s = \frac{i\hbar}{2m}\left[(\partial_x \psi^\dagger)\vec{\sigma}\psi - \psi^\dagger(\partial_x \sigma\psi)\right] \tag{1.37}$$

Within this definition, we can recast the Gross Pitaevskii equations 1.30 in a hydrodynamic equation for the spin vector $\vec{S}$:

$$\partial_t \vec{S} + \partial_x \vec{j} = -\vec{H}(\vec{S}) \times \vec{S} \tag{1.38}$$

where we introduced the effective magnetic field $\vec{H}$, that reads:

$$\vec{H} = (\Omega_R, 0, \delta - n\Delta + \delta g n Z) \tag{1.39}$$

where Δ is defined as in Eq. 1.23. This equation allows us to link the dynamics of the magnetization of the coupled condensates to the more generic dynamics of a spin system under an external field. We can think of this field as an effective *magnetic* field which dictates the dynamics of the atoms.
A few comments can now be expressed. Let us first consider the case of a 0-dimensional sample, where the spatial degrees of freedom are frozen. In this case, we can neglect the current term $\vec{j}$ in Eq. 1.38. This *single mode approximation* has been realized experimentally in [42, 46, 47].
We also notice that, in then limit $n \to 0$, Eq. 1.38 reduces to the model of a two-level atom subject to an external coherent radiation, or of a spin subject to a spatial magnetic field of the form $\vec{H} = (\Omega_R, 0, \delta)$. In the Bloch sphere formalism, the eigenstates of the Hamiltonian correspond to the *dressed states* of the atom-light interacting system [48].
Interesting dynamics arises instead in the case $n \neq 0$, as the time evolution of the spin vector directly depends on the spin state itself, through the term $\delta g n Z$. The latter introduces also a coupling to the density channel, through the dependence on n. At last, we observe that, in this picture, an imbalance between the intraspecies coupling constants leads to a detuning term [43], also proportional to the total density.

1.3.2 Internal Josephson Junction

We have discussed how the presence of mean-field energy shifts affects the external coupling with a density-dependent detuning. The physics is much deeper, as interactions introduce a non-linear term $\delta g n Z$. The latter can be seen as a rotation around the z-axis, with magnetization-dependent angular velocity, a general effect known as "one-axis twisting" [49].

In a more general context, the quantum properties of a system with an external coupling and mutual interactions have been studied in the contest of superconductors by [50]. Such a system has been implemented also in atomic BECs as in [51, 52, 53], where the coupling takes the form of a tunneling link. In the case of coherent coupling between spin states, the system is instead referred to as an *internal Josephson junction* [42].
The equations governing the dynamics of the system are expressed in terms of the variables (Z, ϕ), equivalently to the previous description in terms of the Bloch sphere. Eq. 1.38 can be recasted as

$$\begin{aligned} \partial_t Z(t) &= -\sqrt{1 - Z(t)^2}\sin\phi(t) \\ \partial_t \phi(t) &= \frac{\delta}{\Omega_R} + \frac{\delta g n}{\hbar\Omega_R} Z(t) + \frac{Z(t)}{\sqrt{1 - Z^2(t)}}\cos\phi(t) \end{aligned} \tag{1.40}$$

which explicitly depend on the ratio $\delta g n/\hbar\Omega_R$. This is not a surprise, as we already anticipated with an energetic argument 1.28 the presence of two different ground states as a function of the same parameter. Given this framework, we can now build a more complete picture.

Dynamical Regime Here we assume the simple case $\delta = 0$, since the presence of detuning doesn't qualitatively alter the dynamics of the system. If $\delta g n \ll \hbar\Omega_R$, the dynamics reduces to the simple Rabi oscillations, with orbits of period $2\pi/\Omega_R$, and mean magnetization $Z = 0$ and phase $\phi = (0, \pi)$. In the phase space of the system, these are fixed points of the dynamics, corresponding to the lowest and highest eigenstate, for $\phi = 0$ and $\phi = \pi$ respectively. Notice that the correspondence between $\phi = \pi$ and the highest energy eigenstate finds its route in the locking of the phase in the energy functional 1.26, imposed by the coupling. For stronger interactions, $\delta g n \lesssim \hbar\Omega_R$, the velocity field due to interactions distorts the orbits. While it still preserves the location of the fixed points, it affects the oscillation frequency, see Fig. 1.5. Small oscillations around the fixed points are called *plasma oscillation* ($\phi = 0$) and *pi oscillations* ($\phi = \pi$) and read:

$$\omega_{\rm pl} = \Omega_R\sqrt{1 + \frac{\delta g n}{\hbar\Omega_R}}; \qquad \omega_\pi = \Omega_R\sqrt{1 - \frac{\delta g n}{\hbar\Omega_R}} \tag{1.41}$$

Note that the frequency of plasma oscillations is identical to the result we found for dispersion relations around the unpolarized ground state, Eq. 1.32, strengthening the link between a coherently-coupled system and the Josephson dynamics.
A careful look at ω_π reveals that, for positive δg, crossing $\delta g n = \hbar\Omega_R$ the frequency becomes imaginary, revealing an unstable fixed point. This labels the transition towards a new dynamical regime that occurs at $\delta g n = \hbar\Omega_R$, called *macroscopic quantum self trapping* [54]. In this regime, two new stable fixed points appear in the system, characterized by a symmetric and degenerate magnetization $Z_0 = \pm\sqrt{1 - \left(\frac{\hbar\Omega_R}{\delta g n}\right)^2}$. This phenomenon is called pitchfork bifurcation, and it hints at a second-order symmetry breaking phase transition [55, 43].

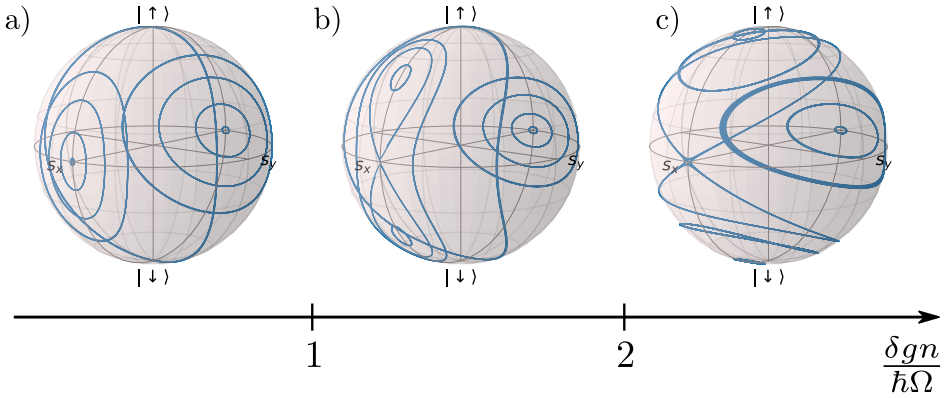

Figure 1.5: Dynamics of the spin vector on the Bloch sphere for different ratios $\Lambda = |\delta g| n/(\hbar\Omega_R)$, computed from Eq. 1.38 with $\delta g < 0$ and no detuning. a) $\Lambda = 2/3$, b) $\Lambda = 4/3$, c) $\Lambda = 4$

Around the degenerate fixed points the relative phase is locked to revolve around $\phi = \pi$, by the presence of a separatrix which separates the phase space. However, for $\delta g n > 2\hbar\Omega_R$ the self trapping region is so large that the separatrix encompasses the poles of the Bloch sphere, and the phase is free to move between $0 - 2\pi$, entering the so-called *running-phase mode*.
While the magnetization of the fixed point is the same independently of the sign of $\delta g n$, its phase depends on it. For $\delta g > 0$ (miscible mixture) the bifurcation occurs at $\phi = \pi$, i.e. in the excited state. The opposite holds for $\delta g < 0$, where the bifurcation occurs in the ground state. Fig. 1.5 show the orbits that the system can sustain in the different dynamical regimes.
The phase-dependence of the fixed point is not crucial in 0-dimensional systems, but it is important in finite size systems. In this case, if one analyzes the dispersion relation, the energy gain in the excited state introduces an imaginary frequency component in the elementary excitations, thus leading to the growth of unstable modes that propagate in the system, eventually altering the dynamics [56].

1.3.3 Extension to finite size systems

In the previous discussion we have focused on the internal spin dynamics and found a suitable representation on the Bloch sphere, neglecting any spatial dynamics. This description holds until the size of the sample is smaller than the size of the minimum spin excitations, which is dictated by the spin healing length ξ_s, or equivalently by the spin chemical potential μ_s. If $\xi_s > R_i$, for $i = x, y, z$, (or $\mu_s < \hbar\omega_i$), then the sample can be approximated as a giant spin vector of length n (see [57] for an in depth discussion). However, richer physics arises if one realizes samples with $\mu_s > \hbar\omega_i$ along at least one spatial direction, as this allows the study of spatial fluctuations and excitations in the spin channel [48, 58, 59, 60]. In the case of our axially symmetric harmonic potential,

it is possible to freeze only the radial degrees of freedom, so that the spin dynamics is ruled by a 1D Landau Lifshitz equation (LLE) [61, 62] (assuming that the total density remains constant), simplifying the comparison between theory and experiments. As a consequence of the harmonic trapping, density, and thus interaction energies, will depend on space. It is then possible to tune the Rabi frequency Ω_R to obtain spatially different regimes, for example with $\delta g n > \hbar\Omega_R$ (Josephson dynamics) in the center of the trap and $\delta g n < \hbar\Omega_R$ (Rabi dynamics) on the tails of the cloud. Notice that, due to the scaling of ξ_s with δg instead of g, the requirement of a strict 1D sample, which in the density channel would require extremely strong trapping frequencies, and it would rise the issue of phase diffusion in one dimension, can be relaxed.

Reduction of an elongated system to 1D The particular case relevant to the following chapters is the elongated cigar-shaped condensate, with axial symmetry around the horizontal axis x. The 3-dimensional density profile can be expressed as

$$n^{3D}(r_\perp, x) = n_0^{3D}\left(1 - \frac{x^2}{R_x^2} - \frac{r_\perp^2}{R_\perp^2}\right) \tag{1.42}$$

where n_0^{3D} is the density in the center of the trap. Assuming that in the spin channel only the axial degrees of freedom are excited, while the total density is not affected, the spatial spin vector 1.34 can be decomposed as:

$$\vec{S}(r_\perp, x, t) = n^{3D}(r_\perp, x)\vec{S}(x, t) \tag{1.43}$$

where $\vec{S}$ is a vector which depends on spatial coordinates, and is defined in spin space in the basis of the Pauli matrices. We can insert this ansatz in the Landau-Lifshitz Eq. 1.38 to obtain:

$$n^{3D}(r_\perp, x)\partial_t\vec{S}(x, t) = n^{3D}(r_\perp, x)\begin{pmatrix}\Omega_R\\ 0\\ \delta - n\Delta + \delta g n^{3D}(r_\perp, x)Z\end{pmatrix} \times \vec{S}(x, t) \tag{1.44}$$

where we have neglected spin currents, for the sake of simplicity. Integrating out the radial directions on both sides, the previous equation reduces to

$$\partial_t\vec{S}(x, t) = \begin{pmatrix}\Omega_R\\ 0\\ \delta - n\Delta + \kappa n(x)Z\end{pmatrix} \times \vec{S}(x, t) \tag{1.45}$$

Here, we have substituted

$$\kappa n(x) = \frac{2}{3}\delta g n^{3D}(r_\perp, x) \tag{1.46}$$

which is a renormalization of the coupling constant δg, that we will use in the remaining chapters. It naturally arises from the integration along $r_\perp$ of Eq. 1.44, in particular

from

$$\begin{aligned} n_1^{1D}(x) &= \int dr_\perp n^{3D}(r_\perp, x) = \frac{\pi R_\perp^2}{2} n_0^{3D}\Big(1 - \frac{x}{R_x}^2\Big)^2, \\ n_2^{1D}(x) &= \int dr_\perp \Big[n^{3D}(r_\perp, x)\Big]^2 = \frac{\pi R_\perp^2}{3} (n_0^{3D})^2\Big(1 - \frac{x}{R_x}^2\Big)^3 \end{aligned} \tag{1.47}$$

The relevant quantity to extract is the ratio between the two integrated densities, which enters explicitly in the effective field $H(\vec{S})$, and it reads

$$n(x) = \frac{n_2^{1D}(x)}{n_1^{1D}(x)} = \frac{2}{3} n_0^{3D}\Big(1 - \frac{x^2}{R_x^2}\Big) \tag{1.48}$$

Thus, in the 1D regime the non-linear term in the LLE takes the form of an exact 1-dimensional system with linear density $n(x)$, the only difference being the renormalization of the interaction constant $\delta g \to \kappa$. Notice that the same result could have been equivalently derived by a direct renormalization of the coupling constant, as shown in [63].

Chapter 2

Production and manipulation of spin mixtures

Contents

In the previous chapter I described the physics of miscible and immiscible spin mixtures subject to an external field which coherently couples the hyperfine states employed in the mixture. In this chapter I will describe the setup of our laboratory, where we produce BECs of ^{23}Na. While BECs have been realized in many different laboratories with different atomic species, the quest for long coherence times poses additional requirements on the stability of the apparatus against the environmental noise.
The structure of this Chapter is the following. In the first section I will describe the current setup of the experimental apparatus. In the second section I will describe the protocol used to cool the atoms to quantum degeneracy. The third section is devoted to the description of the coupling scheme of the two spin mixtures studied during my PhD. The fourth section contains a detailed description of the spin-selective absorption imaging protocols. In the last section I will describe the protocol we use to daily calibrate with high precision the bias field, and characterize its stability in time. Throughout this Chapter, I will often use the notation $|F, m_F\rangle$ to label hyperfine states.

2.1 Experimental apparatus

Particular care was taken in the original design of the apparatus, to make it compatible with the installation of a magnetic shield around the science chamber, used to protect the sample from environmental magnetic field noise. In the following I will briefly summarize the instrumentation used in our apparatus. A more detailed description can be found in [63, 64].

2.1.1 Vacuum system

The vacuum system is composed of two separate chambers [65], made of stainless steel tubes, one at high-vacuum (HV), and the other one at ultra-high-vacuum (UHV). A sketch of the compact experimental apparatus is present in Fig. 2.1.
The HV chamber contains in the lower part a solid source of ^{23}Na atoms, which is heated with an oven at 250° C to produce the atomic vapour. The pressure inside the chamber is kept at 1×10^{-9} mbar through a combined non-evaporable getter and ion-pump (NEXTTorr D200-5). The connection to the UHV chamber is realized by a differential pumping channel with a diameter of 2 mm and length of 22.8 mm. Similarly to the HV chamber, a combined vacuum pump (NEXTTorr D500-5) keeps the pressure inside the UHV chamber at 1×10^{-10} mbar.
The science chamber is an octagonal fused silica cell, connected to the UHV chamber by a 65 mm long glass tube. Optical access to the science chamber is guaranteed by two windows of diameter 50.8 mm along the vertical direction, and by seven windows of diameter 23 mm to give optical access for beams propagating on the x-y plane. The design of the chamber is shown in the right panels of Fig. 2.1. All surfaces of the windows are treated with a Random-Anti-Reflection coating[1], a nano-textured treatment that

[1] Manufactured by Precision Glassblowing, Colorado, USA.

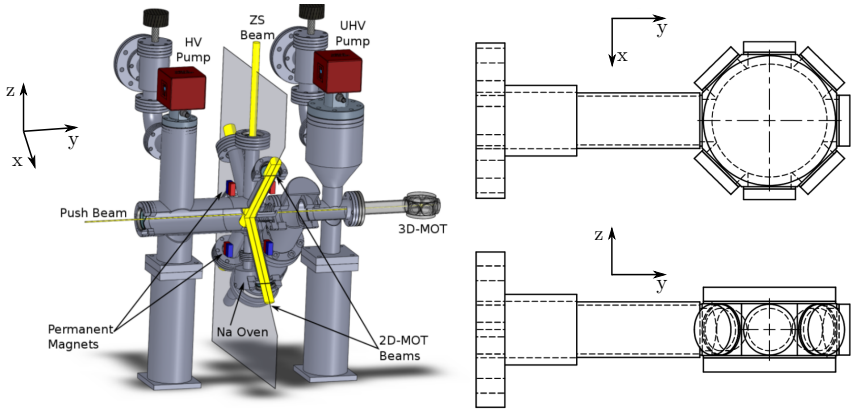

Figure 2.1: Sketch of the experimental apparatus. Yellow lines represent the optical access for the ZS and the 2D MOT beams. On the left the schematics of the science chamber is shown.

reduces reflections below 0.3% for wavelengths in the range 532-1064 nm. This reduces spurious optical effects, that might be observable as interference fringes in atomic images.

2.1.2 Laser source

For both laser cooling and imaging we use 589 nm laser light with two independent sources, one emitting near the ^{23}Na D2 line ($3^2S_{1/2} \rightarrow 3^2P_{3/2}$) and one near the D1 line ($3^2S_{1/2} \rightarrow 3^2P_{1/2}$). Both lights are produced with a frequency-doubling optical cavity starting from infrared light at 1178 nm, emitted by two Fiber Coupled Distributed-Feedback Laser Diode (Innolume DFB-1178-YY-50). The two sources are independently locked at the working frequency by saturated absorption spectroscopy. Each laser light is distributed among different paths, whose current setup is described in [64].
The primary cooling light is locked on resonance on the $|F = 2\rangle \rightarrow |F' = 3\rangle$ transition of the D2 line. This light is used for the Zeeman Slower (ZS), 2D magneto-optical trap (MOT), 3D MOT, Dark Spot (DS), imaging repumper, push, and imaging beams. In particular, DS and repumper light are used to recapture atoms exiting the cooling transition towards the $|F = 1\rangle$, from where they are repumped to the $|F' = 2\rangle$ state.
Light locked on resonance on the $|F = 2\rangle \rightarrow |F' = 2\rangle$ D1 transition line is instead used only for grey molasses (GM) cooling [66].

2.1.3 Magnetic shield

The manipulation of coherently-coupled spin mixtures poses severe requirements on the stabilization of the system against environmental noise. In particular, the main source of disturbance comes from fluctuations in the bias magnetic field. Such fluctuations are sources of decoherence, due to jitters or drifts in the resonance condition. A common

solution is to employ active magnetic field stabilization systems [67, 68], with a magnetometer placed near the atomic sample, and a negative feedback loop acting on the coils current to keep the reading of the magnetometer constant. Another choice is the use of passive suppression of magnetic fields, that can be achieved surrounding the apparatus with a layer of high-conductivity or high-permeability material, such as μ-metal. Even if it is not possible to cover the entire apparatus with such a shield, a solution is to enclose only the science chamber with a multi-layer shield, with small openings for optical access. The design of such a shield has been extensively described in [69], and the implementation in the actual experimental apparatus in [63].
The magnetic shield has a cylindrical shape and is composed of four layers of high-permeability material. The three outer levels are composed of μ-metal, which has a relative permeability $\mu_r = 4.5 \times 10^5$ and a saturation value of 0.75 T, while the inner core is composed of Supra-50, a metal alloy with $\mu_r = 2.5 \times 10^5$ but with a saturation value of 1.5 T. Attenuation measurements performed on the shield [70] reported a suppression of 5-6 order of magnitudes of the external magnetic field.

2.1.4 Magnetic coils

Several pairs of magnetic coils are required to apply controllable and uniform magnetic fields on the sample. All the coils used in the experiment are mounted on a 3D-printed support structure that surrounds the science chamber, placed in the innermost layer of the magnetic shield, see Fig. 2.2.
A first set of circular coils provides the quadrupole magnetic field used for both the MOT and the levitation magnetic field. Each of them is realized with 6 loops of a square copper tubing of 3 mm width. Cooling water circulates in the tube to dissipate the heat generated during the MOT operation. The magnetic field produced by these

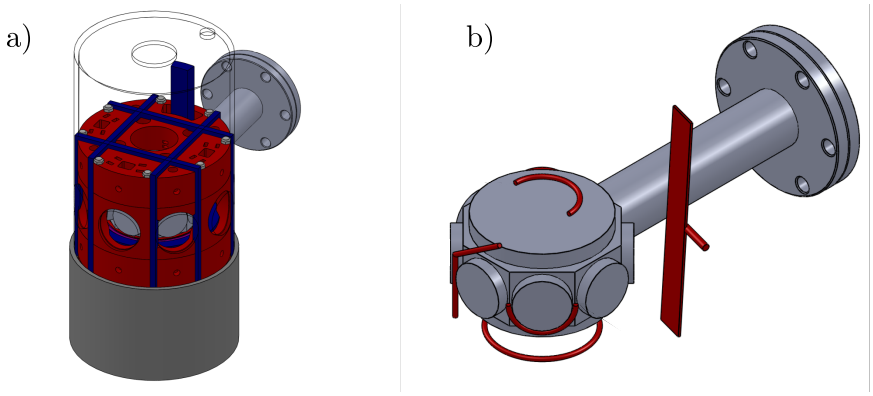

Figure 2.2: a) CAD design of the apparatus surronding the science chamber, placed inside the inner layer of the magnetic shield. Magnetic coils are shown in blue, science chamber in grey. b) Position of the antennas used for microwave transfer around the science chamber. Figures from [63].

coils is $|B| = 1.34\,\mathrm{G/A}$, and the associated gradient is $0.43\,\mathrm{G/(cmA)}$ along z.
Two pairs of squared coils, mounted outside the support structure, are used to produce weak compensation and gradient fields along the x and y axis. Each coil produces a magnetic field of $|B| = 1\,\mathrm{G/A}$ and a gradient of $\partial B/\partial \hat{e}_i = 0.19\,\mathrm{G/(cmA)}$, with $\hat{e}_i$ the axial direction of the coils.
Another pair of coils (BCompZ_fine), operating in the Helmholtz configuration, is used to produce a high-stability vertical field, with $|B| = 2.6\,\mathrm{G/A}$ and magnetic gradient $\partial B/\partial z = 0.9\,\mathrm{G/(cmA)}$. To minimize field inhomogeneities on the sample, these coils are the closest to the glass cell. A similar geometry is used to realize two additional coils for bias field and gradient along z. The magnetic field and gradient produced by these last coils are $|B| = 1.05\,\mathrm{G/A}$ and $\partial B/\partial z = 0.19\,\mathrm{G/(cmA)}$ respectively.

2.1.5 Microwave system

An apparatus that generates either radiofrequency or microwave fields with high precision is required to explore the energy landscape of the hyperfine Zeeman sublevels. For sodium, the energy difference between the $|F = 1\rangle$ and $|F = 2\rangle$, that can be calculated using the Breit-Rabi formula [71], is approximately $1.773\,\mathrm{GHz}$, while the splitting between Zeeman sublevels in the same F is of the order of $700\,\mathrm{kHz/G}$.
In our experiment, we mainly drive transitions in the microwave regime, both for imaging and for physical manipulation of spin mixtures. To this purpose, the experimental setup must possess a fast controllable switch, high frequency stability at high and low power, and controllable phase. Furthermore, for the realization of coherent coupling with a two photon transition, the frequency generator must be able to output two tones from the same clocking device.
The main source is a microwave synthesizer (Marconi Instruments 2024) that produces a carrier at $1.68\,\mathrm{GHz}$ ($1.67\,\mathrm{GHz}$ for experiments in Chapters 5 and 6). Such a synthesizer is also used as a switch, that can be controlled remotely via a TTL signal. The carrier is then mixed with two tones, produced by a direct digital synthesis emitter (DDS, based on the Analog Devices AD9958 chip). This produces two phase coherent waves with tunable amplitude and frequency, in the range 0-120 MHz, and can be controlled remotely with a $30\,\mu\mathrm{s}$ response time. The output signal from the mixer is then filtered with a bandpass filter, and later amplified using a $100\,\mathrm{W}$ amplifier (Minicircuits ZHL-100W-272+). At the output of the amplifier we use a multi-stub tuner (Maury Microwave Triple-stub 1819A) to match the impedance of the antenna that radiates the sample. Several antennas are available [63], all of them have been installed around the science chamber in the inner core of the magnetic shield prior to the final assembly, as shown in Fig. 2.2(b).
A similar setup is used to produce an auxiliary microwave field, that we use to couple the $|1, 0\rangle$ and $|2, 0\rangle$ states (*dressing* radiation), exploiting the induced light-shift to prevent spin changing collision in the miscible mixture (see 2.3.1).

2.1.6 Low-noise current source

While environmental magnetic fluctuations are handled by the magnetic shield, a major source of noise comes from the current generator driving the bias field coils. To mitigate this effect, we use a pair of high stability Laser-Diode Controller (SRS LDC-501), that can produce currents up to 500 mA with a rms noise of 1.5 μA and a long-term drift of 15ppm over 24h [72]. We use this generator to drive a constant current of $\approx 490\,\mathrm{mA}$, further modulated by a floating DAC in a range of $\pm 10\,\mathrm{mA}$. This allows to finely tune the bias field in a range of approximately $\pm 20\,\mathrm{mG}$ around the typical value of 1.3 G.

2.1.7 Imaging system

As in the majority of cold atoms experiment, we use absorption imaging to gather information about the density of the ultracold atomic sample. We have currently implemented three cameras, two along x and one along z.

Hor1 : A CCD camera (Stingray F-201B), used to image the atoms along the x direction. It shares with Cam. Hor3 a $f = 50\,\mathrm{mm}$ lens inside the shield, placed so that the atoms are on its focal plane. The telescope is closed by another $f = 50\,\mathrm{mm}$ lens placed before the camera, with a unitary magnification.

Hor3 : A CCD camera (Stingray F-201B) oriented along the same direction of Cam. Hor1, 45 cm further away from the atoms. An additional $f = 300\,\mathrm{mm}$ focuses the image on the camera. The demagnification of this optical system is a factor of 6. This camera is mainly used to image thermal clouds in the MOT stage.

Vert : A fast CMOS camera (Hamamatsu Orca Flash 4.0), which is the main camera used in the experiment. The objective is composed by an achromatic ($f = 75\,\mathrm{mm}$) and a spherical lens ($f = 300\,\mathrm{mm}$), with an effective focal length of 60.8 mm. Image is carried to the camera by a $f = 400\,\mathrm{mm}$ spherical lens, with a magnification of 6.5. In the same path a 2" PBS is present, to allow auxiliary optical access from the bottom of the experiment.

2.1.8 Optical traps

As the primary objective of the experiment is the study of mixtures of hyperfine states, a stringent requirement in devising the apparatus is the implementation of non-spin-selective trapping potentials. An ideal approach is to employ optical potentials, that we use for both evaporative cooling and BEC trapping. Indeed, it can be calculated [73] that the potential of a laser field on (alkali) atoms, in the limit where the detuning Δ of the laser with respect to the center of the D-line dublett exceeds the fine structure splitting Δ'_{FS}, reads

$$U_{\mathrm{dip}}(\boldsymbol{r}) = \frac{3\pi c^2}{2\omega_0^3}\frac{\Gamma}{\Delta}\left(1 + \frac{1}{3}P g_F m_F \frac{\Delta'_{FS}}{\Delta}\right) I(\boldsymbol{r}) \tag{2.1}$$

Here, ω_0 is the optical resonance frequency, g_F the Landè factor, P the polarization (0, ± 1 for π, $\sigma^{\pm}$) and $I(\boldsymbol{r})$ the spatial intensity profile of the light beam. In this regime, if the beam light is linearly polarized with respect to a bias magnetic field, the trapping potential felt by the atoms is spin insensitive, making it a suitable choice for our experiments. Furthermore, the dependence of $U_{\text{dip}}(\boldsymbol{r})$ on the sign of Δ makes it possible to build either attractive or repulsive potentials.
The main optical source used in our apparatus is a CW fiber laser (Azur Light Systems ALS-1064-50-I-SF) which produces 40 W of infrared (1064 nm) laser light, currently used to create both attractive and repulsive potentials.
We use a Second Harmonic Generation crystal, placed in the focus of the laser, to produce green light at 532 nm with a conversion efficiency of 25% of the total incident power. We then use a dichroic mirror to separate the remaining infrared light from the green one, see in Fig. 2.3. The latter is carried to the other side of the table and shined onto

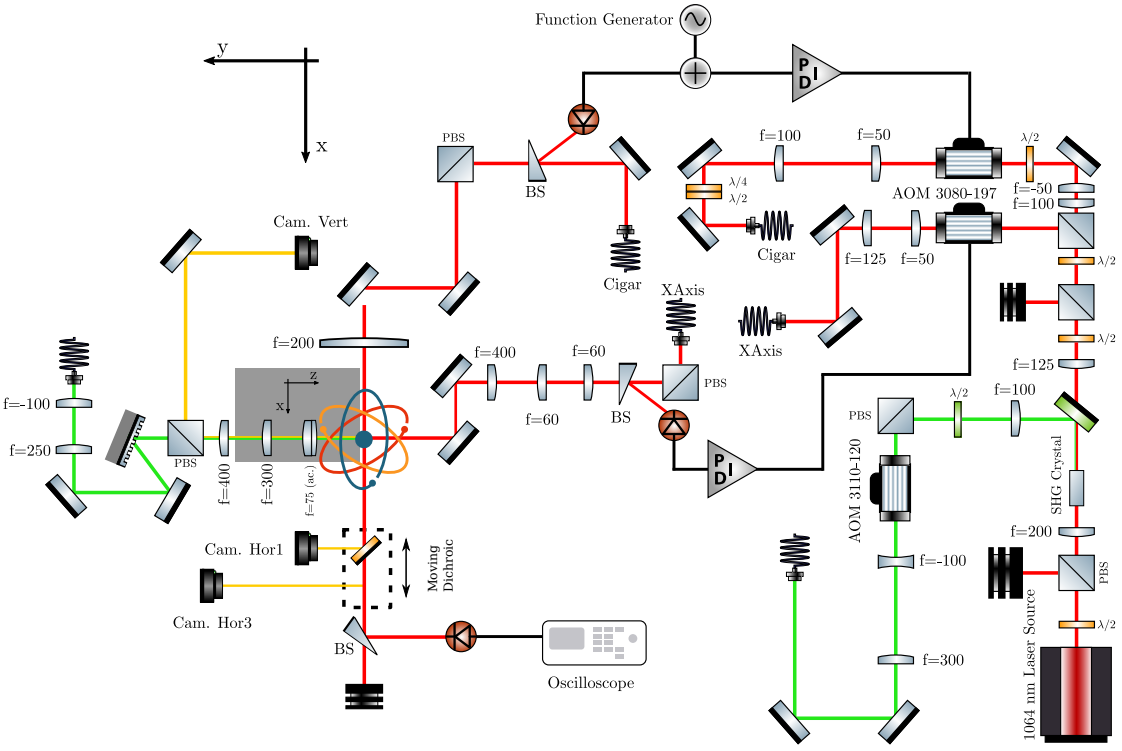

Figure 2.3: Full optical path for trapping beams used in the experiment, the Cigar beam and the Xaxis beam. On top, the electronic circuit used for the modulation of the Cigar is also represented, with the signal coming from a function generator summed to the setpoint of the PID input, to ensure the correct locking during the modulation. Green lines refer to the path of the 532 nm light shined on the DMD, yellow ones to the imaging path, and red ones to infrared light. The grey area on the left of the atoms indicates a path perpendicular to the x-y plane.

a rectangular Digital Micromirror Device (DMD, TI DLP LightCrafter6500, 1080x1920 width), whose full path is currently under construction. We use two telescopes with cylindrical lenses to transform and magnify the circular beam exiting the fiber into an elliptical one, that better matches the dimension of the DMD. In the future, the use of the DMD will allow to create repulsive potentials with arbitrary shapes along the x-y plane [74].
The remaining infrared light is instead used to create attractive potentials. A fraction of it is sampled and carried by a fiber, to be directed along the y axis (*Xaxis* beam), to create a crossed ODT in the x-y plane, mainly used to prevent sloshing along the x axis. While this path is present in the setup, we will only use it in Chapter 3, as it produces a more three-dimensional sample. The majority of the light is instead used for the *Cigar* beam, which enters the main chamber along the x direction. This beam has a maximum power of 7 W and is focused on the sample with a $f = 200\,\text{mm}$ lens to a waist of $18\,\mu\text{m}$. Along each optical path, light is carried to the science chamber through large-mode-area photonic crystal optical fibers (NKT Photonics LMA-PM-10). As fast optical switches, before each fiber we use a high power AOM. Each AOM is also used to regulate the laser intensity using a PID controller (SRS SIM960) with an error signal sampled after the fiber. The setpoint of the error signal is controlled remotely through a DAC. In the electronic circuit driving the RF amplitude of the Cigar beam AOM we also included a waveform generator (SIGLENT SDG2122X), summed to the DAC signal. This allows to introduce a sinusoidal modulation of the beam intensity, and hence of the trapping frequency, which we used for the generation of Faraday waves (see Chapter 4). Modulating the setpoint of the PID allows for a precise variation of the intensity of the beam. To monitor frequency, amplitude and phase of the modulated signal, we capture the intensity of the Cigar beam with a fast photodiode (Thorlabs DET36A/M), placed at the output of the science chamber, as shown at the bottom of Fig. 2.3.

2.2 Production of a BEC

In the following section I will describe the current experimental sequence used to create the condensed sample.

2.2.1 Pre-Cooling in the HV chamber

In the HV chamber, an atomic vapour at 250° C is heated in the oven, and then slowed down in the vertical direction by a 12-cm-long Zeeman slower. The magnetic field for the ZS is produced by four permanent magnets, while the optical radiation is a 1" beam laser to increase capture efficiency. The laser beam has an intensity of $I = 160\,\text{mW/cm}^2$, and it propagates in the negative z direction with a linear polarization orthogonal to the magnetic field. The laser frequency is red-detuned by 330 MHz from the D2 line. To increase the cooling efficiency, it is also necessary to use an EOM to produce sidebands. In this way, 50% of the total power is used for cooling, 25% address the repumper transition, and the remaining 25% sideband is out of resonance. Once slowed down by

the ZS, the atomic vapour enters the capture zone of the 2D Magneto-Optical-Trap (2D MOT).
The 2D MOT is oriented to capture the atoms in the x and z directions. The magnetic field is provided by the same permanent magnets used for the ZS. The laser radiation is composed of two orthogonal beams and is produced with the same EOM of the ZS, so it has the same spectral decomposition, only the carrier being 13 MHz red-detuned from the D2 line. The two laser beams are orthogonal to each other, and propagate along the z-x plane, rotated by 45° from the cartesian axis (see Fig. 2.1) and retro-reflected. Their intensity is of $I = 10\,\mathrm{mW/cm^2}$, and are circularly polarized with respect to the magnetic field.
The atomic vapour trapped in the 2DMOT enters the UHV chamber passing through the differential stage, pushed by a low-intensity *push* beam, resonant with the D2 line, which propagates along the positive y axis.

2.2.2 Dark Spot MOT

Atoms cooled by the 2DMOT enters the science chamber, where are captured by a Dark-Spot (DS) 3DMOT [75]. The trap uses the MOT coils in anti-Helmholtz configuration, with a magnetic field gradient of the order of $7.5\,\mathrm{Gcm^{-1}}$ along z.
The light used for cooling is 18 MHz red-detuned from the cooling transition, is divided into three pairs of counter-propagating beams with opposite polarization σ^+ and σ^-. Beams propagate along three orthogonal axis: a vertical one, which coincides with the z axis, and two horizontal ones, oriented with a 45° angle with respect to the x (or y) axis. The beam propagating along the positive z axis is carried to the science chamber by a motorized translation stage, placed below the magnetic shield. The mirror is removed at the end of the MOT stage, since the optical path of the MOT overlaps with the path of the vertical imaging.
Due to the relatively small splitting, of 58 MHz [71], between the $|F' = 3\rangle$ and $|F' = 2\rangle$ states, there is a finite probability that a fraction of the atoms decays in the $|F = 1\rangle$ state. Such a state is a dark state for the cooling transition. To circumvent this issue, we use an additional repumper beam, resonant with the $|F = 1\rangle \rightarrow |F' = 2\rangle$ transition, to reinsert the atoms in the cooling cycle. We optimize the cooling efficiency using an Axicon and a circular obstacle to convert a collimated Gaussian beam in a hollow-core beam, imaged on the atoms by a $f = 150\,\mathrm{mm}$ spherical lens. Such a configuration is known as Dark Spot [75]. The key advantage is that only hot atoms, located on the outer regions of the MOT, are reintroduced in the cooling transition. This limits light-assisted collisions and re-absorption of scattered photons in the center of the trap, where colder atoms are located.
The MOT stage reaches a steady state with 2×10^9 atoms in 15 s from the beginning of the experimental sequence, with a temperature of $300\,\mu\mathrm{K}$. This temperature is slightly above the Doppler limit $T_D = \hbar\Gamma/(2k_B)$ ($\Gamma = 10\,\mathrm{MHz}$ is the natural linewidth), which for ^{23}Na is around $225\,\mu\mathrm{K}$.

2.2.3 Grey Molasses

The subsequent step toward quantum degeneracy is to employ a sub-Doppler cooling mechanism. In our laboratory we operate a scheme called Grey Molasses (GM) [76], which was demonstrated for ^{23}Na in [66]. The efficiency of this scheme relies on a combination of polarization gradient cooling [77] with Velocity Selective Population Trapping [76, 78, 79]. This combination gives the advantage of moving atoms with the lowest velocity in a dark state, thus reducing light-scattering induced reheating.
The coupling radiation used for GM cooling must be blue-detuned from transitions of type $|F\rangle \rightarrow |F' = F\rangle$ or $|F\rangle \rightarrow |F' = F - 1\rangle$ [64]. Given the energy structure of ^{23}Na, this implies the use of the D1 line, coupling the hyperfine states $|F = 2\rangle \rightarrow |F' = 2\rangle$.
During the GM stage, all magnetic fields are switched off, and a pulse of 40 MHz blue-detuned light, with intensity 150 mW/cm^2, is shined for 0.5 ms. After this first stage, the atomic cloud is cooled down at approximately 25 μK. In a second stage we first quench the detuning to 100 MHz, and then we reduce the intensity of the laser with a 5 ms long linear ramp. This final stage allows to reach a temperature of 13 μK. This temperature is just an order of magnitude above the single photon recoil energy $T_{rec} = \hbar^2 k_L^2 / m k_B$, which for sodium atoms amounts to 2.4 μK.
After GM cooling, the atoms are ready to enter the final evaporation stage and reach quantum degeneracy.

2.2.4 Evaporative Cooling

After sub-Doppler cooling, a standard procedure to reach Bose-Einstein condensation is implemented to perform evaporative cooling [80]. In our apparatus, we perform the evaporation step directly in the optical trap, with the protocol discussed in [81], to produce a BEC of approximately 2 millions atoms, in the hyperfine state $|1, -1\rangle$.
Loading of the atoms in the optical trap occurs using a Hybrid Trap configuration. It consists of a magnetic quadrupole field with gradient $\partial B/\partial z = 13$ G/cm, with the additional *Cigar* trapping beam turned on at maximum power (7 W), which corresponds to a depth of k_B 440 μK. The loading in the optical potential is assisted by an adiabatic compression of the quadrupole to 22 G/m in 500 ms, that allows to accumulate up to 30×10^6 atoms. Atoms not collected by the optical trap are let escape by ramping the quadrupole field to 7.7 G/cm, so that gravity is compensated but the confinement vanishes.
The remaining atoms undergo a first evaporation cycle, performed by linearly lowering the depth of the trap to k_B 52 μK in 2s. We then turn on a uniform high-stability bias field of 1.3 G in the z direction, while adiabatically removing all other fields. In the last step, we perform a half-gaussian ramp in 1 s to complete the evaporation procedure, reaching a typical trap depth of k_B 3.5 μK with 2×10^6 atoms and neglectable thermal component. The same trap is then recompressed adiabatically in 1s.
The final condensate has the typical shape of an elongated cigar, with axial symmetry around the x direction. Typical Thomas-Fermi radii are $(R_x, R_\perp) = (300, 3)\mu$m for the experiments shown in Chapters 3 and 4, and $(R_x, R_\perp) = (200, 2)\mu$m for the ex-

periments discussed in Chapters 5 and 6. The corresponding trapping frequencies are $(\omega_x, \omega_r) = (10, 1000)$Hz and $(20, 2000)$Hz, respectively. As a side effect, the compression to a higher trapping frequencies introduces heating, that enhances the thermal fraction at the expense of the number of atoms in the BEC, which reduces to 1×10^6.

2.3 Spin manipulation

The most important part of the experiment involves the generation and control of Bose-Bose spin mixtures. In contrast with their close cousins, i.e., mixtures involving different atomic species, the former are much more simple to create, since they do not require a dedicated laser cooling system, but rather an apparatus which guarantees the possibility to generate and manipulate the mixture. In my PhD, I worked on the realization of two different mixtures, one already studied in previous works [63, 82, 58] and the other which constitutes a novelty in the field.
As explained in the previous section, during the transfer to the Hybrid trap we prepare a sample in the $|1, -1\rangle$ state. From this state, we populate other states using microwave driven transitions. The exact transition frequency can be calculated using the Breit Rabi formula [71], but, in first approximation, the energy of each Zeeman sublevel is given by $\Delta E = g_F m_F \mu_B B$, which is well resolved at the bias field $B_z = 1.3\,\mathrm{G}$. Looking at the values of scattering length listed in Appendix 6.3, one can then find two suitable configurations for a miscible and immiscible mixture, highlighted in Fig. 2.4(a) and (b) respectively. The advantages and disadvantages of these specific choices will be discussed in the following, for each configuration separately.
For both configurations, our apparatus allows us to switch off the coupling at will, giving us the possibility to study the properties of spin mixtures within and without the

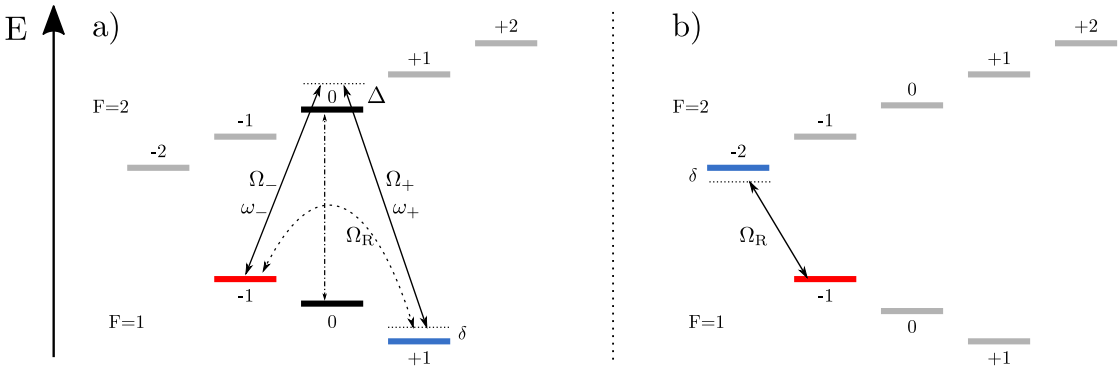

Figure 2.4: Scheme of the hyperfine splitting of the ground state of ^{23}Na. In both panels, grey state represent Zeeman sublevels not involved in the coupling, the red represent $|\downarrow\rangle$ state and the blue the $|\uparrow\rangle$ state. a) Raman transition used to create and couple the miscible mixture. Solid arrows represent the two coupling fields, while the dashed-dot arrow represent the dressing. b) Single photon coupling used to create and couple the immiscible mixture.

presence of the coupling, with tunable population imbalance. The majority of this thesis is focused on the study of mixtures in the presence of the coherent coupling. However, we will study the use of uncoupled spin mixture as an atomic magnetometer in Section 2.5.1, and their collective oscillation in Chapter 4. Specific details on the spin manipulation protocols used in the experiments will be given in each Chapter.

2.3.1 Realization of a miscible mixture

We produce a miscible mixture by coupling the states $|1,-1\rangle \equiv |\downarrow\rangle$ and $|1,+1\rangle \equiv |\uparrow\rangle$ via a two-photon (Raman) transition [see Fig. 2.4 (a)]. One can demonstrate that such a system can be mapped exactly to a two level system [83].
We use two microwaves (with frequencies ω_+, ω_-), to drive the off-resonance single photon transitions $|1,\pm1\rangle \rightarrow |2,0\rangle$, with tunable detuning $\Delta_{2,0} \pm \delta/2$ from the $|2,0\rangle$ state. This state must be highly detuned, as populating it will break coherence, as well as induce phase separation in the BEC. The two single-photon transitions have Rabi frequencies Ω_+ and Ω_-. An additional asymmetric frequency term $\pm\delta/2$ can be applied to the two fields to introduce a detuning δ from the two-photon-resonance. The resonance condition corresponds then to $E_\downarrow - E_\uparrow = \hbar(\omega_+ - \omega_- + \delta)$.
The total Rabi frequency which couples $|1,-1\rangle$ and $|1,+1\rangle$ reads $\Omega_R = \frac{\Omega_+\Omega_-}{2\Delta_{2,0}}$, and reduces to $\frac{\Omega^2}{2\Delta_{2,0}}$ if the condition $\Omega_+ = \Omega_-$ is satisfied, which corresponds to the maximum value of Ω_R. For practical purposes, the easiest to tune parameter is the detuning $\Delta_{2,0}$, which allows to cover a range of Ω_R from a few tens of Hz up to the kHz. Typical values of Ω_+ and Ω_- are instead around 5 kHz.
At $B_z = 1.3\,\mathrm{G}$, a Breit Rabi evaluation of the Zeeman sublevels energy of the $|F=1\rangle$ manifold shows that $E_{-1} + E_{+1} > 2E_0$, meaning that it is allowed for spin-changing collision to populate the $|1,0\rangle$ in time. We prevent this effect addressing the $|1,0\rangle \rightarrow |2,0\rangle$ transition with an additional microwave radiation of Rabi frequency 2.27 kHz, 20 kHz blue-detuned from resonance. This produces a light shift on the $|1,0\rangle$ that inverts the previous energy-balance.
Particular care must also be taken when tuning Ω_R to high values, as reducing the detuning $\Delta_{2,0}$ introduces atom losses. Indeed, at low Ω_R the $1/e$ lifetime is around 1 s, but decreases to 200 ms at $\Omega_R/\hbar \approx 1\,\mathrm{kHz}$. This, however, does not really affect the results presented in this thesis, as the explored physics is in the regime with $\hbar\Omega_R \sim \mu_s$.
At last, it is useful to estimate an order of magnitude for the energy scale of this mixture. As discussed in Chapter 1, the magnitude of the spin chemical potential, given by Eq. 1.25 for a uniform system, is related both to the atomic density n and to the difference between intraspecies $(g_{\uparrow,\uparrow}, g_{\downarrow\downarrow})$ and interspecies coupling constant $g_{\uparrow\downarrow}$. As reported in Appendix 6.3, the scattering lengths a_{ij}, related to the coupling constants through $g_{ij} = 4\pi\hbar^2 a_{ij}/m$, read:

$$a_{\downarrow\downarrow} = 54.5a_0, \quad a_{\uparrow\uparrow} = 54.5a_0, \quad a_{\downarrow\uparrow} = 50.8a_0 \tag{2.2}$$

Within this values, and a typical atomic density in the optical trap (with the parameters given in Section 2.2.4) of $4 \times 10^{14}\,\mathrm{atoms/cm^3}$, one can calculate that the spin chemical potential is of the order of $\mu_s/\hbar \propto (g - g_{\downarrow\uparrow})n \approx 200\,\mathrm{Hz}$. Furthermore, this mixture

has the nice property of being $\mathbb{Z}_2$ symmetric, due to the symmetry in the intraspecies coupling constants $g_{\uparrow\uparrow} = g_{\downarrow\downarrow} = g$.
This mixture has been used in the experiment presented in Chapter 3 and Chapter 4.

2.3.2 Realization of an immiscible mixture

Starting from $|1,-1\rangle = |\downarrow\rangle$, an immiscible mixture can be created populating the $|1,0\rangle$ state, either with a single photon RF transition, or with a two-photon Raman transition in the microwave range. Another possibility could be to populate the $|2,-2\rangle = |\uparrow\rangle$ state with a single photon microwave transition. While the former would be in principle preferable due to the similarity of the coupling constants (see Table 3), preliminary attempts revealed difficulties in stabilizing the mixture. The choice of the stretched states has instead the key advantages to be realized with a single-photon coupling on a transition with unitary Clebsch-Gordan coefficient, and to be robust again spin-changing collisions, which induce decoherence. It also avoid all the problems related to the loss of atoms arising from the two-photon coupling.
The Rabi frequency Ω_R can be directly tuned through the amplitude of the microwave field, up to a maximum value of about 6 kHz. The detuning on the other hand is simply given by $\hbar\delta = E_{2,-2} - E_{1,-1} - \hbar\omega$, easily tunable either by changing the bias field or by changing the microwave frequency.
For this mixture, the value of the scattering lengths are

$$a_{\downarrow\downarrow} = 54.5a_0, \quad a_{\uparrow\uparrow} = 64.3a_0, \quad a_{\downarrow\uparrow} = 64.3a_0 \tag{2.3}$$

At equal density of the sample, the spin chemical potential is 1.3 times larger than the one of the miscible mixture. However, while performing experiments we discovered that a much larger trapping frequency was required to freeze the radial spin degree of freedom (see discussion in Section 1.3.3). As a result of using a larger trapping frequency, the density of the sample increased, leading to a spin chemical potential $\mu_s \sim 1200\,\text{Hz}$. A much larger spin chemical potential, introduces a key advantage, since it relaxes the stability condition for the magnetic field. Using the expression for the linear Zeeman energy $\Delta E/B = h2.1\,\text{MHz/G}$ it is easy to calculate that, in order to have fluctuations of 10 Hz, it is required to have shot-to-shot fluctuations of the order of 5 μG.
As a final note, the asymmetry in the intra-species coupling constants, $g_{\downarrow\downarrow}/g_{\uparrow\uparrow} \approx 0.85$, introduces an asymmetry in the ground state configuration of the mixture, as explained in Section 1.2.1 and shown in Fig. 1.1. Due to the harmonic confinement of the ODT, in an immiscible mixture with $n_\uparrow = n_\downarrow$, the $|\downarrow\rangle$ state will always be the center of the cloud while the $|\uparrow\rangle$ on the side.

2.4 Spin-selective imaging

As in many experiments involving mixtures, a spin selective imaging is required [84].
For Cam. Hor1 (and Cam. Hor3), we distinguish different spin states performing a Stern-Gerlach (SG) operation. In particular, after a given spin manipulation of the system, we

release the optical trap and let the atoms expand, to avoid imaging saturation, and fall for 5 ms. We then turn on the quadrupole magnetic field to introduce a magnetic field gradient of 8 G/cm, enough to compensate gravity for a few ms. Gradient compensation is exact only for the state $|F = 1, m_F = -1\rangle$, while the other state will either fall or accelerate, depending on the sign of g_F.
Standard resonant absorption imaging is then performed. We first populate the $|F = 2\rangle$ manifold with a fast pulse of the repumper light, and then illuminate the atoms with a circularly polarized probe beam propagating in the x direction, resonant with the $|F = 2\rangle \rightarrow |F' = 3\rangle$ transition. Since probe polarization is important in order to correctly count the atom number [85], we switch off the magnetic field gradient just before the probe pulse, and turn on a small bias field along y.
This imaging direction is useful for measurements that characterize the global response of the sample, e.g. the Rabi frequency measurements, spectroscopic calibration of the magnetic field (see Section 2.5), or temperature measurements.
The z direction provides a better field of view, since it allows to observe axial dynamics in the condensate. However, the cylindrical shape of the magnetic shield does not allow for a SG imaging, since a strong gradient in the horizontal plane could permanently magnetize the shield. Instead, we use microwave spin selective imaging to gather multiple images of each $|m_F\rangle$ state, with a 1 ms delay between each image. This is allowed by the fast acquisition rate of the CMOS camera [86].
Specifically, we use a technique based on Partial Transfer Absorption Imaging (PTAI), which has been useful for in-situ imaging [82, 87] where, in order to avoid density-related saturation, only a fraction of the sample is imaged. This is achieved by promoting atoms from the ground state to an auxiliary state, resonant with the probe pulse.
In our spin selective imaging protocol, 1 ms after releasing the trap, we apply a resonant microwave transfer, which lasts a few tens of μs, to transfer atoms from the $|1, -1\rangle$ to the stretched state $|2, -2\rangle$, and then shine a probe pulse to gather the image of the first state. The same procedure is repeated for the state $|1, +1\rangle$, with a time delay of 1 ms, that can be handled with a careful choice of the exposure timings, and the dimension of the region of interest (ROI) of the camera. Indeed, as the camera records photos row by row [86] starting from the central one, choosing a smaller ROI in the vertical direction allows for a faster acquisition rate.
We address the problem of in-situ saturation by applying a small TOF of 1 ms before starting the imaging procedure. As a result of the expansion, the dimensions of the sample will change as $R_i(t)/R_i(0) = \sqrt{1 + \omega^2 t^2}$ [88], where $i = x, \perp$. This quantity is approximately 12 in the radial direction and 1.01 in the axial direction. In this way, we reduce the density by a factor 100, enough to avoid saturation, while leaving the dynamics along the axial direction unaltered.
In particular, for experiments on the miscible mixture, we separately send the atoms in $|1, \pm 1\rangle$ to the stretched states $|2, \pm 2\rangle$ with a π-pulse, using the same antennas used for coherent coupling, with Rabi frequencies of the order of 25 kHz, higher than any other energy scale. For experiments on the immiscible mixture, since the stretched state is already occupied by the mixture itself, we first gather the image of the state $|2, -2\rangle$ then

perform the π-pulse transfer and image the $|1,-1\rangle$. In this experiment, due to the radial trapping frequency at 2 kHz, the radial size of the atomic sample in the second image will be twice as large as the one in the first image.

2.5 Low magnetic field noise environment

For the realization of coherently-coupled mixtures at low Rabi frequency, two important requirements are the precise knowledge of the detuning between the microwave frequency and the atomic resonance, fundamental to control the population imbalance of the mixture, and coherence times long enough to perform experiments. In the following, I will discuss the protocol we use to precisely calibrate the resonance condition through a fine-tune of the bias field, and show a characterization of its stability over a day of measurements.

2.5.1 Calibration of the resonance condition

To create spin mixtures, it is fundamental to finely tune either the transition frequency or the bias field to match the resonance condition. In both cases, a precise measurement of the magnetic field is required. The optimal solution for our setup, since it is impossible to place a magnetometer inside the shield, is to use the atoms as a sensor. Several ideas have been developed in the past years to use atomic spin systems as magnetic sensor [89]. A fast and sufficiently precise measurement is Rabi spectroscopy, which, in the regime $\hbar\Omega_R \gg \delta g n$, works for both mixtures discussed in the previous section. For a generic Rabi-coupled system, we can identify the two states as $|\uparrow\rangle$ and $|\downarrow\rangle$. Starting with all the atoms in $|\downarrow\rangle$, the population of $|\uparrow\rangle$ varies as a function of Ω_R, δ and t as

$$\rho_{\uparrow\uparrow} = \frac{\Omega_R^2}{\Omega_R^2+\delta^2}\sin^2\left(\frac{\sqrt{\Omega_R^2+\delta^2}}{2}t\right) \tag{2.4}$$

As discussed in Chapter 1, it is useful the introduce the relative magnetization $Z \equiv \rho_{\uparrow\uparrow} - \rho_{\downarrow\downarrow}$, so that $Z \in [-1,1]$. A spectroscopic measurement of δ can be performed, for a known Rabi frequency Ω_R, applying a squared pulse of duration π/Ω_R at different detunings δ. The detuning is varied applying a small correction to the bias field with respect to a reference value, keeping fixed the microwave frequency. After the pulse, we separate the two states with a SG and measure the two populations with Cam. Hor1. The magnetization Z as a function of δ, measured after the π-pulse, has a characteristic sinc-shape, and can be fitted with the function

$$Z = -\frac{\delta^2+\Omega_R^2\cos\left(\sqrt{\Omega_R^2+\delta^2}\right)t}{\Omega_R^2+\delta^2} \tag{2.5}$$

with δ as a fitting parameter. The last expression can be derived by expressing $Z = 2\rho_{\uparrow\uparrow} - 1$ and using Eq. 2.4. In order to avoid density-related shifts in the resonant

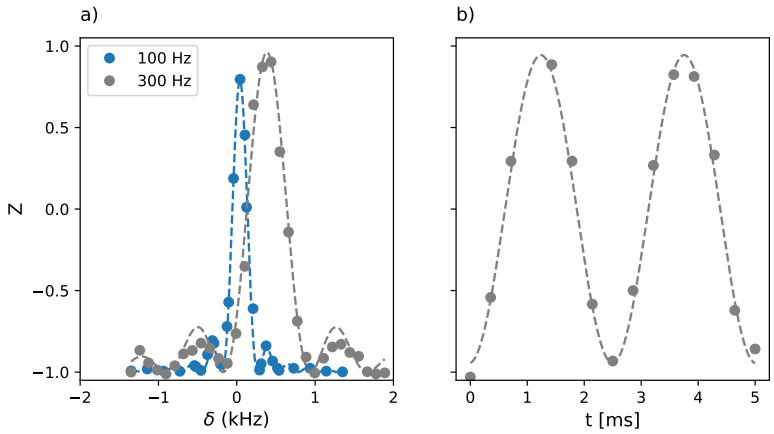

Figure 2.5: a) Spectroscopic measurement of the resonance condition at $\Omega_R = 100\,\text{Hz}$ and 300 Hz. The broadening of the linewidth with increasing Ω_R is clearly visible. Measurements are taken in two different days. b) Example of calibration of the Rabi frequency, once the resonance condition is known.

frequency, one can either work with a BEC with very large Ω_R, but this leads to a less precise measurement as the linewidth of the sinc is given by Ω_R [see Fig. 2.5(a)]. An optimal choice is then to work with a dilute thermal cloud, which allows to reduce Ω_R around a few hundred Hz. We produce low density thermal clouds lowering the initial intensity of the Cigar beam during the loading in the Hybrid Trap, without modifying other parameters in the evaporation procedure. This allows us to reduce the number of atoms, thus drastically lowering the critical temperature necessary to achieve condensation[2].
Once the resonance condition is known, the same procedure can also be used to measure the Rabi frequency, by applying pulses of different duration at zero detuning. Indeed formula 2.5, for $\delta = 0$, reduces to the usual cosine function. An example of this measurement is reported in Fig. 2.5(b).

2.5.2 Daily stability

While the former procedure allows to measure the resonant condition in a few minutes, more precise measurements can be performed to quantify its time variation. Shot-to-shot fluctuations, for example, can be extracted measuring the population imbalance over time. This is achieved applying a pulse of duration π/Ω_R at $\delta \neq 0$, such that the resulting magnetization is $Z = 0$. The shot-to-shot value of Z can then be mapped to a value of B_z with the help of the spectroscopy reported in Fig. 2.5. A 3-hour long measurement performed at $\Omega_R = 150\,\text{Hz}$ is reported in Fig. 2.6 (a). The measurement shows a slow drift of the magnetic field, that occurs on a time scale of approximately two hours. As a

[2]We recall that, for a gas at equilibrium in a harmonic trap, the critical temperature reads $T_c = 0.94\hbar\omega_{ho}N^{1/3}$[6].

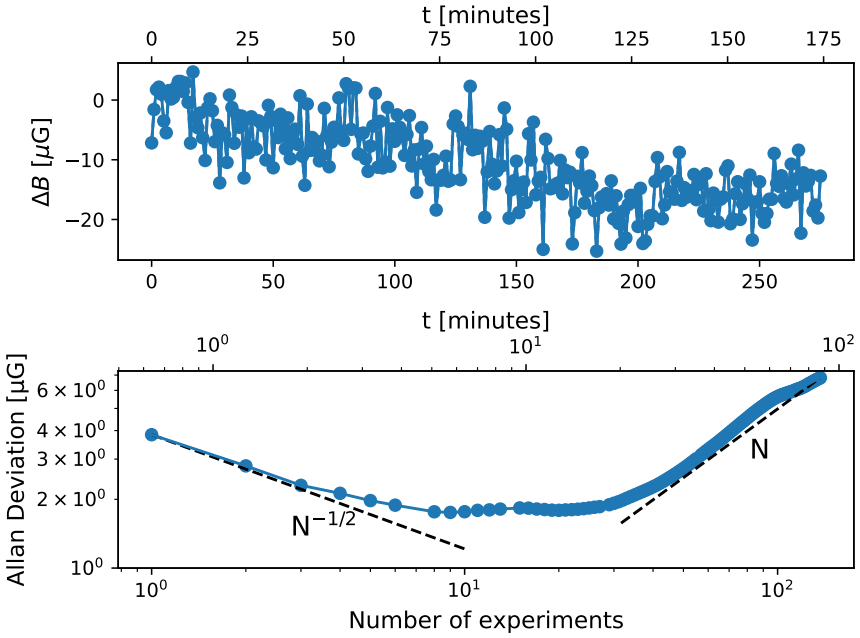

Figure 2.6: a) Drift of the magnetic field in time, which show a drift of approximately $20\,\mu$G. b) Allan deviation calculated on the same dataset.

more quantitative measurement, I also report the Allan deviation [90] calculated on the same dataset in Fig. 2.6 (b). The Allan deviation can be used to estimate the nature of the noise. We observe that up to 10-12 experiments (approximately 7-8 minutes) fluctuations are dominated by white noise, which scales as $1/\sqrt{N}$, with $\sigma \approx 4\,\mu$G. For integration time of up to 10 minutes, magnetic noise is as low as $2\,\mu$G. At longer times, we observe a drift which scales linearly with N in the Allan deviation, compatible with a low-frequency noise. This can be due to temperature effects on the magnetic shield, or on the current source driving the bias magnetic coils.
This measurement confirms that magnetic field noise in our apparatus is low enough for the apparatus to produce and manipulate coherently-coupled condensates with high precision, even if the Rabi frequency is much lower than the spin interaction energy. The studies presented in Chapters 5 and 6 will heavily rely on this stability, as the detuning from resonance will become an important tuning knob in the experiment.

Chapter 3

Characterization of a Coherently Coupled miscible mixture

Contents

In Chapter 1 we discussed the ground state properties and dynamics of a miscible spin mixture in the presence of an external radiation that coherently couples the two states. The dynamics of such a system is described by a dissipationless Landau-Lifshitz equation, Eq. 1.38, and it is equivalent to the Josephson dynamics, as demonstrated experimentally in coherently-coupled [42] and double-well [52, 91] systems.
We have also briefly anticipated that the presence of an inhomogeneous density profile introduces an additional tuning parameter to the dynamics, as the relevant parameter $\kappa n/\hbar\Omega$ smoothly varies in space. In this case, we refer to the system as an elongated Josephson junction, which has been studied both theoretically [54] and experimentally [53, 91, 92] in double-well systems. On top of this results, the possibility to engineer a Josephson junction in the internal state of the atoms [42], makes a further step in the study of Josephson systems, introducing a bridge towards the study of magnetic materials with ultracold atomic gases. Particularly important is the presence of a spatial degree of freedom, as it adds to the picture the possibility of engineering magnetic heterostructures [58] and study the behaviour of magnetic fluctuations [93, 94]. In this Chapter, I will discuss the experimental realization of a one-dimensional elongated Josephson junction using a coherently-coupled two-component miscible mixture of ^{23}Na atoms, describing the characterization of the system dimensionality, as well as different methods to manipulate the sample. The results of this work are published in Ref.[95].

3.1 Investigation of spin dimensionality

As anticipated in the previous chapters, we produce three dimensional condensates with the shape of an elongated cigar, with a Thomas-Fermi density profile $n(x, r_\perp) = n_0 \left[1 - \left(\frac{x}{R_x}\right)^2 - \left(\frac{r_\perp}{R_\perp}\right)^2\right]$, R_x and $R_\perp$ being the axial and radial radii. Being fully 3D in the density channel, in principle the system can support both three dimensional as well as lower dimensional spin excitations, as in the latter case the relevant mean-field energies are more than one order of magnitude smaller as compared to the density ones. A natural question to address is about the parameters for which the crossover between the two regimes occurs. As already discussed in [96, 97], the transition between the 1D and 3D regime for a single component condensate confined in an axially symmetric trap occurs when the radial trapping frequency $\omega_\perp$ is much larger than the mean-field interaction, which is equivalent to $\xi_d > R_\perp$, a necessary condition to essentially freeze the radial excitation of the condensate. In analogy, for a spin mixture this occurs when the minimum length scale for spin excitations, i.e., the spin healing length ξ_s, is comparable with the transverse Thomas-Fermi radius, $R_\perp/\xi_s \sim 1$. Using the definition of the healing length for the density and the spin channel, we obtain

$$\begin{aligned} \frac{R_\perp}{\xi_d} &= \frac{2n_0 g}{\hbar\omega_\perp} \\ \frac{R_\perp}{\xi_s} &= \frac{2n_0 g}{\hbar\omega_\perp}\sqrt{\frac{\delta g}{g}} \end{aligned} \tag{3.1}$$

with the definition of g and δg given in Chapter 2. For ^{23}Na atoms at 1.3 G, we have that $\sqrt{g/\delta g} = 0.26$, see Appendix 6.3. This last consideration relaxes the condition to reach the 1D regime, since the ratio required for the spin channel can be approximately 4 times larger than the one needed to have a one dimensional single component condensate.
The dimensionality of spin dynamics can be investigated by employing a protocol that produces spin excitations along the transverse direction. The key idea is to take advantage of the Josephson dynamics of the system, along with the inhomogeneity of the density profile, to create different dynamical regions in the sample. Let us focus on a region around the $x = 0$ plane, with peak density n_0, limited at $R_\perp$. An ideal protocol would start with all the atoms in the $|1, -1\rangle \equiv |\downarrow\rangle$, to which one applies a squared Rabi pulse at resonance with $|1, +1\rangle \equiv |\uparrow\rangle$, for a time which would correspond to a π-pulse for an ensemble of non-interacting atoms. If we choose $2\hbar\Omega < \delta g n_0$, the center part of the cloud will remain self-trapped [see Fig. 1.5 (c)], whereas the low-density tails, at some finite value of $r_\perp$, will follow the usual Rabi dynamics. The resulting magnetization profile would present transverse spin excitations if $R_\perp > \xi_s$, otherwise they would be suppressed. The presence or absence of radial excitations would then distinguish between the 3D and 1D regimes.

Experimental Protocol We run a set of experiments to determine for which parameters the spin dynamics can be reduced to be effectively one dimensional. Every

experiment begins with a BEC of 2×10^6 atoms in the state $|1, -1\rangle$, produced with the protocol described in Chapter 2, with the atom loaded in a crossed optical dipole trap composed of Cigar and Xaxis beams. The Cigar beam is the main trapping beam, propagating along x, while the Xaxis is only used to prevent axial sloshing of the BEC. Due to the axial symmetry of the Cigar, the sample has an elongated cigar shaped distribution, confined by an harmonic trap with longitudinal trapping frequency $\omega_x = 10\,\text{Hz}$. The radial trapping frequency can be instead tuned by acting on the intensity of the Cigar after the recompression ramp. We use this latter as a control parameter to vary the ratio $R_\perp/\xi_s$, by changing the value of $\omega_\perp$ in each experiment. This allows us to tune the radial trapping frequency $\omega_\perp/2\pi$ between 500 Hz and 1000 Hz, only little affecting the axial trapping frequency.
After trap compression, we turn on the coupling and apply a resonant π-pulse on the cloud, with $\hbar\Omega_R = 0.3\delta g n_0$, to ensure that the center of the cloud remains self trapped. The value of Ω_R and the resonance condition $\delta = 0$ are independently calibrated on a very dilute thermal cloud, as explained in Chapter 2.
After the π-pulse, we gather absorption images from the z direction using Cam. Vert. to image the radial and longitudinal spin distributions. Details about the imaging procedure are given in section 2.4. We gather data for different values of the control parameter $\omega_\perp$, tuning $R_\perp/\xi_s$ from 1.2 to 4.9.
Results for the optical density of the two components are shown in Fig. 3.1, at the crossover from the 1D (a) to the 3D (b) regimes. In the first case (panel a), $R_\perp/\xi_s = 1.6$, one can observe that the self trapped region around $x = 0$ extends homogeneously along the y direction. Atoms in the low-density tails of the BEC have been instead promoted to

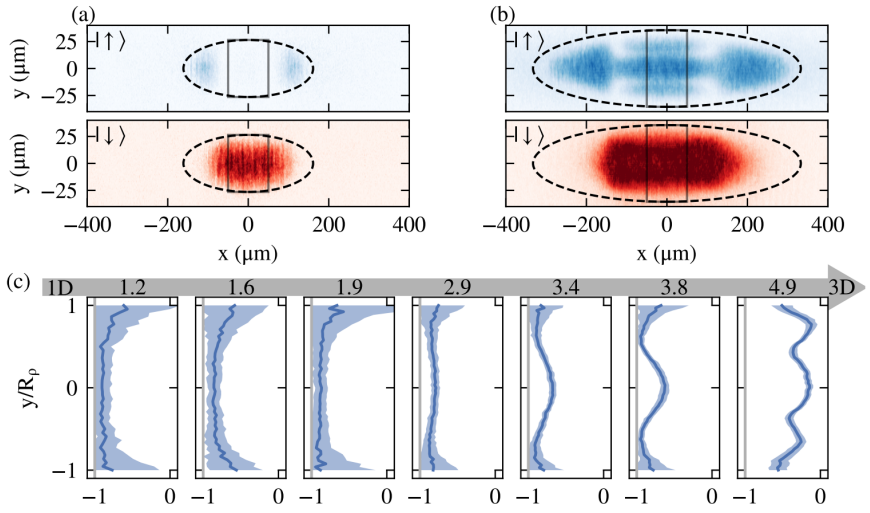

Figure 3.1: Spatial distribution of the two components, $|\uparrow\rangle$ in blue and $|\downarrow\rangle$ in red for (a) 1D regime and (b) 3D regime. $R_\perp/\xi_s$ are 1.6 and 4.9 respectively. (c) Magnetization along y, integrated along z, in the different regimes. Shaded areas represent confidence intervals of one standard deviation.

the $|\uparrow\rangle$ state, due to the π-pulse. In the other regime (panel b), $R_\perp/\xi_s = 4.9$, and regions with atoms in $|\uparrow\rangle$ are present also around $x = 0$. Due to the imaging integration along the z direction and the axial symmetry of the sample, the ODs shown do not strictly represent the true radial shape of the excitation. The latter could be best reconstructed through an inverse Abel transform. Nevertheless, it is clear that radial spin excitations are present in the system.
To better investigate the transition between the two regimes, we measure the radial magnetization $Z(y)$, averaging over the central 100 μm of the trap. Results are shown in panel (c), for different values of $R_\perp/\xi_s$. We observe that $Z(y)$ is constant for $R_\perp/\xi_s \leq 3$. Above this value, oscillations along y are present, reflecting the structures present in absorption images. Throughout the rest of the work, we will then set $R_\perp/\xi_s < 3$, to reduce to the simpler 1D study case. This allows us to integrate out the radial degrees of freedom and monitor only the behaviour of $Z(x)$, simplifying the study of the relevant physics that arises from the inhomogeneity. Working in the 1D regime implies also that the parameter δg must be substituted with the renormalized constant $\kappa = \frac{2}{3}\delta g$, as discussed in Section 1.3.3.

3.2 Density dependent spectroscopic shift

In dense atomic clouds, transitions between atomic levels are strongly affected by the presence of interactions. In the GPE framework, this effect is well captured by the mean-field energy shifts, arising from intra and inter-species interactions. In a Josephson system, they manifest when the linear coupling strength is smaller than the non-linear interaction energy κn.
To probe this effect, we perform a set of experiments, following the same spirit of the

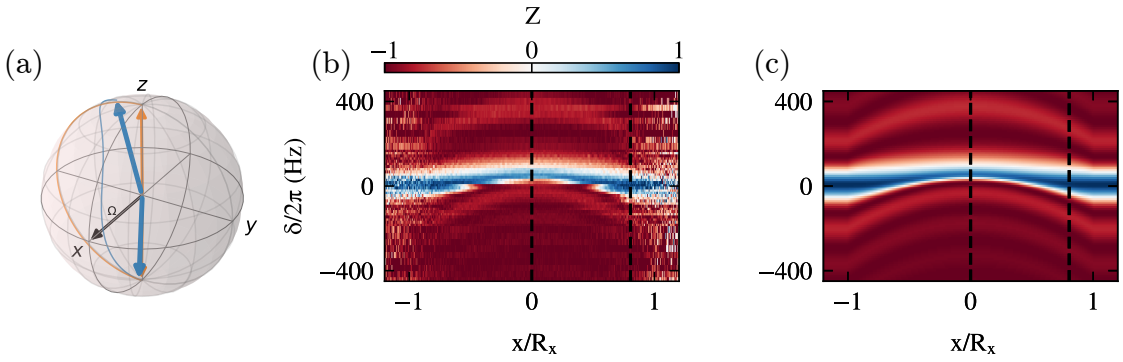

Figure 3.2: (a) Spin dynamics represented on the Bloch sphere, with blue (orange) lines in the presence (absence) of the nonlinear contribution. Direction of the Rabi vector is represented by a black arrow. (b) Local magnetization $Z(x)$ for different values of detuning δ. The center of the cloud is at $x = 0$ and extends up to $R_x = \pm 1$, external regions being filled with the thermal component. (c) Numerical solution of the LLE for a Thomas-Fermi shaped nonlinear interaction $\kappa n(x)$, calculated at different values of δ.

spectroscopic measurement presented as a calibration in Chapter 2. Each experiment starts with a sample in $|\downarrow\rangle$, to which we apply the linear coupling $\Omega_R/2\pi = 68.5(5)$ Hz for a period $t = \pi/\Omega$, to transfer the population to $|\uparrow\rangle$. We repeat the measurement for different values of the detuning δ from the resonant transition frequency for a single atom, which we refer to as $\delta = 0$. This protocol consists in a rotation of the spin vector on the y-z plane of the Bloch sphere, perpendicularly to the Rabi vector, which, for $\delta = 0$, is oriented along x [see Fig. 3.2(a)]. As we vary δ, the Rabi vector acquires an additional component along z, whose amplitude is given by δ. Since we work in the 1D regime, for each δ we can extract the 1D magnetization $Z(x)$, calculated from previous separate integration of the 2D densities along y.
Results for $Z(x)$ are shown in the color plot of Fig. 3.2(b), as a function of space and detuning. We also compare the experimental data with the numerical solution of the Landau-Lifschitz equation, shown in panel (c). The latter is evaluated in the Local Density Approximation (LDA), with $\kappa n(x)$ that varies is space, following a 1D Thomas-Fermi profile. Although this simulation does not keep into account spatial dynamics arising from spin currents, it remarkably matches the experimental data.
At first, we observe that thermal atoms ($|x| > R_x$) and the low density tails of the cloud are not affected by the presence of interactions, and behave as an ensemble of non-interacting atoms. We refer to this behaviour as the deep Rabi regime. The dynamics in this region, and hence the local magnetization Z, is governed only by the value of the detuning δ, as expected for a two-level system. The dependence of Z on δ is characterized by the common squared sinc-like shape, shown in orange (dots and lines) in Fig. 3.3(a). On the other hand, the central region of the cloud $x = 0$ satisfies the condition $\hbar\Omega < \kappa n_0$, thus Josephson dynamics is expected. The different behaviour of the center of the cloud, as compared to the dynamics of the tails, is evident from data

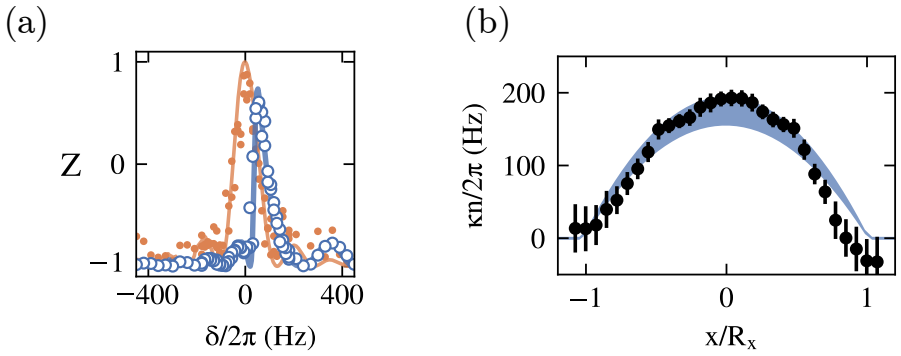

Figure 3.3: (a) Vertical cuts of data shown in Fig. 3.2(b) at $x = 0$ (blue points) and at $x = 0.8R_x$ (orange points), fitted with the Josephson equations with κn as free paramater (blue and orange lines). (b) Black points show the value of κn at different x, with the error resulting from the fit. Blue shaded area shows the predicted $\kappa n(x)$ extracted knowing the Thomas-Fermi profile, the trapping frequency and total atom number.

of panel (b).
In particular, the spectroscopy curve measured at $x = 0$, plotted in Fig. 3.3(a), becomes asymmetric and shifted towards positive value of δ. The direction of this shift, and the degree of asymmetry, depend respectively on the sign and the strength of the nonlinear parameter κn. Both these quantities can be extracted by fitting the experimental data with a numerical integration of the Josephson equations, leaving κn as the free parameter.
Points in Fig. 3.3(b) show the value of κn extracted from several fit of $Z(\delta)$, performed at different spatial position x, and compared with the expected Thomas-Fermi profile (blue shaded area). The shaded area is obtained measuring the atom number from absorption imaging, averaged over the whole dataset. From the fit, we obtain $\kappa n_0/2\pi = 192(11)$ Hz, which is consistent with the expected value for $\kappa n/2\pi = 173(20)$ Hz.

3.3 Density dependent Adiabatic Rapid Passage

The discussion of the previous section demonstrates that a Rabi pulse cannot be used to produce states with spatially homogeneous magnetization, unless one works in the deep Rabi regime, with $\hbar\Omega_R \gg \kappa n_0$ even in the center of the cloud. Nevertheless, the preparation of a state with uniform magnetization at low coupling strength gives substantial advantages for further manipulation of the mixture [98, 99]. A different approach could be to employ Adiabatic Rapid Passage (ARP) techniques [100], which could be used, for instance, to generate number-squeezed states [101]. This procedure heavily relies on the existence of an avoided crossing between the energies of the dressed states of a two-level system coupled with a coherent radiation [102].
During an ARP, the coupling is applied to a fully polarized state ($|\downarrow\rangle$ for example) with an initially large detuning $|\delta| \gg \Omega$. This ensures that no spin dynamics is excited, as the system is close to the ground state. The detuning is then slowly swept towards lower absolute values (*frequency chirping*), with a speed $\partial_t\delta(t) \ll \Omega^2(t)$, that ensures adiabaticity. If the evolution is adiabatic, the system will follow the change of δ and rotate on the Bloch Sphere with the Rabi vector [see Fig. 3.4(a)], passing through a state with $Z = 0$, until the system has been fully converted to $|\uparrow\rangle$.
During the ramp, the values of Z and δ are related by [101]:

$$\hbar\delta = \hbar\Omega\frac{Z}{\sqrt{1-Z^2}} + \kappa n Z \tag{3.2}$$

This expression can be obtained from the Josephson equations 1.40 imposing that the phase is null, $\phi = 0$, and constant during the evolution, $\partial_t\phi = 0$. This approximation might fail in two cases. The first occurs if the initial detuning is not large enough. In this case, turning on the coupling abruptly will introduce spin oscillations on the Bloch sphere, around the Rabi vector, with an amplitude that will become larger and larger during the Adiabatic Passage. The second case occurs instead if the change in detuning $\partial_t\delta(t)$ is too fast compared to the Rabi frequency, thus breaking the adiabaticity condition. If this occurs, a portion of the state might jump over the avoided crossing,

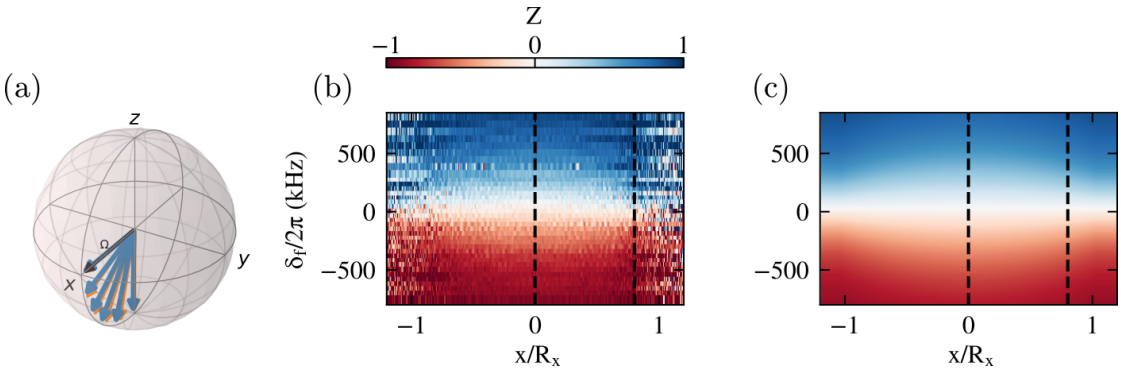

Figure 3.4: (a) Illustration of the change in the Rabi (orange) and spin (blue) vectors during the ARP. (b) Experimental data for the integrated magnetization $Z(x)$, represented as a colorplot for varying detuning and spatial position. (c) 1D numerical evaluation of the Josephson dynamics with the same parameters used in the experiment.

resulting in a incoherent superposition of the two states.
From Eq. 3.2, we can see that in the deep Rabi regime the magnetization Z depends only on δ/Ω, while a correction due to the Josephson dynamics appears for larger values of κn. In both cases, however, the magnetization reaches $Z = 0$ at $\delta = 0$, independently of the value of κn. In addition, interactions helps stabilizing the mixture against magnetic field fluctuations, as the sensitivity of Z to a change in δ, given by

$$\left.\frac{\partial Z}{\partial \delta}\right|_{Z=0} = \frac{1}{\Omega_R + \kappa n} \tag{3.3}$$

is decreased by κn. This effect can be used to produce number squeezed state [101].
A crucial detail is the initial sign of the detuning, as it determines whether, during the ARP, the system will cross the $\delta = 0$ plane of the Bloch sphere as the lowest energy ($\phi = 0$) or the highest energy ($\phi = \pi$) dressed state. For a coherently-coupled BEC, this is even more dramatic as spin instabilities [56] develop when the system acquires a relative phase $\phi = \pi$. As we identify the GS of the BEC with the highest energy state of the $|F = 1\rangle$ manifold of the atomic Hamiltonian, then the coupling must start *blue* detuned. However, as the choice of the detuning sign is only a convention, and we represent $|1, -1\rangle$ as $|\downarrow\rangle$ on the Bloch sphere, we will still refer to this as a *negative* detuning.
We investigate the response of the elongated Josephson junction to an ARP with a dedicated set of experiments, all starting with all the atoms in $|\downarrow\rangle$. After condensation, we turn on the coupling with $\Omega_R/2\pi = 273(1)$ Hz and initial detuning $\delta_i/2\pi = -3$ kHz. The detuning is swept adiabatically with a 50 ms long half-gaussian ramp (with HWHM = 25 ms) up to a value δ_f. The detuning can be tuned either through the microwave generator, or by finely adjusting the magnitude of the bias field at constant microwave

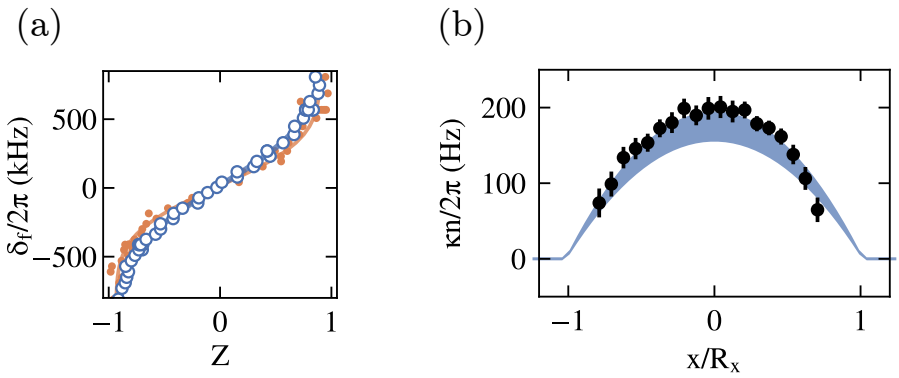

Figure 3.5: (a) Vertical cuts of data shown in Fig. 3.4(b) at $x = 0$ (blue points) and at $x = 0.8R_x$ (orange points), fitted with the Josephson equations with κn as free parameter (blue and orange lines). (b) Black points shows the value of κn at different x, with the error resulting from the fit. Shaded area shows the predicted $\kappa n(x)$ extracted from trapping frequency and atom number.

frequency. We choose the latter for practical purposes[1]. According to the previous discussion, to reduce the detuning we increase the value of the bias field.
This protocol is applied for different values of δ_f. The behaviour of the magnetization Z as a function of x and δ_f is shown in Fig. 3.4(b). At the beginning of the ramp, the cloud is uniformly in the state $|\downarrow\rangle$. During the evolution, regions with different spin density $\kappa n(x)$ evolve differently, with a transition towards $|\uparrow\rangle$ that is smoother in the trap center with respect to the tails. Nevertheless, the cloud homogeneously reaches $Z = 0$ at vanishing detuning $\delta = 0$, as expected from Eq. 3.2; a non-trivial result since the rotation speed varies in space. This behaviour also stems from the symmetric intraspecies coupling constant of the mixture (see Appendix 6.3), which results in a $\mathbb{Z}_2$ symmetric mixture. This will not be the case for the immiscible mixture studied in Chapter 5 and 6. At last, further increasing the detuning leads to a full transfer of the cloud in the $|\uparrow\rangle$ state.
As we did in the previous section, we can compute the local value of κn, by fitting $Z(\delta)$ at different x, with a numerical model extracted from the Josephson equation. In this case, we fit $Z(\delta)$ with a sigmoidal function, from which we can extract both the slope in the center and the value of κn, using formula 3.3. Examples are given in Fig. 3.5(a) in the center (blue points) and on the side (orange points) of the condensate. With this procedure we obtain $\kappa n_0/2\pi = 200(15)$ Hz in the center. The values of κn fitted in different regions are shown in panel (b), and compared with the expected Thomas-Fermi profile, reconstructed from atom number.

[1]Specifically, the value of the bias field can be varied smoothly, as it is set by a digitally-controlled current source, with a time delay in the order of a few μs resulting from the impedance of the coils. On the other hand, a ramp in microwave frequency is limited by the writing time of the Look-Up-Table of the DDS, which takes around 30 μs to update, but it features a "sharp" frequency change. This might introduce discretization effects in the ramp.

As a final remark, this procedure allows to prepare a uniform $Z = 0$ ground state of a balanced mixture, since the condition $\phi = 0$ that minimizes the energy (see Eq. 1.26) is satisfied for any value of δ. This method of mixture manipulation will be also used for the preparation of a balanced miscible mixture in Chapter 4.

3.4 Plasma Oscillation and Scaling of the gap

The ground state of the mixture, at finite Ω_R and $\delta = 0$, is a homogeneous state with $Z = 0$ and $\phi = 0$. Once represented on the Bloch sphere (Fig. 3.6(a)), it is also a fixed point of the dynamics. For small deviations from this state, Josephson dynamics predicts the appearance of small amplitude oscillations in Z around the fixed point (see Fig. 3.6(a)), called *plasma oscillations* [52], with frequency:

$$\omega_{pl} = \sqrt{\Omega_R(\Omega_R + \kappa n/\hbar)} \tag{3.4}$$

The dependence of the plasma frequency on the nonlinear interaction term κn suggests the possibility of measuring the latter from independent measures of Ω_R and ω_{pl}. The dependence of κn only on frequencies provides a key advantage, as compared to the previously discussed methods, in terms of high precision and insensitivity to systematic errors coming from imaging calibrations.
To measure plasma oscillations in our system, we prepare a stationary state at $Z = 0$ and $\phi = 0$ with the ARP protocol described in the previous section, stopping the ramp at $\delta_f = 0$. To start the dynamics, we suddenly change the phase of the coupling from 0 to 0.1π, and measure the time evolution of the state, shown in Fig. 3.6(b). For different positions x, we extract $Z(t)$, and fit it with a sinusoidal function, to extract the frequency of oscillation. We initialize the fit by setting as an initial guess the Fourier transform of the data. Since Ω_R is homogeneous in space to a few percent (see [63] for a

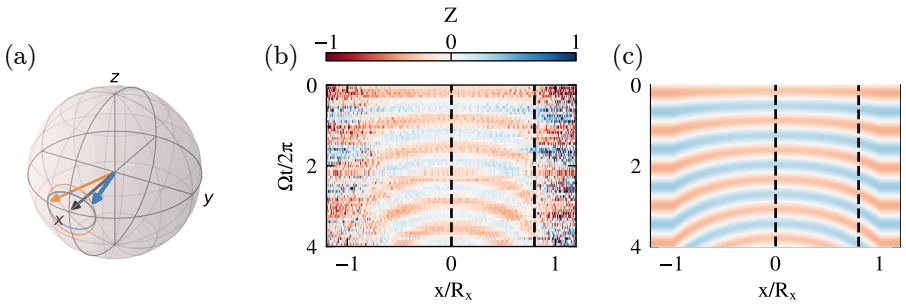

Figure 3.6: (a) Spin dynamics represented on the Bloch sphere, with blue (orange) lines in the presence (absence) of the nonlinear contribution. Direction of the Rabi vector is represented by a black arrow. (b) Experimental values of the integrated magnetization $Z(x)$, as a function of time after the quench in the coupling phase. (c) Evolution of $Z(x)$ obtained from numerical evaluation of the Josephson equation, with the same protocol used in the experiment.

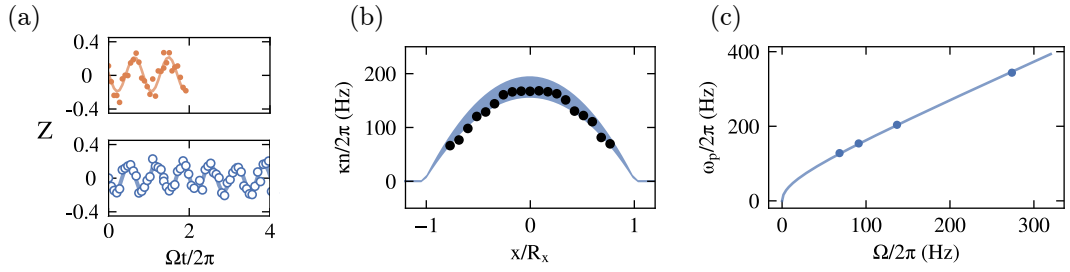

Figure 3.7: (a) Plasma oscillation extracted in the center (blue points) and on the edge (orange points) of the trap, fitted with a sinusoidal curve (solid lines). At the edge of the trap, oscillations last only two Rabi periods, probably due to interactions with thermal atoms. (b) Black points show extracted values of $\kappa n(x)$ from a sinusoidal fit. Solid area is the estimation of $\kappa n(x)$ from atom number and trapping frequency. (c) Scaling of the plasma frequency as a function of the Rabi coupling Ω_R (blue points), compared with the theoretical prediction, Eq. 3.4.

detailed discussion), this measurement allows to reliably reconstruct the local non-linear parameter from Eq. 3.4. The efficiency of this method is high in the center of the trap, where we extract $\kappa n_0/2\pi = 161(3)\,\mathrm{Hz}$ [Fig. 3.7(a), blue points and lines] with a relative error of 4%. The efficiency is also supported by the long coherence times of the oscillations. Close to the edge of the trap, signal-to-noise ratio is lower and oscillations are less visible, so we can track only a couple of periods. Results of the fit [orange points and lines in panel (a)] show that the dynamics is determined by the Rabi frequency only, which is compatible with the value independently calibrated. As we did in the previous sections, we reconstruct the Thomas-Fermi profile, shown in Fig. 3.7(b).

To further validate our result, we repeat the same experiment for different values of Ω_R. In every experiment, we perform the ARP at fixed Ω_R, then we quench both the phase ϕ and Ω_R, set by changing the detuning from the virtual state. The quench in Ω_R does not trigger dynamics, as the adiabatic preparation ensures that the spin and the Rabi vectors are aligned on the Bloch sphere.

By extracting the plasma frequency for each dataset, we measure the scaling of the plasma frequency on Ω_R, shown in Fig. 3.7(c). A fit of ω_{pl} as a function of Ω_R in the trap center allows again to extract $\kappa n_0/2\pi = 164(3)\,\mathrm{Hz}$, which corroborates the robustness of the previous measurement.

Given the high precision and reliability of the measure of κn_0 with plasma oscillations, in the next chapter we will use this method to obtain a precise measurement of the density in the center of the trap.

Chapter 4

Faraday waves in Miscible spin mixtures

Contents

Bose-Einstein condensates, when perturbed, can exhibit a rich variety of oscillations, sustained by superfluidity. In trapped BECs, elementary excitations, like dipole, quadrupole, breathing or scissor mode, can be excited by introducing time dependent trapping potentials. On top of this, a different class of excitations can be created in a BEC. They are known as Faraday waves, as they were first studied by Michael Faraday in vertically shaken fluids [103]. These modes are nonlinear parametric excitations occurring in a fluid system, visible as spatial and temporal oscillations of the fluid itself. A coupling between the external driving and the medium is required, which usually occurs through nonlinear properties of the medium itself.
The study of Faraday waves in superfluid systems, such as BECs, has attracted theoretical attention in recent years [104, 105, 106] due to the high degree of tunability of ultracold atoms setups and the reduced damping compared to their classic counterpart. In quantum fluids, the first experimental investigation was carried out in an elongated cigar-shaped BEC of ^{87}Rb [107], by modulating in time the transverse trapping frequency. It was demonstrated theoretically [106] that this protocol allows to modulate the nonlinear mean-field interaction term, through a modulation of the density. After this pioneering work, research on the topic has also expanded to superfluid fermionic

systems of ^{6}Li [108], to generation of Faraday patterns by direct modulation of the interaction term [109], as well as production of matter-wave jets in BECs of Cs atoms [110, 111]. Interestingly enough, Faraday waves have also been identified with discrete space-time crystals [112, 113].
In this chapter I will describe the novel generation of Faraday excitations in a two-component mixture of ^{23}Na atoms in two different miscible spin states, with and without the presence of external coupling between the two states. In the first section I will introduce the theoretical background we developed, to describe, at a quantum level, the generation of Faraday waves as excitations of a pair of entangled phonons with opposite momenta $\pm k$. In the second section, I will discuss the experimental protocol, along with the method we used to extract relevant information from absorption images. A characterization of the dynamics and the dependence on external parameters is also reported. In the last section, I will demonstrate how Faraday waves can be used as a spectroscopic tool to measure dispersion relations, in both density and spin channels. All results discussed in this chapter are published in Ref.[114].

4.1 Theoretical introduction to Faraday waves

In classical systems, Faraday waves are excited by a parametric resonance of the system, when it is subject to a periodic driving at some frequency ω_M [115], that couples to a non-linearity of the system. After some time, a pattern with a well defined wavevector grows in the fluid, whose visibility grows exponentially and oscillates in time. The dynamics of the excited mode is well captured by a Mathieu equation. In single component harmonically trapped BEC, it has already been shown [106, 116] that the GPE can be reduced to a Mathieu equation. In this case, the excited non-linearity is the mean-field term $\propto gn$, modulated either through a direct modulation of the coupling constant g [110], or through an indirect modulation of the density [106].
Our derivation follows a different approach, as we derive the equation of motion at the quantum level [117]. Indeed, the parametric process can be seen as the emission of pairs of entangled phonons, at frequency $\omega_M/2$ and momentum $\pm k$ each, in the BEC. This derivation is more suitable for an analogue gravity [118] interpretation, as the process of phonon generation resembles the preheating phase of the early universe [119]. In this context, the external modulation plays the role of the oscillating inflaton field, whose oscillation produces entangled particles out of the vacuum [120]. An experimental investigation of this analogy in BECs, focused on the measurement of density-density correlation [121], is carried out with metastable He* in Paris [122].
In a BEC, the pair of phonons originates from the *Beliaev decay* of a phonon with frequency ω_M and momentum $k = 0$, injected in the condensate by the driving itself. The emitted phonons, in order to conserve energy and momentum, must follow the dispersion relation of elementary quasi-particle in a BEC, i.e., they are Bogoliubov modes. In a spin mixture, the decay can in principle occur in both channels separately, as sketched in Fig. 4.1. The interaction of the phonons with the bulk will then give rise in time to the classical pattern with momentum k. We can start the derivation considering in

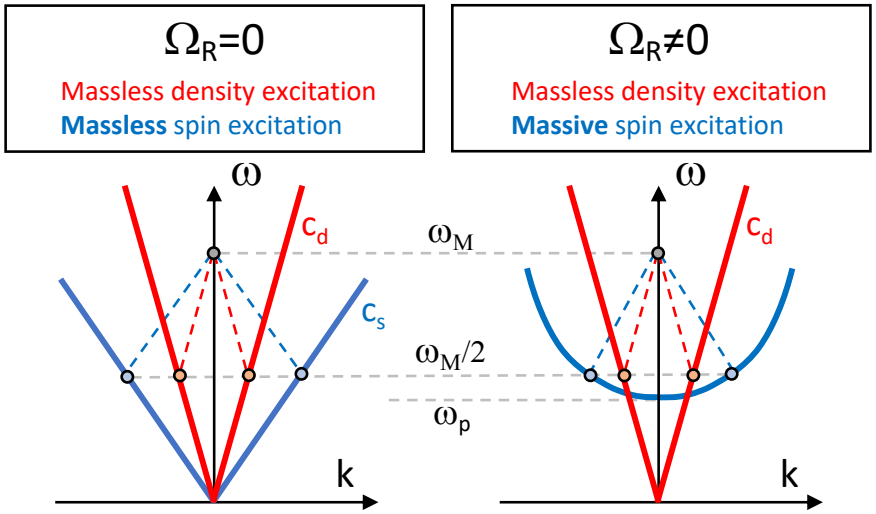

Figure 4.1: Illustration of the Beliaev decay in spin mixtures. The modulation of the trapping potential introduces phonons with zero momentum, which decay to the density (red) or spin (modes). In a spin mixture, the presence of a finite coherent coupling, Ω_R, introduces a curvature at $k \sim 0$, which makes the excitation acquire a mass.

first approximation a 1D homogeneous BEC with total density n and chemical potential $\mu = gn$. The presence of an external modulation $f(t) = \alpha sin(\omega_M t)$ can be modelled as a modulation of the coupling constant in time, $g(t) = g[1 + f(t)]$. The dynamics of the excitation, within Bogoliubov theory, is given by the time dependent Hamiltonian

$$\hat{H}(t) = \sum_{k\neq 0}[\varepsilon(k) + \mu S(k) f(t)]\hat{b}_k^\dagger \hat{b}_k + \sum_{k>0} \mu S(k) f(t)(\hat{b}_k^\dagger \hat{b}_{-k}^\dagger + h.c) \tag{4.1}$$

Here, b_k ($b_k^\dagger$) is the annihilation (creation) operator of the quasi-particle of momentum k, with $\varepsilon(k) = \hbar\omega(k)$ its energy, as discussed in Chapter 1, and $S(k)$ is the static structure factor, related to the probability that a density probe transfers a momentum k to the system. This Hamiltonian describes the process of generation of pairs of phonons out of the Bogoliubov vacuum, which, to same extent, resembles also the dynamical Casimir effect [123, 124].
From the Hamiltonian 4.1, we can compute the Heisenberg equation of motion for the operators $\hat{b}$ and $\hat{b}^\dagger$, as:

$$i\hbar\partial_t \begin{pmatrix} \hat{b}_k \\ \hat{b}_{-k}^\dagger \end{pmatrix} = \begin{pmatrix} \varepsilon_k(t) & \mu S(k) f(t) \\ -\mu S(k) f(t) & -\varepsilon_k(t) \end{pmatrix} \begin{pmatrix} \hat{b}_k \\ \hat{b}_{-k}^\dagger \end{pmatrix} \tag{4.2}$$

Where we have introduced, for convenience, a time dependent energy $\varepsilon_k(t) = \varepsilon(k) + \mu S(k) f(t)$. We can then perform a Bogoliubov transformation to obtain the time evolu-

tion of the operators $\hat{b}_k$, $\hat{b}^\dagger_{-k}$, using the Ansatz:

$$\begin{pmatrix} \hat{b}_k(t) \\ \hat{b}^\dagger_{-k}(t) \end{pmatrix} = \begin{pmatrix} \beta_1(t) & \beta_2(t) \\ \beta_2^*(t) & \beta_1^*(t) \end{pmatrix} \begin{pmatrix} \hat{b}_k(0) \\ \hat{b}^\dagger_{-k}(0) \end{pmatrix} \tag{4.3}$$

where the Bogoliubov coefficients $\beta_1(t)$, $\beta_2(t)$ are time-dependent complex amplitudes. Solving Eq. 4.2 with the previous Ansatz leads to an equation for the Bogoliubov coefficient β_i of the form $i\hbar\partial_t\beta_i = \varepsilon_k\beta_i + \mu S(k)f(t)\beta^*_{3-i}$, for $i = 1, 2$. We can then solve the problem for the real and imaginary part of β introducing $\beta_\pm = \beta \pm \beta^*$. This leads to the equation:

$$i\hbar\partial_t\beta_\pm = [\varepsilon_k(t) \mp \mu S(k)f(t)]\beta_\mp \tag{4.4}$$

We can now derive again on both side of the previous equation to obtain

$$\hbar^2\partial_t^2\beta + \left[\varepsilon_k^2(t) - (\mu S(k)f(t))^2\right]\beta = 0 \tag{4.5}$$

where we have removed the index $\pm$, since the equation of motion is the same for both. If we introduce the dimensionless variable $\tau = \omega_M t/2$, we can derive a Mathieu equation for the excitation amplitude β:

$$\partial_t^2\beta + A(k, \omega_M)[1 + B(k)\sin(2\tau)]\beta = 0 \tag{4.6}$$

where the parameters A and B are defined as :

$$A(k, \omega) = \frac{\omega^2(k)}{(\omega_M/2)^2} \qquad B(k) = 2\mu\alpha\frac{S(k)}{\hbar\omega(k)} \tag{4.7}$$

The stability chart of the Mathieu equation, which can be found, e.g., in [125], shows a series of unstable modes, $\beta(t) \propto e^{\gamma\tau}\xi(\tau)$, where $\xi(\tau)$ is an oscillating function with the same periodicity of the driving. In the case of small driving, $B(k) \ll 1$, such instabilities are narrow in k and centered around $A(k, \omega_M) = l^2$ [126], with l integer. The instability rate associated to each mode is given by [119, 125]:

$$\gamma(k, \omega_M) = \frac{1}{4}\sqrt{A^2(k, \omega_M)B^2(k) - 4\left[A(k, \omega_M) - 1\right]^2} \tag{4.8}$$

The most unstable mode occurs for $l = 1$, which corresponds, in terms of frequency, to the excitation of a mode with $2\omega(k) = \omega_M$, coherent with the quantum picture we have developed. In this case, the growth rate simplifies to:

$$\gamma(q, \omega) = \frac{B(q)}{4} = \alpha\mu\frac{S(q)}{2\hbar\omega(q)} \tag{4.9}$$

where q is the wavevector satisfying the resonant condition. Note that if $B \sim 1$, the parametric amplification process results in a broadening of the instability lobe in k, leading to the population of secondary unstable modes with higher wavevector.
In the previous derivation we have only assumed the Hamiltonian to have the form

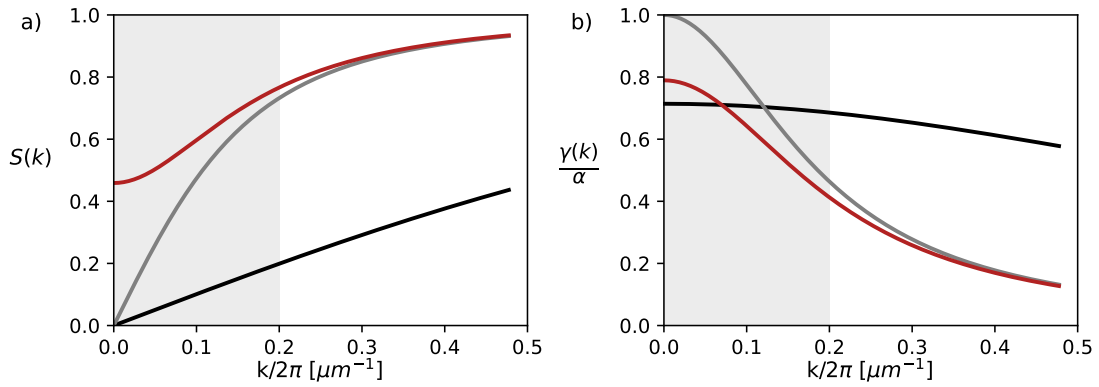

Figure 4.2: Structure factors (a) and values of $\gamma(k)$ normalized on the modulation amplitude α, for $\mu_d/h = 3\,\mathrm{kHz}$, $\mu_s/h = 145\,\mathrm{Hz}$ and $\Omega_R/2\pi = 80\,\mathrm{Hz}$. In both panels, the black curve shows the density channel, the grey one the spin channel and the red one the spin channel ($\Omega_R = 0$) with a finite value of the coherent coupling. The grey area indicates the range in k that can be measured in the experiment, due to the imaging resolution.

of Eq.4.1. In the case of an unpolarized BEC mixture, density and spin modes are decoupled (see Chapter 1), and the Hamiltonian can be written as the sum of density and spin Hamiltonians. A direct consequence is that Eq. 4.6 allows for the generation of Faraday waves both in the density and spin channels independently, with and without the coupling. Mathematically, one has to substitute the chemical potential $\mu \to \mu_{d,s}$ with the density (or spin) chemical ones, as defined in Eq. 1.25, along with the appropriate structure factors, which read:

$$S_d(k) = \frac{\hbar k^2/2m}{\omega_d(k)}, \quad S_s(k,\Omega) = \frac{\hbar k^2/2m + \Omega_R}{\omega_s(k)} \tag{4.10}$$

where we have considered also the presence of the Rabi frequency Ω_R. The structure factors $S_{d(s)}(k)$ are plotted in Fig. 4.2, along with the corresponding curve of $\gamma(k)$, calculated with the parameters used in the experiment.
In the region of k that can be experimentally measured (grey area in Fig. 4.2) the structure factors of the density and the spin channel differ. Indeed, the higher value of the spin healing length compared to the density one shifts $S_s(k)$ towards lower values of k. Furthermore, the presence of the gap in $\omega_s(k)$, arising from the coherent coupling, introduces a gap in the structure factor (see red curve in Fig. 4.2). The scaling of the gap in $S_s(k)$ is the same of the scaling in $\omega_s(k)$: lower values of Ω_R tend to close the gap.
It is also interesting to look at the shape of the growth rate $\gamma(k)$, plotted in Fig. 4.2(b), normalized to the value of the modulation amplitude α. There exists a region where, due to the different shapes of the structure factors, and the difference between μ_d and μ_s, the growth rate for spin modes is higher than the density one. For our experimental

parameters, this occurs around $k/2\pi = 0.12\,\mu\text{m}^{-1}$, if $\Omega_R = 0$. For finite values of Ω_R, instead, the crossing point is shifted toward lower values of k, as the value $\gamma(0)$ decreases for increasing Ω_R, up to $\hbar\Omega_R = \mu_s$, when the growth rate for the spin channel drops below the density one. Anticipating the results discussed below, in the experiment we find that this point is a crossover between the excitation of spin modes and density modes, above which only density modes are excited.

4.1.1 Reduction of GPE to Mathieu equation

In the previous section we have derived a Mathieu equation, starting from a time-dependent Hamiltonian that describes the excitation of pairs of quasi-particles with energy $\varepsilon(k)$, which we assumed to be Bogoliubov modes. We wish now to derive an explicit formula for the excitation spectrum resulting from the modulation, as the geometry of the system might change the shape of the dispersion relation 1.31. We start considering the coupled Gross-Pitaevskii equations 1.30, with a radial potential $V(r) = \frac{1}{2}m\omega_\perp^2 r^2$, with $r = \sqrt{y^2+z^2}$. This approximates the condensate as a cylinder with homogeneous density along the axial direction x. This is a rough but good approximations in the center of the cloud, as in our experiment $\omega_x \ll \omega_\perp$. Defining $n_{\uparrow,\downarrow}(r) = |\psi_{\uparrow,\downarrow}(r)|^2$, the density of the two components, we can write two hydrodynamic equations [6] for density and spin perturbations $\delta n_{d,s} = \delta n_\uparrow \pm \delta n_\downarrow$ in the density and spin channel. In the more general form, the hydrodynamic equations for the density and spin channel, read:

$$\begin{aligned}\partial_t^2 \delta n_d &= \frac{(g+g_{12})}{2m}\nabla(n\nabla\delta n_d + P_d)\\ \partial_t^2 \delta n_s &= \left[\frac{1}{2m}\nabla(n\nabla) - \frac{\hbar\Omega}{n}\right]\left[\left(g - g_{12} + \frac{\hbar\Omega}{n}\right)\delta n_s + P_s\right]\end{aligned} \tag{4.11}$$

where we have set $g_{11} = g_{22} = g$, which is valid for our experimental settings, see Section 2.3. Here, $P_{d,s}$ are second order correction, arising from the inclusion of the quantum pressure term, which corresponds to:

$$P_{d,s} = -\frac{\hbar^2}{2mn}\nabla\left[n\nabla\left(\frac{\delta n_{d,s}}{n}\right)\right] \tag{4.12}$$

This term can be neglected if the healing length of the excitation ξ is much smaller than the transverse size of the condensate, a limit known as the *hydrodynamic regime*.
Since we are interested in the longitudinal modes, it is useful to find solution of Eq. 4.11 of the form $\delta n = f(z)w(r)$. For the sake of simplicity, we will discuss separately the solution for the density and the spin channels.

Density Modes For the configuration of the experiment, $\xi_d \ll R_\perp$. This implies that the term P_d vanishes and thus the hydrodynamic equation takes the simple form:

$$\partial_t^2 \delta n_d = \frac{(g+g_{12})}{2m}\nabla(n\nabla\delta n_d) \tag{4.13}$$

As long as $\xi_d \ll R_\perp$, an appropriate Ansatz for the radial profile of the perturbation is a uniform one $w(r) = \theta(R_\perp - r)$. Under this condition, in the region $r \leq R_\perp$, the previous equation reduces to:

$$\partial_t^2 f = \frac{(g + g_{12})}{2m} n(r) \partial_x^2 f \tag{4.14}$$

We can now eliminate the radial dependence in the region $r \leq R_\perp$, integrating along the radial and polar coordinates the previous equation. This leads to

$$\partial_t^2 \delta n_d = \frac{(g + g_{12})}{2m} n_{d,eff} \partial_x^2 f \tag{4.15}$$

where $n_{d,eff} = n_0/2$ is the density in the center of the trap, rescaled by a factor of 2. In the hydrodynamic formulation, this leads to a decrease in the speed of sound by a factor $\sqrt{2}$ [127], whose physical origin can be understood as an averaging of the inhomogeneous density in the radial direction.

Spin Modes In contrast with density modes, in the experiment spin modes are soft enough to violate the hydrodynamic regime, as $\xi_s \sim R_\perp$. In this case, while it is still correct to assume the propagation of longitudinal modes, the correct Ansatz for the radial profile of the excitation is $w(r) = n(r)$. In this case, Eq. 4.11 for the spin modes can be rewritten as:

$$n\partial_t^2 f = -\frac{n}{\hbar^2}\left(-\frac{\hbar^2 D_x^2}{2m} + (g - g_{12})n\right)\frac{\hbar^2 D_x^2}{2m} f + \frac{(g - g_{12})}{2m}\nabla(n\nabla n) f \tag{4.16}$$

with $D_x^2 = \partial_x^2 - 2m\Omega_R/\hbar$ a modified spatial derivative. As we did for density modes, we can integrate along the radial and polar coordinates to obtain:

$$\partial_t^2 f = \left(-\frac{\hbar\partial_x^2}{2m} + \frac{(g - g_{12})n_{s,eff}}{\hbar} + \Omega_R\right)\left(\frac{\hbar\partial_x^2}{2m} + \Omega_R\right) f \tag{4.17}$$

where $n_{s,eff} = 2n_0/3$ is the renormalized density for the spin channel. As for the density channel, a lower value of the density comes out naturally from the integration along the radial direction. Notice that, while the physical meaning of the renormalization is the same of the density modes, the use of a different Ansatz in the choice of $w(r)$ leads to a different prefactor, which is the same factor we have derived at the end of Chapter 1.

To summarize the results, longitudinal modes propagate in the condensate following the dispersion relations

$$\omega_d(k) = \sqrt{\frac{\hbar k^2}{2m}\left(\frac{\hbar k^2}{2m} + \frac{2\mu_d}{\hbar}\right)} \tag{4.18}$$

$$\omega_s(k) = \sqrt{\left(\frac{\hbar k^2}{2m} + \Omega_R\right)\left(\frac{\hbar k^2}{2m} + \frac{2\mu_s}{\hbar} + \Omega_R\right)} \tag{4.19}$$

where, according to the previous discussion, the density and spin chemical potentials are given, in terms of the peak density n_0, as:

$$\mu_d = \frac{(g+g_{12})}{2}\frac{n_0}{2}, \quad \mu_s = \frac{(g-g_{12})}{2}\frac{2n_0}{3}. \tag{4.20}$$

Notice that, in the case of a homogeneous 1D condensate of density n, the chemical potentials read $\mu_{d,s} = (g \pm g_{12})n/2$, and we recover expressions 1.31 for Bogoliubov excitations.

4.2 Experimental Realization of Faraday Waves

As in a classical system, Faraday waves in a BEC can be excited by modulating the trapping frequency [107], or equivalently by modulating the scattering length via Feschbach resonances [109]. As the modulation of the scattering length in our apparatus is prohibited by the strong magnetic fields required [128, 129], we generate Faraday patterns modulating the frequency of the harmonic potential.

Experimental Protocol The protocol we use to produce Faraday waves is sketched in Fig. 4.3. We start each experiment by preparing a cloud of 2×10^6 atoms in the $|1,-1\rangle$ state, with Thomas-Fermi radii $R_\perp = 3\,\mu$m and $R_x = 300\,\mu$m, and negligible thermal component, obtained by a slow recompression of the trapping frequency after evaporation [panel (I)]. At the end of the compression ramp, we produce a two-component BEC with homogeneous zero magnetization [panel (II)] using the ARP procedure described in Section 3.3, with $\Omega_R/2\pi = 180\,$Hz. After the ARP, we either switch off the driving microwave, or quench it at some desired value [panel (III), black or grey line respectively]. Following the protocol used in Ref. [107], we excite the mixture modulating in time the intensity of the Cigar laser, applying an electronic sinusoidal modulation, of angular frequency ω_M, to the RF amplitude of the beam AOM, as explained in Section 2.1.8. Exploiting the dependence of the trapping frequency on the intensity I_0 of the laser, $\omega_\perp^2 \propto I_0$ [73], this allows us to introduce a modulation of the trapping frequency as $\omega_\perp(t) = \omega_\perp(0)[1+\alpha\sin\omega_M t]$, see panel (III) of Fig. 4.3.
The modulation amplitude α has a value between [0.38-0.6], depending on the value of ω_M. The need to vary the modulation amplitude results mainly from the lifetime of the condensate, which limits the number of modulation cycles that can be applied to the sample. The modulation time t_m is varied between 50 and 400 ms.
We gather results for $\omega_M/2\pi$ between 40 Hz and 600 Hz. Since the modulation frequency is always higher than the axial trapping frequency and lower than the radial one, the radial Thomas Fermi radius will follow adiabatically the compression and decompression cycle of the trapping potential, preventing the excitation of radial modes. The opposite is true in the axial direction, where 1D Faraday waves are generated [106, 130]. After N_{cycle} modulation cycles, we release the harmonic trap and image independently the atoms in the two states, along the vertical direction, as explained in Section 2.4. At last, in order to increase the signal-to-noise ratio, for each set of control parameters

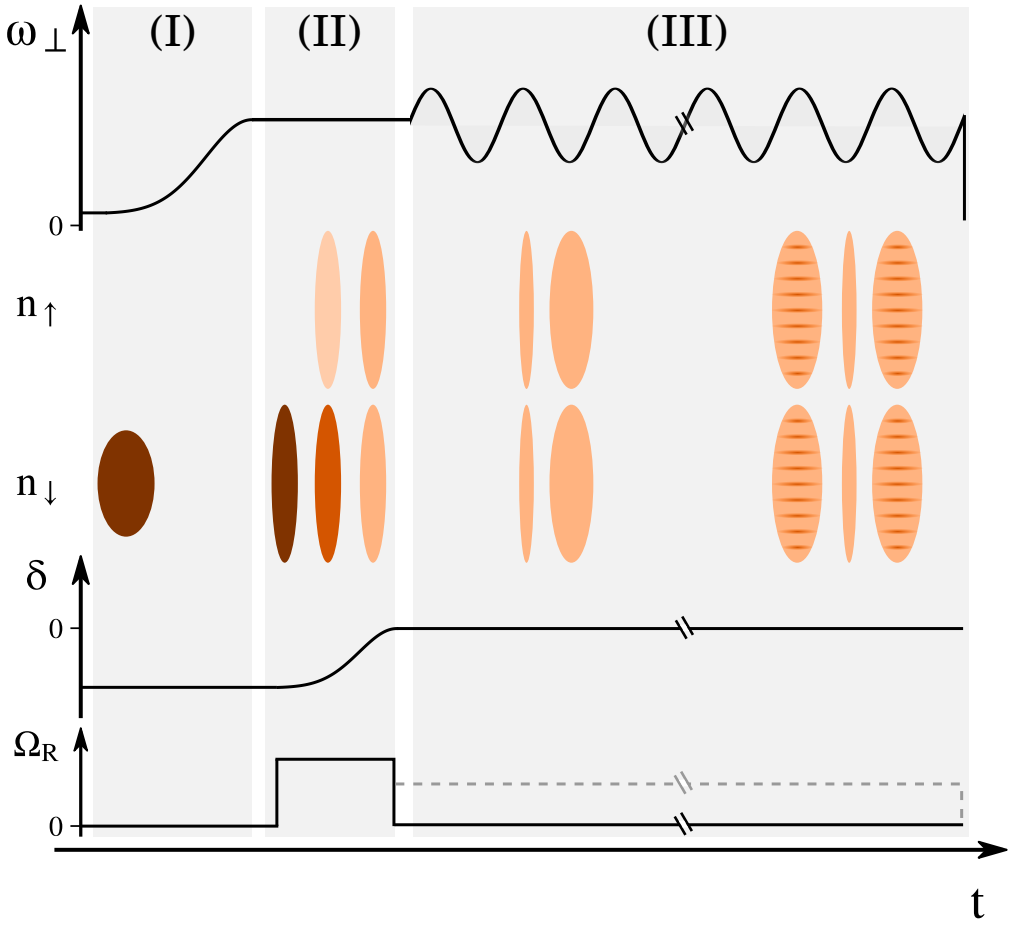

Figure 4.3: Protocol used to generate Faraday waves. Top panel shows the frequency of the trapping potential, middle panel a representation of the dynamics of the condensate, bottom panels the detuning and intensity of the coupling. (I) Compression of the radial trap after evaporation, to create a one-component elongated cigar-shaped BEC. (II) Adiabatic Rapid Passage at constant $\omega_\perp$ and finite Ω_R, with decreasing detuning to transfer part of the population from $n_\downarrow$ to $n_\uparrow$. (III) Modulation of $\omega_\perp$ squeezes in time radially the mixture, eventually generating a longitudinal pattern. Ω_R is either 0 (black solid line) or kept at a finite value (grey dashed line).

(namely α, ω_M, t_M or N_{cycle}) we collect data from 10 to 30 repetitions. We find that in the regime of strong driving (identified by $B(k) \sim 1$ in the Mathieu equation 4.6), in which the experiment is performed, this number is sufficient to clean the signal.
We first conduct experiments turning off the coupling at the end of the ARP. However, the analysis method discussed below applies also to the case of the coupled mixture.

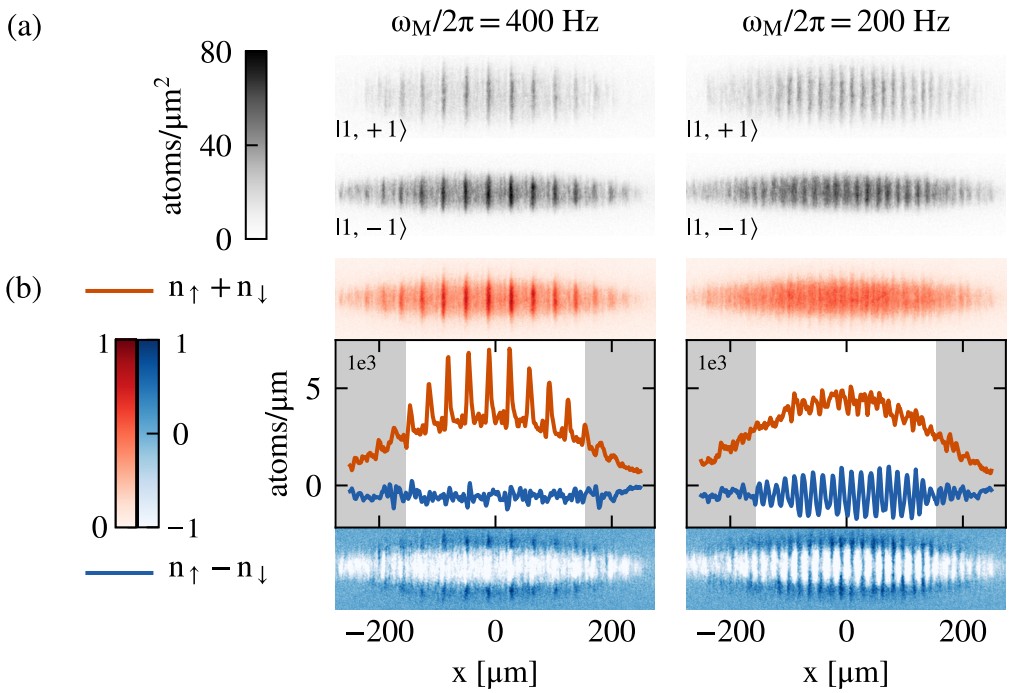

Figure 4.4: Density and spin Faraday waves at $\Omega_R = 0$ for $\omega_M/2\pi = 400\,\text{Hz}$ (left) and $\omega_M/2\pi = 200\,\text{Hz}$ (right). (a) Absorption images of the two states. Faraday patterns appears as longitudinal stripes on the both the components. (b) Density (red) and spin (blue) 2D Faraday patterns, along with their integrated 1D profile (central panel). The white areas in the central panels indicate the region of calculation of the PSD.

Results and image analysis Absorption images of the two states are shown in Fig. 4.4(a), for two different modulation frequencies, namely $\omega_M/2\pi = 200\,\text{Hz}$ and $\omega_M/2\pi = 400\,\text{Hz}$, with $N_{cycle} = 80$.
The data clearly show that a regular pattern appears in both components. From the images, we extract the 2D total density $n = n_\uparrow + n_\downarrow$ [Fig. 4.4(b) top, shown in orange] and the spin $s = n_\uparrow - n_\downarrow$ [Fig. 4.4(b) bottom, shown in blue]. It is straightforward to observe that, at $\omega_M/2\pi = 400\,\text{Hz}$ the two components are spatially modulated in phase, and the pattern is visible as a density modulation. Out-of-phase modulation is instead observed at 200 Hz, where the pattern is visible as a spin modulation. Furthermore, as expected, no radial excitations are present in both cases. For this reason, the analysis can be simplified by separately calculating the integrated profile (in the radial direction) of each component, and then summing or subtracting the two to obtain n and s along the axial direction only. Results of this procedure are shown in the central panel of Fig. 4.4(b). As expected, the radial integration preserves the nature of the pattern in the two direction.
In order to gather quantitative information about the nature of the pattern, we calculate

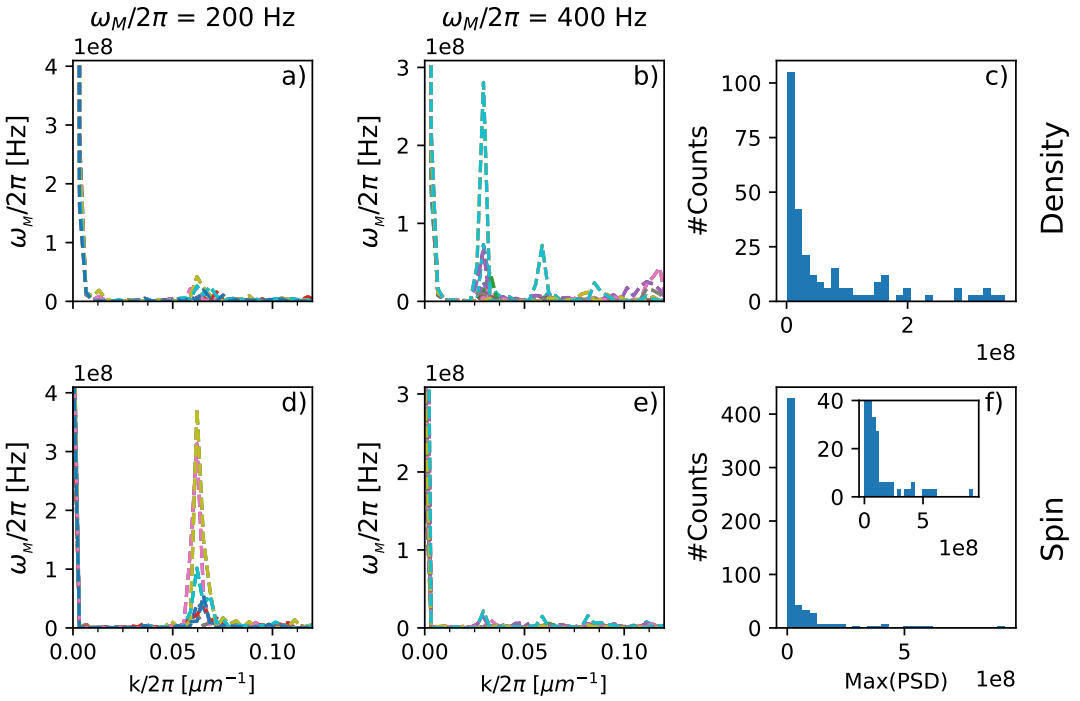

Figure 4.5: Analysis of the PSD of integrated 1D profiles, for density (top) and spin (bottom) modes. Different colors represent different shots with the same parameters. At $\omega_M/2\pi = 200\,\text{Hz}$ only a peak in spin is visible, with a density one at low k suppressed by one order of magnitude. At $\omega_M/2\pi = 400\,\text{Hz}$, a peak is instead visible only in the density channel. In both cases, the amplitude of the modes changes drastically from shot to shot. Panels c) and f) capture the distribution of the amplitude of the most excited k (excluded the signal at $k = 0$) for all the experimental data discussed in this Chapter, for density and spin modes respectively.

the Power Spectral Density (PSD) of the 1D profile, as

$$PSD_{d,s}(k) = \left| \int (n_\uparrow \pm n_\downarrow) e^{ikx} dx \right|^2 \tag{4.21}$$

which corresponds to the squared modulus of the Fourier Transform. To suppress inhomogeneous broadening effects in the peaks of the PSD, we focus the analysis in the $300\,\mu$m-wide central region of the condensate [white region in Fig. 4.4(b)], where the condensate is approximately flat. Our methodology is justified by the studies conducted in Ref. [106], where it was shown numerically that a small inhomogeneity in the background density only gives tiny corrections to the spacing between Faraday peaks. As the signal is discrete, we calculate the Fast Fourier Transform using a built-in python function. Example of the PSD are shown in Fig. 4.5 for both density (top panels) and spin channels (bottom panels).

To improve the signal to noise ratio, we average PSDs of absorption images taken with the same control parameters. This is necessary since Faraday waves are characterized by an exponential growth with a random seed, which depends on the noise present in the experiment. The noise in the peak visibility, the latter being defined as the amplitude of the most excited mode with respect to the background noise, is clearly shown in Fig. 4.5, where the histograms represents the peak visibility measured over a wide range of modulation frequencies.
As a last note, the use of the FFT introduces a discretization in the observable range of k. In particular, due to the imaging resolution of $dx = 1\,\text{pixel} = 1\,\mu\text{m}$, the resolution in k-space is fixed to $dk/2\pi = 1/(Ndx) = 0.0033\,\mu\text{m}^{-1}$, where $N = 300$ is the number of pixels. Correspondingly, the maximum wavevector observable is $k_{max}/2\pi = Ndk/2 = 0.49\,\mu\text{m}^{-1}$.

4.2.1 Faraday waves dynamics

Faraday patterns are characterized by a time-oscillation, at frequency ω_M, of the visibility of the most excited mode, with a growing exponential envelope. Both this features are well characterized, for example, in Ref.[108].
We prove that the excited patterns correspond to Faraday waves by measuring the time oscillation of the amplitude of the excited mode. We perform this measurement by releasing the trap at different phases of the modulation frequency. This allows us to measure the excitation during a cycle. Precise information about the phase of the modulation are gathered by monitoring the intensity of the trapping beam with a photodiode, placed after the science chamber.

Oscillation of most excited mode Let us focus our attention on the case of $\omega_M/2\pi = 200\,\text{Hz}$. From the PSD of absorption images we extract the amplitude of the dominant peak at different times. Results for density and spin modes are shown in color plots of Fig. 4.6(a) and (b) respectively, with the most excited mode shown with a darker color, compared with the reference signal measured by the photodiode.
The observed time oscillation of the most excited mode is in agreement with theoretical prediction for a single component condensate [106, 130], and, remarkably, extends also to the spin channel. In particular, comparing the phase of the driving (top panel) with the phase of Faraday waves, we observe that the visibility of the excited mode, in both the density and spin channels, is maximal when $\omega_\perp(t)$ is minimum, at $t = (2j + 3/2)\pi/\omega_M$, with $j \in \mathbb{Z}$. Based on this measurement, data shown in the following sections are obtained releasing the trap at the minimum of the modulated signal, in order to maximize the visibility of the peaks. It is also interesting to look at the time behaviour of the whole PSD distribution as a function of k. From the color plot, it is clear that, on top of the oscillating character of the excited mode, no incoherent excitations are produced: in particular, the position of the excited mode in wavevector space remains fixed, and no broadening is observed. It is true, however, that small-amplitude auxiliary modes are generated in the density channel. The wavevectors of this modes are integer multiples of

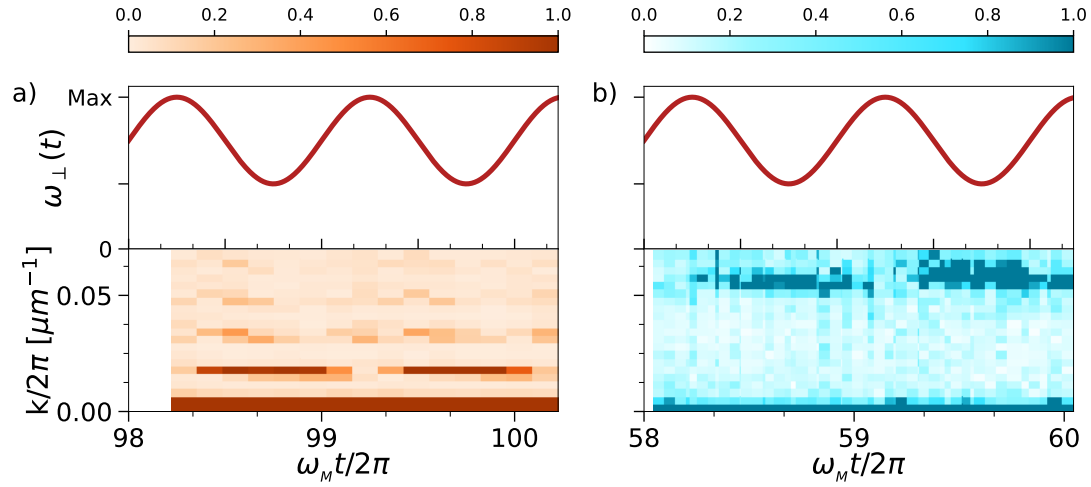

Figure 4.6: Time oscillation of the Faraday waves amplitude for the density [panel a)] and spin [panel b)]. The top panel shows the modulation amplitude in time, while the corresponding fringe visibility is shown at the bottom. Data are obtained with $\omega_M/2\pi = 200\,\mathrm{Hz}$.

the primary excitations, and are generated from the strong pumping applied to observe the signal, as predicted by the Mathieu equations.

Radial Dynamics It is also interesting to extract the local dynamics of the transverse Thomas-Fermi radius $R_\perp$, in particular for the spin channel, where the two components could in principle oscillate out of phase in the radial direction. We measure it fitting a 1D Thomas-Fermi profile for each axial position x of 2D absorption images of the previous dataset. Results are reported in Fig. 4.7, for $n_\downarrow$ [panel b)] and $n_\uparrow$ [panel c)], and compared with the reference signal. We observe that $R_\perp$ in both components oscillates at the modulation frequency. The oscillation is homogeneous in space (as evident from the color scale) and, remarkably, in phase between the two components. To verify this, we first perform a sinusoidal fit for each position x. From these, we extract the phase shift of $R_\perp(t)$ with respect to the modulation, plotted as a histogram in panel d). We observe that the distribution, for both $n_\uparrow$ and $n_\downarrow$, is skewed and centered around a value of $\phi = \pi/16$, indicating a delay with respect to the driving. A measurement of the relative phase shift of the components, $\delta\phi = \phi_\uparrow - \phi_\downarrow$, confirms instead that the relative phase shift follows a Gaussian distribution with zero average (panel e)). Points on the tails of the distribution are further away from the center of the condensate, where density variations starts to become appreciable.
This analysis, in first place, confirms that for frequencies $\omega_M \ll \omega_\perp$ the radial direction follows adiabatically the perturbation, as stated before. More interestingly, it suggests that spin Faraday waves originate from perturbation of the density channel, as the two components always oscillate radially in phase.

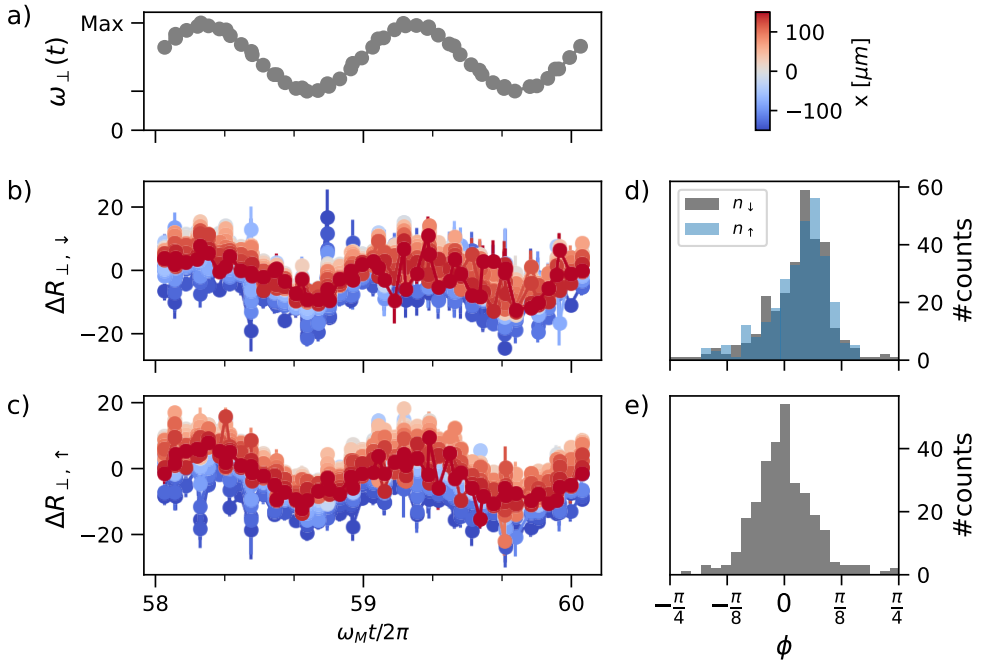

Figure 4.7: Dynamics of $R_\perp(t)$. Panel a) shows the modulation signal, as a reference for $R_\perp(x)$ of component $n_\downarrow$, $n_\uparrow$ shown in panel b), c) respectively. Colors indicate axial position. Panel d) represents the phase ϕ distribution of the two components with respect to the perturbation, whereas panel e) shows the distribution of relative phase $\phi_\uparrow - \phi_\downarrow$.

4.2.2 Dependence on the initial magnetization

In a two-component spin mixture, the spin and density channels are independent only in the case of equal densities $n_\uparrow = n_\downarrow = n/2$. A small imbalance between the two, instead, leads to a hybridization of the two modes [41]. To investigate this effect, we perform experiments varying the imbalance between the two populations, tuned changing the final detuning of the ARP, while fixing the modulation frequency $\omega_M/2\pi = 200\,\text{Hz}$, the amplitude $\alpha = 0.6$, and the number of modulation cycles $N_{cycle} = 60$. For each value of the detuning, we extract the amplitude of the dominant mode, which is stable at $k = 0.06\,\mu\text{m}^{-1}$, as a function of the imbalance. The latter is expressed in terms of the normalized magnetization $Z = \frac{n_\uparrow - n_\downarrow}{n_\uparrow + n_\downarrow}$. Results are shown in Fig. 4.8.
Starting from equal populations, the visibility increases, eventually reaching a maximum value at $Z = 0.07$. As expected, the hybridization between the two channels introduces a coupling, which makes spin excitations more sensitive to density perturbations. At increasing value of Z, however, the visibility decreases, eventually reaching zero for a fully polarized mixture, where the spin channel disappears.

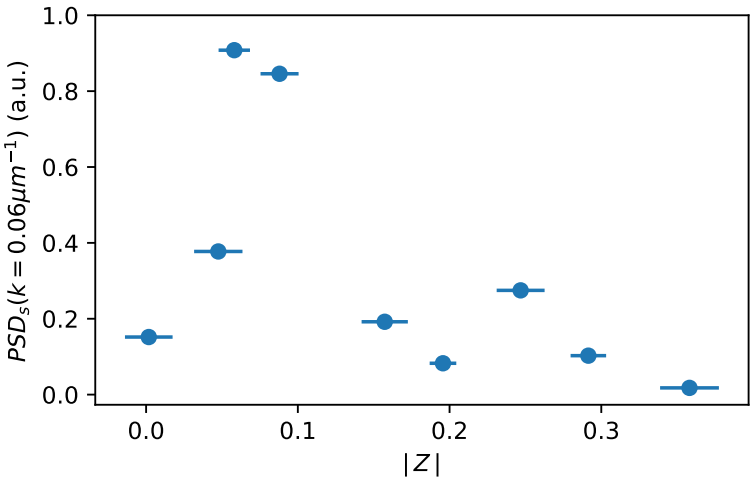

Figure 4.8: Amplitude of the dominant spin mode at $k = 0.06\,\mu\mathrm{m}^{-1}$ for different population imbalances. The maximum amplitude of the spin mode is at small but finite imbalance, due to the increased coupling to the density channel where the modulation happens. In this dataset, the experimental parameters are $\omega_M/2\pi = 200\,\mathrm{Hz}$, modulation time 300 ms, $\alpha = 0.6$.

4.3 Measurement of dispersion relations

We already theoretically discussed how modulation frequency and wavevector of the excited pattern are fixed by the dispersion relations of Bogoliubov modes. Fig. 4.6 already provides an experimental proof of the different response of the two channels for a given modulation frequency. This suggests the possibility of experimentally measuring both dispersion relations. In a single component condensate, this measurement was performed in [9], using a Bragg spectroscopy technique, i.e., by exciting a wavevector k and measuring the frequency ω of the excitation. In the same spirit, we can exploit the dependence of k on the modulation frequency to attempt the same experiment, exciting ω instead of k. In comparison with the measurement of two distinct sound velocities in a two component ^{23}Na condensate, performed in [37], our methodology allows to directly map the dispersion relation, even outside the sonic regime.

4.3.1 Miscible Mixture without coupling

We apply the protocol discussed in the previous sections to a balanced mixture ($Z = 0$) scanning the modulation frequency ω_M. We first conduct this measurement on the miscible mixture without the coupling ($\Omega_R = 0$). To obtain a good visibility of the fringes, we modified the driving amplitude: we use $\alpha = 0.6, 0.48, 0.38$ for frequencies $\omega_M/2\pi$ between 40 and 90 Hz, between 100 and 300 Hz, and between 310 and 600 Hz, respectively. The results are shown as colorplots in Fig. 4.9, for the density channel [panel (a)] and the

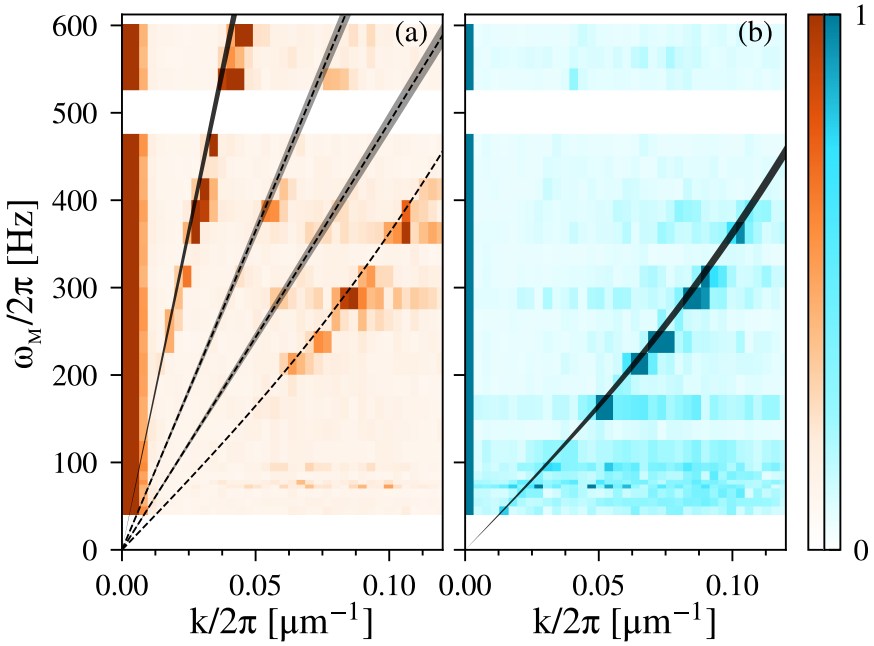

Figure 4.9: PSD of density (a) and spin (b) excitations as a function of the modulation frequency. The thick lines indicate the parameter-free theoretical predictions (Equations 4.19) for the dispersion relations (dark) and sub-harmonics (light), with $\Omega_R = 0$ and no fitting parameters. The line thickness corresponds to one standard deviation confidence interval originating from the uncertainty in the atomic density. The dashed line in panel (a) indicates the position of the spin branch, where a spurious signal is present due to some crosstalk between spin and density modes.

spin channel [panel (b)]. The dominant wavevectors at different modulation frequencies follow extremely well the dispersion relation of the Bogoliubov density and spin modes of Eq. 4.19, shown as solid black lines, computed without free parameters. In the evaluation of the dispersion relations, the only non-trivial parameter is the peak density n_0. We calibrate it by measuring the plasma oscillations frequency in the coherently-coupled mixture, with the protocol described in Chapter 3. This measurement leads to an estimate of the density and spin chemical potentials of 3 kHz and 145 Hz respectively.
From the data, we observe that the position of the most excited mode of density Faraday waves grow linearly with the modulation frequency, and starts being visible around $\omega_M/2\pi \sim 200$ Hz. The linear growth results from the scan of frequencies contained in the sonic region of the dispersion relations up to $\omega_M \approx \mu_d/\hbar$, or equivalently, $k/2\pi \approx 1/\xi_d \approx 0.2\,\mu\text{m}^{-1}$. On the other hand, spin Faraday waves exhibit non-linear behaviour, typical of the dispersion relations for wavelength shorter than the healing length. For our experimental parameters, this occurs at $k \approx 2\pi \times 0.05\,\mu\text{m}^{-1}$, where $\hbar\omega_M \approx \mu_s$.

A crossover between the two channels occurs around $\hbar\omega_M \approx 2\mu_s$, where spin Faraday waves disappear, and only the density ones are excited. Interestingly enough, a comparison with the theoretical evaluation of the growth rate $\gamma(k)$ [Fig. 4.2(b)], shows that the crossover between the two modes occurs when the growth rate of spin modes becomes lower than the density one.
Additional interesting features arise from density channel data. First, one can observe in the PSD the existence of higher harmonics of the most excited mode, for example around $\omega_M/2\pi = 400\,\mathrm{Hz}$. These signals, which lie on subharmonics of the dispersion relation (grey lines), are typical of Faraday waves, and come out naturally from the solution of the Mathieu equation, as excitations of instabilities with $l > 1$.
At last, we observe that there exists a residual signature of spin modes in the density channel, and viceversa. This originates from a weak coupling between the density and spin channels due to a possible imbalance in the magnetization, as well as from some crosstalk arising from the imaging procedure.

4.3.2 Coherently-Coupled miscible mixture

We now perform the same experiment in the presence of coherent coupling ($\Omega_R \neq 0$), for which the spin dispersion relation is gapped at $k = 0$. As the system now possesses an additional tuning parameter, given by the strength of the Rabi coupling, we gather results for two different values of $\Omega_R/2\pi$, specifically 30 Hz and 80 Hz.
Compared to the uncoupled case, we observed that the growth rate of spin Faraday waves becomes much smaller when $\omega_M \sim 2\omega_p$. As a consequence, we had to fine tune the driving parameters, in particular the modulation amplitude α, starting from 0.38 at $\omega_M = 2\omega_{pl}$ up to 0.66 for $\omega_M > 2\omega_{pl}$.
Interestingly enough, in contrast with the previous result, this time we had to increase the modulation amplitude to observe a signal in the spin channel when driving above the plasma frequency, up to the point where spin modes are impossible to be excited within the range of parameters available in the experiment.
Experimental results are plotted in Fig. 4.10 for both $\Omega_R = 30\,\mathrm{Hz}$ [panel (a)] and 80 Hz [panel(b)], with the corresponding density modes shown below each panel. Plasma frequencies are $\omega_{pl}/2\pi = 120\,\mathrm{Hz}$ and $\omega_{pl}/2\pi = 175\,\mathrm{Hz}$.
From the data presented in Fig. 4.10, it is clear that our protocol is able to excite Faraday waves even in the presence of a finite coupling strength. The observed signals nicely follow the theoretical predictions, with spin excitations present only above $\omega_M = 2\omega_{pl}$. The observation of spin waves only above $2\omega_{pl}$ clearly shows the tunability of the gap with the coupling strength Ω_R. In addition, in the case of $\Omega_R/2\pi = 30\,\mathrm{Hz}$, we measured Faraday waves with a well-defined wavevector, around, $k \approx 2\pi \times 0.04\,\mu\mathrm{m}^{-1}$. At $\Omega_R/2\pi = 80\,\mathrm{Hz}$ the excitation spectrum is broadened in Fourier space, probably due to the fact that we increased the modulation time, introducing further nonlinear dynamics or turbulence in the system [131, 132, 133]. Nevertheless, increasing the modulation time allows to efficiently sample the sonic dispersion relation in the density channel, which remains clearly unaffected by the coupling.
The experimental generation of spin excitations with a gapped mode is appealing for

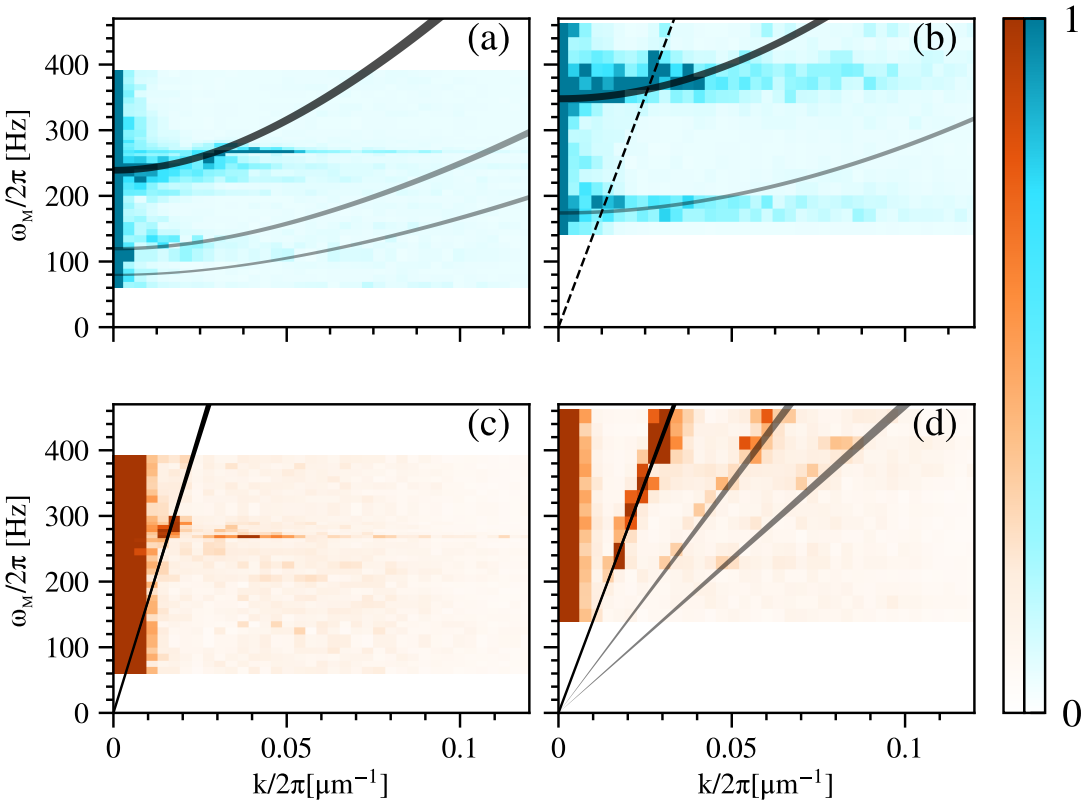

Figure 4.10: PSD of the spin excitations in the presence of a coherent coupling. In (a), $\omega_{pl}/2\pi = 120\,\mathrm{Hz}$, $\Omega_R/2\pi = 33\,\mathrm{Hz}$, $\mu_s/\hbar = 225\,\mathrm{Hz}$; in (b), $\omega_{pl}/2\pi = 175\,\mathrm{Hz}$, $\Omega_R/2\pi = 80\,\mathrm{Hz}$, $\mu_s/\hbar = 150\,\mathrm{Hz}$. The thick lines indicate the theoretical predictions for the dispersion relations (dark) and subharmonics (light). The line thickness corresponds to one standard deviation confidence interval originating from the uncertainty in the atomic density. Panels (c) and (d) show the corresponding PSD of the density channel (unaffected by the coupling). The dashed line in panel (b) indicates the position of the density branch, where a spurious signal is present due to the crosstalk between spin and density modes.

studies in the context of analogue gravity, as the excited gapped mode acquires a massive character. This is evident if one writes the spin dispersion relation 4.19 for small k as:

$$\hbar\omega_s(k) \sim \hbar\omega_{pl} + \frac{\hbar^2 k^2}{2M}; \qquad M = \frac{2m\omega_{pl}\Omega_R}{\omega_{pl}^2 + \Omega_R^2} \tag{4.22}$$

where M is a tunable effective mass of the excitation. For the data shown in panels (a) and (b), the effective mass is approximately 25% and 75% of the atomic mass respectively. The demonstration of the creation of massive many-body excitations might extend the current research on two-component atomic BECs as analogue systems [134, 135, 136] to

the investigation of massive fields interacting with the gravitational background [118], and to back-reaction processes of the field with the background space-time [137].

Chapter 5

Quantum Phase Transitions with Coherently-Coupled BECs

Contents

Phase transitions are ubiquitous in nature, and can occur in ordinary systems, like the boiling of water or the melting of ice, or in more exotic scenarios, like the low temperature transition of a bosonic gas in the condensed state or the transition of a metal to the superconducting regime. In classical systems, phase transitions occur upon a variation

of an external parameter, usually temperature, and are characterized by a qualitative change in system properties, from a disordered (high temperature) to an ordered (low temperature) state, upon crossing a critical point. This phenomenon is usually captured by the behaviour of an *order parameter*, which is non-zero only in the ordered state. For instance, in the ferromagnetic transition, well described by the Ising Model [138], the order parameter is the total magnetization.
A modern classification of phase transitions, similar to the original proposed by Ehrenfest [139], distinguishes between first-order phase transitions, where the order parameter jumps at the transition, from second-order transitions, where the order parameter vanishes continuously at the transition point, but its first derivative is discontinuous. In the latter case, even if the order parameter averages to zero in the disordered phase, its (thermal) fluctuations do not vanish, and their correlation length in space and time exhibits a power law divergence as a function of the distance from the transition point. These divergences imply that, at the critical point, fluctuations occur at all length and time scales, leading to a highly correlated state of the system, which is usually said to be scale-invariant. Accordingly, all observable quantities have a power law scaling, fully characterized in terms of a set of *critical exponents* [140, 141]. The divergence of the correlation length also implies that, at the transition point, the system averages its dynamics over large volumes, rendering microscopic details of the Hamiltonian irrelevant. As a consequence, critical exponents identify a *universality class* for the phase transition, which depends only on the system dimensions and symmetries.
A different class of phase transitions occurs in nature, when temperature is sufficiently close to zero for quantum effects to dominate. In this case, the critical point is approached upon the variation of a control parameter different from temperature. The transition is ruled by quantum fluctuations, and is known in the literature as a quantum phase transition (QPT) [142, 143]. In the quantum version of the Ising model, for example, temperature is substituted by the competition of interactions between neighbouring spins with a transverse magnetic field.
The role of interactions is peculiar in QPTs. In solid state system, an example is the Mott transition [144], while in spinor Bose-Einstein Condensate [21] interactions are critical in determining the structure of the spinor order parameter, and the transition from a disordered state to magnetic ordering [145].
In recent years, quantum phase transitions have been vastly investigated with ultracold atomic gases. Examples are the superfluid-to-Mott-insulator phase transition [146], magnetic phases in spin-orbit coupled spinor gases [147], and parity-symmetry breaking phase transitions [148, 149].
In coherently-coupled spin mixtures, it was theoretically anticipated [40] the existence of a QPT from a disordered (paramagnetic) state to a $\mathbb{Z}_2$-symmetry-breaking ordered (ferromagnetic) state. The transition, within mean-field theory, is fully driven by interactions, and belongs to the quantum Ising universality class. The low-energy magnetic fluctuations near the critical point are well described by a ϕ^4 theory, based on the Ginzburg-Landau functional for second-order phase transitions [150].
Some properties of this QPT, such as the existence of a classical bifurcation for the

spin order parameter [42], and hysteresis phenomena for a single component BEC in a tunable double-well potential [148], have been already investigated with ultracold gases. However, the lack of an extended dimension inhibited the possibility of describing the observed phenomena in terms of a quantum phase transition, as it is impossible to define a typical correlation length. Critical exponents were instead measured with a spatially extended mixture [94], following the evolution of the system after a quench of the order parameter.
In this Chapter I will describe the experimental characterization of the static phase diagram of the ferromagnetic phase transition, along with the possibility of generating magnetic domain walls, taking advantage of the spatial extension of the sample. In the first section, I will discuss in details the ferromagnetic phase diagram, derived in a semi-classical approximation, and show how it exactly maps on an immiscible spin mixture coupled with a coherent radiation. In the second section I will describe the protocol we used to experimental measure the ground state phase diagram, along with the image analysis method. In the third section I will discuss in details our procedure to extract quantitative information to characterize the phase transition, such as the hysteresis cycle and the divergence of magnetic susceptibility and related fluctuations. In the fourth section I will show how our platform gives the possibility to perform an experimental measurement of the fluctuation-dissipation theorem. In the last section, I will demonstrate how our system supports the generation and precise control of magnetic domain walls. All results discussed in this chapter are published in Ref.[93].

5.1 Paramagnetic to Ferromagnetic Phase Transition

In Chapter 1 we already discussed both the ground state properties and the dynamics of the internal degrees of freedom of coherently-coupled spin mixtures. In particular, we have seen how we can construct a spin vector $\vec{S}$, that evolves on the Bloch sphere under the effect of the coupling, with amplitude Ω_R and detuning Δ. The dynamic of such a system is very similar to the dynamics of a magnetic material, whose spin dipole $\vec{\mu}$ couples to an external field $\vec{B} = (B_1, B_2, B_3)$. Let us first recall the semiclassical continuous description, based on a mean field theory, of a ferromagnetic material.

5.1.1 Magnetic Model

We consider a generic magnetic material, with a local spin vector $\vec{S} = (S_1, S_2, S_3)$, subject to internal spin-spin interactions, parameterized by a matrix $\bar{\bar{K}}$, that keeps into account crystalline anisotropies. Interactions are of outstanding importance for magnetic properties, as they are responsible for the macroscopic magnetization. An additional external field $\vec{B}$ can be added, whose effect is to give a preferential direction for spin alignment. At finite temperature, a discrete model of this system is the notorious *Ising model* [138], which predicts a phase transition from a paramagnetic to a ferromagnetic state at a critical temperature, which depends on the interaction, $T_c \propto \bar{\bar{K}}$. At zero temperature, this model has to be replaced with its quantum version, called Quantum

Ising model, or Transverse Field Ising model [138, 143] due to the presence of a transverse, field perpendicular to the alignment direction of the spins. A continuous version of this model can be derived by integration of the Ising Hamiltonian [151], leading to the energy functional:

$$E(\vec{S}) \propto -\int \vec{B}\cdot\vec{S} - \frac{1}{2}\vec{S}\cdot\bar{\bar{K}}\cdot\vec{S} - \frac{1}{2}|\nabla\vec{S}|^2 dV \tag{5.1}$$

Here, the first term is the well known dipole interaction $\vec{\mu}\cdot\vec{B}$, for which each spin must be aligned to the external field to minimize the energy. The second term contains the energy arising from spin-spin interactions, and it sets the preferential directions for spin self-alignment, called *easy axes*, if $B = 0$. The last term adds an energy cost in the formation of magnetic domains, and arises from exchange energy between neighbouring spins. At a quantum level, it corresponds to the Heisenberg energy functional [151].
The dynamics of the local spin, in the absence of damping, is given by a dissipationless Landau-Lifshitz equation [61]:

$$\partial_t\vec{S} = -\vec{H}_{\text{eff}}\times\vec{S}; \qquad \vec{H}_{\text{eff}} = -\frac{\partial E}{\partial\vec{S}} \tag{5.2}$$

To better connect this model with the more familiar 1D spin chain, and for later analogy with our atomic platform, we considered the ferromagnet to be translationally invariant, $\nabla\vec{S} = 0$, with spin density $n = |\vec{S}|$ and uniaxial magnetic anisotropy such that the only non-zero element is $K_{33} = \alpha < 0$. We also consider the magnetic field to have the shape $\vec{B} = (B_1, 0, B_3)$, with B_3 called *longitudinal* field and B_1 the *transverse* field, in analogy with the Ising model. With this assumptions, the effective field reads:

$$H_{\text{eff}} = (B_1, 0, B_3 - \alpha S_3) \tag{5.3}$$

while the energy functional reduces to:

$$E(Z,\phi) \propto -B_3 Z - \frac{|\alpha|n}{2}Z^2 - B_1\sqrt{1-Z^2}\cos\phi, \tag{5.4}$$

where the $Z = S_3/n$ is the relative magnetization and $\phi = \arctan(S_2/S_1)$ is the angle of the spin on the transverse plane.
Useful information come from the calculation of the ground state (Z_{GS}, ϕ_{GS}). This can be extracted by minimizing the energy functional Eq. 5.4 with respect to (Z, ϕ). One can notice that, assuming $B_1 > 0$, the only ϕ-dependent term is the last element of Eq. 5.4, which is minimized by setting $\phi = 0$. Thus, the calculation reduces to the evaluation of Z_{GS} as a function of the parameters B_3/B_1 and $|\alpha|n/B_1$.
We numerically solve Eq. 5.4 to reconstruct the phase diagram of a magnetic material, shown in the central panel of Fig. 5.1. Examples of 8 different energy profiles, as a function of Z, for 8 different values of B_3/B_1 and $|\alpha|n/B_1$ are shown in the side panels. Several features can be extracted from both the phase diagram and the energy profiles. In the absence of a longitudinal field, $B_3 = 0$, the physics is dominated by the competition between the transverse field, which tends to align the spins along direction 1, and magnetic interactions $|\alpha|n$. One can identify a phase transition, shown in the bottom

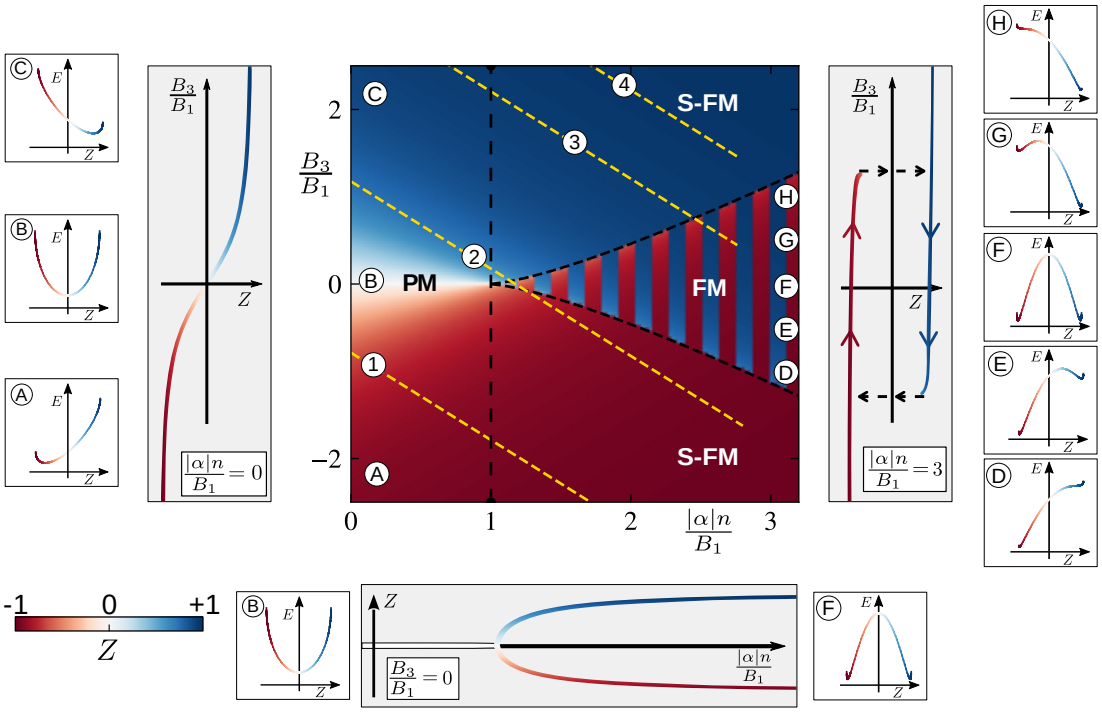

Figure 5.1: Phase diagram of the magnetic model. The relative magnetization Z of the system's stationary states is shown as a function of the non-linearity and of the longitudinal magnetic field strength, both in units of the transverse field. The system can be paramagnetic ($|\alpha|n < B_1$), ferromagnetic ($|\alpha|n > B_1 \gg B_3$), or saturated ferromagnetic ($|\alpha|n > B_1$ and $B_3 \gg B_1$). Panels (A)–(H) show the dependence of the energy (Eq. 5.4) on the relative magnetization Z in several points of the phase diagram. Three gray side panels show the value of Z at the energy minimum, as a function of $|\alpha|n/B_1$ for $B_3 = 0$ (bottom) and as a function of B_3/B_1 for $|\alpha|n/B_1 = 0$ (left) or $|\alpha|n/B_1 = 3$ (right). Numbered dashed yellow lines mark four different single-shot experimental realizations in the atomic system as reported in Fig. 5.2. See Section 5.1.2 and Table 5.1 for mapping from magnetic to atomic system.

panel of Fig. 5.1, as the energy landscape goes from a single minimum with $Z = 0$, when $|\alpha|n/B_1 < 1$, to a symmetric double minimum with $Z \neq 0$, for $|\alpha|n/B_1 > 1$, associated with a spontaneously broken $\mathbb{Z}_2$ symmetry, $Z \leftrightarrow -Z$. The emergence of two ground states corresponds to an ordered state, dominated by ferromagnetic interactions, where all spins tend to align along the easy axis.
At finite B_3, the ground state is shifted towards positive or negative values of Z. For $|\alpha|n/B_1 < 1$, Z smoothly follows a variation of the longitudinal field, as the energy is minimized when the spins are aligned with the external field. This behaviour, shown on the right panel of Fig. 5.1, is typical of paramagnetic materials, so we identify the left side of the phase diagram with a *paramagnetic phase*. For $\alpha|n|/B_1 > 1$, a finite

longitudinal field introduces a preferential direction for spin alignment, as it breaks the degeneracy between the two ground states at $\pm Z$, see panels (E)-(G). Depending on the sign of B_3, one of the two becomes a ground state, while the other becomes a metastable state. The appearance of a metastable state implies that a system, originally prepared with the all spins aligned to the longitudinal field, will maintain its magnetization, even when the longitudinal field is anti-parallel to the spins. Such a behaviour is typical of a *ferromagnetic phase*, and is at the origin of the hysteresis cycle, of the magnetization as a function of an applied external field. The latter is shown in the left grey panel, as well as in the central dashed region of the main panel, where is evident that the size of the hysteresis cycle in B_3/B_1 monotonically grows moving away from the critical point $|\alpha|n/B_1 = 1$.
At last, if B_3 is strong enough, one of the two metastable states disappears (panels (D) and (H)), corresponding to a *saturated ferromagnetic phase*.
We will now discuss how this model can be mapped one-to-one to our superfluid platform.

5.1.2 Atomic System

The magnetic model can be exactly mapped on a coherently-coupled superfluid mixture, where the spin vector arises from the internal degree of freedom, and evolves on the Bloch sphere. Recalling the notation used in Chapter 1, we identify the component $S_3 = n_\uparrow - n_\downarrow$ with the population imbalance. The components S_1 and S_2 are instead identified with the intercomponent coherences, i.e., with the relative phase with respect to the coupling vector Ω_R. The latter plays instead the role of the transverse field, being oriented along direction 1. A detuning of the coupling with frequency ω from atomic resonance, defined as $\delta_B = \omega - \omega_0$, adds a component along direction 3 to Ω_R, hence it can be identified with the longitudinal field B_3. The frequency ω_0 is the frequency difference between the two internal hyperfine states, including the Zeeman linear shift. At last, spin-spin interaction are mediated by the difference between intracomponent and intercomponent mean field energy $\delta g n$, as defined in Eq. 1.24, which represents the anisotropic magnetic interaction, uniaxial along direction 3.
In the case of a highly elongated spin mixture, as the one used in our experiment, it is also important to take into account the spatial dimension. If spin dynamics is strictly 1D, the radial direction can be integrated out, leading to the substitution $\delta g n^{3D}(x, r_\perp)$ with $\kappa n(x)$, that takes into account the transverse inhomogeneity (see Eq. 1.46). The axial inhomogeneity cannot be averaged, however it is always possible to work in the Local Density Approximation (LDA), $n = n(x)$, if density variations are smooth.
As we discussed in details in Chapter 1, the magnetization $Z = S_3/n$, n being the total density, undergoes a bifurcation at $\Omega_R = \kappa n$ for $\phi = 0, \pi$, which we can now identify with a phase transition. For the bifurcation to occur in the ground state, $\phi = 0$, it is necessary that $\kappa < 0$, i.e., that the mixture is immiscibile. In the ferromagnetic phase, where $Z \neq 0$, the magnetization grows like $S_3 \sim [-(\kappa n + \Omega_R)]^\beta$, with the typical mean-field critical exponent $\beta = 1/2$ [40].
We also recall that an imbalance between the two intracomponent coupling constants

introduces an additional mean-field correction, as for equal densities the two chemical potentials are different. The energy of the bare atomic states coupled by the radiation will be shifted accordingly by different amounts, and the net energy difference $n\Delta \propto n(g_{\downarrow\downarrow} - g_{\uparrow\uparrow})$ has to be compensated for the coupling to be resonant. One can then define an effective detuning as $\delta_{\text{eff}} = \delta_B + n\Delta$.
The one-to-one mapping between magnetic and atomic quantities is shown in Table 5.1.

Physical Quantity	Magnetic System	Atomic System
Anisotropic Interactions	αn	κn
Axial field	B_3	$\delta_{\text{eff}} = \delta_B + n\Delta$
Transverse field	B_1	Ω_{R}
Spin States	$\|\uparrow\rangle$	$\|2,-2\rangle$
	$\|\downarrow\rangle$	$\|1,-1\rangle$
Magnetization	$\mathbf{S}(\|\mathbf{S}\| = n)$	
Relative Magnetization	$Z = S_3/n$	

Table 5.1: Mapping between magnetic and atomic systems.

Recalling the definition we gave in Chapter.1, the effective magnetic field for the atomic system is given by

$$H_{\text{eff}}\left(\vec{S}\right) = (\Omega_R, 0, \delta_B + n\Delta - \kappa n Z) + \frac{\hbar^2}{2mn}\nabla^2\vec{S} \tag{5.5}$$

which is very similar to Eq. 5.3, including also the contribution of quantum mechanical currents in the effective field, contained in the term $\propto \nabla^2\vec{S}$. This last term, which we neglect at the moment, arises from the superfluid character, in particular from the quantum pressure term of the GPE, and describes the energy that the system has to pay to sustain the formation of a domain wall, or more in general, a spin interface [58].
A straightforward substitution of both the effective field and the new spin variables in the energy functional 5.1 leads to the expression

$$E(Z,\phi) \propto -\delta_{\text{eff}} Z + \frac{\kappa n}{2} Z^2 - \Omega_R\sqrt{1-Z^2}\cos\phi, \tag{5.6}$$

which describes the energy density of a uniform spin mixture with density n, or the local energy of an inhomogeneous spin mixture in the LDA. Stationary solutions are found minimizing Eq. 5.6 with respect to Z and ϕ, leading to

$$\begin{cases} (-\delta_{\text{eff}} + \kappa n Z)\sqrt{1-Z^2} + \Omega_R Z = 0 \\ \sin\phi = 0 \end{cases} \tag{5.7}$$

from where solution for Z_{GS} can be found numerically. We will now use this formulation to derive analytical expressions for characteristic magnetic quantities, such as the width of the hysteresis region and the magnetic susceptibility.

Magnetic Hysteresis It is useful, for later purposes, to find a mathematical definition for the width of the hysteresis region. We can start the derivation by calculating the value of δ_{eff} in the stationary case. For practical calculations, as Eq. 5.7 contains terms in Z and $\sqrt{1-Z^2}$, it is useful to make use of the parametrization of Z on the Bloch sphere, defining $Z = \cos\theta$. With this substitution, the expression for δ_{eff} from Eq. 5.7 reads

$$\frac{\delta_{\text{eff}}}{\Omega_R} = \left(\frac{|\kappa|n}{\Omega_R} - \frac{1}{\sin\theta}\right)\cos\theta \tag{5.8}$$

In the FM phase, the edge of the hysteresis region $\delta_{hys,\pm}$ corresponds to an abrupt jump in Z, thus $\partial Z/\partial\delta_{\text{eff}}|_{\delta_{\text{eff}}=\delta_{hys,\pm}} \to \infty$. It is more convenient, however, to evaluate $\partial\delta_{\text{eff}}/\partial Z \to 0$, as the latter derivative has a simple analytical expression:

$$\frac{1}{\Omega_R}\frac{\partial\delta_{\text{eff}}}{\partial Z} = \frac{1}{\Omega_R}\frac{\partial\delta_{\text{eff}}}{\partial\cos\theta} = \frac{|\kappa|n}{\Omega_R} - \frac{1}{\sin^3\theta} = 0 \implies \sin\theta = \left(\frac{\Omega_R}{|\kappa|n}\right)^{1/3} \tag{5.9}$$

Inserting this solution in Eq. 5.8 one finds

$$\frac{\delta_{hys}}{\Omega_R} = \frac{\delta_{hys,+} - \delta_{hys,-}}{\Omega_R} = 2\left[\left(\frac{|\kappa|n}{\Omega_R}\right)^{2/3} - 1\right]^{3/2} \tag{5.10}$$

which gives the size of the hysteresis region in the FM phase.

Magnetic Susceptibility In a magnetic system, the susceptibility is defined as the variation of the material magnetization to a small change in the external field, i.e.

$$\chi = \left|\frac{\partial Z}{\partial\delta_{\text{eff}}}\right|_{\delta_{\text{eff}}=0} \tag{5.11}$$

As before, it is easier to seek an expression for $1/\chi$, where we can use the previously calculated formulas. In this case, one must distinguish between the PM and the FM phases. In the former, at $\delta_{\text{eff}} = 0$ we expect $Z = 0$, or equivalently $\cos\theta = 0$, as only one minimum is present. As a result we get

$$\frac{1}{\chi_{PM}} = \left|\frac{\partial\delta_{\text{eff}}}{\partial Z}\right|_{\sin\theta=1} = |\kappa|n\left(\frac{\Omega_R}{|\kappa|n} - 1\right) \tag{5.12}$$

In the FM phase, the magnetization is instead finite, and takes the value (see e.g. Chapter 1) $Z = \pm\sqrt{1-\left(\frac{\Omega_R}{|\kappa|n}\right)^2}$, or equivalently, $\sin\theta = \frac{\Omega_R}{|\kappa|n}$. The susceptibility thus reads:

$$\frac{1}{\chi_{FM}} = \left|\frac{\partial\delta_{\text{eff}}}{\partial Z}\right|_{\sin\theta=\frac{\Omega_R}{|\kappa|n}} = |\kappa|n\left[\left(\frac{|\kappa|n}{\Omega_R}\right)^2 - 1\right] \tag{5.13}$$

Combining the two expressions, we get the final result

$$\frac{1}{\chi} = \left|\frac{\partial\delta_{\text{eff}}}{\partial Z}\right|_{\delta_{\text{eff}}=0} = |\kappa|n\begin{cases}\dfrac{\Omega_{\text{R}}}{|\kappa|n} - 1 & |\kappa|n < \Omega_{\text{R}},\\ \left(\dfrac{|\kappa|n}{\Omega_{\text{R}}}\right)^2 - 1 & |\kappa|n > \Omega_{\text{R}}.\end{cases} \tag{5.14}$$

5.2 Space-resolved measurement of magnetic phase diagram

The dependence of the magnetic phases on the atomic density $n(x)$ suggests the possibility of measuring, in principle in a single-shot experiment, different magnetic phases within the same elongated condensate. In particular, as for harmonic trapping the density is always higher in the center, for sufficiently low strength of the Rabi frequency there will always be a central ferromagnetic region, with paramagnetic regions on the tails, where the density is lower and eventually reaches zero.
Furthermore, in contrast with previous experiments on spatially extended coherently-coupled mixtures [48, 94], the magnetic field stability at the few μG level allows to investigate static properties of the system across the QPT. Indeed, the combination of a very high spin interaction energy $\mu_S \sim |\kappa| n_0$ and of a very low Zeeman shift induced by magnetic fluctuations, $\delta E_{Zeeman}/\hbar \ll |\kappa| n_0$ (see discussion in Sections 2.3 and 2.5.2), allows us to finely tune the relevant parameter $|\kappa| n/\Omega_R$ around the critical point.

5.2.1 Sample Preparation

In our experiments we create an immiscible superfluid mixture of states $|1,-1\rangle = |\downarrow\rangle$ and $|2,-2\rangle = |\uparrow\rangle$. Condensation is achieved following the protocol described in Section 2.2.4, producing a sample with typical atom number and peak density of $N_0 = 1 \times 10^6$ and $n = 7 \times 10^{14}\,\mathrm{atoms/cm^3}$, held in the optical trap provided by the Cigar beam, with trapping frequencies $\omega_x/2\pi = 20\,\mathrm{Hz}$ and $\omega_\perp = 2\,\mathrm{kHz}$. The resulting geometry is a cigar-shaped condensate, with Thomas-Fermi radii $R_x = 200\,\mu\mathrm{m}$ and $R_\perp = 2\,\mu\mathrm{m}$. In this configuration, due to the value of the coupling constants and atomic densities, the mixture has a peak spin chemical potential $\kappa n_0/2\pi \sim -1100\,\mathrm{Hz}$, and possesses the $\mathbb{Z}_2$ symmetry-breaking term $n\Delta/2\pi \sim -1100\,\mathrm{Hz}$[1].
The compression to a stronger trapping frequency, as compared to the samples studied in Chapters 3 and 4, is required to have 1D spin dynamics [96, 97]. This procedure, however, introduces a relevant thermal fraction in our samples. We measure, on a single component BEC, from Camera Horizontal 1 (see Section 2.4) a condensed fraction of $N_0/N = 35\%$, with an associated temperature of $T \sim 1\,\mu\mathrm{K}$, measured with time of flight thermometry [152]. Since a non neglectable thermal fraction has a relevant impact on the measurements, we will remove it with a specific data analysis procedure. A detailed explanation on this procedure will be given in Section 5.2.3.

5.2.2 Experimental Protocol

To characterize the magnetic phase diagram presented in the previous section, it is important to guarantee that the system remains locally in its ground state. To ensure this, we adopt the Adiabatic Rapid Passage protocol, characterized in Chapter 3. As we did previously, we control the value of δ_B acting on the magnetic field. Since the

[1] This values have been first estimated with the spectroscopic protocol described in Chapter 3, and later confirmed with a more sophisticated measurement, explained in Section 5.3.1

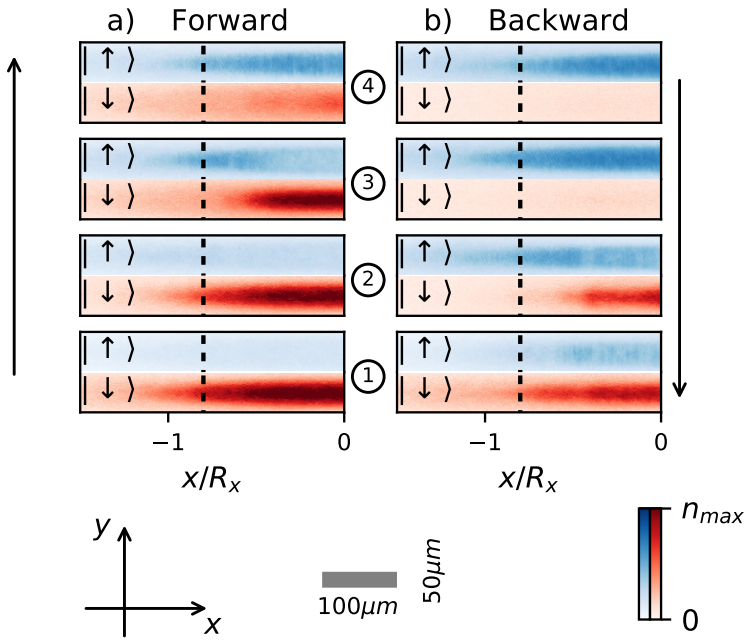

Figure 5.2: (a-b) Absorption images of the atoms in the states $|\uparrow\rangle$ and $|\downarrow\rangle$ (only the left half of the system is shown) for the parameters marked by the yellow lines in Fig. 5.1, for forward (a) and backward (b) ramps of δ_B. The solid arrows on the side of the plot indicate the direction of the ramp on δ_B. The vertical black dashed line marks the position where $|\kappa|n = \Omega_{\mathrm{R}}$ and the system switches from PM to FM.

hyperfine state $|1,-1\rangle$ is less energetic than the state $|2,-2\rangle$ (see Fig. 2.4), to decrease the detuning, at fixed frequency ω_0, we increase the value of the bias field.
We perform a first set of experiments starting with all the atoms in state $|\downarrow\rangle$, to which we apply the coherent coupling, with a strength Ω_R and an initial detuning of $-3.5\,\mathrm{kHz}$, which we linearly ramp to a final positive value with a speed of $100\,\mathrm{Hz/ms}$ (*forward ramp*). The choice of the ramp speed is a compromise between adiabaticity, which requires a very slow ramp, and decoherence induced by collisions [45]. We will characterize more in depth the effect of the ramp speed in Section 5.3.3.
In a second set of similar experiments, we transfer all the atoms with a fast π-pulse ($\Omega_R/2\pi \sim 25\,\mathrm{kHz}$) to the state $|\uparrow\rangle$, and apply a linear ramp to decrease the detuning, starting from $4\,\mathrm{kHz}$ (*backward ramp*). In this case we have to use a higher value of initial detuning to compensate for the density-dependent frequency shift $n_0\Delta$. Usual ramp times ranges between 30 ms and 55 ms for forward ramps, and between 20 ms and 45 ms for backward ones. Both are compatible with the expected coherence times of 100 ms, estimated from collision properties and condensate densities [153, 45]. For all values of Ω_R and δ_B, we get at least 3 shots, to reduce errors in δ_B due to fluctuations in the magnetic bias field.

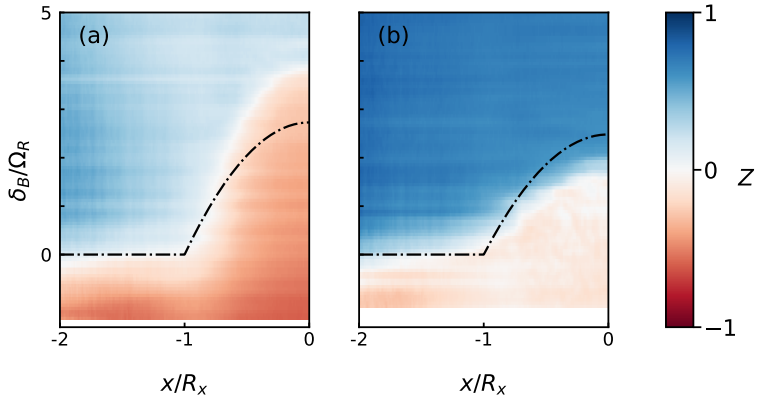

Figure 5.3: (a-b) Bare experimental data of the axial magnetization as a function of δ_B and position x for forward (a) and backward (b) ramps at fixed $\Omega_\mathrm{R}/2\pi = 400\,\mathrm{Hz}$. The yellow dashed lines mark experimental shots shown in panels (a-b), corresponding to number ①-④ as in Fig. 5.1 ($\delta_{B,1}/\Omega_\mathrm{R} = -0.8$, $\delta_{B,2}/\Omega_\mathrm{R} = +1.2$, $\delta_{B,3}/\Omega_\mathrm{R} = +3.2$, $\delta_{B,4}/\Omega_\mathrm{R} = +4.2$). Dot-dashed black lines in panels mark the local resonance condition $\delta_B = -n(x)\Delta$.

In both the experiments, we stop at different detunings δ_B and gather absorption images of the two states with Cam. Vertical 1 (see Section 2.4). Absorption images of the clouds, at four different values of δ_B, with $\Omega_R/2\pi = 400\,\mathrm{Hz}$, are shown in Fig. 5.2, for the forward [panel a)] and backward [panel b)] ramps. Due to the symmetry of the cloud, we only show the left side of the cloud, so that density, and thus $|\kappa|n$, grows on the positive x-axis.

As one can assert from absorption images, transverse spin dynamics is suppressed, hence we can extract the 1D magnetization $Z(x)$ by integrating along the y axes. The integrated magnetization is shown in the color plot of Fig. 5.3 as a function of position x and detuning δ_B, where it is evident that the response of the system to the forward [panel a)] or backward [panel b)] ARP ramps is different, especially in the center of the cloud. We first observe that the thermal tails of the cloud, $x < -R_x$, rotates homogeneously when $\delta_B = 0$, in both the backward and forward ramp, since mean-field effects are neglectable.

The appearance of a parabolic dome, starting at $x = -R_x$, is instead a consequence of the density dependent detuning $n(x)\Delta$, which makes the position where Z changes sign space dependent. In a fully paramagnetic cloud, where $|\kappa|n(x) < \Omega_R\ \forall x$, the $Z = 0$ line follows a parabola in the (x, δ_B) plane, represented by the dashed black line in the figure, and is given by the locus of points satisfying $\delta_\mathrm{eff} = 0$ (*local resonance*).

Despite this effect, we observe that, at fixed x the amplitude of the dome in δ_B, differs between the two ramps, a signature of the appearance of an hysteresis behaviour, as the magnetization depends on both the initial state and the direction of the detuning ramp. The amplitude of the hysteresis region, given by the deviation from the $\delta_\mathrm{eff} = 0$ curve,

and marked by the interface $Z = 0$, is also space dependent, increasing towards the center of the trap, in qualitative agreement with the ferromagnetic model. Indeed, at fixed δ_B, we observe that the interface spatially lags behind the local resonance: toward the tail of the cloud in the forward ramp, and toward the center for a backward ramp. Furthermore, we observe a dependence of the slope of the interface on the detuning δ_B, becoming steeper for higher δ_B.
While the main physical features of magnetic phenomena are qualitative described by the previous data, a quantitative measurement of magnetic properties is hindered by the presence of the thermal component, which alters the measured value of the magnetization of the condensate and must be subtracted.

5.2.3 Thermal part subtraction

We remove the thermal distribution directly on 2D absorption images with a postprocessing imaging analysis divided in several steps.
The *in-situ* distribution of a harmonically trapped bosonic gas at finite temperature, represented in Fig. 5.4 (a), is characterized by a dense condensed part in the center of the cloud, which expels thermal atoms from the center of the trap. To quantify the strength of this effect, we run a Hartree-Fock calculation [4, 87, 154] for a single component condensate, with 30% of condensed fraction (measured with Cam. Hor 1) and $T = 1\,\mu$K. This calculation predicts a thermal fraction of only 10% in the center of the cloud $n(0,0,z)$ [see central figure of panel (b)], much lower than the global one. To mimic the effect of the integration along the line of sight z, naturally performed to obtain 2D absorption images [152], we numerically integrate the 3D distribution along the line of sight, shown in panel c). It is evident that, at least in the center, the thermal distribution seen in our ODs is almost flat.
Assuming that during the small time-of-flight expansion the thermal distribution does not change significantly, we first reconstruct the total density profile of the cloud. To do so, we radially rescale the image of $|\uparrow\rangle$ to match the dimension of $|\downarrow\rangle$, in order to eliminate the effect of the radial expansion during the TOF. Once the two images matches, we calculate the total density summing the two. To identify the thermal part contribution, we fit the 2D total density with a bimodal distribution, i.e., $n(x,y) = n_{BEC}(x,y) + n_{th}(x,y)$, where

$$\begin{cases} n_{BEC}(x,y) = n_{BEC,0}\left[1 - \left(\frac{x-m_x}{R_x}\right)^2 - \left(\frac{y-m_y}{R_y}\right)^2\right]^{3/2} & \frac{x^2}{R_x^2} + \frac{y^2}{R_y^2} \leq 1; \\ n_{th}(x,y) = n_{th,0}\exp\left\{\left[-\frac{(x-m_x)^2}{2\sigma_x^2} - \frac{(y-m_y)^2}{2\sigma_y^2}\right]\right\} & \frac{x^2}{R_x^2} + \frac{y^2}{R_y^2} > 1. \end{cases} \tag{5.15}$$

Although the use of a Bose distribution [152] would be more appropriate to extract quantitative information about the thermal fraction, we found that for our purposes a Gaussian fit is good enough. Indeed, from the bimodal fit we only extract the size and location of the BEC fraction, in terms of the parameters m_x, m_y, R_x, R_y. We then use this parameters to construct an elliptic mask that isolates the thermal component on

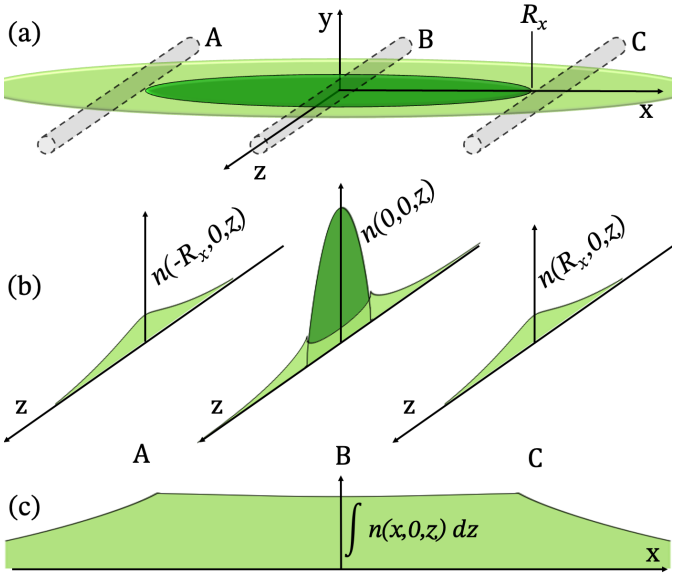

Figure 5.4: Thermal and condensate atomic distribution. (a) Schematic three-dimensional view of the condensate (dark green) and thermal (light green) distribution. A, B and C cylinders highlight the lines of sight of the central atoms and of the thermal atoms just outside R_x. (b) Line density profiles along the imaging direction for $x = -R_x, 0, +R_x$, calculated using Hartree-Fock theory for our partially condensed (30%) gas. (c) The integrated density for the thermal component $\int n(x, 0, z)dz$ has an almost flat distribution in the region occupied by the condensate.

the tails of both images of $|\uparrow\rangle$ and $|\downarrow\rangle$, to which we apply a second, more precise, 2D Gaussian fit.
At last, considering the results of Hartree-Fock calculation, we remove the contribution of the thermal component from each image by subtracting the fitted Gaussian profile (outside the condensate) and a flattop one(inside). The flattop profile, which resemble the result of the Hartree-Fock calculation, is set to a level by given the average of n_{th} at $(x, y) = (\pm R_x, 0)$ and $(x, y) = (0, \pm R_y)$. The impact of this choice will be further discussed in 5.3.5.

5.3 Quantitative measurement of magnetic properties

To obtain quantitative information about magnetic properties of the system we gather data at different values of $\Omega_R/2\pi$, namely 400 Hz, 600 Hz, 800 Hz and 1200 Hz, for both forward and backward detuning ramps. The dependence of the spatial extension of the ferromagnetic region on $|\kappa|n(x)/\Omega_R$ implies that, at constant $|\kappa|n_0$, for stronger Ω_R the position of the transition point moves toward the center. Indeed, the critical point scales

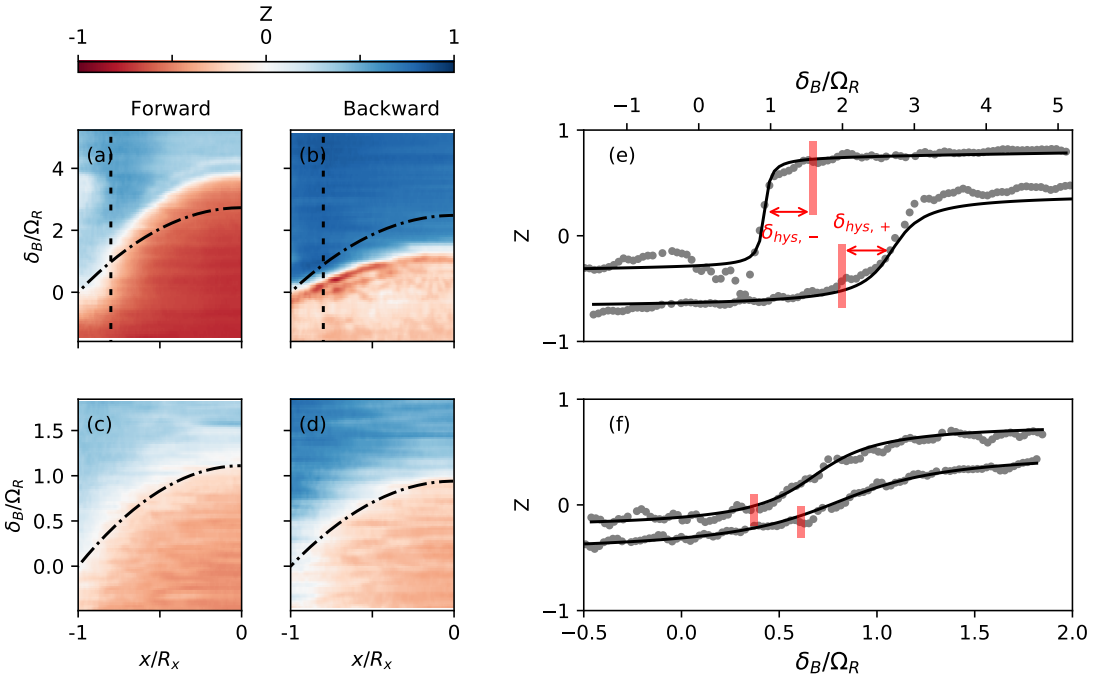

Figure 5.5: (a-d) Thermal fraction removed magnetization as a function of δ_B/Ω_R for forward (left) and backward (right) ramps, at $\Omega_R/2\pi = 400\,\text{Hz}$ (a-b) and $\Omega_R/2\pi = 1200\,\text{Hz}$ (c-d). Data shown in panels (a-b) are the same of Fig. 5.3, without the thermal component. (e-f) Magnetization as a function of δ_B/Ω_R, measured at $x = -0.52R_x$ for $\Omega_R/2\pi = 400\,\text{Hz}$ (e) and $\Omega_R/2\pi = 1200\,\text{Hz}$ (f). In both panels, red rectangles mark the point of local resonance, grey points are experimental data, and black lines are the *arctan+lin* fit (see Sec. 5.3.2).

in space as:

$$x_{CP} = \pm R_x \sqrt{1 - \left(\frac{\Omega_R}{|\kappa| n_0}\right)^2} \tag{5.16}$$

which becomes imaginary for $\Omega_R > |\kappa| n_0$. Here we assumed that the spin-interaction energy $|\kappa| n(x)$ scales as a 1D Thomas-Fermi. This is the underlying assumption we also used at the end of Chapter 1 to derive the renormalization $\delta g \to \kappa$. We will come back to the verification of this assumption in Section 5.3.1.
The possibility of performing detuning ramps at different Ω_R adds an additional tuning parameter, on top of the already spatially varying spin-spin interaction energy: it allows to gather data in a vast portion of the $|\kappa| n(x)/\Omega_R$ axis, rendering the cloud almost fully ferromagnetic or fully paramagnetic. We use this tunability of the critical point in space to measure both the width of the hysteresis region δ_{hys} and the magnetic susceptibility χ, as defined at the end of Section 5.1. We will show that, as expected, when the magnetization is plotted in terms of universal quantities, such as δ_B/Ω_R and $|\kappa| n/\Omega_R$,

the behaviour of both δ_{hys} and χ is almost independent of both the sample and specific parameters.
In Fig. 5.5 we show an example of such tunability, for both forward and backward ramps at $\Omega_R/2\pi = 400\,\text{Hz}$ [panels (a) and (b)] and $\Omega_R = 1200\,\text{Hz}$ [panels (c) and (d)]. At first, one can appreciate how the removal of the thermal distribution has increased the contrast in the magnetization. It is also easy to see how the deviation of the $Z = 0$ interface from local resonance vanishes at high Ω_R even in the center of the cloud, as compared to the case at $\Omega_R/2\pi = 400\,\text{Hz}$.
More importantly, for $\Omega_R/2\pi = 1200\,\text{Hz}$, the value of δ_B at which Z changes sign is almost the same for both ramps, independently from our determination of the curve $\delta_{\text{eff}} = 0$. This marks the absence of an hysteresis cycle, thus the whole cloud is in the paramagnetic regime.

5.3.1 Calibration of the local resonance

We calibrate the local resonance curve from the dataset with $\Omega_R/2\pi = 1200\,\text{Hz}$, using both a forward and a backward ramp. As the whole cloud is now paramagnetic, the only term which contributes to the formation of the parabolic dome with $Z = 0$, in the plane (x, δ_B), is the density dependent detuning $n(x)\Delta$. Since Δ and $|\kappa|$ differ only at the 1×10^{-3} level (see Appendix 6.3), a measurement of $n_0\Delta$ allows to determine also $|\kappa|n_0$. We first isolate the $Z = 0$ interface calculating the absolute value of the magnetization,

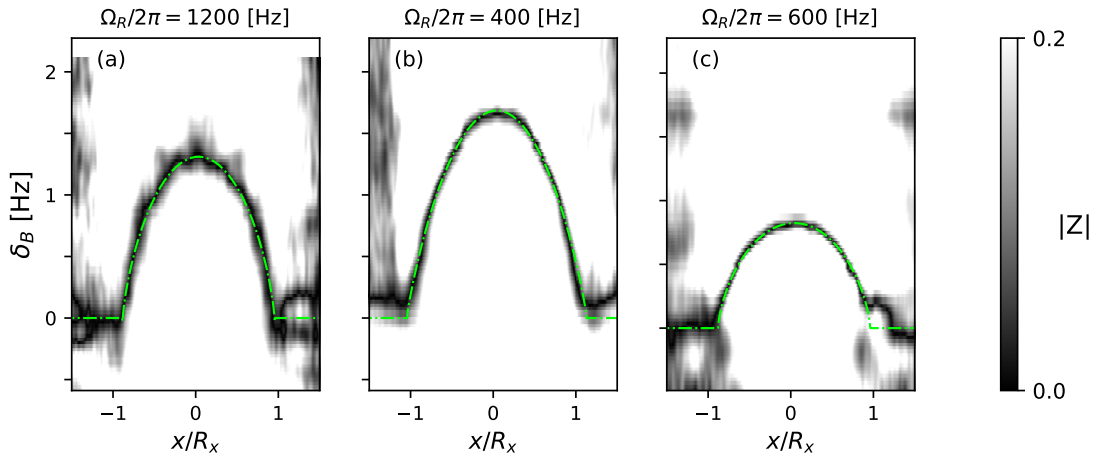

Figure 5.6: (a) Calibration of local resonance for a fully paramagnetic cloud, and examples of determination of m_x, R_x for forward [panel (b)] and backward ramps [panel (c)] in a ferromagnetic sample. In all panels, the grey scale corresponds to the value of $|Z|$, while green lines are fit of the function 5.17.

$|Z|$, to which we fit a modified Thomas-Fermi profile

$$n(x) = n_0 \left[1 - \left(\frac{x - m_x}{R_x}\right)^2\right]^\alpha \tag{5.17}$$

where we included a positive exponent α to include possible deviations from a pure one-dimensional profile. To perform the fit on the 2D magnetization $Z_{2D}(x, \delta_B)$, we first construct a 2D matrix M_{TF}, with the same dimensions of Z_{2D}, which has unitary values only at the Thomas-Fermi profile shown above, and zero everywhere else. The optimal parameters are then calculated by minimizing the mean of the element-wise multiplication between Z_{2D} and M_{TF}. An example of this fit is shown in Fig. 5.6 (a).
This procedure returns values of $n_0\Delta/2\pi \sim |\kappa|n_0/2\pi = 1100\,\text{Hz}$ and $1000\,\text{Hz}$ for forward and backward ramps respectively. We also find $\alpha \sim 1$, confirming our previous assumption of a 1D Thomas-Fermi profile and a value for the radius R_x, compatible with the one obtained fitting the density.
We then apply the same procedure for each dataset at different Ω_R, with α as a free exponent, once again to fit the $Z = 0$ interface. Examples of such fits are shown in Fig. 5.6 (b) and (c) for a forward and backward ramp respectively. We are mainly interested in precisely knowing R_x and m_x, which we then use to construct the local resonance curve $\delta_{\text{eff}} = 0$. In this case, the inclusion of the exponent $\alpha \neq 1$ as a free parameter helps adjusting the fit to the $|Z| = 0$ interface. At last, the peak density of the *i-th* dataset is obtained comparing the average atom number N_i with the one of the calibration dataset, as $|\kappa|n_{0,i} = |\kappa|n_{0,cal}(\langle N_i\rangle \,/\, \langle N_{cal}\rangle)^{2/5}$.

5.3.2 Measurement of hysteresis

Quantitative information about the phase transition are better obtained as a function of $[|\kappa|n(x)/\Omega_R, \delta_{\text{eff}}/\Omega_R]$, as this plane is independent of the details of the experimental platform. From the raw data shown in Fig. 5.5(a-b), we reconstruct the phase diagram shown in the central panel of Fig. 5.1 plotting the same data as a function of the adimensional quantities $x \to |\kappa|n(x)/\Omega_R$ and $\delta_B/\Omega_R \to \delta_{\text{eff}}/\Omega_R$.
For each dataset we apply the procedure described above, to extract R_x, m_x and the local resonance curve $\delta_{\text{eff}} = 0$. Once these parameters are known, the reference profile is translated pixel-wise along the y axis, to obtain $\delta_{\text{eff}}/\Omega_R$, while the x axis is transformed in the Thomas-Fermi density, $x \to n(x)$, and multiplied for $|\kappa|n_0/\Omega_R$.
Results of this procedure are shown in Fig. 5.7 for $\Omega_R = 400\,\text{Hz}$. Panels (a) and (b) show that the magnetization Z of the atomic system closely resembles the one calculated numerically from Eq. 5.4. In particular, one can appreciate how the magnetization smoothly crosses zero around $\delta_{\text{eff}}/\Omega_R = 0$ for $|\kappa|n/\Omega_R < 1$, while the position of the $Z = 0$ interface shifts towards positive (negative) values of $\delta_{\text{eff}}/\Omega_R$ for the forward (backward) ramp, as expected from hysteresis. Comparing this result with the phase diagram of Fig. 5.1, one can assert that for $|\kappa|n/\Omega_R > 1$ the $Z = 0$ interface found experimentally separates the saturated ferromagnetic (SFM) region from the ferromagnetic one (FM).
From the phase diagram it is interesting to quantify the width of the hysteresis region

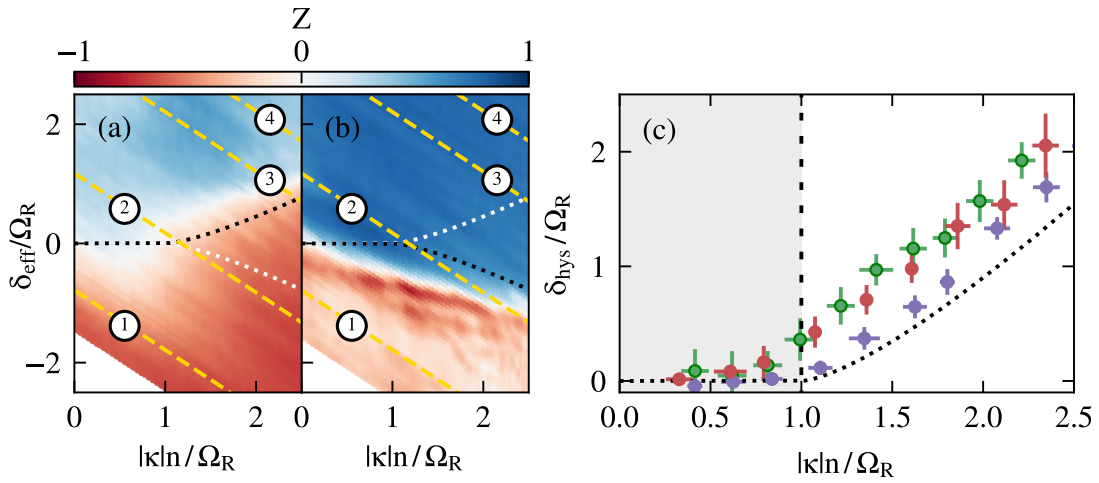

Figure 5.7: Magnetic hysteresis. (a)-(b) Experimental magnetization data from Fig. 5.5(a-b), rescaled according to the $|\uparrow\rangle$-$|\downarrow\rangle$ asymmetry and to the density profile, see main text. White regions in the bottom-left corner are due to a lack of data that manifests when applying the vertical-axis rescaling. Yellow dashed lines mark experimental shots shown in panel (a), corresponding to number 1-4, as in Fig. 5.1. Black and white dashed lines show the border of the hysteresis region as predicted from theory (Eq. 5.10. (c) Width of the hysteresis δ_{hys}. Green points are experimental data with their uncertainties resulting from the binning procedure and systematic errors. The dotted line stands for theory, while the purple and red points results from numerical 1D and 2D simulations respectively.

as a function of $|\kappa|n/\Omega_R$. To extract it, we slice the phase diagram of Fig. 5.7 (a) and (b) at fixed $|\kappa|n(x)/\Omega_R$, to obtain $Z(\delta_{\mathrm{eff}})$, and then find the position of the interface. For practical purposes, we take columns of data as a function of x/R_x, after averaging $Z(x)$ in a window of 10 pixels, where the curvature of $Z(x)$ due to the dome is almost negligible. Examples of such profiles, measured at $x = -0.52R_x$, were shown in Fig. 5.5 (e) and (f), as a function of δ_B/Ω_R. We fit each profile $Z(\delta_B/\Omega_R)$ with an empirical function, composed of an arctangent and a linear function

$$Z_{fit}\left(\frac{\delta_B}{\Omega_R}\right) = A\left[\frac{1}{2} + \frac{1}{\pi}\arctan\left(\frac{\delta_B - \delta_0}{\Omega_R\,\sigma}\right)\right] + \left[m\frac{\delta_B}{\Omega_R} + q\right] \tag{5.18}$$

from which we extract the slope σ and the center δ_0. The linear function is a tiny correction necessary to reduce the χ^2 of the fit.
From the results of each fit, we identify the position of the interface with the center of the sigmoid δ_0. Notice that δ_0 slightly differs from the value of δ_B at which Z vanishes, due to the saturation of Z to a value smaller than 1 at the end of the ramps. As shown in Fig. 5.5 (e) and (f), we then calculate δ_{hys} as the distance (red arrow) between δ_0 and δ_{eff} (shown as a red rectangle for each profile). Averaging and binning with data

extracted from all the dataset at different Ω_R we are able to reconstruct the width of the hysteresis region in a wide range of the distance from the critical point.
The behaviour of δ_{hyst} as a function of $|\kappa|n/\Omega_R$ is shown in Fig. 5.7 (c), compared with the theoretical curve (dashed-dot) line and both 1D and 2D GPE simulations [93]. The uncertainty along the δ_{hys}/Ω_R axis takes into account both fluctuations of the magnetic field, which we estimate to be in the order of 10 Hz, and the standard deviation of points averaged in the binning region. The uncertainty along $|\kappa|n/\Omega_R$ is calculated as the standard deviation in each binning region.
The results well capture the presence of hysteresis above the critical point $|\kappa|n = \Omega_R$ and its monotonic growth within the ferromagnetic region. However, we observe that δ_{hys}/Ω_R is much larger than the theoretically predicted one, and it starts to grow in the PM side, before the critical point. We attribute the discrepancy to both a loss of adiabaticity (see Section. 5.3.3) and a residual transverse dynamics. While the effect of a loss of adiabaticity can be easily investigated experimentally, the effect of transverse dynamic is much more difficult to capture, as a change in the trap configuration would affect other parameters, like the spin interaction energy κn_0. We instead decided to run 2D GPE simulations [93, 155], assuming axial symmetry, and compare the result with the ones obtained by 1D GPE simulations. We find that, with the inclusion of the transverse direction, simulations better match experimental results. Finally, it is worth to point out that additional beyond-LDA effects, given by the term $\propto \nabla^2 \vec{S}$, included in the GPE but neglected in our theoretical model, still might play a small, although not neglectable, role, increasing the extension of the hysteresis region.
The same measurement of an hysteresis cycle was performed in details in [148] in a zero dimensional system trapped in a tunable double well potential. Building on this work, the hysteresis cycle measured in a coupled mixture has the crucial difference that it originates spontaneously from atom-atom interactions, and it is well described within mean-field theory. Furthermore, the spatial extension of our platform allows for the study of the interplay between relaxation from hysteresis and spatial dynamics [156, 157].

5.3.3 Dependence of the hysteresis width on ARP parameters

A crucial detail in the characterization of δ_{hys} is the choice of the parameters of the ARP, such as the shape of the ramp, initial detuning and detuning sweep rate. As already stated, the time scale for the change in $\Omega_R(t)$ should be much larger than the inverse of the energy difference between the ground and the excited state, which is given by $\hbar\Omega_R$ itself. However, in real experiments, this requirement is hard to accomplish, especially at low Rabi coupling.
To investigate the impact of different choices of sweep rate $\partial_t \delta_B(t)$, we use the same protocol described above, performing forward ramps at ramp speeds of 600 Hz/ms, 100 Hz/ms and 50 Hz/ms. To evaluate possible effects in both the PM and FM phases, we set $\Omega_R/2\pi = 400$ Hz for all ramps. Data are shown in Fig. 5.8.
We observe that, for a very fast ramp [panel (a)], it is difficult to dynamically keep the system in its ground state at all times. In particular, while on the paramagnetic side there is a full transfer of atoms to the $Z = 1$ state, in the central ferromagnetic regions

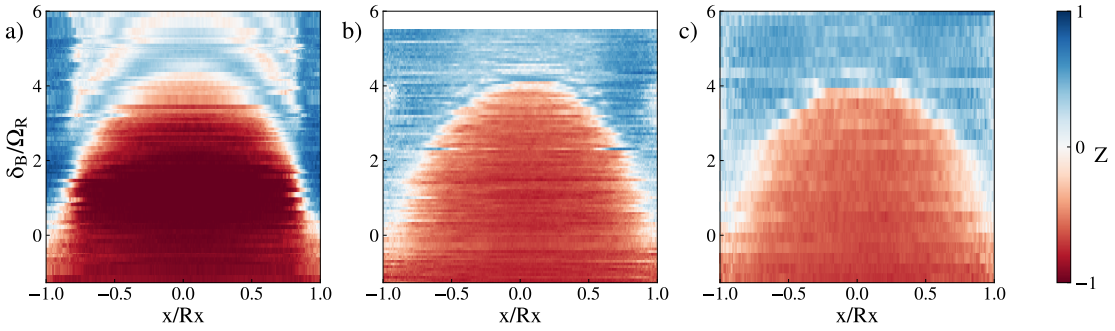

Figure 5.8: Comparison between ARP ramps. In all panels we show the cleaned axial magnetization as a function of δ_B/Ω_R for different detuning sweep speed, namely 600 Hz/ms, 100 Hz/ms and 50 Hz/ms from left to right.

strong spin waves are excited. This results from a sudden energy gain when the system transits from the FM to the SFM phase. While this is true for any adiabatic ramp in the ferromagnetic phase, in this case spin waves are enhanced by the extra energy injected by the loss of adiabaticity.
On the other hand, for a very slow ramp [panel (c)] no ripples are visible, but the final value of Z is suppressed, especially in the paramagnetic region, due to decoherence arising from magnetic collisions. The width of the hysteresis region is also slightly lower as compared to the measurement at 600 Hz/ms. This effect however is neglectable, as compared to the shift induced by the transverse direction, in the measurement of δ_{hys} reported in Fig. 5.7 (c).
A good compromise is shown in panel (b), where some small wavelength excitations are visible, right after the change in Z from red to blue, which damp quickly. On top of this, the transfer of atoms in the PM region is more efficient, even if not optimal, as compared to data at 50 Hz/ms.

5.3.4 Measurement of the magnetic susceptibility

When a system approaches the critical point of a phase transition, many quantities characterizing the system's response to external parameters are expected to diverge [143], due to the divergence of the correlation length of the system. In the para-ferro magnetic phase transition, one of this quantity is the susceptibility χ, defined in section 5.1, which measures the response of the order parameter Z to a variation in the longitudinal field. As such, it is expected to acquire a finite value in the paramagnetic phase, corresponding to a smooth change in magnetization, and to approach zero in the ferromagnetic phase, at vanishing transverse field, as Z is locked in state $|\uparrow\rangle$ or $|\downarrow\rangle$ by interactions. Finally, it should diverge at the critical point $|\kappa|n = \Omega_R$, where the response of the system to external fluctuations is enhanced.
Within our data, we can extract the value of χ, leveraging on the fact that the derivative

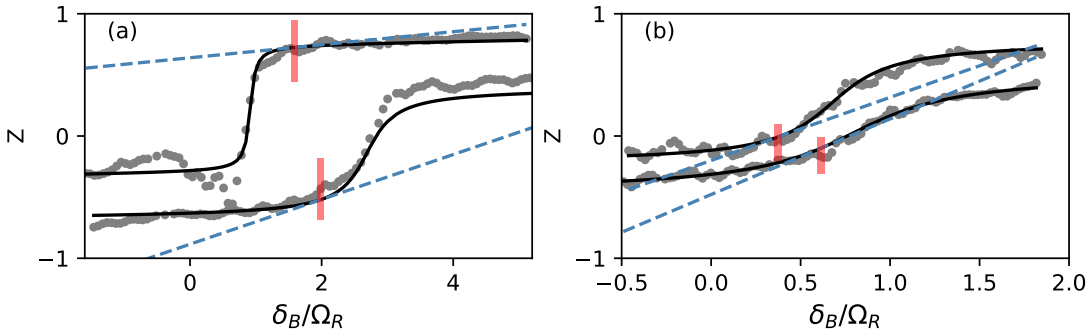

Figure 5.9: Magnetization as a function of δ_B/Ω_R, measured at $x = -0.52R_x$ for $\Omega_R/2\pi = 400\,\text{Hz}$ (a) and $\Omega_R/2\pi = 1200\,\text{Hz}$ (b). In both panels, red rectangles mark the point of local resonance, grey points are experimental data, black lines are the *arctan+lin* fit (see Sec. 5.3.2) and blue dashed lines are linear fits to the black lines used to measure the susceptibility. Same data shown in Fig. 5.5.

with respect to δ_{eff} is equivalent to the derivative with respect to δ_B, thus:

$$\chi = \frac{1}{n}\frac{\partial s_z}{\partial \delta_{\text{eff}}}\Big|_{\delta_{\text{eff}}=0} = \frac{1}{n}\frac{\partial s_z}{\partial \delta_{\text{B}}}\Big|_{\delta_{\text{eff}}=0} \underbrace{\frac{\partial \delta_B}{\partial \delta_{\text{eff}}}\Big|_{\delta_{\text{eff}}=0}}_{1}. \tag{5.19}$$

We follow the same analysis procedure applied to extract the hysteresis width δ_{hys}, only this time we calculate the derivative of the *arctan+lin* fit at $\delta_{\text{eff}} = 0$. Examples are shown as dashed lines in Fig. 5.9. We make use of the fit instead of the direct calculation of the derivative of the data since the latter enhances the noise of the measurement. In addition, for each χ_i the value of $|\kappa|n$ is given by an averaged density profile of the experimental shot with δ_{eff} closest to zero. Since the determination of the $\delta_{\text{eff}}(x) = 0$ curve is not reliable on the tails, due to the strong gradient in $n(x)$, we omit points with $|\kappa|n/\Omega_R < 0.3$.

Example of values of χ_i obtained with this procedure are shown in panels panel (c-d) of Fig. 5.10, measured for a forward ramp at $\Omega_R/2\pi = 400\,\text{Hz}$ and a backward one at $\Omega_R/2\pi = 600\,\text{Hz}$. Different colors indicate the distance from the center of the cloud. Spatial positions where we evaluated χ are shown as points in panels (a) and (b). As we did for the hysteresis, we bin and average the data along $|\kappa|n/\Omega_R$ axis to reduce statistical errors, and obtain the curve shown in Fig. 5.10 (e) (green dots), which is compared with theoretical prediction of Eq. 5.14 (red lines) and with numerical solution of noisy 1D GPEs (purple dots, see [93] for details).

We observe a very good agreement between experimental data, numeric and theory on the ferromagnetic side, while in the paramagnetic region experimental data for χ are lower then expected. This behaviour can be justified by the enhanced decoherence when $Z = 0$, which mostly affect the paramagnetic side, because the interface lies approximately on the local resonance curve, leading to a smaller contrast in $Z(\delta_{\text{eff}})$.

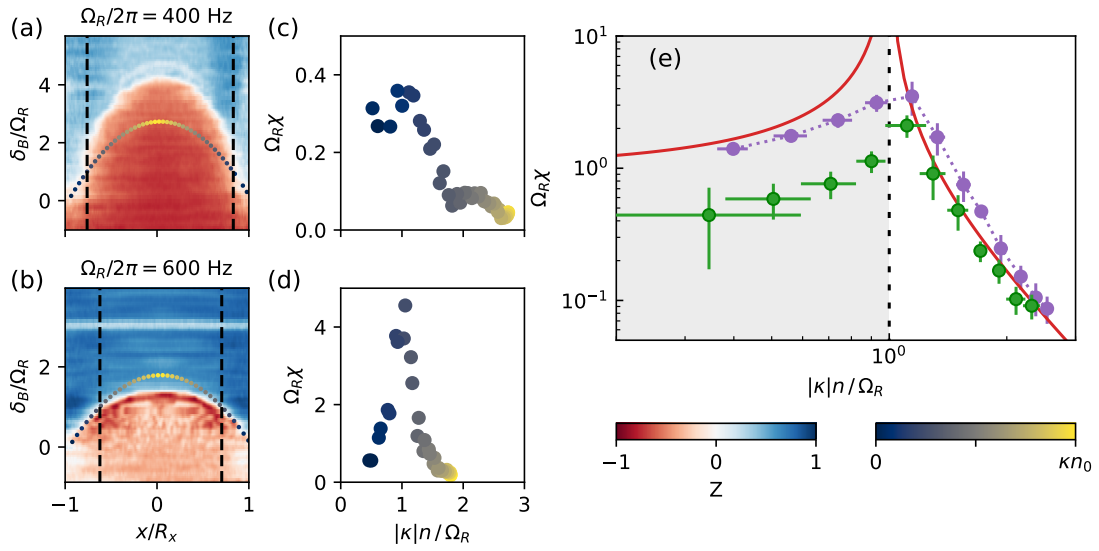

Figure 5.10: Measurement of susceptibility. Panel (a) and (b) show a forward ramp at $\Omega_R/2\pi = 400\,\text{Hz}$ and a backward one at $\Omega_R/2\pi = 600\,\text{Hz}$ respectively. In both panels dots represent the position along the curve $\delta_{\text{eff}} = 0$ where we measure χ. (c-d) Example of values of χ extracted from data in (a-b). Colors of the points are a visual guide to identify the spatial position of each of them in panels (c-d). Values of χ measured from the backward ramp are systematically higher than the one obtained with a forward one. (e) Susceptibility obtained after averaging over all datasets. Green points are experimental data with their uncertainties resulting from the binning procedure and systematic errors, red line is the theory prediction, purple points connected by dashed line are simulation results.

Furthermore, both experimental data and simulations show a peak at the $|\kappa|n = \Omega_R$, rather then a divergence, with the peak position slightly shifted above the critical point. While the shift is likely a result of both a loss of adiabaticity and the presence of a small but finite temperature in the system [158], the absence of a divergence in the data is most probably due to finite size effects [159, 160].

Critical Exponents In statistical mechanics it is well known that the divergence of characteristic quantities, such as χ, has a power-law scaling as a function of the distance to the critical point, as

$$\chi \sim \left| \frac{|\kappa|n}{\Omega_R} - 1 \right|^{-\gamma} \tag{5.20}$$

where γ is called *critical exponent*. Theoretical values of critical exponents can be found within a renormalization group approach [142, 143], and are expected to be universal, i.e. they do not depend on the microscopic details of the Hamiltonian.
Critical exponents ν and z, which predicts the scaling of spatial and time correlation

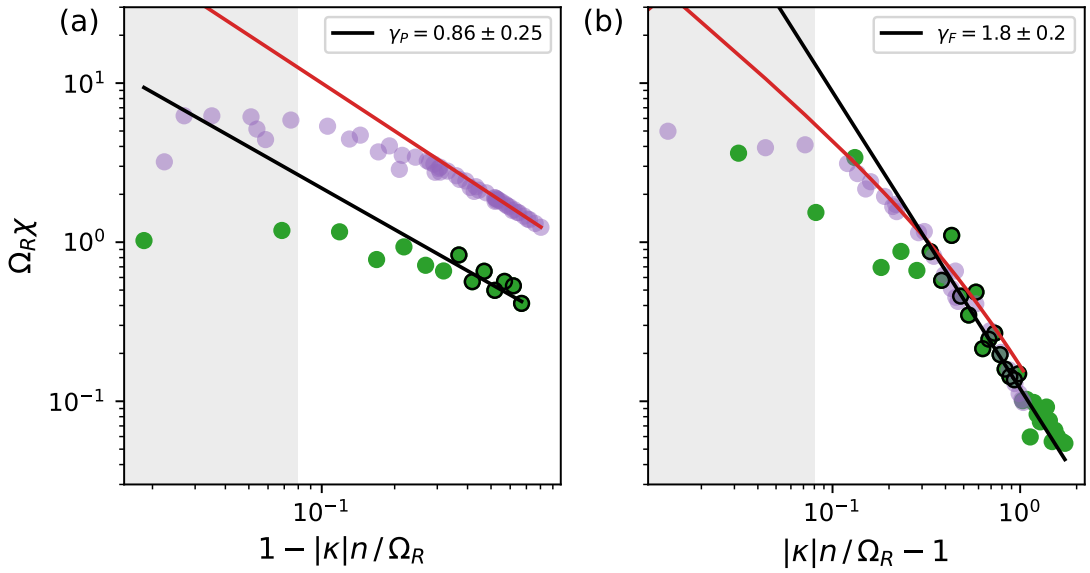

Figure 5.11: Calculation of critical exponents. Panels (a) and (b) show values of χ in the PM and FM phase respectively, obtained with a smaller binning compared to data shown in Fig. 5.10 (e). Green points are experimental data, purple ones come from numerical simulations, while red lines show the theory prediction. Linear fits, evaluated on a subset of data (highlighted with a black contour), to extract γ are shown as black lines.

length, have been already measured, in a coherently coupled mixture of ^{87}Rb atoms [48], following the evolution of the magnetization, crossing the critical point after a quench in the transverse field. Since we can keep the system in its local ground state, we have instead, in principle, access to both the order parameter critical exponent β and the susceptibility one γ. To measure the latter, it is useful to look at the values of susceptibility in log-log scale as a function of $||\kappa|n/\Omega_R - 1|$, plotted in Fig. 5.11, as in this plane a linear fit of the data would allow to extract the critical exponent in both phases.

Within the Landau class of universality, the critical exponent γ associated with the divergent susceptibility should be $\gamma = 1$ in both phases, for $|\kappa|n/\Omega_R$ approaching 1. Performing a linear fit we obtain $\gamma_{PM} = 0.86 \pm 0.25$ and $\gamma_{FM} = 1.8 \pm 0.2$. While in the PM phase we find an agreement with the predicted exponent for mean-field theory, in the FM region the experimental value differs from the theoretical one.

This discrepancy arises from the lack of a true divergence in both experimental data and GPE simulations (purple dots in Fig. 5.11). Indeed, the critical exponent can be defined only in the proximity of the critical point (shown as a grey region in Fig. 5.11), where, unfortunately, finite size effects [160] bend the data toward a finite value. This issue is apparently not present in the PM phase, only because χ is predicted to always scale

with $\gamma = 1$, see Eq. 5.14. This is not true, however, in the FM phase, as it is evident from both Eq. 5.14 and the theoretical curve, shown in red in panel (b).
Finally, it is important to notice that the presence of the density dependent detuning $n\Delta$ prevents a measurement of the exponent β, related to the scaling of the order parameter $Z \propto [-(\kappa n + \Omega_R)]^\beta$, since the phase transition is only crossed at a specific point in space, corresponding to the condition of local resonance. Such a measurement would be instead possible in a spatially homogeneous BEC with constant density n, where the condition of local resonance can be simultaneously satisfied across the sample.

5.3.5 Systematic errors induced by thermal part subtraction

The relevant quantities that we extracted in the previous sections, namely the width of the hysteresis region and the susceptibility χ are sensitive to the amplitude of the magnetization Z, especially for what concerns the susceptibility. As such, systematic errors on Z might originate in our procedure to remove the thermal part. Indeed, the choice of the central thermal profile, which coexist with the BEC, might alter the value of one population with respect to the other. To check the magnitude of this effect, we perform the previous analysis extracting δ_{hys} and χ after having removed the thermal fraction with four different profiles:

- a full Gaussian, constructed from the parameters of the 2D gaussian fits;

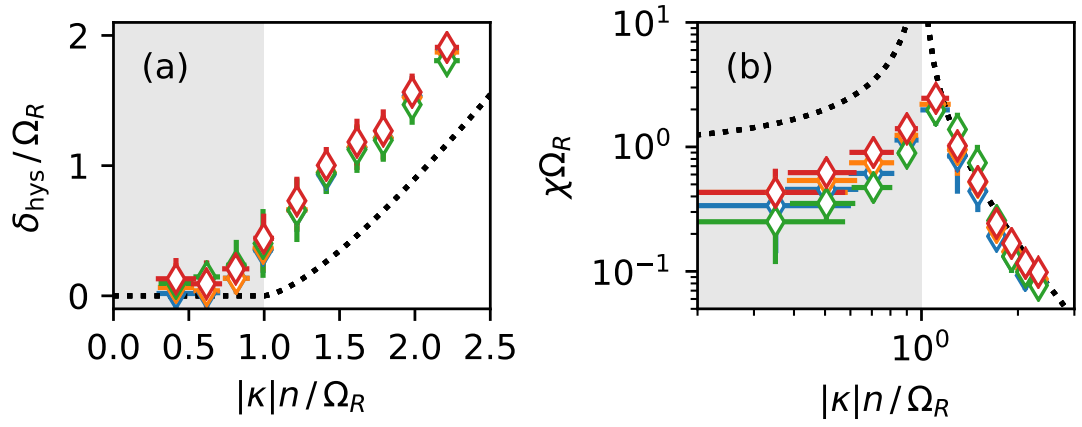

Figure 5.12: Effects of removing the thermal component. Panel (a) shows the hysteresis width obtained through the four different methods of thermal part subtraction, as explained in the text. Correspondingly, panel (b) presents the same comparison performed on the susceptibility. In both panels blue empty symbols correspond to paraboloid, orange to flat top, green to linear and red to Gaussian profiles. Both panels show a good agreement between the four methods. Black dotted lines are the theory predictions. Error bars are standard variations resulting from averaging different experimental realization and from systematic errors.

- a linear plane with non-zero slope along the x direction, extracted from the value of the thermal components at $x = \pm R_x$, where the y value is the mean of $n_{th}(0, \pm R_y)$. This profile should account for spatial asymmetries;
- a flattop profile, with height given by the average of n_{th} at $(x, y) = (\pm R_x, 0)$ and $(x, y) = (0, \pm R_y)$;
- an inverse paraboloid with fixed height, to take into account depletion.

Results of this test are shown in Fig. 5.12. From these data, it is clear that the main features, like the growth of the hysteresis region for stronger ferromagnetic interactions, and the peak in the susceptibility, are not affected by the choice of the flattop profile. We observe, however, that a quantitative measurement of χ in the paramagnetic region is highly sensitive to the thermal profile. This is natural, as a change in the extremes of $Z(\delta_{\text{eff}})$ is reflected in a higher or lower derivative, which is even more sensitive at $\delta_{\text{eff}} = 0$.

5.3.6 Measurement of magnetic fluctuations

Another interesting quantity to measure are the fluctuations of the order parameter, which are expected to diverge at the critical point. To measure fluctuations, we gather a set of data tuning Ω_R above and below the critical point, while setting the detuning δ_B to local resonance in the center of the cloud. In this way, the almost zero spatial gradient of δ_{eff} in the center of the trap allows us to measure *spatial fluctuations* of the order parameter. In particular, in order to increase the SNR of our measurement, we gather up to 100 shots for 20 values of Ω_R.
For each shot i, we calculate the distance from the critical point comparing the number of atoms N_i in each shot with the reference N_{cal} of the calibration dataset, as we did in the calculation of both hysteresis and susceptibility. Once the shot-to-shot value of $|\kappa|n/\Omega_R$ is known, we calculate fluctuations as the standard deviation σ of the spatial magnetization $Z(x)$, in a region $w_x = 120\,\text{pixel} \sim 123\,\mu\text{m}$. As the size of this region corresponds to 1/3 of the Thomas-Fermi radius, we can consider the density $n(x)$ to be constant within a 10%. To reduce inhomogeneities arising from the integration along the transverse direction, we calculate $Z(x)$ in a region with size $w_y = 20\,\text{pixel}$ in the center, slicing the 2D image prior to integration. This region is shown as an orange box in Fig. 5.13 (b). Finally, as the fluctuations strongly depend on the volume element that contributes to the signal [161, 162, 163], it is important to reduce systematic errors arising from the finite resolution of the imaging system. Our strategy is to perform the σ^2 analysis grouping N_p pixels, with various N_p, and averaging the resulting values of $\sigma^2_{N_p}$. The main idea behind this procedure is to try to emulate the effect of having half, a third, etc.., of the actual imaging resolution. The procedure behind this calculation of the fluctuation can be summarized by the formula

$$\sigma^2 = \left\langle \frac{1}{w_x/N_p} \sum_i^{w_x/N_p} \left(Z_i - \sum_j^{w_x/N_p} \frac{Z_j}{w_x/N_p} \right) \right\rangle_{N_p} \tag{5.21}$$

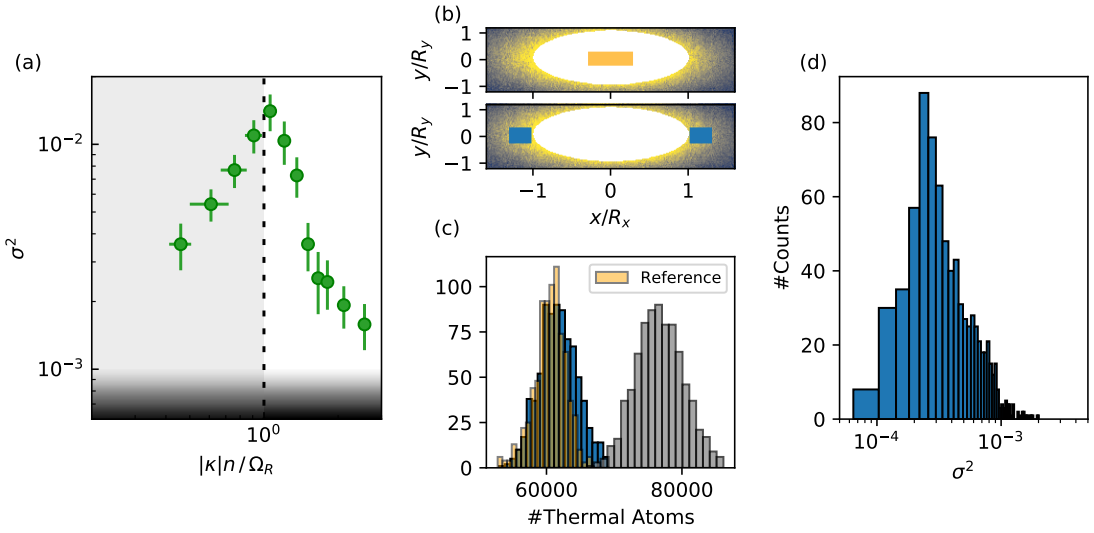

Figure 5.13: Magnetic fluctuations. Panel (a) shows experimental data, obtained with formula Eq. 5.21. (b) Examples of the optical density of the removed thermal distribution. Inner white region is the position of the BEC. The orange rectangle (top panel) shows the region where σ^2 and $N_{th,ref}$ are measured. Blue rectangles (bottom panel) on the side show the region where σ^2_{th} is calculated. (c) Histograms of the reference distribution $N_{th,ref}$ (orange) and of the thermal distribution $N_{th,ext}$ (blue). An example of a non-optimal thermal distribution $N'_{th,ext}$, calculated on a different region, is shown in grey. (d) Histogram of σ^2_{th}, showing the fluctuations of the thermal component.

Here, Z_i is the relative magnetization of the i-th grouping element and $\langle ... \rangle_{N_p}$ indicates the average over different grouping size. The appearance of w_x/N_p is only a normalization factor. Final results are plotted in Fig. 5.13 (a), binned in intervals of $|\kappa|n/\Omega_R$. Here, errorbars are given as the combination of the standard deviation of the fluctuations and the scattering of the points arising from both different binning and N_p grouping.
The data clearly shows a peak around the critical value, which reflects the observed divergence of the susceptibility. The last fact comes with no surprise, as the two are related via the fluctuation-dissipation theorem [164].

Contribution of thermal atoms It is important to exclude that the enhancement of magnetic fluctuations around the critical point is correlated with fluctuations of the underlying thermal distribution, which are not supposed to show magnetic phenomena. This problem arises from the fact that our procedure to remove the thermal contribution only subtracts the bulk distribution, leaving untouched fluctuations (or noise) of the thermal component.
To quantify the magnitude of this contribution, since we do not have direct access to thermal fluctuations within the BEC bulk, we have to find a spatial region with only

thermal atoms. We follow a procedure divided in different steps:

- we first find, over the entire dataset, the distribution of the number of atoms $N_{th,ref}$ in the central 120×20 pixel region of interest [see orange rectangle in Fig. 5.13 (b)] where we measured σ^2. This distribution is shown in orange in panel (c).

- We then select several areas in the 2D magnetization of the thermal component, i.e., where $|x| > R_x$, with different position and size. For each of them, we calculate the atom number distribution $N_{th,ext}$ over the entire dataset.

- We then compare the mean and variance of each $N_{th,ext}$ with the one of $N_{th,ref}$. The optimal distribution, shown in blue in Fig. 5.13(c) is measured in two regions, starting at $(x, y) = (\pm|R_x + 10|, -6)$, with dimensions $w_x = 54\,\text{px}$, $w_y = 12\,\text{px}$. These regions are shown in the bottom figure of panel (b) as blue rectangles.

- For each image, we evaluate the fluctuations of Z_{th} in the two regions, as we did for Z_{BEC}.

Shot-to-shot results for σ^2_{th} obtained with this procedure are shown in the histogram of Fig. 5.13(d). The main result of this analysis is that σ^2_{th} seems to follow a Poisson distribution, with mean value centered at 5×10^{-4}, which is well below any value measured in the condensate.

5.4 Fluctuation-Dissipation theorem

The measurement of the width of the hysteresis region and of the diverging susceptibility justify the validity of the mean-field description of our system. However, beyond mean-field terms, such as magnetic fluctuations, play a crucial role while approaching the phase transition. Indeed, as the correlation length in the system diverge [143] at the critical point, also fluctuations of the order parameter are expected to diverge. Linear response theory provides a brilliant connection between the response of the system in the presence of an external force, and its fluctuation in the absence of driving. This connection is known as *fluctuation-dissipation theorem* [164] and is a fundamental and general theorem, which applies to many out-of-equilibrium systems. In solid-state systems, for example, it gives the mathematical foundation to the use of neutron scattering techniques, widely employed to extract relevant information about the crystalline structure.
As demonstrated above, in our system we have access to both magnetic fluctuations, within a spatially extended probe region, and to the magnetic susceptibility, which constitute the response of the system to the variation of the external field. As such, our experimental platform provides an optimal test-bed for a direct measurement of the fluctuation-dissipation theorem. In the following, we will first derive an exact formulation of this theorem in an uniform sample. We will then compare analytical results with experimental data, and discuss the validity of this measurement.

5.4.1 Theoretical model in uniform BEC

In single component BECs, a notorious example of the fluctuation-dissipation theorem is the link between fluctuations in the number of particles of the condensate and the system compressibility [6]. For single component condensates, particle number fluctuations $\langle \delta N^2 \rangle$ in a finite cell of volume V can be calculated starting from the 2-point density-density correlations $ng(|\boldsymbol{r}_1 - \boldsymbol{r}_2|) = \langle n(\boldsymbol{r}_1)n(\boldsymbol{r}_2)\rangle - n^2$, see e.g. [161, 162, 163] as:

$$\langle \delta N^2 \rangle = n \int g(\boldsymbol{r}) H(\boldsymbol{r}) d\boldsymbol{r} \tag{5.22}$$

where $H(\boldsymbol{r})$ is a geometrical factor that keeps into account the shape of the probe region. On the other hand, it is well known, in any condensed matter system, that density-density correlation are related to the structure factor through the Fourier transform [162, 165], as

$$g(\boldsymbol{r}) = \int \frac{d^3\boldsymbol{k}}{(2\pi)^{3/2}} S(\boldsymbol{k}) e^{i\boldsymbol{k}\boldsymbol{r}} \tag{5.23}$$

Thus, the evaluation of the fluctuation term reduces to

$$\langle \delta N^2 \rangle = n \int S(\boldsymbol{k}, T) H(\boldsymbol{k}) d\boldsymbol{k} \tag{5.24}$$

where $H(\boldsymbol{k})$ is the Fourier transform of the volume element where fluctuations are probed. The effect of a finite and low temperature, below T_c, can be included in the structure factor through detailed balance [6], leading to the expression for the structure factor of the density channel [163]

$$S(k, T) = \frac{\hbar^2 k^2}{2m\varepsilon(k)} \coth \frac{\varepsilon(k)}{2k_B T} \tag{5.25}$$

This expression stems from the fact that the imaginary part of the response function is T independent for a weakly interacting gas [6]. The T dependence is particularly important, as it dramatically changes the shape of the structure factor for $T \neq 0$, as shown in [163].
In analogy with the density channel case, one can write an expression for the fluctuations of the magnetic order parameter Z in a coherently-coupled spin mixture:

$$\langle \delta M^2 \rangle = n \int S_s(\boldsymbol{k}, T) H(\boldsymbol{k}) d\boldsymbol{k} \tag{5.26}$$

expressed in terms of the magnetization $M = nZ$, for a better analogy with the previous formulation.
If the probe volume V is large enough, the integral is dominated by the $k \to 0$ components, and we can find the simple approximation

$$\langle \delta M^2 \rangle \sim N S_s(0, T); \quad S_s(k, T) = \frac{\hbar^2 k^2 / 2m + \Omega_R}{\varepsilon_s(k)} \coth \frac{\varepsilon_s(k)}{2k_B T} \tag{5.27}$$

where $S_s(k,T)$ is the structure factor in the spin channel at finite temperature T, and $\varepsilon_s(k)$ is the dispersion relation, evaluated around the ground state. For a single component condensate, in this limit one recovers the well known result linking fluctuation of number of particles to the system compressibility [6]. This expression have been also used to measure the (density) dynamic structure factor in a 2D-Bose gas [166].
In our system, we can push the derivation further, and connect magnetic fluctuations to the response of the system, given by the magnetic susceptibility χ. This is straightforward in the PM phase, as for $k = 0$ the dispersion relation simplifies to $\varepsilon(k) = \sqrt{\hbar\Omega_R(\hbar\Omega_R - |\kappa|n)} = \sqrt{\hbar\Omega_R\chi_{PM}^{-1}}$, where we have used the definition given in Eq.5.14 in the last passage. Combining this result with Eq.5.27 we obtain the expression

$$\sigma_z^2 = \frac{\langle \delta M^2 \rangle}{N^2} = \frac{\sqrt{\chi}}{N} \coth \frac{\hbar\Omega_R}{2k_B T\sqrt{\chi}} \tag{5.28}$$

which is a form of the fluctuation-dissipation theorem for the magnetic spin mixture. Here we have introduced $\sigma_z^2 = \langle \delta M^2 \rangle / N^2$ to connect with our experimental measurement of magnetic fluctuations, and substituted $\chi \to \chi/\Omega_R$, to match the results of Fig. 5.13. We have also dropped the PM index in the susceptibility, as the same relations holds also in the FM phase.
Two important cases are worth discussing, in the limit of high and low temperature. In the spin channel, the correct energy scale for the temperature T is given by the temperature associated with the gap $\varepsilon_s(0)$. At low temperatures, $k_B T \ll \varepsilon_s(0)$, Eq. 5.28 reduces to $\sigma^2 = \sqrt{\chi}/N$, as thermal effects on the structure factor disappear, and fluctuations are purely quantum. Thermal fluctuations are instead recovered in the opposite limit, $k_B T \gg \varepsilon_s(0)$, where fluctuations grow linearly with the susceptibility as $\sigma^2 = 2k_B T/(N\hbar\Omega)\chi$.
With this machinery in mind, we can attempt a direct measurement of the fluctuation-dissipation theorem with our previous measurements of both χ and σ^2.

5.4.2 Measurement of the fluctuation-dissipation theorem

In Fig. 5.14 (a) we plot the magnetic fluctuations σ^2, as measured in Section 5.3.6, as a function of $\Omega_R\chi$. We observe a nice scaling between the two quantities for all $|\kappa|n/\Omega_R$ (represented as a colorscale for each point), a signature of the expected correlation. This gives a qualitative proof of the fluctuation-dissipation theorem. To extract more quantitative information, we fit formula 5.28 to our data. Results of the fit are shown as red diamonds, calculated at each value of $\Omega_R\chi$. A crucial point in the fit is the evaluation of the number of atoms in the probe region. We fix N to

$$N = N_a w_y \langle N_p \rangle \tag{5.29}$$

where $N_a = 60$ is the number of atoms in each pixel, measured from the optical density $n(x,y)$ of the condensate, w_y is the size of the integration region along y and $\langle N_p \rangle$ is the average of different grouping sizes, see Eq.5.21. Then, the only free parameter of the fit is the temperature T, which we found to be $T = 1.3(1)\,\mu$K.

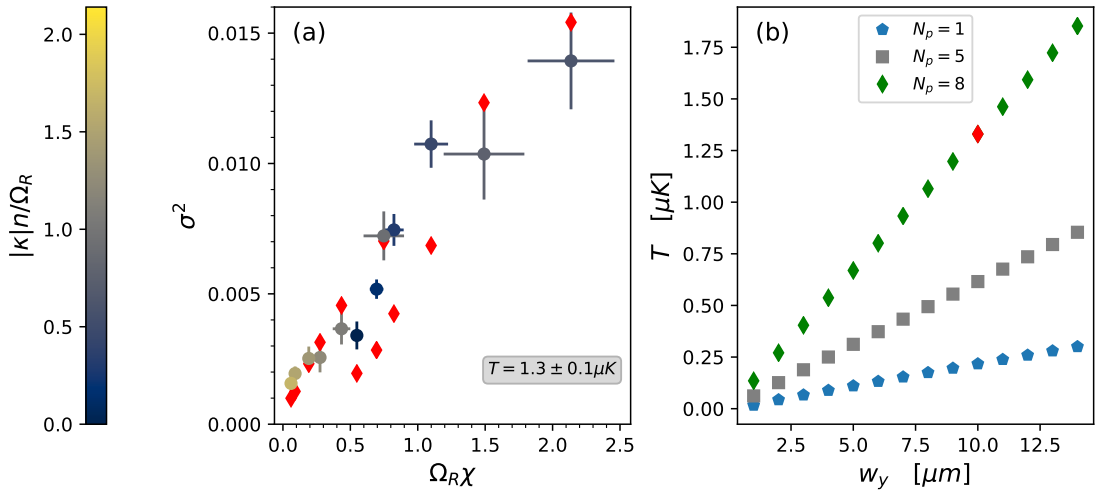

Figure 5.14: (a) Correlation between fluctuations σ^2 and susceptibility χ. The colorcode is used as a reference to label the values of $|\kappa|m/\Omega_R$. Red dots are fit of Eq.5.28. (b) Scaling of the measured spin temperature with the number of atoms in the probe region, see Eq.5.29, for three different grouping size N_p. The red point in panel (b) refers to a result of a fit similar to the one shown in panel (a).

Despite the agreement with a time-of-flight measurement of the temperature of a single-component sample, one has to be careful in the interpretation of the previous result. In particular, the temperature found from fluctuation-dissipation theorem should be interpreted as an emerging temperature associated to the spin degree of freedom, being extracted from magnetic fluctuations, and might differ from the equilibrium temperature of the condensate. In this framework, our value seems to be to high as compared to the spin interaction energy $|\kappa|n_0 \sim k_B 50\,\mathrm{nK}$. In fact, one could argue that such a high temperature would smear out any detail of the phase transition around the critical point, making impossible to measure the onset of the histeresis region or the divergence of the susceptibility.

As the previous formula heavily relies on the exact evaluation of the number of atoms contributing to the signal, we test our result calculating σ^2 for different integration regions w_y and for different grouping sizes N_p. Indeed, varying both w_y or N_p affects both the value of σ^2 and N. In particular, fluctuations, according to Eq.5.28, should scale with $1/N$, and the temperature T should remain constant. In Fig. 5.14 (b) we report the values of T obtained from fit of Eq. 5.28 as a function of w_y, for three different values of N_p. We observe that in both cases T grows with the number of atoms, instead of remaining constant, demonstrating that the measurement of the temperature, as reported in panel (a), is not reliable. Further investigations show that this effect arises from a scaling of $\sigma^2 \sim 1/N^2$ instead of $1/N$. Experimentally, we attribute this scaling to a combination of a high shot-to-shot variance of the number of atoms and to the inhomogeneous density profile. The conclusion of this analysis is that, although we capture a

correlation between fluctuations and susceptibility, confirming at a qualitative level the validity of the fluctuation-dissipation theorem, a quantitative and precise measurement, which would help discriminating between quantum and thermal fluctuations, cannot be performed with the current experimental setup.

5.5 Domain walls

In an extended ferromagnetic material, the presence of two equally energetic ground states allows for the formation of extended domains with opposite magnetization. The interface separating two domains is the least energetic excitation in a ferromagnet, and is called a *domain wall* (DW). In a spin chain, or in any discrete lattice model, with only two possible value of $\hat{\sigma}_z$, domain walls are sharp interfaces, often called *kinks* [167], that interpolates between two adjacent and opposite spin domains. On the other hand, in an extended system with a continuous spin degree of freedom, such as a ferromagnetic BEC, they have a finite size, with the magnetization Z continuously changing value from $Z \to -Z$ or viceversa, eventually crossing $Z = 0$ at some point in space.
The formation of different domains can be of stochastic nature [25], via the Kibble-Zurek mechanism [168, 169, 170, 171], if the system is quenched across the critical point starting from a paramagnetic phase. Another possibility is to engineer different phases with a deterministic protocol. Recent investigations on the spontaneous and deterministic generation of DWs in ferromagnetic BECs under periodic driving were conducted in [172, 173].
In our platform, we are able to control precisely the size of the ferromagnetic region, with both the coupling strength Ω_R and the detuning δ_B, and control the position of an interactions-sustained DW in a flexible, yet precise, way.

Deterministic creation of domain walls To control the position of the DW, we exploit the dependence of the $Z = 0$ boundaries, separating the inner FM region from the outer SFM one, on the detuning δ_B, see for example Fig. 5.3. In particular, for a forward ramp, increasing δ_B shrinks the FM region, moving the interface towards the center of the trap.
Our protocol to generate the DW is divided in three steps:

I we first ramp the detuning δ_B, from negative values, to some value δ_{DW} for which part of the system is in the ferromagnetic regime. This step determines the location of the DW in space;

II we wait 25 ms to let the system relaxes. This is motivated by our finding that non-adiabatic ramps increase the hysteresis width δ_{hys}, thus leaving the interface with some extra energy, which we suppose is dissipated through a slight shift of the interface towards the center;

III we then ramp back δ_B to a fixed detuning $\delta_{ref} = 2.5\Omega_R$, with $\Omega_R = 400\,\text{Hz}$. This step is crucial to enlarge the ferromagnetic region.

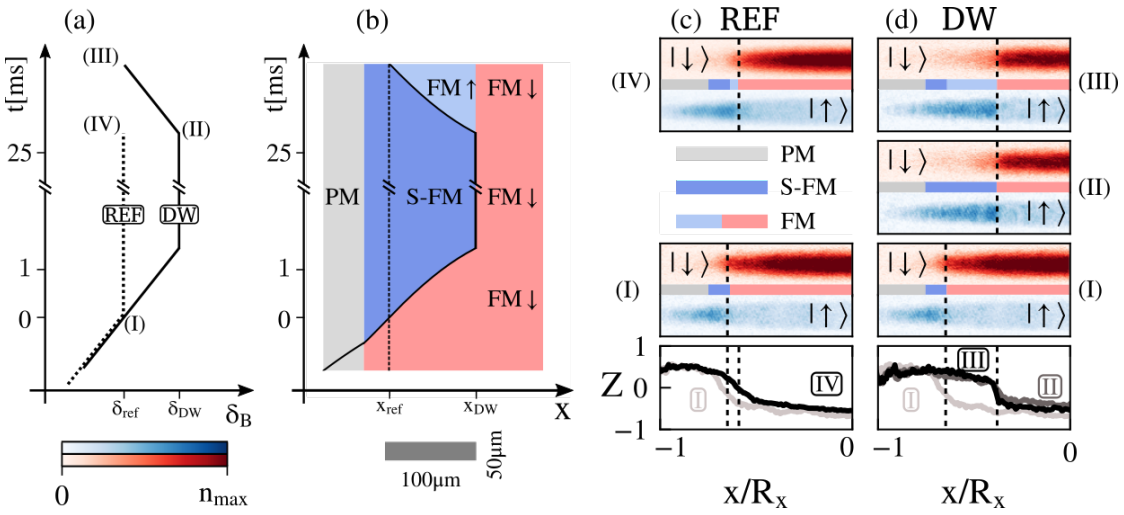

Figure 5.15: Deterministic creation of FM domain walls. (a) Experimental protocol used to create DWs through a ramp on δ_B. (b) Schematics of the spatial variation of the phase diagram as a result of the protocol shown in (a). Different regimes are labelled with the same color as in (c) and (d). (c) Absorption images of the two components (left half of the system only) at the initial point (I) and after a wait time of 25 ms (IV), when $\delta_B/2\pi = \delta_{\text{ref}}/2\pi = 1\,\text{kHz}$ [dashed line in panel (a)]. (d) Absorption images of the two components corresponding to the solid line ramp in panel (a), where δ_B reaches $\delta_{\text{DW}}/2\pi = 1.13\,\text{kHz}$ (II) and is then ramped back down to δ_{ref} (III). PM, S-FM and FM regions are illustrated in the line between the absorption images. The third (III) image in panel (d) shows the presence of a DW between two FM domains with opposite magnetization. In both panels (c) and (d) dashed lines marks the position at which $Z = 0$.

This protocol is illustrated in Fig. 5.15 (a), along with the time diagram in panel (b), showing the various magnetic phases and the position of the boundaries during the ramp of δ_B.

In the first step, the ramp in δ_B moves the boundaries of the FM region towards the center of the BEC, approximately following a curve in the (x, δ_B) plane given by the hysteresis curve $\delta_{hys}(x)/2$ summed to the Thomas-Fermi profile. The detuning δ_{DW} fixes the size of the FM region at the end of the ramp, and consequently, the position of the boundaries. During the 25 ms at fixed δ_B (step II), the position of the interface remains in first approximation stable in space. In the third step, ramping δ_B towards lower values enlarges again the FM region [see black line in panel (a)], leaving the interface in its position. We compare this protocol with a reference signal, obtained applying only steps (I) and (III) [line (IV) in panel (a)].

In Fig. 5.15 (c) and (d) we show the left half of the cloud from absorption images of the two states at each step, for the reference signal and the actual protocol respectively, gathered at $\Omega_R = 400\,\text{Hz}$. For each image, we represent the size of the different magnetic

phases as a colorbar. We first observe that, in the reference images [panel (c)], the position of the DW remains almost constant, with a slight shift toward the center, which could result both from relaxation dynamics after the ARP ramp or from shot-to-shot noise, for instance in the atomic density $|\kappa|n(x)$. On the other hand, we notice that applying our protocol [panel (d)], the interface moves towards the center of the BEC (in agreement with Fig. 5.5 data), in step II, and it remains in this position also after step III. As a result of lowering δ_B, the blue region, which previously was in the SFM regime, is now a FM domain, thus the $Z = 0$ has now become a domain wall.
We characterize the degree of tunability of the position of the DW gathering data for δ_{DW} ranging from 1 kHz to 1.16 kHz. The displacement of the DW with respect to the reference position x_{ref}, measured at $\delta_{ref} = 1$ kHz is shown in Fig. 5.16, as a function of δ_{DW}. We check the outcome of our protocol with numerical simulation of the 1D GPE, which shows a complete agreement, further corroborating the validity of the mean-field description. A deviation from the simulations starts at $(\delta_{DW} - \delta_{ref})/\Omega_R = 0.5$. Interestingly enough, this value is approximately equal to $n_0\Delta$, which sets the onset of the hysteresis region in the center of the condensate. We suspect that this deviation is linked to further relaxation dynamics [156, 157], triggered while entering the hysteresis region for $\delta_{DW} > n_0\Delta$.
Nevertheless, what stems out clearly is the smooth variation of the position of the DW as a function of the detuning. This demonstrates a great advantage with respect to condensed matter platforms, where usually DWs are pinned in space by some defects or

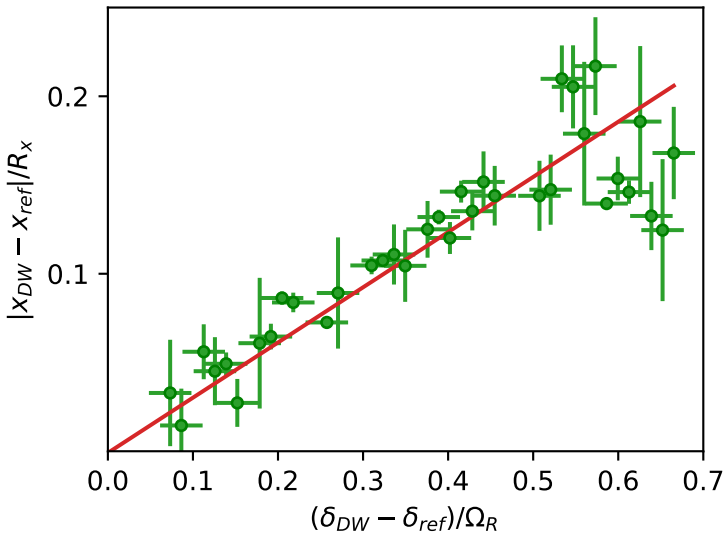

Figure 5.16: Continuous dependence of the position x_{DW} of the DW with respect to the initial interface position x_{ref} (in units of R_x) as a function of $(\delta_{\mathrm{DW}} - \delta_{\mathrm{ref}})/\ \Omega_{\mathrm{R}}$. The red line is extracted from numerical simulations. Error bars show the experimental uncertainties (horizontal axes) and the shot-to-shot standard deviation (vertical axes).

impurities in the material [174]. In a ferromagnetic BEC, such problems are overcome by the smoothness of the trapping potential and by the superfluid character of the system.

Chapter 6

False Vacuum Decay in ferromagnetic BECs

Contents

Metastability, originating from first order phase transitions, is ubiquitous in physical systems. A notable example is superheated or supercooled water, where the passage to the true gaseous or solid ground state occurs via bubble nucleation, when the surface tension of the bubble is compensated by the energy gain provided by the inner gas. In classical physics the decay occurs when the metastable state jumps over the energy barrier separating it from the ground state, and is driven by thermal fluctuations [175] or by the presence of impurities in the system, which act as nucleation seed.
The extension of this idea to quantum systems, in particular to quantum field theories, is a fascinating subject. It ranges from the understanding of the early universe [176, 177, 178] to the characterization of spin chains [156, 179, 180]. In a field theory, the first order phase transition originates from a field-dependent asymmetric double well potential, where the metastable minimum is identified as the *false vacuum*. In this case, it is the field itself that changes configuration, after a macroscopic tunneling through the barrier. The resulting configuration is a bubble of true vacuum, which expands in a sea of false vacuum. The key difference with classical decay lies in the dependence of the characteristic decay rate on the area of the energy barrier, rather than on its height.

In its purest form, the false vacuum decay process is driven by quantum vacuum fluctuations, as first studied by Coleman [181, 182]. However, as for example in the early universe, the tunneling is equally likely to be boosted by thermal fluctuations, and is called "finite temperature false vacuum decay" [183, 184].
Despite intense theoretical effort in the study of the tunneling process, its experimental observation in the framework of quantum field theories, such as the inflaton or Higgs field in the cosmological scenario, proved to be elusive so far, due to energy scales well above any experimental range.
Taking advantage of the degree of tunability of the control parameters in ultracold atomic platforms, several experiments have been proposed in order to address such fundamental questions [185, 186, 187, 188, 189, 190]. Many of these works [185, 186] proposed the use of coherently-coupled BEC to create a metastable stable in the relative phase between the two components, through a time modulation of the coupling strength. Another work [191] extended this proposals suggesting the use of additional coupling radiations to get rid of instabilities introduced by the time modulation.
Alongside the promising route opened by the previous proposals, we demonstrated in the previous Chapter that a first order phase transition spontaneously occurs in coherently-coupled BECs, provided that the ground state is a ferromagnetic one. Such a system naturally admits a field description, in terms of the magnetization $Z(x)$, and has an interaction-dependent energy functional similar to the one of a ϕ^4-theory. Our apparatus also offers the experimental capability to study the decay process, thanks to the spatial extension of the sample and, most importantly, to the high stability and accuracy of the tuning parameters.
In this Chapter I will describe the first experimental observation of finite temperature false vacuum decay via bubble nucleation. In the first Section I will give a tentative and concise summary of the instanton theory used to describe the tunneling process in quantum field theories. This section is written following the lines of the original works of Coleman [181, 182] and of the recent theoretical review [192]. In the second Section I will describe the experimental protocol and characterize relevant quantities related to the bubble nucleation process. Particular care will be given to the measurement of the characteristic decay time τ of the tunneling. In the last Section I will compare the dependence of the measured decay rates on the control parameters to the predictions of instanton theory. The results reported in this Chapter are available as a preprint in Ref. [157].

6.1 Theory of False Vacum Decay

The phenomenon of tunneling through a potential barrier is very well known in quantum mechanism. It states that, for example, if an electron beam with energy E scatters through a potential $U(x)$ greater than E, the beam has a finite probability of crossing the barrier. A similar process occurs for a quantum particle, with unitary mass $m = 1$, initially at rest in the metastable minima of a tilted double well potential, of the shape $U(x) = \lambda/a^2(x^2 - a^2)^2 + \varepsilon a x$, with $U(a) = U_0 > 0$. An example of this potential

is sketched in Fig. 6.1 (a). While in classical mechanism there is no possibility for

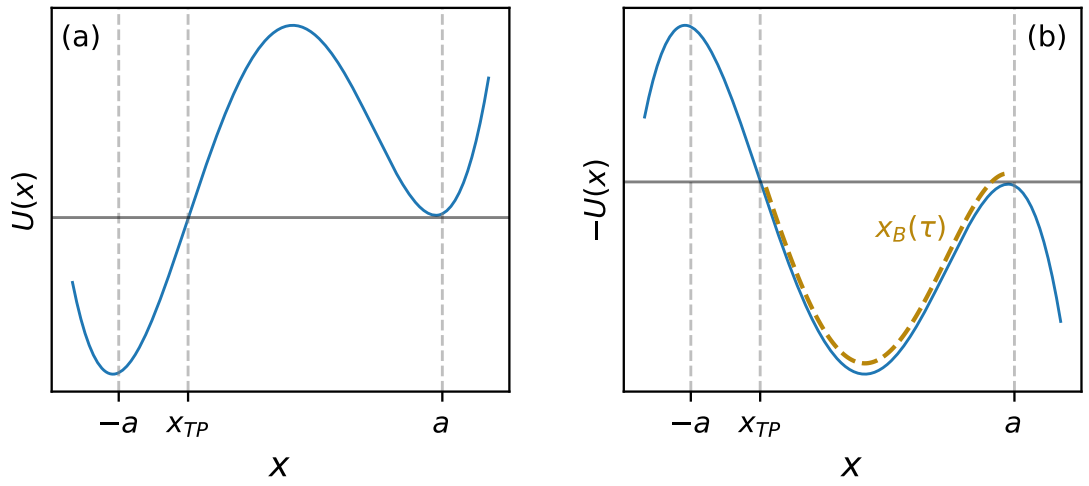

Figure 6.1: (a) Tilted double well potential $U(x)$, with a metastable minimum in $x = a$. (b) Same potential after change of sign. Gold curve is an indication of the bounce solution.

the system to exit the metastable minimum, in quantum mechanism there is a finite probability for this transition to occur, which is given by the matrix element:

$$P = \langle -a|e^{iHt/\hbar}|a\rangle \tag{6.1}$$

In QM, the width of this process, also called the characteristic decay rate, is given, in the semiclassical approximation, by [193]:

$$\Gamma = Ae^{-B}, \quad B = \frac{2}{\hbar}\int_{-a}^{a} dx\sqrt{2[U(x) - U_0]} \tag{6.2}$$

It is useful, for the later extension to a quantum field theory scenario, to show that this result can be equivalently derived within the Lagrangian formalism. The Lagrangian for a moving particle reads:

$$L = \frac{1}{2}\dot{x}^2 - U(x) \tag{6.3}$$

It is useful, and also a standard approach, to work in Euclidean time, $\tau = it$, where the Lagrangian reads:

$$L_E = -\frac{1}{2}\dot{x}^2 - U(x) \tag{6.4}$$

It is well known that the equation of motion associated to the Lagrangian can be derived from the stationary-action principle [194]. This is given by the Euler-Lagrange equation, which in Euclidean time reads

$$\frac{d^2x}{d\tau^2} = U'(x) \tag{6.5}$$

Solutions of this equation constitutes trajectories, in Euclidean time, for which the associated action

$$S_E = \int_{-\infty}^{\infty} d\tau L_E \tag{6.6}$$

is stationary. In a quantum field theory contest, we will refer to these solutions as *instantons* [195], which depend on the specific shape of the potential $U(x)$.
Let us seek solutions for the particular case of the titled double well potential. It is easier to look at Eq. 6.5 as describing the motion in real time of a particle, originally at $x = a$, moving in potential $-U(x)$, shown in Fig. 6.1 (b). It is evident that what was a minimum energy configuration is now an unstable equilibrium point. In this configuration, a small fluctuation can trigger the particle to roll down the potential, reaching the turning point x_{TP} at $\tau = 0$, with $U(x_{TP}) = U_0$, where its kinetic energy vanishes, and then coming back. For this reason, the particular solution $x_B(\tau)$ associated to this process was originally called *the bounce* by Coleman [181]. From energy conservation, or equivalently rearranging Eq. 6.5, we get

$$\frac{1}{2}\left(\frac{d\dot{x}}{dt}\right)^2 = U(x) - U_0 \tag{6.7}$$

from which it is now easy to see that

$$S[x_b] - S[x] = \int_{-\infty}^{\infty} d\tau L_E(\tau, x_b, \dot{x}_b) = 2\int_a^{x_{TP}} dx\sqrt{2[U(x) - U_0]} \tag{6.8}$$

arising from the assumption that the particle at $\tau \to -\infty$ is sit at $x = a$ and that it reaches the turning point x_{TP} at $\tau = 0$ with vanishing kinetic energy.
Remarkably, Eq. 6.8 is exactly the same expression we gave for $\hbar B$ in Eq. 6.2. Thus, the rate associated to the tunneling process is equally given by the Euclidean action, provided that it is evaluated on the instanton solution.

6.1.1 Tunneling in Quantum Field Theories

It is now straightforward to extend this formalism to the case of a one-dimensional scalar quantum field theory for a field ϕ, characterized by a scalar potential $U(\phi)$, which now depends on the field itself, with a local minimum ϕ_{FV} and a global minimum at ϕ_{TF}. An example of such a theory is the ϕ^4-theory, with a potential of the shape $U(\phi) = \lambda/a^2(\phi^2 - a^2)^2 + \varepsilon a\phi$. For a field theory, the bounce solution now satisfies the Euler-Lagrange equation in Euclidean time:

$$\left(\frac{\partial^2}{\partial\tau^2} + \frac{\partial}{\partial x^2}\right)\phi_b = U'(\phi_b) \tag{6.9}$$

and the exponent B is given by

$$B = \frac{S_E[\phi_b] - S_E[\phi_{FV}]}{\hbar} \tag{6.10}$$

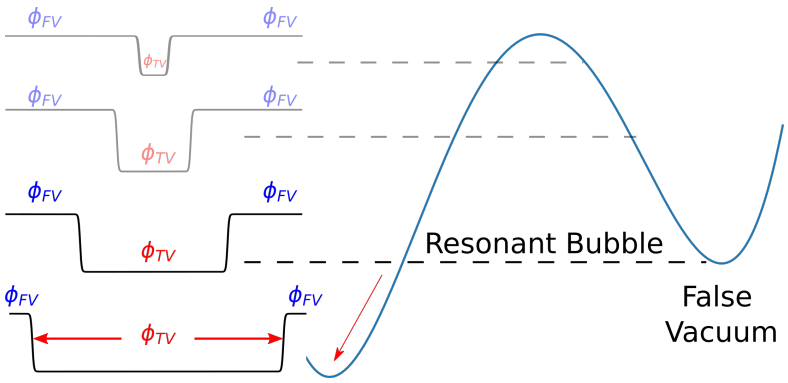

Figure 6.2: Sketch of the false vacuum decay process in the 1+1 ϕ^4-theory. Quantum fluctuations trigger the formation of "virtual" bubbles (on the left), until the energy cost balances the formation of the interfaces. After creation, the bubble expands rapidly in space.

where the action is defined as

$$S_E = \int d\tau dx \left[\frac{1}{2} \left(\frac{\partial \phi}{\partial \tau} \right)^2 + \frac{1}{2} \left(\frac{\partial \phi}{\partial x} \right)^2 + U(\phi) \right] \tag{6.11}$$

Finally evaluating of the action at ϕ_b gives the decay rate as

$$\Gamma = A e^{-(S_E[\phi_B] - S_E[\phi_{FV}])/\hbar} \tag{6.12}$$

There is a small caveat that must be taken into account when dealing with the quantum field treatment of the decay process. Unlikely in quantum mechanism, it is now the field ϕ that, somewhere in space, at $\tau = 0$ tunnels through the potential barrier, from which it evolves classically. While doing so, it passes from a homogeneous configuration in space to a space-dependent configuration, which in three dimensions has the shape of a bubble [181, 196] of true vacuum.
As we said previously, the particular shape of the instanton solution ϕ_b depends on the dimensionality and the shape of the potential $U(\phi)$, and it is usually hard to find analytically. In the case of the 1+1 ϕ^4-theory with the potential $U(\phi)$ given above, in the limit $\varepsilon \to 0$ (*thin wall approximation*) the instanton has the form of a kink-antikink pair [197]. The solution can been found if one looks for static configuration in Eq. 6.9, and has the shape:

$$\phi_B(x) = \tanh(x - b) - \tanh(x + b) \tag{6.13}$$

with b some point in space that locates the boundaries of the 1D bubble.
We immediately see an important point: the bounce solution has a non-vanishing spatial derivative, that introduces a positive energy cost in the evaluation of the action 6.11, that must be taken into account in the bubble nucleation process.
Intuitively, one can understand this contribution in the following manner: quantum

fluctuations will make a bubble appear somewhere in space, but the bubble will be reabsorbed if the energy gain provided by the inner true vacuum region is not enough to compensate for the formation of the bubble walls, which separates the two vacua.
This imposes a strict requirement for the bubble dimension, as for very small imbalance between the two minima (or very high energy barrier), a vast region of space has to turn into ϕ_{TV}, as intended to be shown in Fig. 6.2, making the process very unlikely to occur.

Extension to finite temperature cases The theory developed so far deals with the decay process of a quantum field at $T = 0$. There is however much interest in the study of temperature dependent field theories, developed, for instance, in the study of phase transitions in cosmology [184, 198].
The extension of the theory to the finite temperature case was developed shortly after the work of Coleman by Linde [199, 200, 183]. In its series of papers, he showed that temperature can be taken into account substituting the Euclidean time τ with a "time" given by $\beta = 1/k_B T$.
Considering the previous 1+1 ϕ^4-theory, the action reduces to $S_E = \beta S_1$, where S_1 is simply given by

$$S_1 = \int dx \left[\frac{1}{2} \left(\frac{\partial \phi}{\partial x} \right)^2 + U(\phi) \right] \tag{6.14}$$

and the decay rate takes the value

$$\Gamma = A \left(\beta S_1 \right)^{\frac{1}{2}} e^{-\beta S_1} \tag{6.15}$$

Remarkably, this expression is very similar to a rate equation in the thermodynamic theory of boiling [183], where the transition probability is mediated by the term $\exp\{-\beta \Delta F\}$, with F the free energy. Indeed, it is easy to identify the action S_1 with the free energy of this process, as it contains a "volume" energy U and a surface tension $(\partial_x \phi)^2$. As such, the extension of the false vacuum decay to finite temperature allows to take into account on the same ground bubble nucleation due to both quantum fluctuations and thermal fluctuations.

6.1.2 Model of FVD in ferromagnetic BECs

False vacuum decay originates from the concept of metastability, which is intrinsic of every first order transition. In coherently-coupled BECs, a first order phase transition originates in the spin channel when the system is ferromagnetic, i.e. when $|\kappa| n > \Omega_R$, with $\kappa < 0$, following a variation of the longitudinal field at fixed $|\kappa| n / \Omega_R$. Magnetic properties of this system have already been discussed in great detail in Chapter.5. Here, however, we have to focus on additional terms that we have left aside in the characterization of the QPT. In particular, as already stated, the formation of a resonant bubble is a dynamical process, that carries extra energy with respect to the LDA approximation used in Chapter 5. To take this into account, we have to consider the space-dependent

full energy functional, which reads:

$$E = \int \frac{n}{2} \left\{ \frac{\hbar^2}{4m} \left[\frac{(\nabla Z)^2}{1-Z^2} + (1-Z^2)(\nabla\phi)^2 \right] + \frac{\kappa n}{2} Z^2 - \delta_{\text{eff}} Z - \Omega_R \sqrt{1-Z^2} \cos\phi \right\} dx \tag{6.16}$$

where, with respect to Eq. 5.6, we have included also contributions from the gradient of both phase and magnetization. We have assumed that the density profile varies smoothly in space, on a length scale much larger than ξ_d, and that there is no background flow (total phase is constant in space). At last, we already made the usual substitution $\delta g \to \kappa$, to average the transverse inhomogeneity of the experimental sample. As already seen before, the decay rate for thermally activated bubbles is given by [184]:

$$\Gamma = \frac{1}{\tau} = A \left(\frac{E_c}{k_B T} \right)^{1/2} e^{-\frac{E_c}{k_B T}} \tag{6.17}$$

where A is a prefactor, and we identified the action S_1, previously defined, with the (free) energy of the system E_c. The prefactor exponent 1/2 takes into account the number of translation symmetries of the field Z, which is 1 for spin 1D dynamics. The energy E_c is calculated as the energy gain of the field with respect to the value of the potential in the false vacuum Z_{FV} as

$$E_c = \int \frac{n}{2} \left[\frac{\hbar^2}{4m} \frac{(\nabla Z)^2}{1-Z^2} + \hbar[V(Z) - V(Z_{FV})] \right] dx \tag{6.18}$$

where we approximated the relative phase to be constant and null in space. In order for a bubble to form, the energy gain of the true vacuum region inside the bubble must be enough to compensate the formation of a highly energetic interface. In our case the interface is a magnetic domain wall, separating the external false vacuum from the internal true vacuum region. This makes clear why we had also to include the kinetic energy term inside the energy functional 6.16.
For convenience we rescale the energy barrier as $\hat{E}_c = E_c/(\hbar n_0^2 \xi_s |\kappa|)$, where n_0 is the integrated peak density, and $\xi_s = \hbar/\sqrt{m|\kappa|n}$. The resonant condition for bubble nucleation can be found by solving the Euler-Lagrange equation of motion in imaginary time for the field $Z(x)$, i.e. in the inverted potential, that reads

$$\frac{1}{2} \frac{(\nabla Z)^2}{1-Z^2} = V(Z) - V(Z_{FV}) \tag{6.19}$$

whose analytical solution gives the shape of the bubble, which should be a somehow complicated form of the usual kink-antikink solution.
It is useful to rearrange Eq. 6.19 to extract the differential dx

$$\frac{dZ}{dx} = \left[\frac{2(V - V_{FV})}{\kappa n} \right]^{1/2} (1-Z^2)^{1/2} \tag{6.20}$$

which we can invert to write

$$\hat{E}_c = \frac{1}{4} 2 \int_{Z_{TP}}^{Z_{Z_{FV}}} \left[\frac{2(V - V_{FV})}{|\kappa| n} \right]^{1/2} \frac{dZ}{\sqrt{1-Z^2}} \tag{6.21}$$

where Z_{TP} is the classical turning point in the inverted potential, and the factor 2 in front of the integral takes into account the bounce of the instanton [181]. Here we have relied on the assumption that the magnetization is only x-dependent. The analytical calculation of the previous integral is still tricky, but it can be simplified by considering the *small-barrier limit* [183]. In this approximation, the potential can be expanded to cubic order around an inflection point at Z_c and $\delta_{\text{eff}} = \delta_c$, where:

$$\delta_c = \kappa n(1 - Z_c^3), \quad Z_c = \left(1 - \frac{\Omega_R}{|\kappa| n_0}\right)^{1/2} \tag{6.22}$$

In this case, the energy barrier 6.21 can be calculated exactly, leading to the expression:

$$\hat{E}_c \sim 1.77 \left(\frac{\delta_B - \delta_c}{|\kappa| n_0}\right)^{5/4} \left(\frac{\Omega_R}{|\kappa| n_0}\right)^{1/6} \left(\frac{|\delta_c|}{|\kappa| n_0}\right)^{-1/4} \tag{6.23}$$

We will use this last expression later to compare experimental data with instanton theory.

6.2 Experimental observation of Bubble nucleation

This experiment is the natural extension of the study conducted in Chapter 5, focusing on the characterization of the system dynamics instead of its ground state properties. The basic idea to study the false vacuum decay problem is to prepare a homogeneous field $Z(x)$ located in the metastable stable state of its potential $V(Z)$. We can easily identify this configuration in the x-dependent representation of the magnetic phase diagram of Fig. 5.1, if the system is initialized in the $|\uparrow\rangle$ state. This is shown again, for clarity, in Fig. 6.3 (b). Indeed, a careful look at the energy profiles shows that, for $\delta_B < n_0\Delta$, the magnetization enters a region, which we identified in the previous Chapter as the hysteresis region, where the magnetization is homogeneously in state $|\uparrow\rangle$, but the system is metastable. Due to the Z_2 symmetry breaking term $n\Delta$, the system is not invariant upon a change of initial state, and is not possible to create a metastable state with homogeneous magnetization starting with all atoms in $|\downarrow\rangle$.

Protocol As we did in Chapter 5, we prepare cigar-shaped condensates with $N = 1\times10^6$ atoms and density $n = 7\times10^{14}\,\text{atoms/cm}^3$ in $|1,-1\rangle = |\downarrow\rangle$ trapped in an harmonic potential with frequencies $\omega_x/2\pi = 20\,\text{Hz}$ and $\omega_\perp/2\pi = 2\,\text{kHz}$. The corresponding Thomas-Fermi radii are $R_x = 200\,\mu\text{m}$ and $R_\perp = 2\,\mu\text{m}$, with peak chemical potential $\kappa n_0/2\pi \approx n_0\Delta/2\pi = -1100\,\text{Hz}$. As before, the condensed fraction and single component temperature are $N_0/N = 30\%$ and $T = 1\,\mu\text{K}$ respectively, thus for all data shown in this Chapter we will subtract the thermal distribution, using the same routine developed in Chapter 5.
The internal state of the system is initialized transferring all the atoms in the state $|2,-2\rangle = |\uparrow\rangle$ with a resonant π-pulse, with $\Omega_R/2\pi = 25\,\text{kHz}$.
We then coherently couple the states $|\uparrow\rangle$ and $|\downarrow\rangle$ with an external radiation, with initial detuning $\delta_i/2\pi = 5.5\,\text{kHz}$ and strength $\Omega_R < |\kappa| n_0$, so that the center of the cloud is

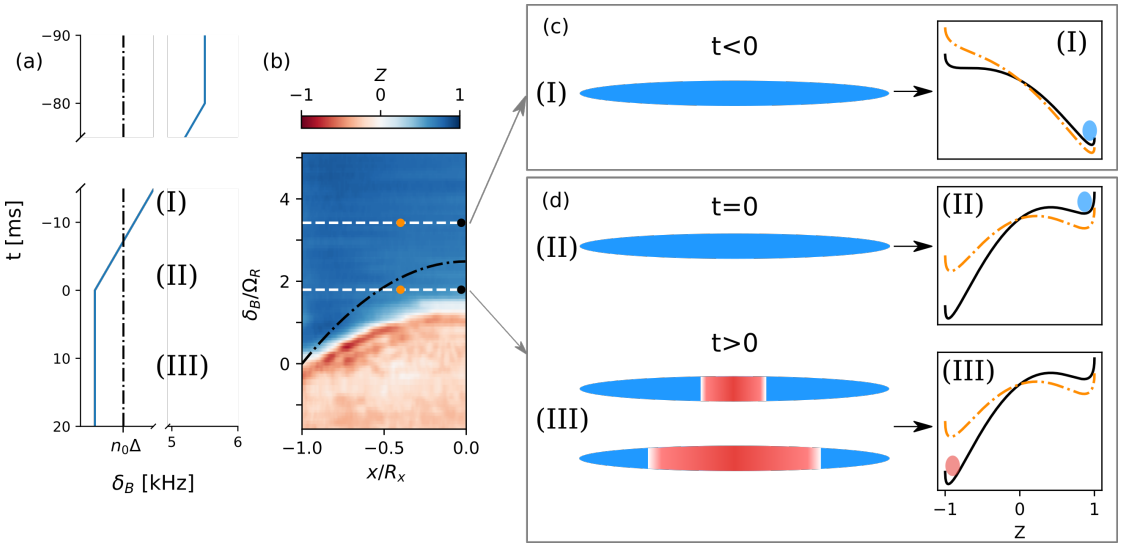

Figure 6.3: Experimental protocol. (a) Adiabatic ramp in detuning δ_B. (b) Magnetization profile $Z(x)$ as a function of detuning at $t = 0$. Dash-dot line labels the upper bound of the hysteresis region, $\delta_B = n_0\Delta$. White lines indicate values of δ where the energy at $x = 0$ has a double well profile. (c) Representation of the expected shape of the cloud at two different values of δ. Corresponding energy profiles are shown on the right at $x = 0$ (black) and $x = -0.4/R_x$ (orange).

ferromagnetic (see Chapter 5). The detuning is then adiabatically reduced to a final value δ_B with a linear ramp of slope $\partial_t\delta_B(t) = 50\,\mathrm{Hz/ms}$ [see Fig. 6.3 (a) and corresponding magnetization $Z(x)$ for different values of δ_B in (b)]. We use a slower ramp as compared to the one used in Chapter 5 as it is now important to keep the system as close as possible to its own ground state, to avoid a boost of the tunneling process induced by oscillations of the field around the stationary state. As the magnetization is almost uniform in $Z \sim 1$ during the ramp, decoherence is not boosted by the presence of an interface, thus the only limitation in the measurement are atom losses. The latter do not play a major role in the spin channel, if not for a small change in the position of the critical point, see Eq. 5.16.

We stop the ramp at various values of δ_B, and we gather separate absorption images of the two states after a variable time t from the end of the ramp.

For $\delta_B > n_0\Delta$ [phase (I)], the system is and remains in the absolute ground state of the energy profile, see panel (I) on the right of Fig. 6.3. Further decreasing δ_B below $n_0\Delta$ [phase (II)] the system enters the metastable region with a homogeneous magnetization. After a long enough time $t > 0$, a macroscopic region in the center of the cloud flips to $|{\downarrow}\rangle$, generating a bubble [phase (III)]. Finally, for small enough δ_B, bearing in mind the results of Chapter 5, the metastable state disappears and the system will be in $|{\downarrow}\rangle$ even at $t = 0$, see panel (b) of Fig. 6.3. We label this value of δ_B as *critical detuning* δ_c, which marks the end of the hysteresis region.

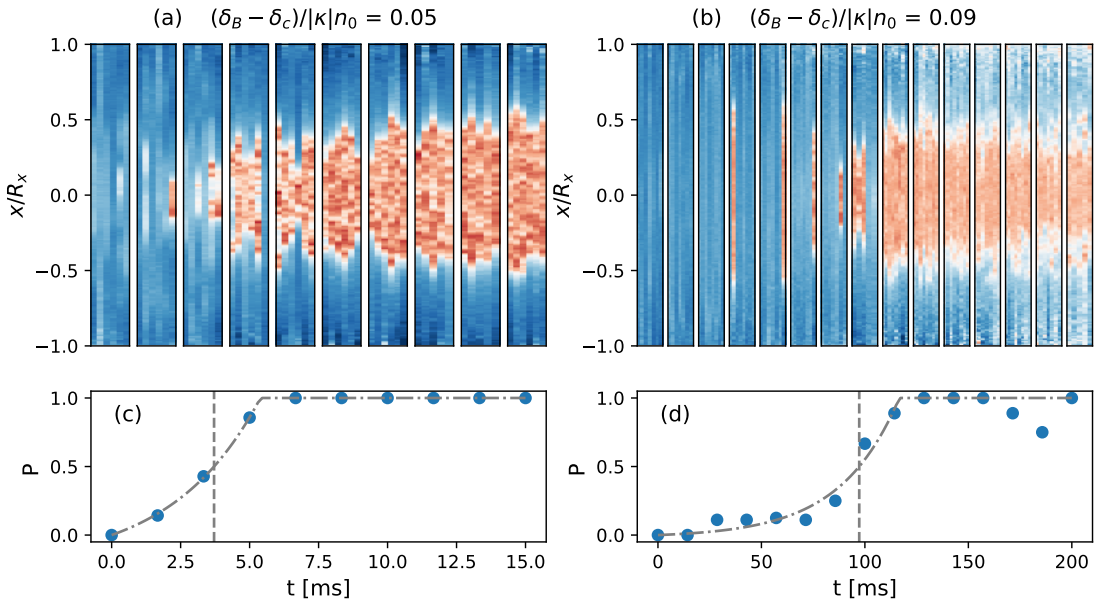

Figure 6.4: (a-b) Collection of integrated magnetization profiles $Z(x)$ after different waiting times t. For each value of t, different realizations are shown. (c-d) Measured probability P (blue circles) to observe a shot with a bubble at fixed time is shown. The probability is well fitted to an exponential curve (grey continuous line) until it saturates to 1. Data gathered at $\Omega_R = 400\,\mathrm{Hz}$.

From 2D absorption images of the two states we reconstruct the 1D magnetization $Z(x)$ after having removed the thermal part. As the process of bubble nucleation is stochastic, being driven by quantum or thermal fluctuations, for each value of t we gather up to 10 shots. Two typical dataset are shown in Fig. 6.4, for two different values of δ_B at $\Omega_R/2\pi = 400\,\mathrm{Hz}$, where shots gathered at same t are grouped in the same windows.

Results After some variable time t, which depends on the detuning δ_B, we observe that a macroscopic fraction of the system flips towards the opposite state $|\downarrow\rangle$. We identify this event with the formation of a bubble. We observe that, within the same time t and detuning δ_B, the occurrence probability of bubble formation grows in time, and eventually, at $t \to \infty$, a bubble is always present.
We observe that, on average, bubbles tend to form near the center of the trap. This results from the combination of both the terms κn_0 and $n_0\Delta$, which makes, at fixed δ_B, the energy barrier $\hat{E}_c$ smaller in the center than towards the tails (see energy profiles in Fig. 6.3), thus favouring the tunneling process. We take advantage of this effect to quantify the bubble occurrence probability P [see panel (c) and (d) of Fig. 6.4] as the number of shots in which a 40% of the atoms has changed state at the same time t. This corresponds to $\langle Z \rangle < 0.2$, where $\langle Z \rangle$ is a spatial average in a 40 pixel wide region around the center. We observe that our measurement of P well captures the behaviour shown

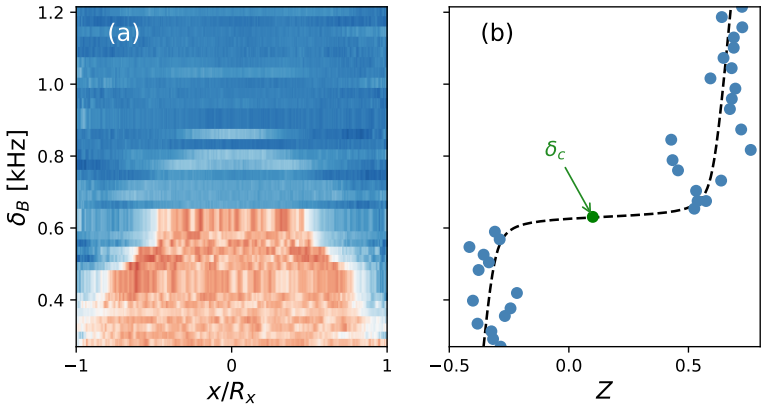

Figure 6.5: Determination of δ_c from the hysteresis end. (a) Integrated profile of the magnetization $Z(x)$ for different detuning δ and no waiting time. (b) The change of sign of the magnetization $Z(x)$ averaged on the central 40 pixels allows to determine $\delta_c = 630(20)\,\mathrm{Hz}$. This calibration is used for a subset of data shown in the main text for $\Omega_R/2\pi = 400\,\mathrm{Hz}$.

by raw data, with P growing at early times, eventually saturating to 1 when bubbles are always visible.
At last, we also observe that, on average, the size of the bubble grows in time, eventually reaching a final dimension σ_f. This is a well known behaviour in the false vacuum decay, resulting from the relaxation towards the global ground state of the system.

Calibration of critical detuning The expected high sensitivity of τ on a small variation of $\delta_B - \delta_c$ requires a very precise calibration of the critical detuning. We first calibrate the resonant condition of the coupling radiation with the spectroscopic protocol described in Section 2.5.1. Once this is known, we initialize the system in $|\uparrow\rangle$ and follow the protocol described above, gathering absorption images at $t = 0$ for different values of δ_B. Data for the magnetization $Z(x)$ are shown in Fig. 6.5 (a) as a function of the absolute value of detuning. In the same spirit of the measurement of the hysteresis width δ_{hys} presented in Chapter 5, we fit $Z(x)$, averaged over the central 40 pixels, with a sigmoidal function (see Section 5.3.2 for more details). For this particular dataset, we find a value of $\delta_c/2\pi = 630(20)\,\mathrm{Hz}$ see Fig. 6.5 (b).
Due to the large amount of statistics required to obtain one value of τ, a typical measurement lasts one to three hours. Unfortunately, the measurement of the stability of the magnetic field in time reported in Section 2.5.2 shows that drifts and shot-to-shot fluctuations are not neglectable in this time interval. To overcome this issue and achieve the high stability required to fine tune $\delta_B - \delta_c$ within, for example, a 100 Hz interval, we calibrated both the resonance condition and the detuning δ_c several times during each experimental run. This allow us to either correct experimental parameters during the data acquisition campaign, or to take into account magnetic field drifts during data

post-analysis.

6.2.1 Measurement of characteristic decay time

In the study of the false vacuum decay, the relevant quantity to extract is the characteristic decay rate Γ, and its dependence on the area of the barrier separating the two vacua. From all our dataset, we measure $\tau = 1/\Gamma$ with two different methods, that lead to very similar results.

Determination of $\tau_{50\%}$ from occurrence probability P The first method relies on the measurement of the previously defined occurrence probability P. We define the characteristic timescale $\tau_{50\%}$ as the time at which the probability to observe a bubble is 50%. We identify $\tau_{50\%}$ by first fitting P as a function of time

$$P(t) = \text{Min}\left[a_1\left(e^{\frac{t}{a_2}} - 1\right), 1\right] \tag{6.24}$$

with a_1, a_2 are fitting parameters. Examples of such fits are shown as grey dash-dot lines in panels (c) and (d) of Fig. 6.4. From Eq. 6.24, we then extract the characteristic timescale, shown as a vertical grey line in the two panels, as:

$$\tau_{50\%} = a_2 \ln\left(1 + \frac{1}{2a_1}\right) \tag{6.25}$$

This method is a valid measurement for dataset with limited number of statistics.

Determination of τ from false vacuum fraction An useful quantity to extract the characteristic decay time τ is the so called *false vacuum fraction*, which we define as

$$F_t = \frac{1}{2}\left(1 + \frac{\langle Z\rangle_t}{\langle Z\rangle_{t=0}}\right) \tag{6.26}$$

in analogy with the definition given in [156], used to compare an exact diagonalization approach in a zero-temperature spin chain to instanton predictions. We observe that, within this definition, F_t has unit value for $t = 0$ and eventually tends to 0 for $t \to \infty$, if a fraction of the system has changed state. We use $\langle Z\rangle_t$ to specify the average, over many experimental realizations, of the magnetization measured at time t. Thus, Eq. 6.26 quantifies the fraction of the system which is still in the false vacuum state after a time t.

Two examples of the average magnetization $\langle Z\rangle_t$ are shown in Fig. 6.6 (a) and (b), as a function of time, for two different values of detuning. It is evident that Z changes smoothly value in time, as compared with the raw data shown in Fig. 6.4 (a) and (b). Since bubbles seems to appear more likely in the center, as it is evident also from the position of the white region at early times, we evaluate F_t only in the central 20-μm-wide region the cloud.

The measured F_t, shown in Fig. 6.6 (c), shows a flat plateau at early times, while

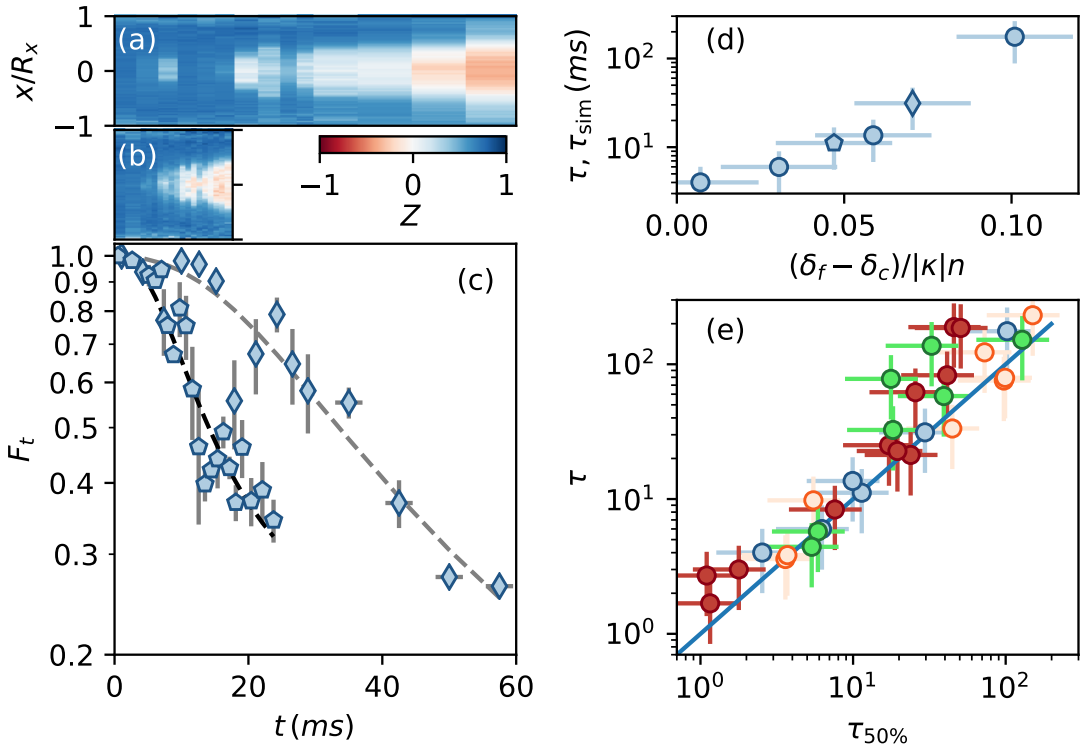

Figure 6.6: Measurement of the time evolution of $Z(x)$ after the ramp on δ for $\Omega_R/2\pi = 300\,\text{Hz}$ for $\delta_B/\Omega_R = 2.13$ in (a) and 2.04 in (b). (c) Values of F_t evaluated in the $20\,\mu\text{m}$ central region of the cloud are fitted by the empirical expression reported in the text [diamonds for data in (a) and pentagons for (b)]. (d) Experimental timescale τ of the bubble formation as a function of $(\delta_B - \delta_c)/|\kappa|n_0$. Error bars include statistical uncertainties on the fit and uncertainty on $(\delta_B - \delta_c)$ coming from magnetic field stability and calibration. (e) Comparison between τ and $\tau_{50\%}$, which shows a full agreement within experimental errorbars. Different colors label different Ω_R.

it decays exponentially due to bubble nucleation for $t \to \infty$, in agreement with the findings of [156]. We extract quantitative information fitting the experimental data with an empirical function of the form

$$F_{t,fit} = \frac{1-\varepsilon}{\sqrt{1+\left(e^{t/\tau}-1\right)^2}} + \varepsilon \tag{6.27}$$

which is 1 for $t = 0$, decreases as t^2 for $t \ll \tau$ and decays exponentially to ε for $t \to \infty$, capturing the expected behaviours for F_t in all regimes. The fitting parameters are τ, which we identify as the characteristic time it takes for the FV to decay, and ε, which we included to take into account the observed finite magnetization $\langle Z \rangle_\infty \neq -1$ at long times. Example of these fits are shown in Fig. 6.6 (c)

This formula proved to be highly robust against the initialization of the fitting parameters, and provides a precise determination of τ that can be compared with theoretical values. However, the use of only a fitting parameter τ considers at the same level both the slope of the exponential decay and the initial plateau, whose duration can be in principle different, and its origin is still an open theoretical question.
The results for 6 values of τ are shown in Fig. 6.6 (d), measured at $\Omega_R/2\pi = 300\,\mathrm{Hz}$, and plotted as a function of the distance from the critical detuning $(\delta_B - \delta_c)/|\kappa|n_0$. Data show an exponential growth of τ, from a few to a hundred of ms, as a response to a very small variation of the tuning parameter. Since moving away from the critical detuning increases the energy barrier, see Eq. 6.23, the observed growth in the characteristic decay time is in qualitative agreement with theoretical expectations.
In Fig. 6.6 (e) we check the consistency between the two methods, comparing the values of $\tau_{50\%}$ and τ measured for all our dataset. Independently of Ω_R and δ_B, we observe an excellent correlation between the two methods, with a Pearson correlation coefficient of 0.82, proving the robustness of our methods to extract τ.

6.2.2 Bubbles Properties

From the data we gathered, it is also possible to extract spatial information of the bubble, like the minimum observable size, the position of the nucleation event and the expansion the bubble in space. To obtain such quantities, we first need to precisely identify the boundaries of the bubble.
For each shot, if a bubble is counted (see previous explanation), we fit the magnetization profile $Z(x)$ with a double sigmoidal function of the shape

$$Z_{fit}(x) = A\left[\arctan\left(\frac{x - x_r}{s_r}\right) - \arctan\left(\frac{x - x_l}{s_l}\right)\right] \tag{6.28}$$

where A is the amplitude and $x_{r(l)}$ and $s_{r(l)}$ are the right (left) centers and sigmas of the sigmoids respectively. Two typical magnetization profiles, for bubbles of different sizes, are shown in Fig. 6.7 (a) and (b). We then use the fitted parameters as initial values for a second fit, that analyses independently the right and left side of $Z(x)$. This second step allows us to measure with high precision the right and left position x_r and x_l of the domains of the bubble. We use them to define the position $\bar{x}_B$ and the width σ_B of each bubble as

$$\bar{x}_B = \frac{x_r + x_l}{2}, \qquad \sigma_B = x_r - x_l \tag{6.29}$$

The definition of $\bar{x}_B$ relies on the assumption that bubbles expand isotropically in x, which is typically assumed to be true in many theoretical models [196].

Bubble Growth A relevant quantity to measure is the expansion dynamics of the bubble after its nucleation [201, 202], as it would shed light, for example, on the study of confinement dynamics [203]. Unfortunately, a precise tracking of a single bubble is not possible within the current experimental apparatus, as it would require a spin-selective [84, 204] non-destructive imaging system [205]. We can, however, follow the averaged

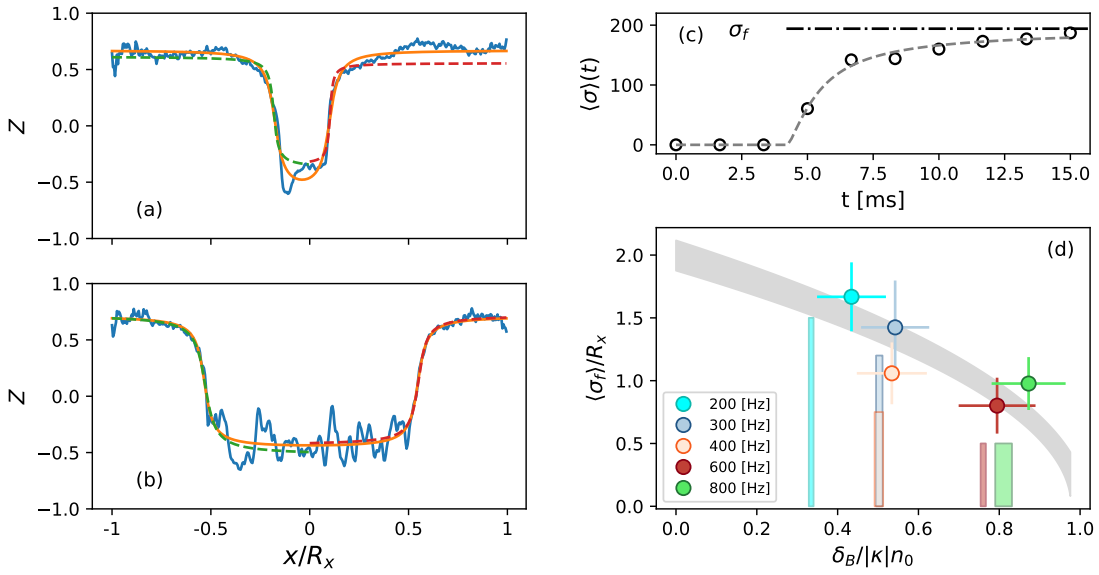

Figure 6.7: (a-b) Magnetization profiles of a typical experimental shot showing the appearance of a bubble. After a first global fit (orange line), two independent fits are performed at the two interfaces (left green and right red). (c) Statistical width σ_B of the bubbles. Dashed grey line show the sigmoidal fit used to extract the asymptotic value σ_f, shown as an horizontal black line. (d) Size of the bubble in the stationary state at $t \gg \tau$. The points of different colour label different Ω_R, and they are in good agreement with the size expected from the numerical model (shaded area). Vertical rectangles show the position of δ_c for each dataset, where the width is given by the uncertainty in the calibration.

size $\langle\sigma_B\rangle$ after a variable time t from the nucleation event, and measure with reasonable accuracy its asymptotic value σ_f.
To calculate it, we first measure $\langle\sigma_B\rangle_t$ by averaging σ_B for shots at equal time, setting $\langle\sigma_B\rangle = 0$ if bubbles are not present. We then fit $\langle\sigma_B\rangle(t)$ with an empirical function of shape

$$\langle\sigma\rangle(t) = \sigma_f \mathrm{Max}\left[0, \arctan\left(\frac{t - t_0}{\tau_\sigma}\right)\right] \tag{6.30}$$

where t_0, τ_σ and σ_f are fitting parameters. An example of this procedure is shown in Fig. 6.7 (c). The resulting values of σ_f are then averaged within the dataset at constant Ω_R to obtain the values shown in Fig. 6.7 (d). As bubbles originate in the ferromagnetic region, its extension bounds σ_f, as intended to be shown with the grey region. For increasing Ω_R, we notice that σ_f gets smaller, as the ferromagnetic region occupies a small fraction of the sample, eventually vanishing for $\delta_B = |\kappa|n_0$.

Bubbles nucleation position and size As an attempt to track the nucleation position of the bubbles, we plot in the histogram Fig. 6.8 (a) the values for $\bar{x}_B$, measured on

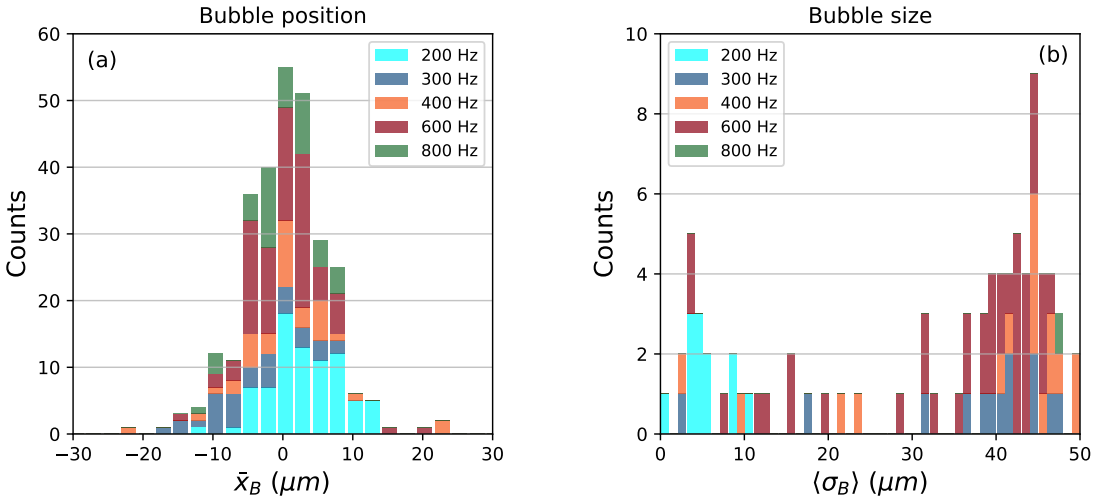

Figure 6.8: (a) Histogram of the initial position of bubbles with size less then 50 μm. (b) Histogram of bubble size σ_B. Different colors label dataset at different Ω_R.

a subset of the data where $\sigma_B < 50\,\mu$m, to take into account only small bubbles. Results show that the initial position of the bubble, independently of Ω_R, follows a Gaussian distribution, centered in the middle of the cloud. This comes with no surprise, as the energy profile strongly favours the tunneling rate in the center of the cloud.
In Fig. 6.8 (b) we instead show the size of the smallest bubbles observed during our data campaign, keeping into account only the ones with $\sigma_B < 50\,\mu$m, for consistency with panel (a). We observe in a very limited number of shots the formation of bubbles whose size is about 2-3 μm, suggesting that the initial size of the bubbles could be much lower than the imaging resolution. In fact, theoretical calculations on a uniform system [155], based on the evaluation of Eq. 6.19 for a typical kink-antikink shape of the bubble, show that the smallest bubble has a size of approximately 0.3 μm.
Comparing the two histograms, we observe that a non-neglectable fraction of the bubbles contributing to the histogram of panel (a) has a size much smaller than the full width of the Gaussian distribution. This observation, along with the theoretical prediction of the nucleation size, proofs that the histogram shown in panel (a) is a measurement of the randomness of the nucleation point of each bubble, and is not just shot-to-shot noise.
This suggest that the location of the nucleation site in the center of the cloud has not to be confused with the existence of a seeding mechanism, as the one proposed in [187], where it was shown that the presence of topological defects can pin the nucleation site and enhance the tunneling rate. In our system, the smoothness of the trapping potential and the homogeneity of Z in space prevent the existing of such a seeding process.

6.3 Dependence of decay rate on control parameters

It is instructive to compare the characteristic decay time τ with the prediction based on the instanton theory, see Section 6.1.2, to confirm the false vacuum decay interpretation of the observed macroscopic tunneling.
For each Ω_R, we measure values of τ at different δ_B with the procedure described in Section 6.2.1. Results are shown in Fig. 6.9, plotted as a function of the distance from the critical point $(\delta_B - \delta_c)/|\kappa n|$. Instanton theory can then be adjusted to our experimental data with a two-parameter fit of equation 6.17, i.e.

$$\ln \tau = -\ln A + b\hat{E}_c - \frac{1}{2}\ln b\hat{E}_c \tag{6.31}$$

with A and $b = n_0\xi_s(\hbar|\kappa|n_0/k_BT)$ as fitting parameters. For each of the four dataset, $\hat{E}_c$, given by formula 6.23, is independently calculated from the known experimental parameters. Results of the fit are shown in Fig. 6.9 as dashed lines, and reported in Table 6.1. We observe that, for every dataset, instanton theory, although being derived

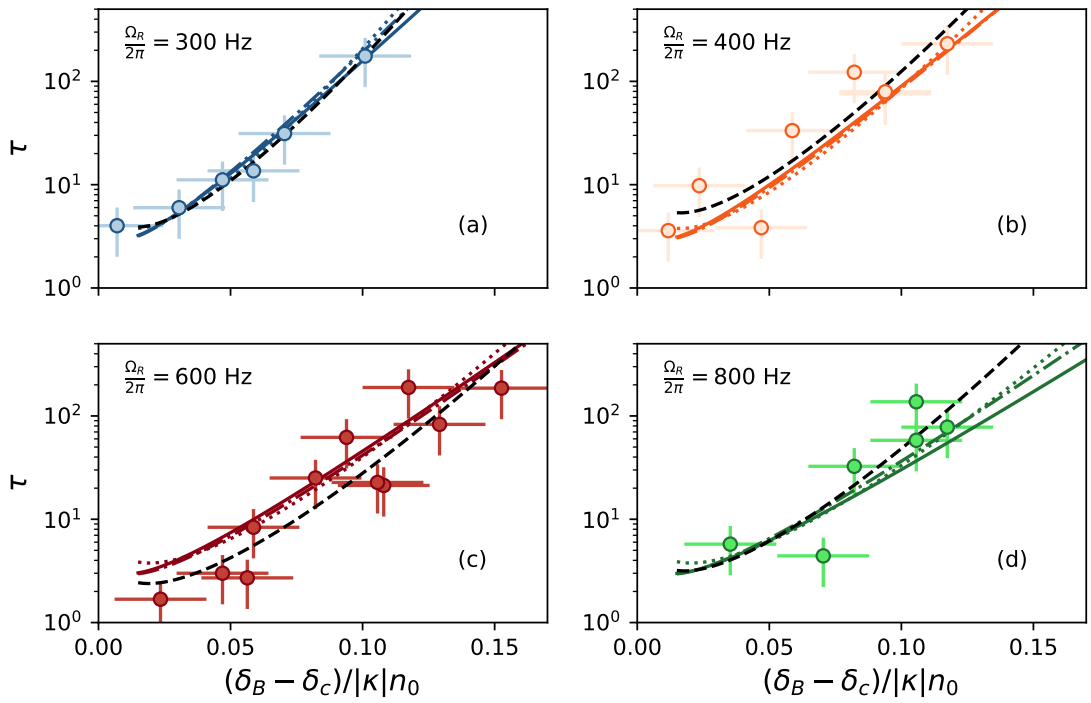

Figure 6.9: Decay time τ and instanton theory. Values of τ are obtained as explained in the text for $\Omega_R/2\pi$ = 300, 400, 600, and 800 Hz. Black dashed curves are fits of the experimental data according to the instanton formula. Dotted lines refers instead to $\hat{E}_c^{(1)}$, dash-dot ones to $\hat{E}_c^{(2)}$, and solid ones to $\hat{E}_c^{(3)}$. Error bars include statistical uncertainties on the fit and uncertainty on the δ_B due to the uncertainty on the magnetic field stability.

in the small barrier approximation with the strong assumptions of a one-dimensional uniform system, well fits experimental data.

$\Omega_R/2\pi$	$A_{\rm exp}(\sigma_A)$	$b_{\rm exp}(\sigma_b)$
300	1.8(0.1)	56.5(1.9)
400	1.54(0.3)	44.4(6.1)
600	3(1)	30.3(3.7)
800	2(1)	25.8(5.7)

Table 6.1: Fitting coefficients for the thermal instanton model of vacuum decay. The fit is limited to $(\delta_B - \delta_{\rm c})/\Omega_R > 0.05$ to ensure that $b\hat{E}_c > 1$.

Despite the agreement between instanton theory and experimental data, we observe a residual dependence of the fitting parameter b, which is related to both the temperature T and the density n of the system, on the Rabi frequency Ω_R. Fitting a power-law $1/b \propto \Omega_R^\beta$, we indeed find $\beta = 0.8 \pm 0.05$. As $1/b$ is proportional to the temperature, at first sight it looks like the effective temperature contributing to the decay process changes with the Rabi frequency, which might sound unphysical, unless heating process induced by the microwave dressing are taken into account.
A sensible explanation is that our approximated instanton formula for $\hat{E}_c$, given by Eq. 6.23, does not completely capture the scaling of τ with the control parameters $(\delta_B - \delta_c)$ and Ω_R. Limitations in the theory might either arise from the non completely 1D dimensionality of the sample, as demonstrated in Chapter 5, from the small barrier approximation of the potential $V(Z)$, or from relative phase contributions, present in Eq. 6.16 and neglected in the calculation of $\hat{E}_c$.
As an attempt to provide scaling exponents for a more refined theory, we correct the expression for $\hat{E}_c$, leaving exponents unbounded. In particular, we try to fit τ with three different definitions of the energy barrier:

$$\begin{aligned}
\hat{E}_c^{(1)} &= 1.77 \left(\frac{\delta_B - \delta_c}{|\kappa| n_0}\right)^{5/4} \left(\frac{\Omega_R}{|\kappa| n_0}\right)^{\beta} \left(\frac{|\delta_c|}{|\kappa| n_0}\right)^{-1/4} \\
\hat{E}_c^{(2)} &= 1.77 \left(\frac{\delta_B - \delta_c}{|\kappa| n_0}\right)^{\alpha} \left(\frac{\Omega_R}{|\kappa| n_0}\right)^{\beta} \left(\frac{|\delta_c|}{|\kappa| n_0}\right)^{-1/4} \\
\hat{E}_c^{(3)} &= 1.77 \left(\frac{\delta_B - \delta_c}{|\kappa| n_0}\right)^{\alpha} \left(\frac{\Omega_R}{|\kappa| n_0}\right)^{\beta}
\end{aligned} \tag{6.32}$$

For each definition of $\hat{E}_c^{(i)}$, $i = 1, 2, 3$, we repeat the fit of $\ln \tau$ merging the dataset at different Ω_R. With this procedure we now obtain, for each $\hat{E}_c^{(i)}$, a single value of b and, more importantly, values for α and β, as reported in Table 6.2.
Results of the fits are also reported in Fig. 6.9, where different definitions of $\hat{E}_c$ are labelled by different lines. We observe that, instanton theory still well matches experimental data, and, independently of Ω_R, the three curves are very similar between one another.

$\hat{E}_c$	$\alpha_{\rm exp}(\sigma_\alpha)$	$\beta_{\rm exp}(\sigma_\beta)$	$b_{\rm exp}$ (σ_b)
$\hat{E}_c^{(1)}$	5/4	-0.84(0.12)	15(2)
$\hat{E}_c^{(2)}$	1.03(0.2)	-0.77(0.13)	10(4)
$\hat{E}_c^{(3)}$	1.01(0.2)	-0.40(0.13)	33(12)

Table 6.2: Fitting exponents for the scaling of the energy barrier $\hat{E}_c$ on the control parameters. Each exponent is extracted from a two-variable fit of $\tau(\hat{E}_c)$. In the first line α is kept fixed.

From the fitted values of α and β, we observe that α is compatible, although slightly lower, with the one predicted by the theory. On the other hand we find a negative value of β, which also varies very much with each definition of $\hat{E}_c$. The theoretical calculation of such a different scaling, along with an in depth investigation of its origin, is still an open question.

Conclusions

In this Thesis, I reported on several experiments done on a Bose-Einstein condensate of ^{23}Na atoms in the presence of a coherent radiation that couples two spin states. Such an effective two-level system can be manipulated with a high degree of control, in particular thanks to the extreme stability of the magnetic field of our apparatus. Our experimental system is well suited for emulating a large variety of systems belonging to different fields of physics. Examples of them are magnetism in solid state matter and false vacuum decay in quantum field theory or particle creation in cosmology.

Two different spin mixtures were used. The first one represents a perfectly symmetric combination that is fully miscible and not subject to buoyancy effects. This represents an ideal experimental platform for the investigation of elementary oscillations and in fact we succeeded in measuring, for the first time, the Bogoliubov spectrum for both density and spin channels on the same system. The measurement was performed generating Faraday waves in the absence of coherent coupling, showing the expected behavior as expected from GPE simulations and revealing the presence of two distinct speeds of sound. The addition of the coherent coupling introduces a gap in the spin channel, that we measured as a function of the coupling strength. In this case, the generation of Faraday waves can be interpreted as the creation of massive excitations, and paves the way for analogue gravity studies with our platform. In particular, on the long run, the use of our protocol for a detailed measurement of density-density or spin-spin spatial correlations could shed light on the generation of entangled massless and massive particles in a modulated space-time.

We also used a second spin mixture that instead undergoes spatial phase separation, in the absence of coherent coupling. In the presence of coupling, the specific interaction constants of such a mixture allow it to exhibit a quantum phase transition from a single-minimum paramagnetic state to a double-minimum ferromagnetic one. Thanks to the exquisite stability of the bias magnetic field and the tunability of the control parameters we were able to experimentally measure the phase diagram of a magnetic material. The emergence of a phase transition was further validated through a measurement of diverging magnetic susceptibility and fluctuations. Taking advantage of the spatial extension of our sample, we also demonstrated the deterministic formation of domain walls, be-

tween ferromagnetic regions with opposite sign. This study places our platform as a promising candidate for the study of magnetic properties and the dynamics of magnetic excitations, in an environment free of dissipation and defects.

Finally, we used the same spin mixture to study the dynamics of a macroscopic field prepared in an extended metastable state. We observed the decay from such a metastable state to the absolute ground state of the field, which occur through the formation of macroscopic spin regions (bubbles), delimited by domain walls, that expand indefinitely. We performed a detailed measurement of the characteristic decay rate, which is characterized by an exponential growth as a function of the control parameters. Experimental data were compared with an instanton theory developed specifically for our platform. This allows us to interpret our results in strong analogy with the problem of false vacuum decay via bubble nucleation in quantum field theory.

The validity of the results detailed in this Thesis already demonstrates the capabilities and tunability of our platform. However there is still room for several upgrades on the experimental apparatus, which would help pushing our research further. A first major upgrade would be the use of a Digital Micromirror Device to generate arbitrary trapping potentials and create a homogeneous sample. This would give the possibility, for example, to create a controlled environment for the test of the fluctuation-dissipation theorem, allowing for a measurement of the spin temperature and for an investigation of the quantum or thermal origin of the magnetic fluctuations. On top of this, the addition of a local coherent coupling with optical radiation would give the possibility to create analogues of magnetic heterostructures and magnetic interfaces.
An arbitrary trapping potential could also be used to create a homogeneous two dimensional BEC, which would allow for a further characterization of the spatial properties of bubbles and for the study of their collisions. The implementation of a non-destructive imaging system is another interesting upgrade, since it would give the possibility to study the expansion dynamics of a stochastically generated bubble after its nucleation.

Scattering Lengths

In this Appendix I report the values of the scattering lengths between all Zeeman sublevels of $|F = 1\rangle$ and $|F = 2\rangle$ of ^{23}Na, calculated for $B = 1.5\,\mathrm{G}$, but valid between 0 and 2 G. We thank E. Tiemann for providing the calculated values [206]. Here, Table 3 reports the absolute value of the scattering length a_{ij}, in units of the Bohr radius $a_0 = 0.53\,\text{Å}$, for interactions between different hyperfine states i and j. Table 4 reports the ratio $\Delta a/a = \frac{a-a_{ij}}{a}$, where i, j again label different hyperfine states, and $a = \frac{a_{ii}+a_{jj}}{2}$ is their mean value.

	1,1	1,0	1,-1	2,-2	2,-1	2,0	2,1	2,2
1,1	54.538	54.519	50.750	56.983	53.156	53.060	56.781	64.273
1,0		52.633	54.495	49.002	60.524	64.273	60.550	48.747
1,-1			54.482	64.273	56.684	52.832	52.830	56.687
2,-2				64.265	64.265	53.587	48.272	41.817
2,-1					56.268	61.605	49.808	48.322
2,0						53.047	61.614	53.655
2,1							56.319	64.265
2,2								64.265

Table 3: Absolute value of the scattering lengths for atoms in different (or same) hyperfine states of the ground state of ^{23}Na.

	1,1	1,0	1,-1	2,-2	2,-1	2,0	2,1	2,2
1,1		-0.018	0.069	0.035	0.040	0.014	-0.024	-0.079
1,0			-0.017	0.187	-0.101	-0.178	-0.101	0.193
1,-1				-0.079	-0.023	0.018	0.049	0.044
2,-2					-0.064	0.090	0.246	0.537
2,-1						-0.113	0.130	0.244
2,0							-0.113	0.088
2,1								-0.064
2,2								

Table 4: Relative difference between intraspecies and interspecies scattering lengths, calculated as explained in the main text. Green (red) cells label miscible (immiscible) mixtures.

Bibliography

[1] M. H. Anderson, J. R. Ensher, M. R. Matthews, C. E. Wieman, and E. A. Cornell. Observation of Bose-Einstein Condensation in a Dilute Atomic Vapor. *Science*, 269(5221):198–201, 1995. Cited at page 1

[2] J. Kasprzak, M. Richard, S. Kundermann, A. Baas, P. Jeambrun, J. M. J. Keeling, F. M. Marchetti, M. H. Szymańska, R. André, J. L. Staehli, V. Savona, P. B. Littlewood, B. Deveaud, and Le Si Dang. Bose–Einstein condensation of exciton polaritons. *Nature*, 443(7110):409–414, Sep 2006. Cited at page 1

[3] Jan Klaers, Julian Schmitt, Frank Vewinger, and Martin Weitz. Bose–Einstein condensation of photons in an optical microcavity. *Nature*, 468(7323):545–548, Nov 2010. Cited at page 1

[4] Franco Dalfovo, Stefano Giorgini, Lev P. Pitaevskii, and Sandro Stringari. Theory of Bose-Einstein condensation in trapped gases. *Rev. Mod. Phys.*, 71:463–512, Apr 1999. Cited at pages 2, 3, 4, 5, and 80

[5] Cheng Chin, Rudolf Grimm, Paul Julienne, and Eite Tiesinga. Feshbach resonances in ultracold gases. *Rev. Mod. Phys.*, 82:1225–1286, Apr 2010. Cited at page 2

[6] Lev Pitaevskii and Sandro Stringari. *Bose-Einstein condensation and superfluidity*. International series of monographs on physics. Oxford University Press, Oxford, 2016. Cited at pages 3, 4, 6, 7, 9, 36, 54, 95, and 96

[7] C. Pethick and H. Smith. *Bose-Einstein condensation in dilute gases*. Cambridge University Press, 2002. Cited at pages 4 and 9

[8] Alexander L. Fetter. Ground state and excited states of a trapped dilute condensed Bose gas. *Czechoslovak Journal of Physics*, 46(6):3063–3069, Jun 1996. Cited at page 5

[9] J. Steinhauer, R. Ozeri, N. Katz, and N. Davidson. Excitation Spectrum of a Bose-Einstein Condensate. *Phys. Rev. Lett.*, 88:120407, Mar 2002. Cited at pages 5 and 63

[10] G. Modugno, M. Modugno, F. Riboli, G. Roati, and M. Inguscio. Two Atomic Species Superfluid. *Phys. Rev. Lett.*, 89:190404, Oct 2002. Cited at page 5

[11] A. Burchianti, C. D'Errico, S. Rosi, A. Simoni, M. Modugno, C. Fort, and F. Minardi. Dual-species Bose-Einstein condensate of ^{41}K and ^{87}Rb in a hybrid trap. *Phys. Rev. A*, 98:063616, Dec 2018. Cited at page 5

[12] A. Mosk, S. Kraft, M. Mudrich, K. Singer, W. Wohlleben, R. Grimm, and M. Weidemüller. Mixture of ultracold lithium and cesium atoms in an optical dipole trap. *Applied Physics B*, 73(8):791–799, Dec 2001. Cited at page 5

[13] Tetsu Takekoshi, Lukas Reichsöllner, Andreas Schindewolf, Jeremy M. Hutson, C. Ruth Le Sueur, Olivier Dulieu, Francesca Ferlaino, Rudolf Grimm, and Hanns-Christoph Nägerl. Ultracold Dense Samples of Dipolar RbCs Molecules in the Rovibrational and Hyperfine Ground State. *Phys. Rev. Lett.*, 113:205301, Nov 2014. Cited at page 5

[14] E. Wille, F. M. Spiegelhalder, G. Kerner, D. Naik, A. Trenkwalder, G. Hendl, F. Schreck, R. Grimm, T. G. Tiecke, J. T. M. Walraven, S. J. J. M. F. Kokkelmans, E. Tiesinga, and P. S. Julienne. Exploring an Ultracold Fermi-Fermi Mixture: Interspecies Feshbach Resonances and Scattering Properties of ^{6}Li and ^{40}K. *Phys. Rev. Lett.*, 100:053201, Feb 2008. Cited at page 5

[15] M. Taglieber, A.-C. Voigt, T. Aoki, T. W. Hänsch, and K. Dieckmann. Quantum Degenerate Two-Species Fermi-Fermi Mixture Coexisting with a Bose-Einstein Condensate. *Phys. Rev. Lett.*, 100:010401, Jan 2008. Cited at page 5

[16] C. Ravensbergen, E. Soave, V. Corre, M. Kreyer, B. Huang, E. Kirilov, and R. Grimm. Resonantly Interacting Fermi-Fermi Mixture of ^{161}Dy and ^{40}K. *Phys. Rev. Lett.*, 124:203402, May 2020. Cited at page 5

[17] F. Schreck, L. Khaykovich, K. L. Corwin, G. Ferrari, T. Bourdel, J. Cubizolles, and C. Salomon. Quasipure Bose-Einstein Condensate Immersed in a Fermi Sea. *Phys. Rev. Lett.*, 87:080403, Aug 2001. Cited at page 5

[18] I. Ferrier-Barbut, M. Delehaye, S. Laurent, A. T. Grier, M. Pierce, B. S. Rem, F. Chevy, and C. Salomon. A mixture of Bose and Fermi superfluids. *Science*, 345(6200):1035–1038, 2014. Cited at page 5

[19] Z. Hadzibabic, C. A. Stan, K. Dieckmann, S. Gupta, M. W. Zwierlein, A. Görlitz, and W. Ketterle. Two-Species Mixture of Quantum Degenerate Bose and Fermi Gases. *Phys. Rev. Lett.*, 88:160401, Apr 2002. Cited at page 5

[20] G. Roati, F. Riboli, G. Modugno, and M. Inguscio. Fermi-Bose Quantum Degenerate ^{40}K–^{87}Rb Mixture with Attractive Interaction. *Phys. Rev. Lett.*, 89:150403, Sep 2002. Cited at page 5

[21] Dan M. Stamper-Kurn and Masahito Ueda. Spinor Bose gases: Symmetries, magnetism, and quantum dynamics. *Rev. Mod. Phys.*, 85:1191–1244, Jul 2013. Cited at pages 6 and 70

[22] D. S. Hall, M. R. Matthews, J. R. Ensher, C. E. Wieman, and E. A. Cornell. Dynamics of Component Separation in a Binary Mixture of Bose-Einstein Condensates. *Phys. Rev. Lett.*, 81:1539–1542, Aug 1998. Cited at page 6

[23] C. J. Myatt, E. A. Burt, R. W. Ghrist, E. A. Cornell, and C. E. Wieman. Production of Two Overlapping Bose-Einstein Condensates by Sympathetic Cooling. *Phys. Rev. Lett.*, 78:586–589, Jan 1997. Cited at page 6

[24] M. R. Matthews, B. P. Anderson, P. C. Haljan, D. S. Hall, M. J. Holland, J. E. Williams, C. E. Wieman, and E. A. Cornell. Watching a Superfluid Untwist Itself: Recurrence of Rabi Oscillations in a Bose-Einstein Condensate. *Phys. Rev. Lett.*, 83:3358–3361, Oct 1999. Cited at page 6

[25] K. Jiménez-García, A. Invernizzi, B. Evrard, C. Frapolli, J. Dalibard, and F. Gerbier. Spontaneous formation and relaxation of spin domains in antiferromagnetic spin-1 condensates. *Nature Communications*, 10(1):1422, Mar 2019. Cited at pages 6 and 98

[26] E. M. Bookjans, A. Vinit, and C. Raman. Quantum Phase Transition in an Antiferromagnetic Spinor Bose-Einstein Condensate. *Phys. Rev. Lett.*, 107:195306, Nov 2011. Cited at page 6

[27] J. Stenger, S. Inouye, D. M. Stamper-Kurn, H.-J. Miesner, A. P. Chikkatur, and W. Ketterle. Spin domains in ground-state Bose–Einstein condensates. *Nature*, 396(6709):345–348, Nov 1998. Cited at page 6

[28] M.-S. Chang, C. D. Hamley, M. D. Barrett, J. A. Sauer, K. M. Fortier, W. Zhang, L. You, and M. S. Chapman. Observation of Spinor Dynamics in Optically Trapped ^{87}Rb Bose-Einstein Condensates. *Phys. Rev. Lett.*, 92:140403, Apr 2004. Cited at page 6

[29] Giacomo Lamporesi. Two-component spin mixtures, 2023, 2304.03711. Cited at pages 7 and 10

[30] D. S. Petrov. Quantum Mechanical Stabilization of a Collapsing Bose-Bose Mixture. *Phys. Rev. Lett.*, 115:155302, Oct 2015. Cited at page 7

[31] C. R. Cabrera, L. Tanzi, J. Sanz, B. Naylor, P. Thomas, P. Cheiney, and L. Tarruell. Quantum liquid droplets in a mixture of Bose-Einstein condensates. *Science*, 359(6373):301–304, 2018. Cited at page 7

[32] G. Semeghini, G. Ferioli, L. Masi, C. Mazzinghi, L. Wolswijk, F. Minardi, M. Modugno, G. Modugno, M. Inguscio, and M. Fattori. Self-Bound Quantum Droplets

of Atomic Mixtures in Free Space. *Phys. Rev. Lett.*, 120:235301, Jun 2018. Cited at page 7

[33] C. D'Errico, A. Burchianti, M. Prevedelli, L. Salasnich, F. Ancilotto, M. Modugno, F. Minardi, and C. Fort. Observation of quantum droplets in a heteronuclear bosonic mixture. *Phys. Rev. Res.*, 1:033155, Dec 2019. Cited at page 7

[34] Tin-Lun Ho and V. B. Shenoy. Binary Mixtures of Bose Condensates of Alkali Atoms. *Phys. Rev. Lett.*, 77:3276–3279, Oct 1996. Cited at page 7

[35] Weizhu Bao, Dieter Jaksch, and Peter A. Markowich. Numerical solution of the Gross–Pitaevskii equation for Bose–Einstein condensation. *Journal of Computational Physics*, 187(1):318–342, 2003. Cited at page 8

[36] Kenichi Kasamatsu and Makoto Tsubota. Multiple Domain Formation Induced by Modulation Instability in Two-Component Bose-Einstein Condensates. *Phys. Rev. Lett.*, 93:100402, Sep 2004. Cited at page 10

[37] Joon Hyun Kim, Deokhwa Hong, and Y. Shin. Observation of two sound modes in a binary superfluid gas. *Phys. Rev. A*, 101:061601, Jun 2020. Cited at pages 10 and 63

[38] Y.-J. Lin, R. L. Compton, K. Jiménez-García, J. V. Porto, and I. B. Spielman. Synthetic magnetic fields for ultracold neutral atoms. *Nature*, 462(7273):628–632, Dec 2009. Cited at page 10

[39] Y.-J. Lin, K. Jiménez-García, and I. B. Spielman. Spin–orbit-coupled Bose–Einstein condensates. *Nature*, 471(7336):83–86, Mar 2011. Cited at page 10

[40] Alessio Recati and Sandro Stringari. Coherently Coupled Mixtures of Ultracold Atomic Gases. *Annual Review of Condensed Matter Physics*, 13(1):407–432, 2022. Cited at pages 11, 70, and 74

[41] Marta Abad and Alessio Recati. A study of coherently coupled two-component Bose-Einstein condensates. *The European Physical Journal D*, 67(7):148, Jul 2013. Cited at pages 11, 13, and 62

[42] Tilman Zibold, Eike Nicklas, Christian Gross, and Markus K. Oberthaler. Classical Bifurcation at the Transition from Rabi to Josephson Dynamics. *Phys. Rev. Lett.*, 105:204101, Nov 2010. Cited at pages 12, 16, 17, 39, and 71

[43] Chaohong Lee, Wenhua Hai, Lei Shi, and Kelin Gao. Phase-dependent spontaneous spin polarization and bifurcation delay in coupled two-component Bose-Einstein condensates. *Phys. Rev. A*, 69:033611, Mar 2004. Cited at pages 13, 16, and 17

[44] Paolo Tommasini, E. J. V. de Passos, A. F. R. de Toledo Piza, M. S. Hussein, and E. Timmermans. Bogoliubov theory for mutually coherent condensates. *Phys. Rev. A*, 67:023606, Feb 2003. Cited at page 13

[45] T. Nikuni and J. E. Williams. Kinetic Theory of a Spin-1/2 Bose-Condensed Gas. *Journal of Low Temperature Physics*, 133(5):323–375, Dec 2003. Cited at pages 15 and 78

[46] Helmut Strobel, Wolfgang Muessel, Daniel Linnemann, Tilman Zibold, David B. Hume, Luca Pezzè, Augusto Smerzi, and Markus K. Oberthaler. Fisher information and entanglement of non-Gaussian spin states. *Science*, 345(6195):424–427, 2014. Cited at page 16

[47] J. Estève, C. Gross, A. Weller, S. Giovanazzi, and M. K. Oberthaler. Squeezing and entanglement in a Bose–Einstein condensate. *Nature*, 455(7217):1216–1219, Oct 2008. Cited at page 16

[48] E. Nicklas, W. Muessel, H. Strobel, P. G. Kevrekidis, and M. K. Oberthaler. Nonlinear dressed states at the miscibility-immiscibility threshold. *Phys. Rev. A*, 92:053614, Nov 2015. Cited at pages 16, 18, 77, and 90

[49] Masahiro Kitagawa and Masahito Ueda. Squeezed spin states. *Phys. Rev. A*, 47:5138–5143, Jun 1993. Cited at page 16

[50] B.D. Josephson. Possible new effects in superconductive tunnelling. *Physics Letters*, 1(7):251–253, 1962. Cited at page 17

[51] R Gati and M K Oberthaler. A bosonic Josephson junction. *Journal of Physics B: Atomic, Molecular and Optical Physics*, 40(10):R61, may 2007. Cited at page 17

[52] Michael Albiez, Rudolf Gati, Jonas Fölling, Stefan Hunsmann, Matteo Cristiani, and Markus K. Oberthaler. Direct Observation of Tunneling and Nonlinear Self-Trapping in a Single Bosonic Josephson Junction. *Phys. Rev. Lett.*, 95:010402, Jun 2005. Cited at pages 17, 39, and 47

[53] Marine Pigneur, Tarik Berrada, Marie Bonneau, Thorsten Schumm, Eugene Demler, and Jörg Schmiedmayer. Relaxation to a Phase-Locked Equilibrium State in a One-Dimensional Bosonic Josephson Junction. *Phys. Rev. Lett.*, 120:173601, Apr 2018. Cited at pages 17 and 39

[54] S. Raghavan, A. Smerzi, S. Fantoni, and S. R. Shenoy. Coherent oscillations between two weakly coupled Bose-Einstein condensates: Josephson effects, π oscillations, and macroscopic quantum self-trapping. *Phys. Rev. A*, 59:620–633, Jan 1999. Cited at pages 17 and 39

[55] Chaohong Lee. Universality and Anomalous Mean-Field Breakdown of Symmetry-Breaking Transitions in a Coupled Two-Component Bose-Einstein Condensate. *Phys. Rev. Lett.*, 102:070401, Feb 2009. Cited at page 17

[56] Nathan R. Bernier, Emanuele G. Dalla Torre, and Eugene Demler. Unstable Avoided Crossing in Coupled Spinor Condensates. *Phys. Rev. Lett.*, 113:065303, Aug 2014. Cited at pages 18 and 45

[57] Tilman Zibold. *Classical Bifurcation and Entanglement Generation in an Internal Bosonic Josephson Junction*. PhD thesis, University of Heidelberg, 2012. Cited at page 18

[58] A. Farolfi, A. Zenesini, D. Trypogeorgos, C. Mordini, A. Gallemí, A. Roy, A. Recati, G. Lamporesi, and G. Ferrari. Quantum-torque-induced breaking of magnetic interfaces in ultracold gases. *Nature Physics*, 17(12):1359–1363, Dec 2021. Cited at pages 18, 31, 39, and 75

[59] E. Nicklas, H. Strobel, T. Zibold, C. Gross, B. A. Malomed, P. G. Kevrekidis, and M. K. Oberthaler. Rabi Flopping Induces Spatial Demixing Dynamics. *Phys. Rev. Lett.*, 107:193001, Nov 2011. Cited at page 18

[60] S. Bresolin, A. Roy, G. Ferrari, A. Recati, and N. Pavloff. Oscillating Solitons and ac Josephson Effect in Ferromagnetic Bose-Bose Mixtures. *Phys. Rev. Lett.*, 130:220403, May 2023. Cited at page 18

[61] L.D. Landau and E.M. Lifshitz. On the theory of the dispersion of magnetic permeability in ferromagnetic bodies. *Phys. Z. Sowjet.*, 8:153–164, 1935. Cited at pages 19 and 72

[62] V. G. Bar'yakhtar and B. A. Ivanov. The Landau-Lifshitz equation: 80 years of history, advances, and prospects. *Low Temperature Physics*, 41(9):663–669, 09 2015. Cited at page 19

[63] Arturo Farolfi. *Spin dynamics in two-component Bose-Einstein condensates*. PhD thesis, University of Trento, 2020. Cited at pages 20, 22, 24, 25, 31, and 47

[64] Giacomo Colzi. *A new apparatus to simulate fundamental interactions with ultracold atoms*. PhD thesis, University of Trento, 2018. Cited at pages 22, 23, and 30

[65] G. Lamporesi, S. Donadello, S. Serafini, and G. Ferrari. Compact high-flux source of cold sodium atoms. *Review of Scientific Instruments*, 84(6):063102, 2013. Cited at page 22

[66] Giacomo Colzi, Gianmaria Durastante, Eleonora Fava, Simone Serafini, Giacomo Lamporesi, and Gabriele Ferrari. Sub-Doppler cooling of sodium atoms in gray molasses. *Phys. Rev. A*, 93:023421, Feb 2016. Cited at pages 23 and 30

[67] Laura Botti, Roberto Buffa, Andrea Bertoldi, Davide Bassi, and Leonardo Ricci. Noninvasive system for the simultaneous stabilization and control of magnetic field strength and gradient. *Review of Scientific Instruments*, 77(3), 03 2006. 035103. Cited at page 24

[68] C. J. Dedman, R. G. Dall, L. J. Byron, and A. G. Truscott. Active cancellation of stray magnetic fields in a Bose-Einstein condensation experiment. *Review of Scientific Instruments*, 78(2), 02 2007. 024703. Cited at page 24

[69] Eleonora Fava. *Static and dynamics properties of a miscible two-component Bose-Einstein condensate*. PhD thesis, University of Trento, 2018. Cited at page 24

[70] A. Farolfi, D. Trypogeorgos, G. Colzi, E. Fava, G. Lamporesi, and G. Ferrari. Design and characterization of a compact magnetic shield for ultracold atomic gas experiments. *Review of Scientific Instruments*, 90(11):115114, 11 2019. Cited at page 24

[71] Daniel Steck. Sodium D Line Data. 2003. Cited at pages 25, 29, and 31

[72] Ldc501 datasheet. `https://www.thinksrs.com/downloads/pdfs/catalog/LDC500c.pdf`. Cited at page 26

[73] Rudolf Grimm, Matthias Weidemüller, and Yurii B. Ovchinnikov. Optical Dipole Traps for Neutral Atoms. volume 42 of *Advances In Atomic, Molecular, and Optical Physics*, pages 95–170. Academic Press, 2000. Cited at pages 26 and 56

[74] Nir Navon, Robert P. Smith, and Zoran Hadzibabic. Quantum gases in optical boxes. *Nature Physics*, 17(12):1334–1341, Dec 2021. Cited at page 28

[75] Wolfgang Ketterle, Kendall B. Davis, Michael A. Joffe, Alex Martin, and David E. Pritchard. High densities of cold atoms in a dark spontaneous-force optical trap. *Phys. Rev. Lett.*, 70:2253–2256, Apr 1993. Cited at page 29

[76] A. Aspect, E. Arimondo, R. Kaiser, N. Vansteenkiste, and C. Cohen-Tannoudji. Laser Cooling below the One-Photon Recoil Energy by Velocity-Selective Coherent Population Trapping. *Phys. Rev. Lett.*, 61:826–829, Aug 1988. Cited at page 30

[77] C. Salomon, J. Dalibard, W. D. Phillips, A. Clairon, and S. Guellati. Laser Cooling of Cesium Atoms Below 3 K. *Europhysics Letters*, 12(8):683, aug 1990. Cited at page 30

[78] M. S. Shahriar, P. R. Hemmer, M. G. Prentiss, P. Marte, J. Mervis, D. P. Katz, N. P. Bigelow, and T. Cai. Continuous polarization-gradient precooling-assisted velocity-selective coherent population trapping. *Phys. Rev. A*, 48:R4035–R4038, Dec 1993. Cited at page 30

[79] M. Weidemüller, T. Esslinger, M. A. Ol'shanii, A. Hemmerich, and T. W. Hänsch. A Novel Scheme for Efficient Cooling below the Photon Recoil Limit. *Europhysics Letters*, 27(2):109, jul 1994. Cited at page 30

[80] Wolfgang Ketterle and N.J. Van Druten. Evaporative Cooling of Trapped Atoms. volume 37 of *Advances In Atomic, Molecular, and Optical Physics*, pages 181–236. Academic Press, 1996. Cited at page 30

[81] Giacomo Colzi, Eleonora Fava, Matteo Barbiero, Carmelo Mordini, Giacomo Lamporesi, and Gabriele Ferrari. Production of large Bose-Einstein condensates in a magnetic-shield-compatible hybrid trap. *Phys. Rev. A*, 97:053625, May 2018. Cited at page 30

[82] A. Farolfi, D. Trypogeorgos, C. Mordini, G. Lamporesi, and G. Ferrari. Observation of Magnetic Solitons in Two-Component Bose-Einstein Condensates. *Phys. Rev. Lett.*, 125:030401, Jul 2020. Cited at pages 31 and 34

[83] C.J. Foot. *Atomic Physics*. Oxford Master Series in Physics. OUP Oxford, 2005. Cited at page 32

[84] J. M. Higbie, L. E. Sadler, S. Inouye, A. P. Chikkatur, S. R. Leslie, K. L. Moore, V. Savalli, and D. M. Stamper-Kurn. Direct Nondestructive Imaging of Magnetization in a Spin-1 Bose-Einstein Gas. *Phys. Rev. Lett.*, 95:050401, Jul 2005. Cited at pages 33 and 116

[85] Carmelo Mordini. *Measurement of the density profile of quantized vortices and of the equation of state in a 3D interacting Bose gas*. PhD thesis, University of Trento, 2019. Cited at page 34

[86] Hamamatsu orca-flash4.0 v3 digital cmos camera. `https://www.hamamatsu.com/eu/en/product/cameras/cmos-cameras/C13440-20CU.html`. Cited at page 34

[87] C. Mordini, D. Trypogeorgos, L. Wolswijk, G. Lamporesi, and G. Ferrari. Single-shot reconstruction of the density profile of a dense atomic gas. *Opt. Express*, 28(20):29408–29418, Sep 2020. Cited at pages 34 and 80

[88] Y. Castin and R. Dum. Bose-Einstein Condensates in Time Dependent Traps. *Phys. Rev. Lett.*, 77:5315–5319, Dec 1996. Cited at page 34

[89] C. L. Degen, F. Reinhard, and P. Cappellaro. Quantum sensing. *Rev. Mod. Phys.*, 89:035002, Jul 2017. Cited at page 35

[90] David W. Allan. Statistics of atomic frequency standards. 1966. Cited at page 37

[91] T. Betz, S. Manz, R. Bücker, T. Berrada, Ch. Koller, G. Kazakov, I. E. Mazets, H.-P. Stimming, A. Perrin, T. Schumm, and J. Schmiedmayer. Two-Point Phase Correlations of a One-Dimensional Bosonic Josephson Junction. *Phys. Rev. Lett.*, 106:020407, Jan 2011. Cited at page 39

[92] S. Levy, E. Lahoud, I. Shomroni, and J. Steinhauer. The a.c. and d.c. Josephson effects in a Bose–Einstein condensate. *Nature*, 449(7162):579–583, Oct 2007. Cited at page 39

[93] R. Cominotti, A. Berti, C. Dulin, C. Rogora, G. Lamporesi, I. Carusotto, A. Recati, A. Zenesini, and G. Ferrari. Ferromagnetism in an Extended Coherently Coupled Atomic Superfluid. *Phys. Rev. X*, 13:021037, Jun 2023. Cited at pages 39, 71, 86, and 88

[94] E. Nicklas, M. Karl, M. Höfer, A. Johnson, W. Muessel, H. Strobel, J. Tomkovič, T. Gasenzer, and M. K. Oberthaler. Observation of Scaling in the Dynamics of a Strongly Quenched Quantum Gas. *Phys. Rev. Lett.*, 115:245301, Dec 2015. Cited at pages 39, 71, and 77

[95] A. Farolfi, A. Zenesini, R. Cominotti, D. Trypogeorgos, A. Recati, G. Lamporesi, and G. Ferrari. Manipulation of an elongated internal Josephson junction of bosonic atoms. *Phys. Rev. A*, 104:023326, Aug 2021. Cited at page 39

[96] D. S. Petrov, G. V. Shlyapnikov, and J. T. M. Walraven. Regimes of Quantum Degeneracy in Trapped 1D Gases. *Phys. Rev. Lett.*, 85:3745–3749, Oct 2000. Cited at pages 40 and 77

[97] A. Görlitz, J. M. Vogels, A. E. Leanhardt, C. Raman, T. L. Gustavson, J. R. Abo-Shaeer, A. P. Chikkatur, S. Gupta, S. Inouye, T. Rosenband, and W. Ketterle. Realization of Bose-Einstein Condensates in Lower Dimensions. *Phys. Rev. Lett.*, 87:130402, Sep 2001. Cited at pages 40 and 77

[98] Chunlei Qu, Lev P. Pitaevskii, and Sandro Stringari. Magnetic Solitons in a Binary Bose-Einstein Condensate. *Phys. Rev. Lett.*, 116:160402, Apr 2016. Cited at page 44

[99] Chunlei Qu, Marek Tylutki, Sandro Stringari, and Lev P. Pitaevskii. Magnetic solitons in Rabi-coupled Bose-Einstein condensates. *Phys. Rev. A*, 95:033614, Mar 2017. Cited at page 44

[100] D. Guéry-Odelin, A. Ruschhaupt, A. Kiely, E. Torrontegui, S. Martínez-Garaot, and J. G. Muga. Shortcuts to adiabaticity: Concepts, methods, and applications. *Rev. Mod. Phys.*, 91:045001, Oct 2019. Cited at page 44

[101] M. J. Steel and M. J. Collett. Quantum state of two trapped Bose-Einstein condensates with a Josephson coupling. *Phys. Rev. A*, 57:2920–2930, Apr 1998. Cited at pages 44 and 45

[102] Daniel Steck. *Quantum and Atom Optics*. revision 0.12.6 edition, 2019. Cited at page 44

[103] M Faraday. On a peculiar class of acoustical figures; and on certain forms assumed by groups of particles upon vibrating elastic surfaces. 1821. Cited at page 49

[104] C. Tozzo, M. Krämer, and F. Dalfovo. Stability diagram and growth rate of parametric resonances in Bose-Einstein condensates in one-dimensional optical lattices. *Phys. Rev. A*, 72:023613, Aug 2005. Cited at page 49

[105] M. Krämer, C. Tozzo, and F. Dalfovo. Parametric excitation of a Bose-Einstein condensate in a one-dimensional optical lattice. *Phys. Rev. A*, 71:061602, Jun 2005. Cited at page 49

[106] Alexandru I. Nicolin, R. Carretero-González, and P. G. Kevrekidis. Faraday waves in Bose-Einstein condensates. *Phys. Rev. A*, 76:063609, Dec 2007. Cited at pages 49, 50, 56, 59, and 60

[107] P. Engels, C. Atherton, and M. A. Hoefer. Observation of Faraday Waves in a Bose-Einstein Condensate. *Phys. Rev. Lett.*, 98:095301, Feb 2007. Cited at pages 49 and 56

[108] Diego Hernández-Rajkov, José Eduardo Padilla-Castillo, Alejandra del Río-Lima, Andrés Gutiérrez-Valdés, Freddy Jackson Poveda-Cuevas, and Jorge Amin Seman. Faraday waves in strongly interacting superfluids. *New Journal of Physics*, 23(10):103038, oct 2021. Cited at pages 50 and 60

[109] J. H. V. Nguyen, M. C. Tsatsos, D. Luo, A. U. J. Lode, G. D. Telles, V. S. Bagnato, and R. G. Hulet. Parametric Excitation of a Bose-Einstein Condensate: From Faraday Waves to Granulation. *Phys. Rev. X*, 9:011052, Mar 2019. Cited at pages 50 and 56

[110] Logan W. Clark, Anita Gaj, Lei Feng, and Cheng Chin. Collective emission of matter-wave jets from driven Bose–Einstein condensates. *Nature*, 551(7680):356–359, Nov 2017. Cited at page 50

[111] Tadej Mežnaršič, Rok Žitko, Tina Arh, Katja Gosar, Erik Zupanič, and Peter Jeglič. Emission of correlated jets from a driven matter-wave soliton in a quasi-one-dimensional geometry. *Phys. Rev. A*, 101:031601, Mar 2020. Cited at page 50

[112] J. Smits, L. Liao, H. T. C. Stoof, and P. van der Straten. Observation of a Space-Time Crystal in a Superfluid Quantum Gas. *Phys. Rev. Lett.*, 121:185301, Oct 2018. Cited at page 50

[113] J. Smits, H. T. C. Stoof, and P. van der Straten. Spontaneous breaking of a discrete time-translation symmetry. *Phys. Rev. A*, 104:023318, Aug 2021. Cited at page 50

[114] R. Cominotti, A. Berti, A. Farolfi, A. Zenesini, G. Lamporesi, I. Carusotto, A. Recati, and G. Ferrari. Observation of Massless and Massive Collective Excitations with Faraday Patterns in a Two-Component Superfluid. *Phys. Rev. Lett.*, 128:210401, May 2022. Cited at page 50

[115] M. C. Cross and P. C. Hohenberg. Pattern formation outside of equilibrium. *Rev. Mod. Phys.*, 65:851–1112, Jul 1993. Cited at page 50

[116] Kestutis Staliunas, Stefano Longhi, and Germán J. de Valcárcel. Faraday Patterns in Bose-Einstein Condensates. *Phys. Rev. Lett.*, 89:210406, Nov 2002. Cited at page 50

[117] Yu. Kagan and L.A. Manakova. Condensation of phonons in an ultracold Bose gas. *Physics Letters A*, 361(4):401–405, 2007. Cited at page 50

[118] Matt Visser and Silke Weinfurtner. Massive Klein-Gordon equation from a Bose-Einstein-condensation-based analogue spacetime. *Phys. Rev. D*, 72:044020, Aug 2005. Cited at pages 50 and 67

[119] Lev Kofman, Andrei Linde, and Alexei A. Starobinsky. Towards the theory of reheating after inflation. *Phys. Rev. D*, 56:3258–3295, Sep 1997. Cited at pages 50 and 52

[120] Xavier Busch, Renaud Parentani, and Scott Robertson. Quantum entanglement due to a modulated dynamical Casimir effect. *Phys. Rev. A*, 89:063606, Jun 2014. Cited at page 50

[121] I. Carusotto, R. Balbinot, A. Fabbri, and A. Recati. Density correlations and analog dynamical Casimir emission of Bogoliubov phonons in modulated atomic Bose-Einstein condensates. *The European Physical Journal D*, 56(3):391–404, Feb 2010. Cited at page 50

[122] J.-C. Jaskula, G. B. Partridge, M. Bonneau, R. Lopes, J. Ruaudel, D. Boiron, and C. I. Westbrook. Acoustic Analog to the Dynamical Casimir Effect in a Bose-Einstein Condensate. *Phys. Rev. Lett.*, 109:220401, Nov 2012. Cited at page 50

[123] Gerald T. Moore. Quantum Theory of the Electromagnetic Field in a Variable-Length One-Dimensional Cavity. *Journal of Mathematical Physics*, 11(9):2679–2691, 10 2003. Cited at page 51

[124] P. D. Nation, J. R. Johansson, M. P. Blencowe, and Franco Nori. Colloquium: Stimulating uncertainty: Amplifying the quantum vacuum with superconducting circuits. *Rev. Mod. Phys.*, 84:1–24, Jan 2012. Cited at page 51

[125] N.W. McLachlan. *Theory and application of Mathieu functions*. (Dover Publications). Dover Publications, 1964. Cited at page 52

[126] L.D. Landau and E.M. Lifshitz. *Mechanics: Volume 1*. Course of theoretical physics. Elsevier Science, 1976. Cited at page 52

[127] S. Stringari. Dynamics of Bose-Einstein condensed gases in highly deformed traps. *Phys. Rev. A*, 58:2385–2388, Sep 1998. Cited at page 55

[128] J. Stenger, S. Inouye, M. R. Andrews, H.-J. Miesner, D. M. Stamper-Kurn, and W. Ketterle. Strongly Enhanced Inelastic Collisions in a Bose-Einstein Condensate near Feshbach Resonances. *Phys. Rev. Lett.*, 82:2422–2425, Mar 1999. Cited at page 56

[129] S. Knoop, T. Schuster, R. Scelle, A. Trautmann, J. Appmeier, M. K. Oberthaler, E. Tiesinga, and E. Tiemann. Feshbach spectroscopy and analysis of the interaction potentials of ultracold sodium. *Phys. Rev. A*, 83:042704, Apr 2011. Cited at page 56

[130] M. Modugno, C. Tozzo, and F. Dalfovo. Detecting phonons and persistent currents in toroidal Bose-Einstein condensates by means of pattern formation. *Phys. Rev. A*, 74:061601, Dec 2006. Cited at pages 56 and 60

[131] Mitchell J. Feigenbaum. The onset spectrum of turbulence. *Physics Letters A*, 74(6):375–378, 1979. Cited at page 65

[132] S. Ciliberto and J. P. Gollub. Pattern Competition Leads to Chaos. *Phys. Rev. Lett.*, 52:922–925, Mar 1984. Cited at page 65

[133] S. Ciliberto, S. Douady, and S. Fauve. Investigating Space-Time Chaos in Faraday Instability by Means of the Fluctuations of the Driving Acceleration. *Europhysics Letters*, 15(1):23, may 1991. Cited at page 65

[134] Salvatore Butera and Iacopo Carusotto. Particle creation in the spin modes of a dynamically oscillating two-component Bose-Einstein condensate. *Phys. Rev. D*, 104:083503, Oct 2021. Cited at page 66

[135] Salvatore Butera, Patrik Öhberg, and Iacopo Carusotto. Black-hole lasing in coherently coupled two-component atomic condensates. *Phys. Rev. A*, 96:013611, Jul 2017. Cited at page 66

[136] Iacopo Carusotto Anna Berti, Luca Giacomelli. Superradiant phononic emission from the analog spin ergoregion in a two-component Bose-Einstein condensate, 2023, arXiv:2304.03711. Cited at page 66

[137] Salvatore Butera and Iacopo Carusotto. Numerical Studies of Back Reaction Effects in an Analog Model of Cosmological Preheating. *Phys. Rev. Lett.*, 130:241501, Jun 2023. Cited at page 67

[138] E. Ising. Beitrag zur Theorie des Ferromagnetismus. *Zeitschrift für Physik*, XXXI:253–258, 1925. Cited at pages 70, 71, and 72

[139] Gregg Jaeger. The Ehrenfest Classification of Phase Transitions: Introduction and Evolution. *Archive for History of Exact Sciences*, 53(1):51–81, May 1998. Cited at page 70

[140] S. Ma. *Modern Theory Of Critical Phenomena*. Taylor & Francis, 2018. Cited at page 70

[141] N. Goldenfeld. *Lectures On Phase Transitions And The Renormalization Group*. CRC Press, 2018. Cited at page 70

[142] Matthias Vojta. Quantum phase transitions. *Reports on Progress in Physics*, 66(12):2069–2110, nov 2003. Cited at pages 70 and 89

[143] S. Sachdev. *Quantum phase transitions*. Cambridge University Press, New York, 2011. Cited at pages 70, 72, 87, 89, and 94

[144] Masatoshi Imada, Atsushi Fujimori, and Yoshinori Tokura. Metal-insulator transitions. *Rev. Mod. Phys.*, 70:1039–1263, Oct 1998. Cited at page 70

[145] K. Jiménez-García, A. Invernizzi, B. Evrard, C. Frapolli, J. Dalibard, and F. Gerbier. Spontaneous formation and relaxation of spin domains in antiferromagnetic spin-1 condensates. *Nature Communications*, 10(1):1422, 2019. Cited at page 70

[146] Markus Greiner, Olaf Mandel, Tilman Esslinger, Theodor W. Hänsch, and Immanuel Bloch. Quantum phase transition from a superfluid to a Mott insulator in a gas of ultracold atoms. *Nature*, 415(6867):39–44, Jan 2002. Cited at page 70

[147] D. L. Campbell, R. M. Price, A. Putra, A. Valdés-Curiel, D. Trypogeorgos, and I. B. Spielman. Magnetic phases of spin-1 spin–orbit-coupled Bose gases. *Nature Communications*, 7(1):10897, Mar 2016. Cited at page 70

[148] A. Trenkwalder, G. Spagnolli, G. Semeghini, S. Coop, M. Landini, P. Castilho, L. Pezzè, G. Modugno, M. Inguscio, A. Smerzi, and M. Fattori. Quantum phase transitions with parity-symmetry breaking and hysteresis. *Nature Physics*, 12(9):826–829, 2016. Cited at pages 70, 71, and 86

[149] Kristian Baumann, Christine Guerlin, Ferdinand Brennecke, and Tilman Esslinger. Dicke quantum phase transition with a superfluid gas in an optical cavity. *Nature*, 464(7293):1301–1306, Apr 2010. Cited at page 70

[150] L.D. Landau and E.M. Lifshitz. *Electrodynamics of Continuous Media. Course of Theoretical Physics.*, volume 8. Oxford: Butterworth-Heineman, 1984. Cited at page 70

[151] Claas Abert. Micromagnetics and spintronics: models and numerical methods. *The European Physical Journal B*, 92(6):120, 2019. Cited at page 72

[152] W. Ketterle, D. S. Durfee, and D. M. Stamper-Kurn. Making, probing and understanding Bose-Einstein condensates, 1999, cond-mat/9904034. Cited at pages 77 and 80

[153] D. M. Harber, H. J. Lewandowski, J. M. McGuirk, and E. A. Cornell. Effect of cold collisions on spin coherence and resonance shifts in a magnetically trapped ultracold gas. *Phys. Rev. A*, 66:053616, Nov 2002. Cited at page 78

[154] Victor V. Goldman, Isaac F. Silvera, and Anthony J. Leggett. Atomic hydrogen in an inhomogeneous magnetic field: Density profile and Bose-Einstein condensation. *Phys. Rev. B*, 24:2870–2873, Sep 1981. Cited at page 80

[155] Anna Berti. *Simulation of curved-space quantum field theories with two-coomponent Bose-Einstein condensates: from black hole physics to cosmology.* PhD thesis, Università of Trento, 2023. Manuscript in preparation. Cited at pages 86 and 118

[156] Gianluca Lagnese, Federica Maria Surace, Márton Kormos, and Pasquale Calabrese. False vacuum decay in quantum spin chains. *Phys. Rev. B*, 104:L201106, Nov 2021. Cited at pages 86, 100, 103, 114, and 115

[157] Alessandro Zenesini, Anna Berti, Riccardo Cominotti, Chiara Rogora, Ian G. Moss, Thomas P. Billam, Iacopo Carusotto, Giacomo Lamporesi, Alessio Recati, and Gabriele Ferrari. Observation of false vacuum decay via bubble formation in ferromagnetic superfluids, 2023, 2305.05225. Cited at pages 86, 100, and 104

[158] Arko Roy, Miki Ota, Franco Dalfovo, and Alessio Recati. Finite-temperature ferromagnetic transition in coherently coupled Bose gases. *Phys. Rev. A*, 107:043301, Apr 2023. Cited at page 89

[159] K. Binder and D. P. Landau. Finite-size scaling at first-order phase transitions. *Phys. Rev. B*, 30:1477–1485, Aug 1984. Cited at page 89

[160] K. Binder. Finite size effects on phase transitions. *Ferroelectrics*, 73(1):43–67, 1987. Cited at pages 89 and 90

[161] S. Giorgini, L. P. Pitaevskii, and S. Stringari. Anomalous Fluctuations of the Condensate in Interacting Bose Gases. *Phys. Rev. Lett.*, 80:5040–5043, Jun 1998. Cited at pages 92 and 95

[162] G. E. Astrakharchik, R. Combescot, and L. P. Pitaevskii. Fluctuations of the number of particles within a given volume in cold quantum gases. *Phys. Rev. A*, 76:063616, Dec 2007. Cited at pages 92 and 95

[163] M. Klawunn, A. Recati, L. P. Pitaevskii, and S. Stringari. Local atom-number fluctuations in quantum gases at finite temperature. *Phys. Rev. A*, 84:033612, Sep 2011. Cited at pages 92 and 95

[164] R Kubo. The fluctuation-dissipation theorem. *Reports on Progress in Physics*, 29(1):255, jan 1966. Cited at pages 93 and 94

[165] Léon Van Hove. Correlations in Space and Time and Born Approximation Scattering in Systems of Interacting Particles. *Phys. Rev.*, 95:249–262, Jul 1954. Cited at page 95

[166] Chen-Lung Hung, Xibo Zhang, Li-Chung Ha, Shih-Kuang Tung, Nathan Gemelke, and Cheng Chin. Extracting density–density correlations from in situ images of atomic quantum gases. *New Journal of Physics*, 13(7):075019, jul 2011. Cited at page 96

[167] G. Mussardo. *Statistical Field Theory: An Introduction to Exactly Solved Models in Statistical Physics*. Oxford Graduate Texts. OUP Oxford, 2010. Cited at page 98

[168] Wojciech H. Zurek. Cosmological experiments in superfluid liquid helium? *Nature*, 317:505–508, 1985. Cited at page 98

[169] W.H. Zurek. Cosmological experiments in condensed matter systems. *Physics Reports*, 276(4):177–221, 1996. Cited at page 98

[170] T W B Kibble. Topology of cosmic domains and strings. *J. Phys. A*, 9(8):1387, 1976. Cited at page 98

[171] T.W.B. Kibble. Some implications of a cosmological phase transition . *Phys. Rep.*, 67(1):183 – 199, 1980. Cited at page 98

[172] Kai-Xuan Yao, Zhendong Zhang, and Cheng Chin. Domain-wall dynamics in Bose–Einstein condensates with synthetic gauge fields. *Nature*, 602(7895):68–72, February 2022. Cited at page 98

[173] Colin V. Parker, Li-Chung Ha, and Cheng Chin. Direct observation of effective ferromagnetic domains of cold atoms in a shaken optical lattice. *Nature Physics*, 9(12):769–774, December 2013. Cited at page 98

[174] E. Albisetti and D. Petti. Domain wall engineering through exchange bias. *Journal of Magnetism and Magnetic Materials*, 400:230–235, 2016. Proceedings of the 20th International Conference on Magnetism (Barcelona) 5-10 July 2015. Cited at page 101

[175] H.A. Kramers. Brownian motion in a field of force and the diffusion model of chemical reactions. *Physica*, 7(4):284–304, 1940. Cited at page 103

[176] CJ Hogan. Gravitational radiation from cosmological phase transitions. *Monthly Notices of the Royal Astronomical Society*, 218(4):629–636, 1986. Cited at page 103

[177] M. E. Shaposhnikov. Baryon Asymmetry of the Universe in Standard Electroweak Theory. *Nucl. Phys. B*, 287:757–775, 1987. Cited at page 103

[178] Stephen M. Feeney, Matthew C. Johnson, Daniel J. Mortlock, and Hiranya V. Peiris. First observational tests of eternal inflation: Analysis methods and WMAP 7-year results. *Phys. Rev. D*, 84:043507, Aug 2011, 1012.3667. Cited at page 103

[179] Jeff Maki, Anna Berti, Iacopo Carusotto, and Alberto Biella. Monte Carlo matrix-product-state approach to the false vacuum decay in the monitored quantum Ising chain, 2023, 2306.01067. Cited at page 103

[180] Ashley Milsted, Junyu Liu, John Preskill, and Guifre Vidal. Collisions of False-Vacuum Bubble Walls in a Quantum Spin Chain. *PRX Quantum*, 3:020316, Apr 2022. Cited at page 103

[181] Sidney Coleman. Fate of the false vacuum: Semiclassical theory. *Phys. Rev. D*, 15:2929–2936, May 1977. Cited at pages 104, 106, 107, and 110

[182] Curtis G. Callan and Sidney Coleman. Fate of the false vacuum. II. First quantum corrections. *Phys. Rev. D*, 16:1762–1768, Sep 1977. Cited at page 104

[183] A.D. Linde. Decay of the false vacuum at finite temperature. *Nuclear Physics B*, 216(2):421–445, 1983. Cited at pages 104, 108, and 110

[184] Mark Hindmarsh, Marvin Lüben, Johannes Lumma, and Martin Pauly. Phase transitions in the early universe. *SciPost Phys. Lect. Notes*, page 24, 2021. Cited at pages 104, 108, and 109

[185] O. Fialko, B. Opanchuk, A. I. Sidorov, P. D. Drummond, and J. Brand. Fate of the false vacuum: Towards realization with ultra-cold atoms. *Europhysics Letters*, 110(5):56001, jun 2015. Cited at page 104

[186] Jonathan Braden, Matthew C. Johnson, Hiranya V. Peiris, and Silke Weinfurtner. Towards the cold atom analog false vacuum. *Journal of High Energy Physics*, 2018:2018, Oct 2019. Cited at page 104

[187] Thomas P. Billam, Ruth Gregory, Florent Michel, and Ian G. Moss. Simulating seeded vacuum decay in a cold atom system. *Phys. Rev. D*, 100:065016, Sep 2019. Cited at pages 104 and 118

[188] Zohreh Davoudi, Mohammad Hafezi, Christopher Monroe, Guido Pagano, Alireza Seif, and Andrew Shaw. Towards analog quantum simulations of lattice gauge theories with trapped ions. *Phys. Rev. Res.*, 2:023015, Apr 2020. Cited at page 104

[189] King Lun Ng, Bogdan Opanchuk, Manushan Thenabadu, Margaret Reid, and Peter D. Drummond. Fate of the False Vacuum: Finite Temperature, Entropy, and Topological Phase in Quantum Simulations of the Early Universe. *PRX Quantum*, 2:010350, Mar 2021. Cited at page 104

[190] Bo Song, Shovan Dutta, Shaurya Bhave, Jr-Chiun Yu, Edward Carter, Nigel Cooper, and Ulrich Schneider. Realizing discontinuous quantum phase transitions in a strongly correlated driven optical lattice. *Nature Physics*, 18(3):259–264, Mar 2022. Cited at page 104

[191] Thomas P. Billam, Kate Brown, and Ian G. Moss. False-vacuum decay in an ultracold spin-1 Bose gas. *Phys. Rev. A*, 105:L041301, Apr 2022. Cited at page 104

[192] Federica Devoto, Simone Devoto, Luca Di Luzio, and Giovanni Ridolfi. False vacuum decay: an introductory review. *Journal of Physics G: Nuclear and Particle Physics*, 49(10):103001, aug 2022. Cited at page 104

[193] L.D. Landau and E.M. Lifshitz. *Quantum Mechanics: Non-Relativistic Theory*. Course of Theoretical Physics. Elsevier Science, 1981. Cited at page 105

[194] L.D. Landau and E.M. Lifshitz. *Mechanics: Volume 1*. Number v. 1. Elsevier Science, 1982. Cited at page 105

[195] Erick J. Weinberg. *Classical Solutions in Quantum Field Theory: Solitons and Instantons in High Energy Physics*. Cambridge Monographs on Mathematical Physics. Cambridge University Press, 2012. Cited at page 106

[196] S. Coleman, V. Glaser, and A. Martin. Action minima among solutions to a class of Euclidean scalar field equations. *Communications in Mathematical Physics*, 58(2):211–221, Jun 1978. Cited at pages 107 and 116

[197] D. Szász-Schagrin and G. Takács. False vacuum decay in the $(1 + 1)$-dimensional φ^4 theory. *Phys. Rev. D*, 106:025008, Jul 2022. Cited at page 107

[198] Anupam Mazumdar and Graham White. Review of cosmic phase transitions: their significance and experimental signatures. *Reports on Progress in Physics*, 82(7):076901, jun 2019. Cited at page 108

[199] A.D. Linde. On the vacuum instability and the Higgs meson mass. *Physics Letters B*, 70(3):306–308, 1977. Cited at page 108

[200] A.D. Linde. Fate of the false vacuum at finite temperature: Theory and applications. *Physics Letters B*, 100(1):37–40, 1981. Cited at page 108

[201] Steven K. Blau, E. I. Guendelman, and Alan H. Guth. Dynamics of false-vacuum bubbles. *Phys. Rev. D*, 35:1747–1766, Mar 1987. Cited at page 116

[202] Marek Lewicki, Kristjan Müürsepp, Joosep Pata, Martin Vasar, Ville Vaskonen, and Hardi Veermäe. Dynamics of false vacuum bubbles with trapped particles. *Phys. Rev. D*, 108:036023, Aug 2023. Cited at page 116

[203] Stefano Scopa, Pasquale Calabrese, and Alvise Bastianello. Entanglement dynamics in confining spin chains. *Phys. Rev. B*, 105:125413, Mar 2022. Cited at page 116

[204] Y. Shin, M. W. Zwierlein, C. H. Schunck, A. Schirotzek, and W. Ketterle. Observation of Phase Separation in a Strongly Interacting Imbalanced Fermi Gas. *Phys. Rev. Lett.*, 97:030401, Jul 2006. Cited at page 116

[205] M. R. Andrews, D. M. Kurn, H.-J. Miesner, D. S. Durfee, C. G. Townsend, S. Inouye, and W. Ketterle. Propagation of Sound in a Bose-Einstein Condensate. *Phys. Rev. Lett.*, 79:553–556, Jul 1997. Cited at page 116

[206] E. Tiemann. Private communication, 2021. Cited at page 125